THE UNIVERSITY OF TEXAS AT AUSTIN
CENTER FOR TRANSPORTATION RESEARCH

TECHNICAL REPORT 0-6332-2
TxDOT PROJECT NUMBER 0-6332

Development of Predictive Model for Bridge Deck Cracking: Final Report

Philip Pesek
Dr. Kyle Riding
Dr. Anton Schindler
Dr. Kevin Folliard
Dr. Thanos Drimalas
Dr. Benjamin Byard

April 2013; Published April 2017

http://library.ctr.utexas.edu/ctr-publications/0-6332-2.pdf

Technical Report Documentation Page

1. Report No. FHWA/TX-13/0-6332-2	2. Government Accession No.	3. Recipient's Catalog No.

4. Title and Subtitle Development of Predictive Model for Bridge Deck Cracking: Final Report	5. Report Date April 2013; Published April 2017 6. Performing Organization Code
7. Author(s) Phil Pesek, Dr. Kyle Riding, Dr. Anton Schindler, Dr. Kevin Folliard, Dr. Thanos Drimalas, and Dr. Benjamin Byard	8. Performing Organization Report No. 0-6332-2
9. Performing Organization Name and Address Center for Transportation Research The University of Texas at Austin 1616 Guadalupe St., Suite 4.202 Austin, TX 78701	10. Work Unit No. (TRAIS) 11. Contract or Grant No. 0-6332
12. Sponsoring Agency Name and Address Texas Department of Transportation Research and Technology Implementation Office P.O. Box 5080 Austin, TX 78763-5080	13. Type of Report and Period Covered Technical Report; 9/1/2008–12/31/2011 14. Sponsoring Agency Code

15. Supplementary Notes
Project performed in cooperation with the Texas Department of Transportation and the Federal Highway Administration.

16. Abstract

Early-age bridge deck cracking has been found to be a prevalent problem worldwide. While early-age cracking will not cause failure of a bridge deck system independently, the penetration of deleterious substances through the early-age cracks into the bridge deck concrete and the bridge superstructure can lead to costly serviceability issues, and possibly the loss of some structural integrity. This report describes research undertaken to evaluate the various factors affecting bridge deck cracking, and the results of this project have been implemented in a new bridge deck cracking module for ConcreteWorks, a software program that addresses a range of concrete properties and performance issues.

17. Key Words ConcreteWorks, bridge, deck cracking, strengthening	18. Distribution Statement No restrictions. This document is available to the public through the National Technical Information Service, Springfield, Virginia 22161; www.ntis.gov.

19. Security Classif. (of report) Unclassified	20. Security Classif. (of this page) Unclassified	21. No. of pages 272	22. Price

Form DOT F 1700.7 (8-72) Reproduction of completed page authorized

THE UNIVERSITY OF TEXAS AT AUSTIN
CENTER FOR TRANSPORTATION RESEARCH

Development of Predictive Model for Bridge Deck Cracking: Final Report

Philip Pesek
Dr. Kyle Riding
Dr. Anton Schindler
Dr. Kevin Folliard
Dr. Thanos Drimalas
Dr. Benjamin Byard

CTR Technical Report:	0-6332-2
Report Date:	October 2012; Revised April 2013; Published April 2017
Project:	0-6332
Project Title:	Development of Predictive Model for Bridge Deck Cracking and Strength Development
Sponsoring Agency:	Texas Department of Transportation
Performing Agency:	Center for Transportation Research at The University of Texas at Austin

Project performed in cooperation with the Texas Department of Transportation and the Federal Highway Administration.

Center for Transportation Research
The University of Texas at Austin
1616 Guadalupe St., Suite 4.202
Austin, TX 78701
www.utexas.edu/research/ctr

Disclaimers

Author's Disclaimer: The contents of this report reflect the views of the authors, who are responsible for the facts and the accuracy of the data presented herein. The contents do not necessarily reflect the official view or policies of the Federal Highway Administration or the Texas Department of Transportation (TxDOT). This report does not constitute a standard, specification, or regulation.

Patent Disclaimer: There was no invention or discovery conceived or first actually reduced to practice in the course of or under this contract, including any art, method, process, machine manufacture, design or composition of matter, or any new useful improvement thereof, or any variety of plant, which is or may be patentable under the patent laws of the United States of America or any foreign country.

Engineering Disclaimer

NOT INTENDED FOR CONSTRUCTION, BIDDING, OR PERMIT PURPOSES.

Project Engineer: David W. Fowler
Professional Engineer License State and Number: Texas No. 27859
P. E. Designation: Researcher

Acknowledgments

The authors express appreciation to the TxDOT Project Director (Mr. Kevin Pruski), members of the Project Monitoring Committee, and the staff at the Concrete Durability Center.

Table of Contents

List of Figures

List of Tables

Chapter 1. Introduction

1.1 Background

Early-age bridge deck cracking has been found to be a prevalent problem worldwide. Studies conducted by Krauss and Rogalla (1996) and Folliard et al. (2003) reported various cases of early-age cracking in bridge deck concrete. While early-age cracking will not cause failure of a bridge deck system independently, the penetration of deleterious substances through the early-age cracks into the bridge deck concrete and the bridge superstructure can lead to costly serviceability issues, and possibly the loss of some structural integrity.

Bridge deck cracking is a multi-mechanistic process, affected by various volume change mechanisms, strength development, and the restraint conditions of the system. Before the concrete has even set, plastic shrinkage cracking due to water loss to the environment must be avoided. At an early age, the volume changes associated with the hydration reactions taking place can lead to chemical and autogenous shrinkage. After the curing system has been removed, the concrete must be able to withstand the drying shrinkage that will occur over the life of the structure. Thermal deformations, both as a gradient and as a bulk temperature change, can lead to significant stresses in the concrete system at both early and later ages. Moisture gradients and carbonation shrinkage, though typically minor factors, will also add to the volume changes occurring in the concrete over time. Restraint conditions and a changing elastic modulus turn these various volume changes into stresses, which must be resisted by the developing strength of the concrete and through relaxation from concrete creep.

To understand the volume changes and strength development that influence early-age bridge deck cracking, one must also understand the factors that affect the rate and magnitude of early-age volume change and strength development. These factors include mixture proportions, aggregate type and gradation, chemistry of the cements and supplementary cementitious materials used, and the changing temperature of the concrete system. While temperature of the concrete generally follows that of the environment at later ages, the early age concrete temperature that governs most of the volume changes and strength development is a complicated interaction between heat generated from concrete hydration, heat transfer with the environment, and heat transfer with elements of the bridge deck support structure.

This report summarizes the main findings from Texas Department of Transportation (TxDOT) Project 6332 and describes how the results of associated laboratory and field testing led to the development of a new bridge deck cracking module within ConcreteWorks 3.0.

1.2 Outline of Report

The remainder of this report is organized into the following chapters:

Chapter 2 presents a literature review of the key factors involved in early-age bridge deck cracking. Though not exhaustive, the literature review provides enough information for a general knowledge of volume changes in concrete, the development of mechanical properties, and of the key parameters affecting bridge deck cracking.

Chapter 3 provides an overview of the laboratory testing program. Physical and chemical descriptions of the materials used, followed by the mixture proportions for the mixture designs that were evaluated. An identification system is provided to aid in uniquely identify the various mixtures that were evaluated. Chapter 3 also includes a description of the procedures that were taken before, during, and after the day of mixing. Chapter 3 concludes with physical and procedural descriptions of the semi-adiabatic, rigid cracking frame, free shrinkage frame, setting time, mechanical property, and drying shrinkage testing that were conducted.

Chapter 4 presents the results of the laboratory testing program. Fresh and hardened concrete properties, hydration parameters, restrained stresses, unrestrained strains, and setting times for each mixture are presented. In addition, Chapter 4 includes a section in which the drying shrinkage data generated under this project and is compared to various predictive models.

Chapter 5 describes a new model to predict early-age creep and stress development in restrained elements.

Chapter 6 presents the results of laboratory study on predicting the early tensile strength of concrete. Aggregate type, w/cm, and SCMs were evaluated to predict early tensile strength

Chapter 7 is describes the field testing program in which several bridge decks were instrumented and monitored. Structural details, instrumentation locations, and instrumentation preparation methods are discussed. Results of return trips to inspect for visible early-age cracking are also provided. In addition to the recorded bridge deck temperatures, fresh concrete properties, hydration parameters, and mechanical strength development are detailed.

Chapter 8 presents the overall conclusions from this study and provides recommendations for future research related to bridge deck volume changes and crack potential. This chapter also describes how the key findings from this research project have been implemented into a new bridge deck cracking module within ConcreteWorks 3.0.

Chapter 2. Literature Review

Chapter 2 includes a literature review of the aspects that affect early-age bridge deck temperature, stress, and strength development. This literature review is not intended to be exhaustive, but rather, to present a general knowledge of the subject matter covered.

2.1 Volume Changes in Concrete

Concrete is a dynamic material with a microstructure that evolves with time and a volume that changes from the early stages of hydration to the later stages of service life. This section briefly describes the most relevant forms of volume change that affect concrete, in general, and bridge decks, in particular.

2.1.1 Plastic Shrinkage

Plastic shrinkage occurs as water is lost from the concrete to the environment while the concrete is still plastic (e.g., prior to setting). Plastic shrinkage cracking can occur in bridge decks or other elements with high surface/volume ratios once the cumulative evaporation from the concrete surface exceeds the cumulative bleeding of the concrete. When cumulative evaporation exceeds cumulative bleeding, water is drawn from within the bulk of the concrete, and the concrete goes into tension. Unfortunately, this event usually occurs before the concrete has developed any significant tensile strength, and if the event is reached, cracking is likely to result. In order to understand and possibly prevent plastic shrinkage, one must know and take into account the bleeding rate (and capacity), evaporation rate (as a function of the surrounding environment and concrete surface temperature), and the early-age strength development.

While this report will not delve into the testing for plastic shrinkage (evaporation and bleeding rates, and early-age strength development), an evaluation of a prediction method for concrete setting time was conducted. When attempting to predict plastic shrinkage cracking susceptibility, a prediction of the concrete setting time will give the engineer an idea of when the concrete mixture has developed a certain level of strength. If cumulative evaporation exceeds cumulative bleeding before initial set, the probability of plastic shrinkage cracking is much higher than if this event occurs after concrete setting. Setting time will be discussed in Section 2.3.3 of the literature review.

2.1.2 Chemical and Autogenous Shrinkage

In recent years, there has been considerable interest in early-age behavior of concrete, and much of this interest has been fueled by the use of high-performance concrete (HPC), which is often characterized by relatively low water-to-cementitious materials ratio (w/cm) of less than 0.40 and the use of supplementary cementing materials. When using such mixtures in field applications, it is important to realize that there may be insufficient water present internally to fully hydrate the portland cement. As the cement hydration proceeds and the amount of free water decreases, air takes the place of water in pores, lowering the pore relative humidity. An air-water meniscus forms with an accompanying surface tension. The surface tension imparts a tensile stress on the matrix, causing shrinkage. This is referred to as “chemical shrinkage,” which is defined as the volume reduction associated with the hydration reactions in a cementitious material (Jensen & Hansen, 2004). When aggregates are present, they are placed in compression by the cement matrix, providing restraint. The degree of restraint that the aggregates provide depends on the aggregate stiffness and the percent volume (Riding, 2007).

Although they are often considered the same property, autogenous shrinkage is different from chemical shrinkage in that it is defined as the bulk strain of a closed, isothermal, cementitious system not subjected to external forces. Chemical shrinkage can then be defined as "a change in the absolute volume," while autogenous shrinkage can be defined as "a bulk change in the apparent volume" (Jensen & Hansen, 2004). The two quantities tend to be identical up until concrete sets; thereafter, they deviate, with chemical shrinkage typically being significantly larger than autogenous shrinkage. As shown in Figure 2.1, "chemical shrinkage is an *internal* volume reduction, [while] autogenous shrinkage is an *external* volume change" (Holt, 2001).

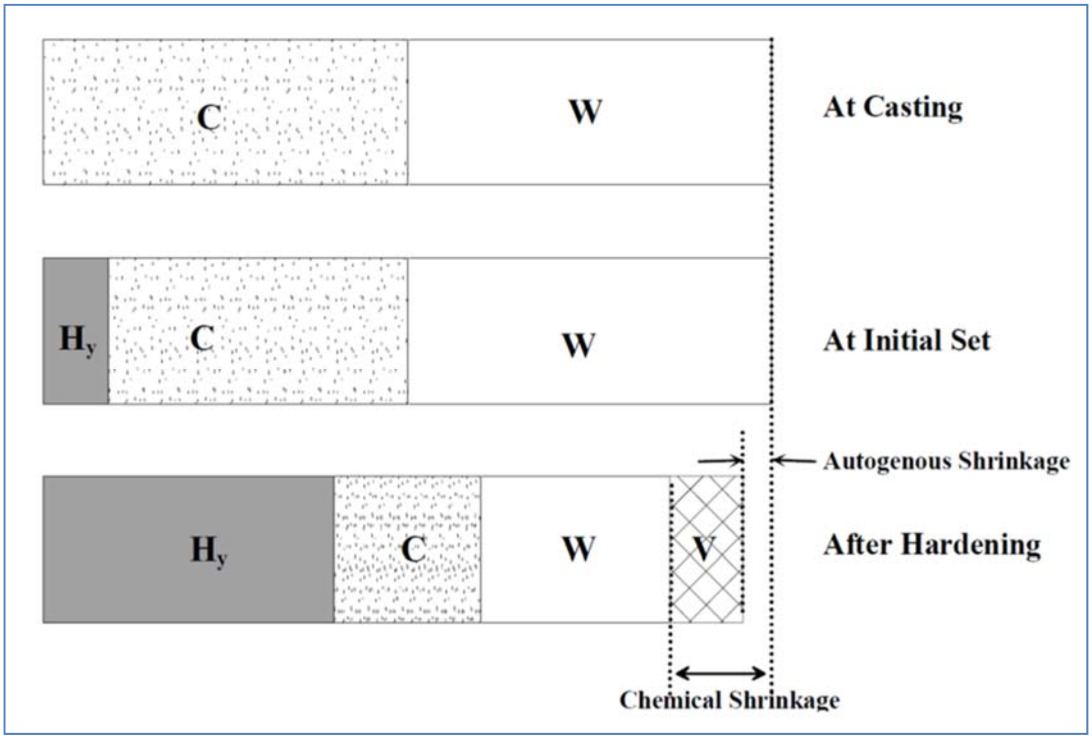

Figure 2.1: Autogenous and chemical shrinkage (Holt 2001).

In the current version of ConcreteWorks, a modified version of the Hedlund model is used for approximating the autogenous shrinkage in concrete (Hedlund, 2000; Riding, 2007). Equations 2.1 through 2.5 provide the autogenous shrinkage model proposed by Hedlund, and the modification used in ConcreteWorks.

Further explanation of the terms, the modifications made to the model, and of the recommended parameters can be found in Hedlund (2000) and Riding (2007).

$$\varepsilon_{SH} = \varepsilon_{su} * \beta_{s0}(t_e) * \beta_{ST}(T) \tag{2.1}$$

$$\varepsilon_{su} = \left(-0.65 + 1.3 * \frac{w}{cm}\right) * 10^{-3} \tag{2.2}$$

$$\beta_{s0}(t_e) = exp\left(-\left[\frac{t_{s1}}{t-t_{so}}\right]^{n_{SH}}\right) \tag{2.3}$$

$$\beta_{ST}(T) = a_0 + a_1 * \left[1 - exp\left(-\left[\frac{T}{T_1}\right]^{b_1}\right)\right] + a_2 * \left[1 - exp\left(-\left[\frac{T}{T_2}\right]^{b_2}\right)\right] \tag{2.4}$$

$$\varepsilon_{ault} = (-0.94 + 2.238 * w/cm) * 10^{-3} \tag{2.5}$$

2.1.3 Drying Shrinkage

Shrinkage caused by water loss from concrete has long been recognized as a cause of cracking of bridge decks and other flatwork. Although drying shrinkage has been somewhat overshadowed in recent years by concerns about autogenous shrinkage, it remains a major concern in the concrete industry. Mechanistically, the driving force behind drying shrinkage, namely the loss of internal water to the environment, is identical to the underlying cause of plastic shrinkage, the only difference being the nominal cut-off point in time when concrete transitions to a solid material (i.e., setting time). When water is lost from concrete, water is lost first from the largest pores, as the water in these pores is held with the least binding energy; water is then lost from smaller and smaller pores, with pores below 50 nm being most responsible for drying shrinkage. As such, data on pore size distributions of the paste phase can be helpful in predicting shrinkage potential. The capillary stress theory, captured by the Kelvin/Laplace-Gibbs equation (Equation 2.6), can be used to estimate the resultant stresses triggered by water loss as a function of pore size radius (r) and surface tension (γ) of the pore water.

$$\sigma = 2\gamma/r \tag{2.6}$$

Various factors, such as w/cm, paste content, water content, cement type and fineness, SCM (dosage and type), chemical admixtures, aggregate type, and aggregate content affect the rate of shrinkage development and ultimate magnitude of shrinkage. One can optimize the pore size distribution to minimize the potential for drying shrinkage and shrinkage-reducing admixtures (SRAs) can be used to reduce the surface tension of the pore water (Folliard & Berke, 1997).

In field structures, factors such as curing method and regime, environmental conditions (temperature, RH, etc.) and surface/volume ratio of the structural elements play major roles in determining drying shrinkage behavior. For bridge decks, drying occurs from the top down, and as such, moisture gradients develop which can generate significant stress gradients, with the highest stress at the top of the deck.

There have been hundreds of studies on the drying shrinkage of concrete, evaluating everything from materials to mixture proportions to curing conditions. Because of this large database of shrinkage data, there have been several attempts to quantify and predict drying shrinkage as a function of time, including the following models; ACI 209, CEB 90, B3, and GL 2000 (ACI Committee 209, 2008; CEB-FIP Model Code '90, 1993; Bazant, 1995; Gardner & Lockman, 2001). Al-Manaseer and Lam (2005) recently evaluated these four models from a statistical perspective, and found that the B3 and GL 2000 models were the best at predicting shrinkage within the RILEM database of mixtures. Mokarem (2002), using a set of mixture designs that were similar to many of those tested under TxDOT 6332, found that the CEB 90 model best predicted straight cement concrete mixtures, while the GL 2000 model most accurately predicted mixtures containing SCMs. Although there is no clear consensus on which of these models is best for predicting shrinkage (and/or creep), the B3 Model (developed by Bazant and included in the RILEM recommendations) is the most recent model and has been favored by researchers and practitioners in recent years.

2.1.4 Thermal Deformations

While thermal deformations are usually thought of as a problem for mass concrete, the effects of thermal shrinkage must also be considered for bridge deck systems. Due to heat released from hydration reactions, concrete temperature will rapidly increase after concrete placement (given typical environmental conditions). After approximately 24 hours have passed, the concrete temperatures start to decrease as heat loss to the environment becomes greater than the heat generated from the hydration reactions. After several days have passed, the concrete heat production will nearly stop, and the concrete system will assume thermal behavior based on heat transfer with the surrounding environment. Although bridge decks usually do not crack due to thermal shrinkage alone, it must be realized that these strains are placed on top of drying and autogenous shrinkage strains that are occurring during the same time period (Babaei & Fouladgar, 1997). In order to predict the strains associated with the thermal changes taking place at early ages, a model was developed under TxDOT Project 4563 to predict the temperature development of concrete elements based on the progression of hydration reactions and their interaction with the surrounding environment. Recent works by Riding and Poole have developed an extensive heat of hydration database over the last decade. This database, populated by isothermal and semi-adiabatic calorimetry data, has led to the development of hydration models for concrete mixtures containing a wide range of cement types, SCM types and dosages, and chemical admixture types and dosages (Riding, 2007; Poole, 2007). The models generated were based on both Bogue's and Rietveld's analyses and were aimed at developing predictive models for quantifying the progress of hydration using Equation 2.7:

$$Q_h\,(t) = H_u * W_c * \left(\frac{\tau}{t_e}\right)^{\beta} * \left(\frac{\beta}{t_e}\right) * \alpha(t_e) * \exp\left(\frac{E_a}{R} * \left(\frac{1}{273+T_r} + \frac{1}{273+T_c}\right)\right) \qquad (2.7)$$

In Equation 2.7, Q_h = rate of heat generation (W/m^3), H_u = total heat available (J/kg), and W_c = cementitious materials content (kg/m^3).

Equations for H_u are available in literature, but a more accurate equation is presented in Poole (2007). E_a, the apparent activation energy, describes the isothermal calorimetry testing that was developed to describe the effects of w/cm, cement chemistry, SCMs, and chemical admixtures on the E_a of Portland cement pastes. The model is also discussed in detail in work done by Poole (2007). The parameters α, β, and τ model the shape of the hydration curve from semi-adiabatic calorimetry. The model shown in Equation 2.7 is based on a range of concrete mixtures that are typically used in mass concrete, bridge decks, and precast elements. Under TxDOT Project 4563, a finite difference-based model was developed to incorporate the heat of hydration models into field structures and to then apply advanced heat transfer principles to generate spatial, time-temperature histories throughout hydrating field elements, including mass concrete elements, bridge decks, and precast girders (Riding, 2007). This model takes into account a wide range of boundary conditions, including solar radiation, convection, irradiation, and other mechanisms, and accounts for practical field issues such as curing conditions and formwork type and removal age. The model integrated into ConcreteWorks includes weather files for 239 cities from across the United States and includes data on temperature, relative humidity, wind speed, solar radiation, cloud cover, etc. The heat generation and transfer models have been calibrated and validated with over 35,000 hours of field data from mass concrete placements, but only minimal field validation was performed under TxDOT Project 4563 for bridge decks.

Other thermal issues that must be accounted for when modeling a bridge deck include thermal conductivity, specific heat, and coefficient of thermal expansion, all of which are already dealt with in the ConcreteWorks module for heat generation and transfer in bridge decks. ConcreteWorks, however, is lacking in that it does not address the fact that coefficient of thermal expansion (CTE) is affected by the moisture content (internal relative humidity) of concrete (Emmanuel & Hulsey, 1977). When typical concrete mixture proportions are used, the CTE of concrete in the partially dry state can be as much as 15% more than the CTE in the fully saturated state.

2.1.5 Moisture Gradients

As mentioned previously, bridge decks will be subjected to drying conditions that will impart a moisture gradient within the deck. This moisture gradient will trigger warping effects in the deck. A variety of detailed laboratory studies and modeling efforts have addressed this issue (Wittman & Roelfstra, 1980; Akita, Fujuwara, & Ozaka, 1997; Bentz, Garboczi, & Quenard, 1997; Grasley & Lange, 2004), although each has focused on laboratory testing under controlled conditions rather than realistic field conditions. Moisture gradients were not accounted for in the mass concrete crack prediction model in ConcreteWorks, as this is a minor issue at early-ages in such elements when compared to thermal effects.

2.1.6 Carbonation Shrinkage

Though not commonly thought to be a problem in bridge deck durability, carbonation shrinkage has the ability to reduce concrete surface strength and induce differential shrinkage in concrete elements. In carbonation shrinkage, cement paste (all hydration products, starting with calcium hydroxide (C-H) will react with carbon dioxide, lowering the pH of the system. This will in turn cause corrosion if the carbonation front reaches steel reinforcement, and will result in shrinkage in the carbonated layer of concrete. Generally, this is usually not a major concern in high-quality concrete, as carbonation typically does not penetrate more than 0.5 in. into the concrete surface. If poor quality concrete is made, or if reinforcing steel is not provided with adequate cover, then carbonation shrinkage may affect a deeper section of concrete, and corrosion of the reinforcing steel my take place (ACI Committee 224, 2001). Carbonation shrinkage also requires a specific range of relative humidity in the concrete; enough to provide essential water for carbon dioxide transport, but not so high that the pore structure is saturated and carbon dioxide cannot move through the saturated pores. A relative humidity of 50% produces the greatest values of carbonation shrinkage (Mindess, Young, & Darwin, 2002). While carbonation shrinkage and resulting corrosion of steel are possible in bridge decks, it is not a common issue. The necessary environmental conditions, the low permeability of carbon dioxide into concrete, and the fact that carbonation profiles rarely exceed the cover depth for reinforced structures make carbonation a minor issue in bridge deck durability.

2.2 Development of Mechanical Properties

In attempting to understand the many factors and forces involved in bridge deck cracking, one must be aware of the mechanical properties of a given bridge deck system. Obtaining a full understanding of how strength development, modulus development, and the mechanisms of creep resist the buildup of tensile stresses is integral in attempting to accurately predict the cracking potential of a bridge deck system.

While an understanding of the failure-inducing stresses that can build up in a concrete structure is very important, no real progress can be made without a firm grasp of the concrete strength development that works to resist the stresses. Since the rate of strength development is a temperature dependent property, maturity methods are needed to calculate the development of mechanical properties. Also important is a general feel for how different factors, such as the water-to-cementitious-products ratio (w/cm), use of supplementary cementitious materials (SCMs), and aggregate type and gradation, play a role in the long- and short-term strength development of concrete. Finally, understanding the empirical relationships between compressive strength, tensile strength, modulus of elasticity, and development of creep behavior will allow the engineer to predict the concrete's ability to resist tensile stresses over time.

2.2.1 Factors Influencing Strength Development

Several factors affect the development of compressive and tensile strength. W/cm is commonly used as the main predictor for concrete strength, with high w/cm ratios producing lower strength concrete, and lower w/cm ratios producing higher strength concrete. Lower w/cm ratios also results in a faster strength development when compared to high w/cm mixtures. Testing done by Abel and Hover (1998) on lower w/cm mixtures only 2–8 hours old showed faster tensile strength development, lower deformation at failure, and higher tensile strengths. These findings are especially relevant to bridge decks, representing the concrete behavior and stresses during the time period in which plastic shrinkage usually occurs (Abel & Hover, 1998). At different w/cm ratios, one must also consider the chemical and physical properties of the cement being used. The levels of C_3S and C_2S are the primary chemical components in influencing long and short term strength of portland cement concrete, with C_2S contributing to long-term strength and C_3S contributing to short-term strength. Focus must also be paid to the fineness of the cement being used, with high percentages of particles under 3μm resulting in high 1-day strength and high percentages of 3–30 μm particles resulting in higher 28-day strengths (Mindess, Young, & Darwin, 2002).

Aggregates are typically thought to have minor effects on concrete compressive strength. In tensile strength and fracture properties, however, aggregates hold more importance. For high strength concrete mixtures, the aggregate strength plays a larger role in the strength of the concrete, due to the fact the failure is forced to act through the aggregates. In normal strength concrete, as is typical of bridge deck mixtures, failures typically happen around the aggregate particles, such that aggregate strength is not as important a factor in the overall concrete strength. Aggregate shape and texture, and maximum aggregate size (MSA), on the other hand, typically play significant roles in the strength of normal strength concrete. Aggregate texture has a strong effect on the bond between aggregate and paste, thereby increasing the tensile strength capacity and the stress at which microcracking begins. While this alone would make for a stronger concrete, rough aggregates that would produce a stronger aggregate-paste bond also decrease workability. This creates a demand for more water in the mix, which usually offsets the strength gains due to the aggregate-paste bond improvements. Aggregate size can have an effect on both the compressive and tensile strength of the concrete. Large aggregates create larger stress concentrations when put under compressive loading, and can also trap more bleed water, increasing the porosity in the interfacial transition zone (ITZ). Large aggregates also tend to resist the volume changes that occur in the paste, which puts larger stresses on the paste fraction. These negative effects, however, are usually offset by increased workability and lower w/cm (due to increased workability), resulting in higher strengths (Mindess, Young, & Darwin, 2002). The use of dense graded aggregates may also have an impact on concrete strength development through the potential increase in interparticle contact; however, the ultimate strength will still primarily be a function of the w/cm and aggregate strength.

2.2.2 Maturity

Concrete strength development is a product of the hydration of cement particles in a concrete mixture. From the moment water comes into contact with cement, hydration reactions take place that will, over time, transform a fluid mixture into hardened structure. The development of this strength is depended on the concrete degree of hydration and temperature development. Maturity methods are used to compare the cement hydration progress for different time-temperature histories. The two most commonly used maturity methods are the Nurse-Saul method and the Equivalent Age method (Riding, 2007). The Nurse-Saul method generates a temperature-time factor that is defined as the integral of the temperature history and may be calculated as shown in Equation 2.8. In the Nurse-Saul, *M(t)* is the maturity at *t* (hrs), T_a is the average concrete temperature over the time step, T_o is the datum, or baseline temperature used (C), and *Dt* is the time step used (hrs).

$$M(t) = \sum (T_a - T_o) * \Delta t \qquad (2.8)$$

Equation 2.9 shows the Equivalent Age method for determining concrete maturity. Equivalent age maturity is defined as the age a concrete sample would have to be cured isothermally at a reference temperature T_r (°C) to have the same degree of reaction or properties as the sample cured at a different temperature. In this method, t_e is the equivalent age maturity (hrs), Q is the activation energy of the mixture being tested, divided by the universal gas constant (°K), T_a is the average concrete temperature over the time step, T_r is the reference temperature (°C), T_a is the average concrete temperature over the time step (°C), and Δt is the time step used (hrs). One of the advantages of the equivalent age method is that it does a better job than the Nurse-Saul method at predicting concrete strength level (Emborg, 1998; Mindess, Young, & Darwin, 2002).

$$t_e = \sum e^{-Q\left(\frac{1}{T_a+273} - \frac{1}{T_r+273}\right)} * \Delta t \qquad (2.9)$$

2.2.3 Setting Time

Setting time is another very important property in concrete strength development. Contractors often use setting time as a point from which decisions on finishing, tining, curing compounds, curing blankets/plastic, and groove cutting are based. The setting time is also important in determining the time duration during which plastic shrinkage is a major concern.

Finally, setting time is used to determine when concrete no longer acts plastically, begins to retain its form, and beings to develop strength.

In order to define the time before which plastic shrinkage is a significant concern and define the point in time which tensile strength begins to develop, it becomes important from a practical and technical perspective to know when concrete sets. A setting time model, which used standard inputs from semi-adiabatic calorimetry (as shown in Equations 2.10 and 2.11), was developed by Schindler (2004) to predict the initial and final setting times of concrete, respectively. This approach has become more useful as an increasing number of concrete practitioners and researchers have recorded and published the heat of hydration parameters for their concrete mixtures.

$$ASTM\ C403\ Initial\ Set \quad t_{ei} = \tau * \left(-ln\left[\frac{0.15 * w/cm}{\alpha_u}\right]\right)^{\frac{-1}{\beta}} \tag{2.10}$$

$$ASTM\ C403\ Final\ Set \quad t_{ef} = \tau * \left(-ln\left[\frac{0.26 * w/cm}{\alpha_u}\right]\right)^{\frac{-1}{\beta}} \tag{2.11}$$

In Equations 2.10 and 2.11, t_{ei} and t_{ef} stand for the equivalent age at initial and final set, respectively (hrs.), τ is the hydration time parameter (hrs.), w/cm is the water to cementitious materials ratio, α_u is the ultimate degree of hydration, and β is the hydration shape parameter.

2.2.4 Compressive Strength

Once the maturity has been determined, models can then be used to predict the compressive strength development of the concrete mixture. While many models exist, two of the more common equations are given in Equations 2.12 and 2.13 (Viviani, 2005).

$$f_c(t) = a + b * \log(log(M(t))) \text{ }, f_c \geq 0 \tag{2.12}$$

$$f_c(t_e) = f_{c,ult} * \exp\left(-\left(\frac{\tau_s}{t_e}\right)^{\beta_s}\right) \tag{2.13}$$

In Equations 2.12 and 2.13, $f_c(t)$ is the compressive strength development (MPa), a is a fit parameter which is usually negative (MPa), b is a fit parameter (MPa/°C/hr), $f_{c,ult}$ is the ultimate compressive strength parameter fit from the compressive strength tests (MPa), τ_s is a fit parameter (hrs.), and β_s is a fit parameter. M(t) and t_e are the inputs to the predictive equations for the Nurse-Saul method and the Maturity method, respectively.

2.2.5 Elastic Modulus

Once compressive strength development has been generated, models can be used to predict the development of the elastic modulus. This value is especially important in the context of bridge deck cracking, allowing the researcher to correlate the various volume change mechanisms that are occurring with the stresses that the changes generate. Essentially, as a concrete mixture generates a higher modulus of elasticity, volume changes generate higher stresses for each unit movement. This relationship is shown in Equation 2.14, where σ is the stress induced (psi), E is the elastic modulus of elasticity (psi), and ε is the strain in the concrete (in/in).

$$\sigma = E * \varepsilon \tag{2.14}$$

While there are many models available for calculating the elastic modulus, most engineers and practitioners in the concrete industry are familiar with the ACI 318 (2008) calculation of elastic modulus:

$$E_c = {w_c}^{1.5} * 33 * \sqrt{f'_c} \tag{2.15}$$

In Equation 2.15, E_c is the elastic modulus of concrete (psi), w_c is the unit weight of the concrete (lb/ft^3), and f'_c is the compressive strength of the concrete (psi).

2.2.6 Tensile Strength

In the case of bridge deck cracking, proper modeling of the concrete tensile strength is of great importance. Without a good model for tensile strength development, the engineer cannot determine whether the volume changes, and the resulting stresses, occurring within a concrete system are enough to produce cracking. Raphael (1984) proposed one model for the development of tensile strength that is commonly used today:

$$f_t = l * (f_c)^m \tag{2.16}$$

In Equation 2.16, f_t is the tensile strength (MPa), f_c is the compressive strength of the concrete (MPa), and l and m are fit parameters.

2.2.7 Creep and Stress Relaxation

Creep and relaxation play a key role in the development of bridge deck stress, and their potential to cause cracking. Creep is a complicated mechanism, influenced by applied stresses, water/cement ratio, curing conditions, temperature, moisture gradients, cement composition, chemical admixtures, aggregate properties, and specimen geometry (Mindess, Young, & Darwin, 2002). Though complicated, its effect on bridge deck cracking must be considered as relaxation due to creep can significantly reduce the stresses that are imposed on a bridge deck due to volume changes (thermal, autogenous, etc.). Time dependence of restrained shrinkage and creep (Mehta & Monteiro, 2005) shows how the process of creep helps delay cracking through stress relaxation (Figure 2.2).

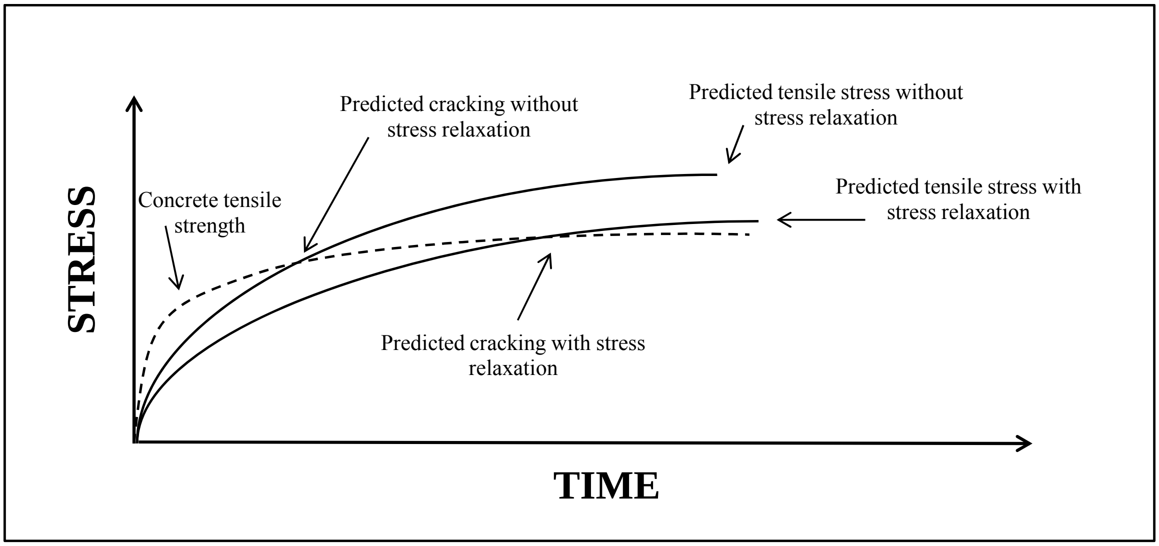

Figure 2.2: Time dependence of restrained shrinkage and creep (Mehta & Monteiro, 2005).

Many different models are available in the literature for evaluation of creep. Previous work at the University of Texas has utilized the Linear Logarithmic Model for calculating the early-age concrete stress relaxation (Larson & Jonasson, 2003). Equations are used to calculate the various slope components of the model, with adjustments for temperature modification, the aggregates used, and the Reitveld analysis of the cement used in the mixture. Further discussion, and the governing equations, of the Linear Logarithmic Model and the adjustments that have been made in ConcreteWorks can be found in (Riding, 2007).

Recent work at Auburn University has yielded a modified version of the commonly used B3 Model. The Modified B3 Model was developed by Byard at Auburn University, and aims to better capture the early-age creep response (Byard, 2011). An abbreviated explanation of the aspects of the B3 Model that are applicable to the rigid cracking frame test is provided below. Modifications to the B3 Model will be presented in Section 4.10. Description of the original B3 Model is made using information from ACI Committee 209 (2008) as well as the original papers from Bazant (1995). Further explanation of the original model can be found in these sources as well. The final version of the Modified B3 Model will be published as a doctoral thesis by Byard later.

In the B3 Model, a compliance term, $J(t, t_o)$, is used to calculate the strain caused by a constant stress, σ, applied at an age of t_o. $\varepsilon_{SH}(t)$ and $\alpha * \Delta T$ are the shrinkage and temperature induced strains, respectively. In $J(t, t_o)$, q_1 is the instantaneous strain calculated using the 28-day elastic modulus. $C_o(t, t_o)$ is the compliance function for basic creep, and $C_d(t, t_o, t_c)$ is the additional compliance function for drying creep. For evaluation against the rigid cracking frame data, $C_d(t, t_o, t_c)$ is taken as zero and will not be explained in this report.

In the compliance function for basic creep, the first term is an aging viscoelastic term, the second is a nonaging viscoelastic term, and the third is an aging flow term. The aging viscoelastic term is multiplied by q_2, a function of cement content and 28-day compressive strength, and calculated with an approximation to a binomial integral. The nonaging viscoelastic term is multiplied by q_3, a function of the water to cementitious materials ratio. The last term, an aging flow term, is multiplied by q_4, a function of the aggregate to cementitious materials ratio.

$$\varepsilon(t) = J(t,t_o) * \sigma \; + \; \varepsilon_{SH}(t) + \; \alpha * \Delta T \tag{2.17}$$

$$J(t,t_o) = \; q_1 + C_o(t,t_o) + C_d(t,t_o,t_c) \tag{2.18}$$

$$q_1 = {}^{0.6}/_{E_{cm28}} \tag{2.19}$$

$$C_o(t,t_o) = q_2 * Q(t,t_o) + q_3 * ln(1 + [t - t_o]^n) + q_4 * ln\left(\frac{t}{t_o}\right) \tag{2.20}$$

$$q_2 = 86.814 * 10^{-6} * c^{0.5} * {f_{cm}}^{-0.9} \tag{2.21}$$

$$q_3 = 0.29 * \left(\frac{w}{c}\right)^4 * q_2 \tag{2.22}$$

$$q_4 = 0.14 * 10^{-6} * \left(\frac{a}{c}\right)^{-0.7} \tag{2.23}$$

$$Q(t,t_o) = Q_f(t_o) * \left[1 + \left(\frac{Q_f(t_o)}{Z(t,t_o)}\right)^{r(t_o)}\right]^{-\frac{1}{r(t_o)}} \tag{2.24}$$

$$Q_f(t_o) = \left[0.086 * (t_o)^{\frac{2}{9}} + 1.21 * \; (t_o)^{\frac{4}{9}}\right]^{-1} \tag{2.25}$$

$$Z(t,t_o) = \; (t_o)^{-m} * ln[1 + (t - t_o)^n] \tag{2.26}$$

$$r(t_o) = 1.7 * (t_o)^{0.12} + 8 \tag{2.27}$$

2.3 Bridge Deck Cracking

Bridge deck cracking is a complicated phenomenon that involves the interactions between volume changes, strength development, and the specific environment (restraint conditions) of the concrete system in use. Through the evaluation of many damaged bridge decks, researchers have been able to identify cracking patterns that are caused by the stresses generated within the concrete system, rather than those applied externally (through traffic and ground movement). Although cracking causes are numerous and interrelated, there are some methods for modeling bridge deck systems that attempt to predict whether a specific deck will be susceptible to cracking during its lifespan. While most of these models only present a simplified approach to the bridge deck cracking problem, usually taking into account only one or two specific factors, they are a good place to start from in the attempt to make a model that accounts for all the mechanisms affecting a bridge deck system.

2.3.1 Mechanisms of Bridge Deck Cracking

As described in the introduction, bridge deck cracking has already been established as a serious concern for the nation’s infrastructure. While initial deck cracking is not a failure of the bridge system, cracking allows the penetration of deleterious substances (air, water, chlorides, etc.) that can cause structural failure in bridge systems. Prediction and prevention of future bridge deck cracking issues can be accomplished only through an understanding of the various mechanisms and factors that are associated with this phenomenon. Figure 2.3 shows the many factors that affect cracking in bridge decks.

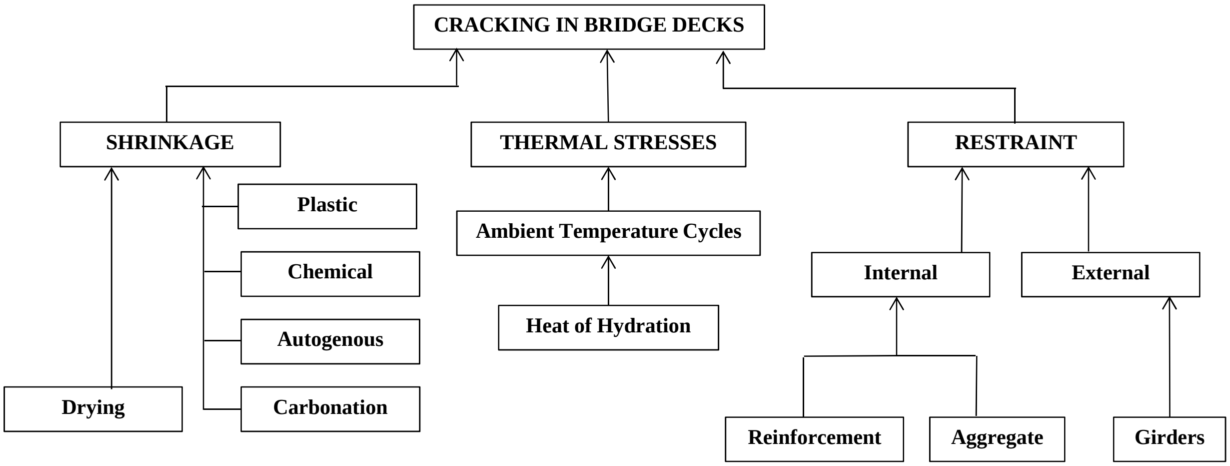

Figure 2.3: Causes of bridge deck cracking.

As Figure 2.3 indicates, and as discussed in this review, volume changes account for much of the driving force in bridge deck cracking. However, all of the volume changes are innocuous until the concrete element is restrained. In bridge deck systems, restraint is typically generated from within the concrete (by aggregate and reinforcing steel) and externally (from the sub-base or superstructure of the bridge). If strains vary though the section, as they do with moisture and temperature gradients, then the member itself may even be considered a restraint to its own internal forces. Figure 2.4 shows a typical bridge deck support structure for Texas highways.

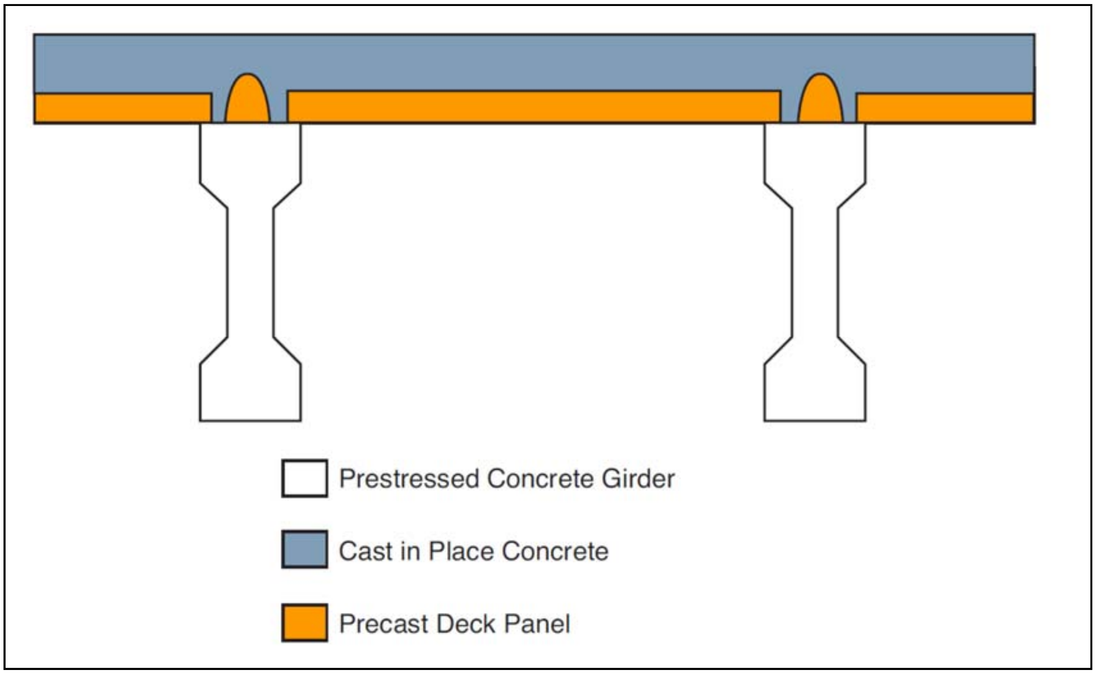

Figure 2.4: Precast, prestressed concrete panel bridge deck system (Folliard, Smith, Sellers, Brown & Breen, 2003).

2.3.2 Bridge Deck Cracking in Texas

Under TxDOT Project 4098, researchers evaluated several bridge decks in Texas that exhibited significant cracking. One of the structures that researchers examined had developed a series of stair step crack patterns. These cracks were located on a deck running alongside a bridge expansion joint, on both sides of the joint. The stair step cracks intersected with pairs of longitudinal cracks that were spaced about 8–10 in. apart, and ran for about 25 ft. The transverse cracks were no longer than 4 ft. Figure 2.5 shows the stair step cracking pattern that was common along the expansion joints of the Louetta Road Overpass in Houston. It should be noted that this deck was part of a FHWA project aimed at high performance concrete (HPC) and within this study, it was clearly shown that HPC bridge decks are more prone to early-age cracking.

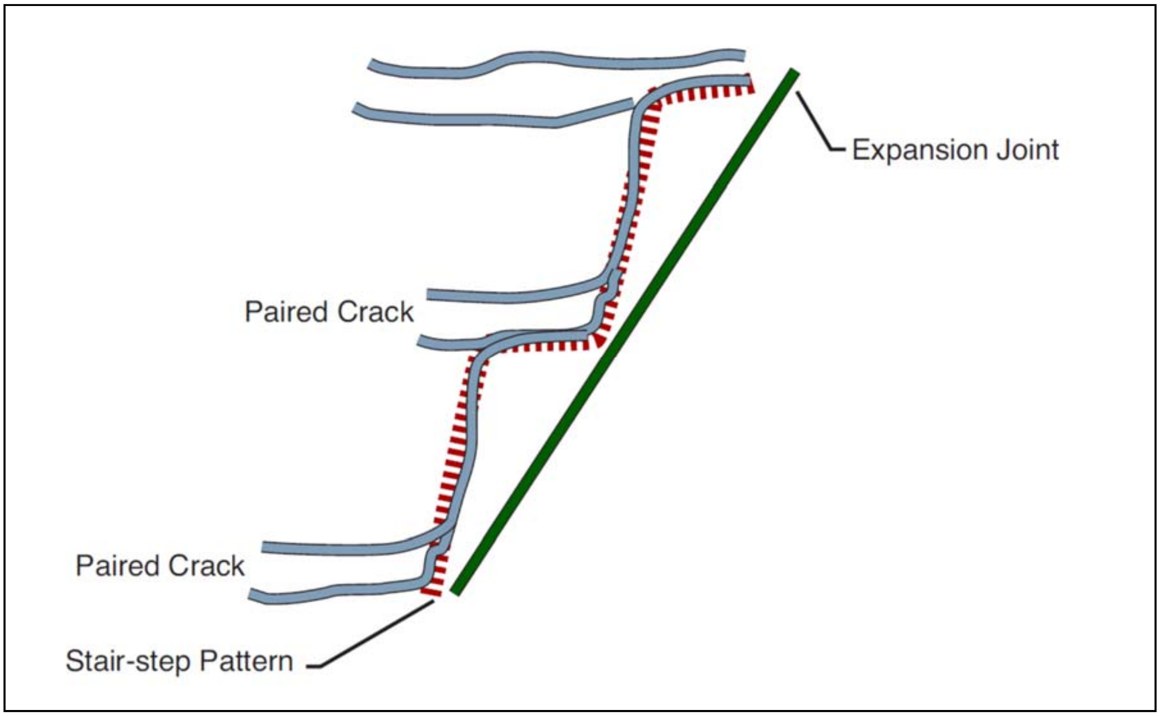

Figure 2.5: Typical stair step cracking on Louetta Bridge (Folliard, Smith, Sellers, Brown & Breen, 2003).

The Dow Barge Canal Bridge in Freeport showed a different cracking pattern. Similar to the Louetta Bridge, the Dow Bridge had pairs of longitudinal cracks that ran along the spans. On the Dow Bridge, however, these longitudinal cracks carried much further than those on the Louetta Bridge, sometimes extending the length of the slab. The stair step pattern that was seen at the Louetta Bridge was also seen at the expansion joints of the Dow Bridge. One aspect that was different in the Dow Bridge was the occurrence of transverse cracks that spanned the length between longitudinal cracks, with about 8 ft. separating one transverse crack from another. The cracking pattern found in the Dow Barge Canal Bridge can be seen in Figure 2.6.

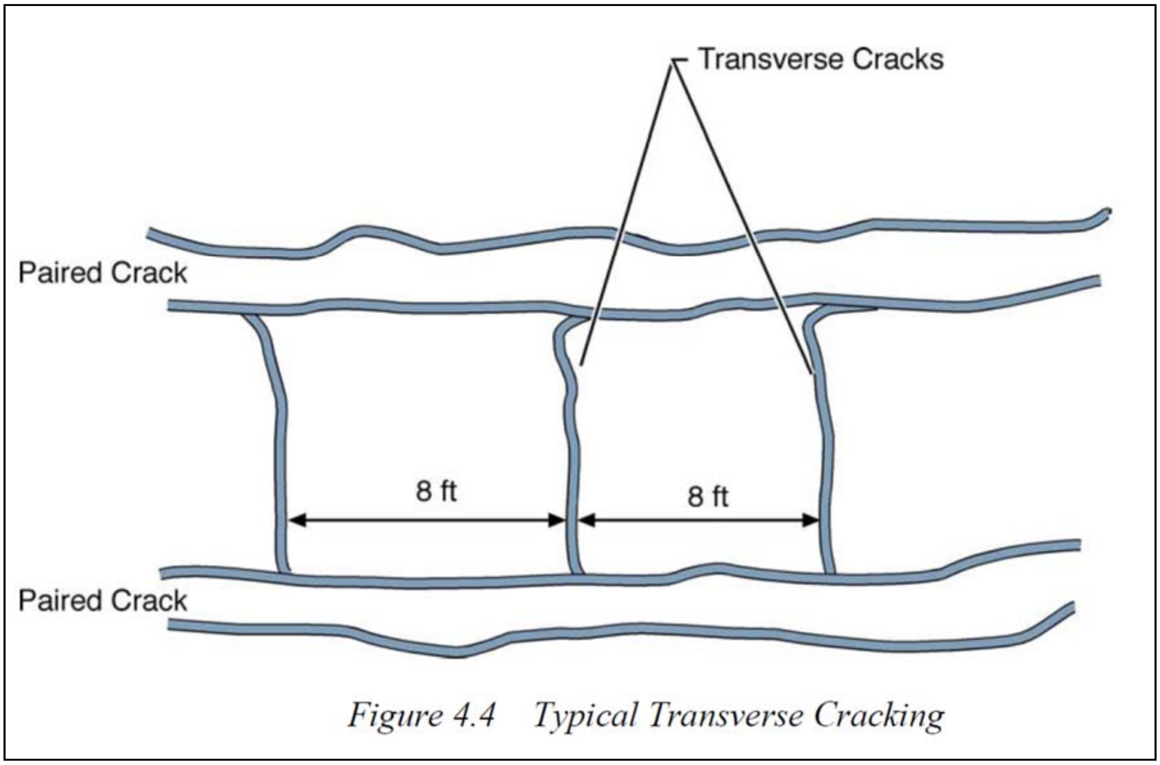

Figure 2.6: Typical transverse cracking on Dow Barge Canal Bridge (Folliard, Smith, Sellers, Brown & Breen, 2003).

Researchers under TxDOT Project 4098 did identify the precast-prestressed concrete panels as a trigger for cracking, generally due to the restraint that the panels provide against volume changes in the new deck concrete. In addition to the differential shrinkage issues, the Dow Barge Bridge also had issues with discontinuities at the butt joints. The precast panels, which are not connected along the longitudinal direction of the bridge, would have small offsets in the height from one panel to the next. When cast-in-place (CIP) concrete was laid continuously over these panels, cracks tended to form at the 8 ft. interval over which the butt joints were located, due to the stress concentration from the differential panel height.

Although significant cases of bridge deck cracking in Texas were evaluated under TxDOT 4098, as depicted in Figures 2.5 and 2.6, Texas does not encounter bridge deck cracking as often as do other states. Regardless, any improvements that can be made to the crack resistance of bridge decks will help to prolong the service life of bridges.

2.3.3 Prediction and Modeling

While just understanding the mechanisms and factors that cause shrinkage in early-age concrete is a significant scientific achievement, it is the development of prediction and modeling systems that make this knowledge valuable to the engineering community. Unfortunately, such a tool does not exist today, at least not in a version that is user-friendly and aimed at TxDOT personnel and contractors. To develop such a tool, or in this case, a module to be integrated into ConcreteWorks, several technical issues must be addressed, as highlighted here:

- Modeling of creep and stress relaxation, bridging the gap between early-age models refined and applied under TxDOT Project 4563 and more classical long-term creep models.
- Understanding and modeling the rate of moisture loss to the environment, and the shape of the moisture gradients that develops due to this loss.
- Evaluation of how the various volume changes, individually or in combination, result in stress and potential cracking.

Chapter 3. Laboratory Materials and Testing Methods

Chapter 3 details the experimental testing program that was undertaken to evaluate the early-age cracking potential of various materials and mixture proportions typically used in Texas bridge deck construction. Testing was performed to characterize each mixture's hydration properties, stress development under simulated environmental conditions, and to evaluate the strength development for the various concrete mixtures. This chapter also describes the identification scheme that was chosen to uniquely identify the various mixtures tested and presents the mixture proportions for these mixtures. The chemical analyses of the cements and SCMs tested and the gradations and physical properties of the aggregates used over the course of this project are also included in this chapter. In addition to work done under TxDOT Project 6332, an inter-agency contract from TxDOT was completed by the research team throughout the spring and summer of 2008. Information gathered from this study has been included in this report, and mixtures that were part of the inter-agency contract have been identified as IAC-FA.

3.1 Materials Tested

The mixture design matrix for TxDOT Project 6332 was developed to span the breadth of mixture designs used in Texas concrete bridge decks. Wherever possible, the research team obtained cements and SCMs from sources within Texas, though some materials outside of Texas were also evaluated to provide a wider range of chemical compositions. The following sections provide the chemical and physical properties of the materials used throughout this project.

3.1.1 Chemistry of Cements and SCMs Tested

Two cements were used under the TxDOT 6332 and IAC-FA studies. CEM-1, an ASTM C 150 Type I/II cement from San Antonio, was used as the low-alkali cement. CEM-2, an ASTM C 150 Type I cement from Buda was used as the high-alkali cement. Cement alkalinity is calculated from the sodium equivalent, Na_2Oe, for the cement. Sodium equivalent can be calculated using Equation 3.1:

$$Na_2Oe = \%Na_2 + 0.658 * \%K_2O \tag{3.1}$$

High and low alkalinities are defined, in this report, according to TxDOT specifications (TxDOT, 2011):

- High-alkali: > 0.60% Na_2Oe
- Low-alkali: ≤ 0.60% Na_2Oe

The cement compounds, calculated using the Bogue calculations from ASTM C150 (2011), and chemical compositions are presented in Table 3.1 and Table 3.2.

Table 3.1: Chemical composition of cements.

	Cements Used	
	CEM-2	CEM-1
SiO_2	18.6	20.1
Al_2O_3	5.4	4.4
Fe_2O_3	2.6	3.6
MgO	1.1	0.7
SO_3	3.3	3.1
Na_2O	0.11	0.05
K_2O	0.98	0.64
Na_2Oe^{***}	0.78	0.47

All values aer in % by weight.

*** Na2O equivalent alkali content

Table 3.2: Bogue calculated cement phases.

Cement Phases	CEM-2	CEM-1
C_3S	62.0	62.4
C_2S	6.6	10.5
C_3A	9.9	5.4
C_4AF	7.8	11.1
Na_2Oe^{***}	0.78	0.47

All values are in % by weight.

*** Na2O equivalent alkali content

Six different SCMs were used under TxDOT 6332 and IAC-FA (Table 3.3). These SCMs were chosen to span the breadth of options that are available for bridge deck concrete mixtures, and to provide a wide range of fly ash CaO contents. Fly ashes tested met the requirements of ASTM C 618 (2008) and the ground granulated blast furnace slag (GGBFS) met the requirements of ASTM C 989 (2010).

Table 3.3: Chemical composition of SCMs.

	SCMs Used					
	FA-1	FA-2	FA-3	FA-4	SLG120*	UFFA**
SiO_2	55.8	45.6	34.7	32.4	35.5	47.6
Al_2O_3	30.5	23.1	19.4	18.9	10.9	28.2
Fe_2O_3	4.6	3.7	6.0	6.4	0.9	2.9
CaO	1.2	15.9	22.8	24.6	43.1	12.1
MgO	0.7	2.5	4.4	4.6	7.8	2.1
SO_3	0.1	0.5	1.4	2.4	1.0	0.8
Na_2O	0.3	0.2	1.4	1.2	0.2	0.3
K_2O	2.3	0.7	0.3	0.3	0.3	1.1

All values are in % by weight.

* Ground granulated blast furnace slag

** Ultra-fine fly ash

3.1.2 Aggregates

For this project, two sources of coarse aggregate and one source of fine aggregate were used. For the majority of the mixtures tested, the coarse and fine aggregates were used as received from the producer (no additional sieving or reproportioning was done). However, for the OL-RG and OL10-RG mixture designs, the river gravel coarse aggregate and river sand were sieved and reproportioned to obtain an optimized aggregate gradation.

3.1.2.1 Coarse Aggregate

Two coarse aggregate sources were used throughout this project. An ASTM C 33 Number 57 siliceous river gravel from Austin was sourced out of the Colorado River. An ASTM C 33 Number 57 limestone was chosen from a quarry in San Antonio. Throughout this report, the coarse aggregates that were kept at ASTM C 33 Number 57 gradations will be denoted as Gr. 57. Six mixtures were tested with the Gr. 57 limestone, and 34 mixtures were tested with the Gr. 57 river gravel. Sieving gradations with the percent passing values for the Gr. 57 limestone and Gr. 57 river gravel, and the ASTM C33 (2011) limits, are presented in Figure 3.1 and Table 3.4. Absorption and specific gravity of the aggregates are presented in Table 3.5.

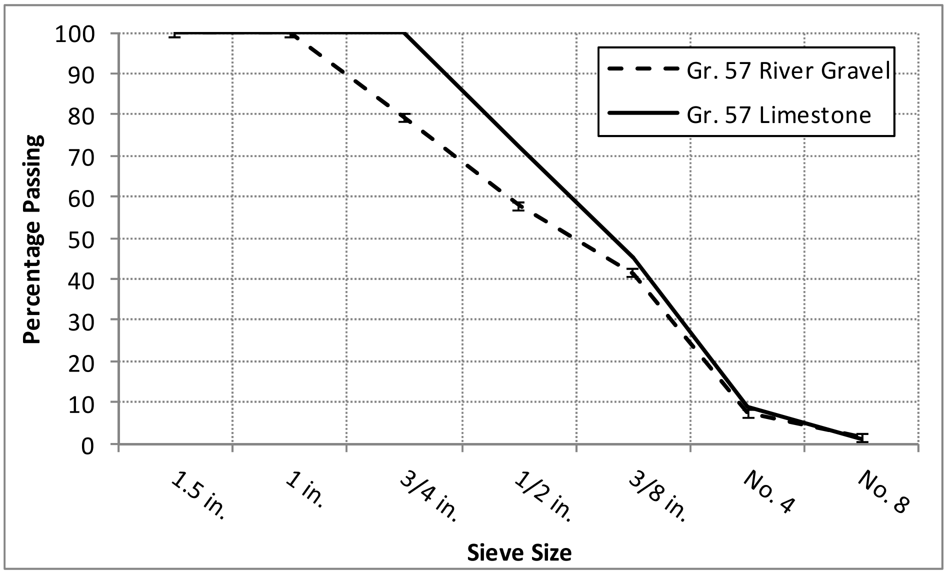

Figure 3.1: Coarse aggregate gradations.

Table 3.4: Coarse aggregate gradations and limits.

Sieve Opening	Gr. 57 River Gravel	Gr. 57 Limestone	ASTM C33 Limits for Gr. 57
1.5 in.	100	100	100
1 in.	100	100	95-100
3/4 in.	79	85	--
1/2 in.	58	44	25-60
3/8 in.	41	19	--
No. 4	7	6	0-10
No. 8	1	2	0-5

All values in percent passing.

Table 3.5: Absorption and specific gravity of aggregates.

Aggregate Source	Absorption	Specific Gravity
River Gravel	1.29%	2.60
Limestone	2.75%	2.75
River Sand	0.76%	2.61

3.1.2.2 Fine Aggregate

All mixtures tested under TxDOT 6332 and IAC-FA used river sand from Austin, sourced from the Colorado River. The river sand passed the requirements of ASTM C 33, and had a fineness modulus of 2.71. The percent passing gradation of the river sand is shown in Figure 3.2 and Table 3.6.

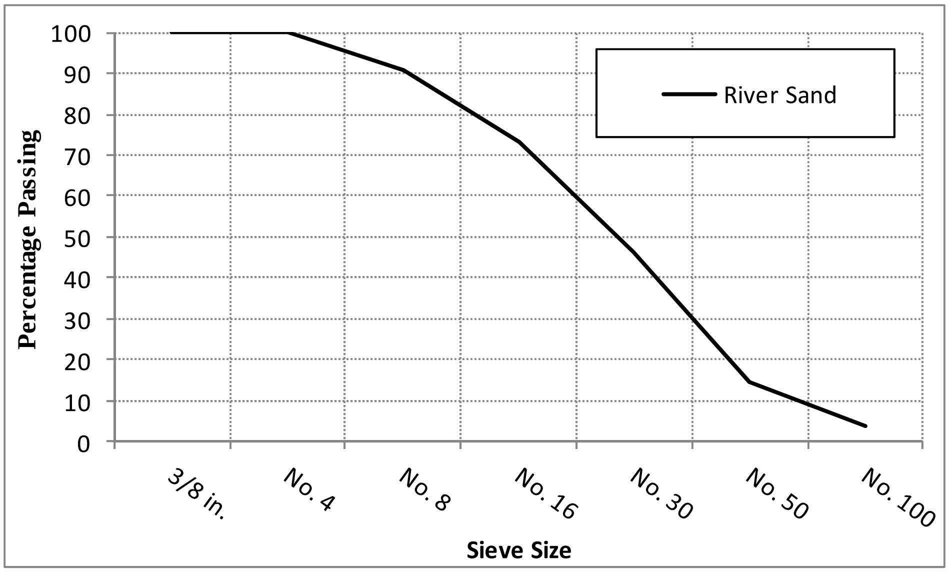

Figure 3.2: Fine aggregate gradations.

Table 3.6: Fine aggregate gradation and limits.

Sieve Size	River Sand	ASTM C33 Limits
3/8 in.	100.0	100
No. 4	99.9	95-100
No. 8	90.7	80-100
No. 16	73.1	50-85
No. 30	46.4	25-60
No. 50	14.6	5-30
No. 100	3.8	0-10

All values in percent passing.

3.1.2.3 Optimized Aggregate Gradation

Under TxDOT 6332, and with collaboration and assistance from TxDOT, two mixture designs were evaluated that used optimized aggregate gradations. While this is most commonly found in asphalt mixtures, there is recent interest in their use in portland cement concrete mixtures. If a mixture is designed properly, optimized aggregate gradations could allow for reduced paste content, while keeping the same strength and workability characteristics for a mixture. Reduced paste content results in a less expensive concrete mixture, less heat generation, and a concrete mixture that is less sensitive to deterioration of the paste fraction. In the first optimized aggregate gradation mixture, OL-RG, the paste volume was kept constant with all the other mixtures in the test matrix. In the second optimized aggregate gradation mixture, OL10-RG, the paste volume of the mixture was reduced by 10% (while keeping a 0.45 w/cm) and replaced with optimized aggregate fractions. The volumetric mixture designs of the optimized aggregate mixtures are shown in Table 3.7, and weight proportions can be found in Table 3.8.

Table 3.7: Volumetric mixture design for optimized aggregate gradation mixes.

Mix Name	Cement ft^3/yd^3	Water ft^3/yd^3	Paste Volume ft^3/yd^3	Coarse Aggregate ft^3/yd^3	Fine Aggregate ft^3/yd^3	Total Aggregate ft^3/yd^3
OL-RG	2.87	4.07	6.94	11.67	8.25	19.91
OL10-RG	2.58	3.66	6.25	12.08	8.53	20.61
		Δ	-0.69		Δ	0.69

To achieve an optimized aggregate gradation, the research team sieved the Gr. 57 river gravel, and the river sand. Three fractions were kept—3/8in., No. 8, and No. 16—and the remaining material was discarded. The sieved fractions were then added back into the general Gr. 57 and river sand distributions in the proportions shown in Table 3.8.

Table 3.8: Weight proportioning for optimized aggregate gradation.

	Coarse Aggregate % by Weight	Fine Aggregate % by Weight
Gr. 57 River Gravel	74.4%	--
River Sand	--	84.3%
3/8in. Sieve	11.1%	--
No. 8 Sieve	14.5%	--
No. 16 Sieve	--	15.7%
Total	100.00%	100.00%

After combining the sieved fractions to generate the new coarse and fine aggregate gradations, the total aggregate gradation fell within the recommended "8–18 bands" and performed much closer to the desired "haystack" shape recommended by Shilstone (1990). This is evident in Figure 3.3 and Figure 3.4, which provide the percent retained values for the typical and optimized aggregate gradations.

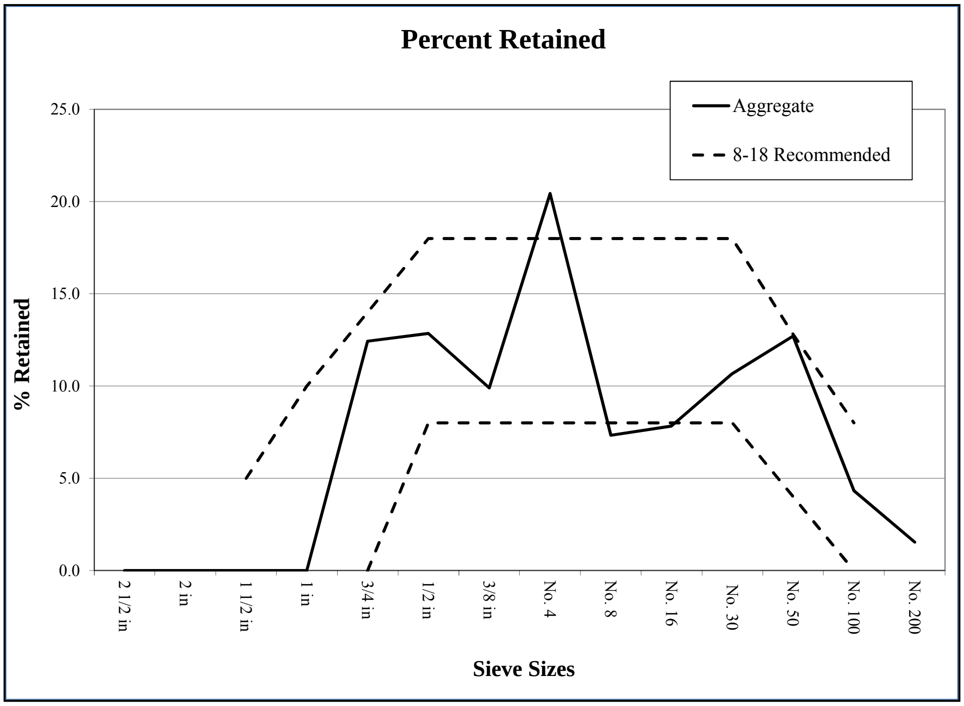

Figure 3.3: Typical aggregate distribution for testing matrix.

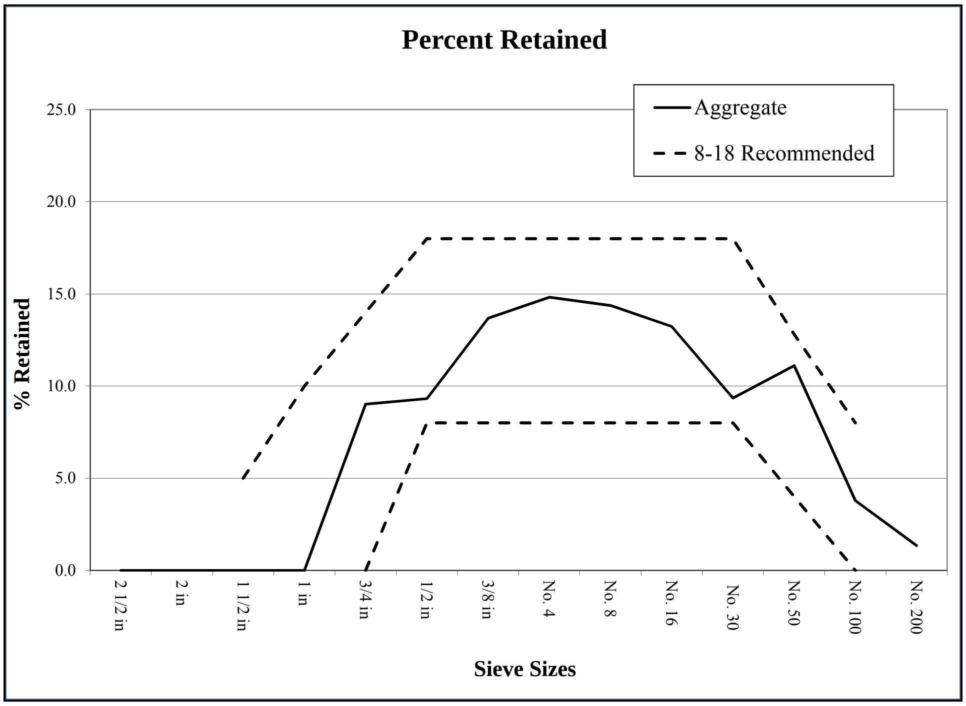

Figure 3.4: Aggregate distribution for optimized aggregate mixes.

3.1.3 Chemical Admixtures

Two admixtures were used throughout this project. WR (water reducer) is a Type A and D water-reducing and retarding admixture that was used in every mixture tested at a dosage of 3 oz./cwt of cementitious materials (ASTM C494, 2010). WR has a 44% solids content by volume (TxDOT, 2011). SRA is a shrinkage reducing admixture that works by reducing the surface tension of the pore water in the concrete. According to Table 3.9, this reduction results in a lower level of stress applied to the bulk concrete when menisci are formed in the concrete pore structure. SRA was added to the "S" mixtures in the testing matrix at the recommended dosage of 1.5 gal/yd^3. Also following the recommendations from the admixture data sheet, SRA was used at a 1-1 ratio as a replacement for mixture water. A summary of the chemical admixture information is shown in Table 3.9.

Table 3.9: Concrete admixture information.

Admixture	Dosage	Specific Gravity	% Solids
WR	3 oz/cwt	1.18-1.22	44%
SRA	1.5 gal/yd^3	0.935	--

3.2 Concrete Mixture Designs Evaluated

Under TxDOT 6332 and IAC-FA, 42 separate mixtures and 23 different mixture designs were evaluated to determine their performance under simulated temperature profiles. The mixture designs were chosen to reflect those used in Texas bridge deck construction.

3.2.1 Identification of Mixture Designs

To delineate the many mixtures performed under this research project, a naming scheme was developed to identify if SCMs were used, if low of high alkalinity cement was used, what percentage of replacement was used for the SCMs, what type of coarse aggregate was used, and whether that specific mixture was being tested under hot, cold, or isothermal temperature simulations. For this report, ground granulated blast furnace slag is abbreviated as GGBFS, supplementary cementitious materials are abbreviated as SCMs, and ultra-fine fly ash is abbreviated as UFFA. Descriptions of the mixtures tested and the mixture proportions used are presented in Tables 3.10 and 3.11.

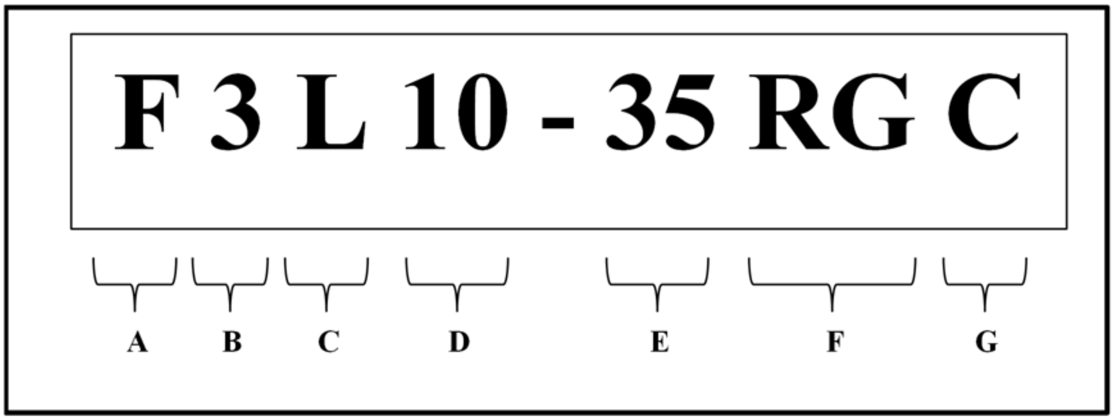

A. Mixture Type: Identifies the type, if any, of SCM or special admixture used.
   - C: Control Mixture—No SCMs or special admixtures used.
   - F: Fly Ash Mixture—Fly ash is used to replace a portion of the cement.
   - G: GGBFS Mixture—GGBFS is used to replace a portion of the cement.
   - O: Optimized—A straight cement mixture, with an optimized aggregate gradation.
   - U: UFFA Mixture—UFFA replaces 10% of the cement. Additional cement replacement from fly ash as well.
   - S: Shrinkage Reducing—A control mixture, with a shrinkage reducing admixture used.

B. Fly Ash Type: Identifies the specific fly ash, if any, that was used.
   - No Number: No fly ash used in the mixture.
   - 1: Class F—FA-1 (CaO = 1.2%)
   - 2: Class F—FA-2 (CaO = 12.1%)
   - 3: Class C—FA-3 (CaO = 22.8%)
   - 4: Class C—FA-4 (CaO = 24.6%)

C. Cement Alkalinity: Identifies the type of cement used.
   - H: High Alkalinity—CEM-2 (Na_2Oeq = .756%)
   - L: Low Alkalinity—CEM-1 (Na_2Oeq = .467%)

D. Paste Reduction: Identifies the percentage of paste volume, if any, that was replaced with optimized aggregate fractions.

E. SCM Replacement: Identifies the percentage of cement, if any, replaced with SCMs.

F. Aggregate Type: Identifies the type of coarse aggregate that was used.
   - RG: River gravel used as the coarse aggregate.
   - LS: Limestone used as the coarse aggregate.

G. Temperature Profile: Identifies the type of temperature profile used for that particular mixture.
   - No final letter: Hot weather temperature profile used.
   - C: Cold weather temperature profile used.
   - I: Isothermal temperature profile used.

3.2.1.1 Control Mixtures Tested

Under the two research projects, seven control mixtures were evaluated. These mixtures, which contained no SCMs, allowed the research team to isolate the effects of fly ash replacement in bridge deck concrete mixtures. Low and high alkali cements, river gravel and limestone coarse aggregate, and hot and cold temperature profiles were used in the evaluation of the control mixtures. In addition, an isothermal temperature profile was used on one of the control mixtures to isolate the benefits of using shrinkage reducing admixture with regard to autogenous shrinkage. Tables 3.10 and 3.11 present the control mixtures and proportions.

Table 3.10: Control mixtures.

	Cement	SCM Source	SCM CaO Content	SCM Replacement
CL-RG	CEM-1	None	--	--
CL-RGC	CEM-1	None	--	--
CL-RGI	CEM-1	None	--	--
CH-RG	CEM-2	None	--	--
CH-RGC	CEM-2	None	--	--
CL-LS	CEM-1	None	--	--
CL-LSC	CEM-1	None	--	--

* Denotes a mixture that was completed under IAC-FA

Table 3.11: Mixture proportions for control mixtures.

Mix ID	Cement lb/yd^3	SCM lb/yd^3	Water lb/yd^3	Coarse Agg. lb/yd^3	Fine Agg. lb/yd^3	WR oz. / cwt
CL-RG	564	--	254	1940	1231	3
CL-RGC	564	--	254	1940	1231	3
CL-RGI	564	--	254	1940	1231	3
CH-RG	564	--	254	1941	1232	3
CH-RGC	564	--	254	1941	1232	3
CL-LS	564	--	254	1922	1220	3
CL-LSC	564	--	254	1922	1220	3

* Denotes a mixture that was completed under IAC-FA

3.2.1.2 Class C Fly Ash Mixtures

Ten mixtures were tested that utilized Class C fly ash (CaO greater than 20%). Class C fly ashes included FA-3, from San Antonio and FA-4 from Thompsons. Under the IAC-FA project, a higher CaO Type C fly ash was used (FA-C), but had to be abandoned due to limited resources. The IAC-FA project was finished with FA-4 as the highest CaO fly ash, and TxDOT Project 6332 used FA-4 exclusively for the high CaO fly ash. Mixtures that used the FA-C fly ash will not be included in this report. See Tables 3.12 and 3.13.

Table 3.12: Class C fly ash mixtures.

	Cement	SCM Source	SCM CaO Content	SCM Replacement
F3L-25RG*	CEM-1	FA-3	22.8%	25%
F3L-35RG*	CEM-1	FA-3	22.8%	35%
F3L-35RGC	CEM-1	FA-3	22.8%	35%
F3L-35LS	CEM-1	FA-3	22.8%	35%
F3L-35LSC	CEM-1	FA-3	22.8%	35%
F4L-25RG*	CEM-1	FA-4	24.6%	25%
F4L-35RGC	CEM-1	FA-4	24.6%	35%
F4H-25RG*	CEM-2	FA-4	24.6%	35%
F4H-35RG	CEM-2	FA-4	24.6%	35%
F4H-35RGC	CEM-2	FA-4	24.6%	35%

* Denotes a mixture that was completed under IAC-FA

Table 3.13: Mixture proportions for Class C fly ash mixtures.

Mix ID	Cement lb/yd^3	SCM lb/yd^3	Water lb/yd^3	Coarse Agg. lb/yd^3	Fine Agg. lb/yd^3	WR oz. / cwt
F3L-25RG*	423	141	254	1929	1224	3
F3L-35RG*	367	197	254	1924	1221	3
F3L-35RGC	367	197	254	1923	1220	3
F3L-35LS	367	197	254	1905	1209	3
F3L-35LSC	367	197	254	1905	1209	3
F4L-25RG*	423	141	254	1929	1223	3
F4L-35RGC	367	197	254	1954	1240	3
F4H-25RG*	423	141	254	1927	1223	3
F4H-35RG	367	197	254	1921	1219	3
F4H-35RGC	367	197	254	1920	1219	3

* Denotes a mixture that was completed under IAC-FA

3.2.1.3 Class F Fly Ash Mixtures

Ten mixtures were tested that utilized Class F fly ash (CaO less than 20%). Class F fly ashes included FA-1, from Stokes County, North Carolina, and FA-2 from Rockdale, Texas. See Tables 3.14 and 3.15.

Table 3.14: Class F fly ash mixtures.

	Cement	SCM Source	SCM CaO Content	SCM Replacement
F1L-25RG*	CEM-1	FA-1	1.2%	25%
F1L-25RGC	CEM-1	FA-1	1.2%	25%
F1H-25RG*	CEM-2	FA-1	1.2%	25%
F1H-25RGC	CEM-2	FA-1	1.2%	25%
F2L-25RG*	CEM-1	FA-2	15.9%	25%
F2L-25RGC	CEM-1	FA-2	15.9%	25%
F2L-35RG*	CEM-1	FA-2	15.9%	35%
F2L-35RGC	CEM-1	FA-2	15.9%	35%
F2H-25RG	CEM-2	FA-2	15.9%	25%
F2H-25RGC	CEM-2	FA-2	15.9%	25%

* Denotes a mixture that was completed under IAC-FA

Table 3.15: Mixture proportions for Class F fly ash mixtures.

Mix ID	Cement lb/yd^3	SCM lb/yd^3	Water lb/yd^3	Coarse Agg. lb/yd^3	Fine Agg. lb/yd^3	WR oz. / cwt
F1L-25RG*	423	141	254	1916	1216	3
F1L-25RGC	423	141	254	1906	1209	3
F1H-25RG*	423	141	254	1916	1216	3
F1H-25RGC	423	141	254	1914	1215	3
F2L-25RG*	423	141	254	1917	1216	3
F2L-25RGC	423	141	254	1916	1216	3
F2L-35RG*	367	197	254	1907	1210	3
F2L-35RGC	367	197	254	1906	1209	3
F2H-25RG	423	141	254	1917	1216	3
F2H-25RGC	423	141	254	1916	1216	3

* Denotes a mixture that was completed under IAC-FA

3.2.1.4 GGBFS Mixtures

Eight mixtures were tested that utilized SLG120 GGBFS, from Chicago, Illinois. See Tables 3.16 and 3.17.

Table 3.16: GGBFS mixtures.

	Cement	SCM Source	SCM CaO Content	SCM Replacement
GL-35RG	CEM-1	SLG120	43.10%	35%
GL-35RGC	CEM-1	SLG120	43.10%	35%
GL-50RG	CEM-1	SLG120	43.10%	50%
GL-50RGC	CEM-1	SLG120	43.10%	50%
GH-50RG	CEM-2	SLG120	43.10%	50%
GH-50RGC	CEM-2	SLG120	43.10%	50%
GL-50LS	CEM-1	SLG120	43.10%	50%
GL-50LSC	CEM-1	SLG120	43.10%	50%

* Denotes a mixture that was completed under IAC-FA

Table 3.17: Mixture proportions for GGBFS mixtures.

Mix ID	Cement lb/yd^3	SCM lb/yd^3	Water lb/yd^3	Coarse Agg. lb/yd^3	Fine Agg. lb/yd^3	WR oz. / cwt
GL-35RG	367	197	254	1932	1226	3
GL-35RGC	367	197	254	1931	1225	3
GL-50RG	282	282	254	1928	1223	3
GL-50RGC	282	282	254	1926	1222	3
GH-50RG	282	282	254	1928	1223	3
GH-50RGC	282	282	254	1926	1222	3
GL-50LS	282	282	254	1908	1211	3
GL-50LSC	282	282	254	1908	1211	3

* Denotes a mixture that was completed under IAC-FA

3.2.1.4 Other Mixtures

In addition to the previous mixtures, seven ‘other’ mixtures were evaluated that examined the effects of a ternary blend, use of shrinkage reducing admixtures, and of the use of optimized aggregate gradations. Two mixtures were evaluated that used a ternary blend of 10% UFFA with 35% FA-4 fly ash. Three mixtures were evaluated that were composed of the low alkali, river gravel control mixture, but with a shrinkage reducing admixture, SRA, used in addition to the mid-range water-reducer, WR, used in all of the mixtures evaluated. Finally, two mixtures were evaluated that utilized an optimized aggregate gradation. One of these mixtures, OL10-RG, utilized a 10% volume reduction in paste to study a more economical mixture design. This was conducted by increasing the optimized aggregate gradation fractions by 10%. See Tables 3.18 and 3.19.

Table 3.18: Other mixtures.

	Cement	SCM Source	SCM CaO Content	SCM Replacement
U4L-35RG*	CEM-1	FA-4 and UFFA	24.6% and 12.1%	35% and 10%
U4L-35RGC	CEM-1	FA-4 and UFFA	24.6% and 12.1%	35% and 10%
SL-RG	CEM-1	None	--	--
SL-RGC	CEM-1	None	--	--
SL-RGI	CEM-1	None	--	--
OL-RG	CEM-1	None	--	--
OL10-RG	CEM-1	None	--	--

* Denotes a mixture that was completed under IAC-FA

Table 3.19: Mixture proportions for other mixtures.

Mix ID	Cement lb/yd^3	SCM lb/yd^3	Water lb/yd^3	Coarse Agg. lb/yd^3	Fine Agg. lb/yd^3	WR oz. / cwt	SRA gal / yd.
U4L-35RG*	367	197 & 56	254	1890	1199	3	--
U4L-35RGC	310	197 & 56	254	1914	1214	3	--
SL-RG	564	--	254	1940	1231	3	1.5
SL-RGC	564	--	254	1940	1231	3	1.5
SL-RGI	564	--	254	1940	1231	3	1.5
OL-RG	564	--	254	1893	1343	3	--
OL10-RG	508	--	229	1959	1390	3	--

* Denotes a mixture that was completed under IAC-FA

3.3 Experimental Procedures

This section outlines the experimental procedures that were taken for each mixture tested. Descriptions of the batching process, the mixing process, and of the fresh and hardened concrete tests that were performed are presented in this section.

3.3.1 Batching

At least 24 hours prior to mixing, the research team batched the materials that were to be used for that week's mixture. Coarse and fine aggregate were taken from outdoor storage bins. Inside the mixing room, the coarse and fine aggregate were placed, at separate times, inside the mixer, and allowed to blend with a small amount of water. The blending with water allowed the dry aggregate to achieve a condition closer to saturated surface dry (SSD) prior to mixing. After being allowed to blend for 1–2 minutes, the aggregate was emptied into 5-gallon buckets and weighed. Samples were collected to evaluate the moisture content of the aggregate. Cement and SCMs were collected from 55-gallon drums that were located inside closed storage containers outside. Cement and SCMs were placed into 5-gallon buckets, weighed, and placed inside.

For mixtures that were to undergo hot weather temperature simulation or isothermal testing, the batched materials were left inside the mixing room. Mixing room conditions were typically kept at 73°F ± 3°F. If a mixture was to undergo cold weather temperature simulation, the materials, as well as buckets of pre-batched mix water, was stored in an environmental chamber that was kept at 45°F. This allowed for a RCF placement temperature of approximately 65°F.

3.3.2 Mixing Procedures

On the mixing day, moisture content samples were reweighed, and the moisture content of the coarse and fine aggregate was calculated. Corrections to the coarse and fine aggregate batch weights, and to the quantity of mixing water, were made. Mixing water and chemical admixtures were then weighed out, and the chemical admixtures were added to and blended with the mixing water. The concrete mixer, wheelbarrows, and fresh concrete testing materials were then lightly wetted just prior to mixing.

Mixing began by adding all of the coarse and fine aggregate into the mixer, starting the mixer, and then adding approximately one-third of the mixing water. The aggregate and water were then allowed to mix for approximately one minute, at which time the mixer was stopped, and the cement and SCMs were added to the mixer. The time was marked at this point as the start of mixing. A lid was then placed on the mixer, the mixer was started, and the mixture was allowed to blend for approximately 30 seconds. The lid was then removed from the mixer, and while still mixing, the remaining two-thirds of the mixing water was slowly added to the mixture. The mixture was then allowed to mix for 3 minutes. If any caking in the back of the mixer was seen, the mixer was momentarily stopped, the caked material was broken up and pulled back into the bulk of the mixture, and the mixer was started again. After 3 minutes of mixing, the mixer was stopped, the lid was placed on the mixer, and the mixture was allowed to sit still for 3 minutes. After the three minute rest, the mixer was turned back on, and the mixture was mixed for a final 2 minutes. At the end of 2 minutes, concrete that was to be used for the rigid cracking frame and free shrinkage frame was placed in one wheel barrow, and taken to the building where the frames were located. The remaining concrete was poured into another wheelbarrow, and fresh concrete tests were performed. After fresh concrete testing was completed, concrete was wet sieved through a No. 4 sieve on a vibrating table to generate the mortar for the time-of-set specimens. When the time-of-set specimens were completed, the specimens and the remaining concrete were taken to the building where the frames were located. The remaining concrete was then placed into 26, 4in. x 8in. cylinders, 24 of which were then placed inside the match-cure water bath. The remaining two 4in. x 8in. cylinders were allowed to cure at air-temperature, and were evaluated for coefficient of thermal expansion later.

3.3.3 Fresh Concrete Testing

For each concrete mixture that was tested, slump, unit weight, and air content were recorded. These tests followed the following ASTM standards:

- Slump: ASTM C 143 (2010)
- Unit Weight: ASTM C 138 (2010)
- Air Content: ASTM C 231 (2010)

3.3.4 Hardened Concrete Testing

For each mixture, 24, 4in. x 8in. cylinder were cast for mechanical testing, 2, 4in. x 8in. cylinder were cast for evaluation of the mixtures coefficient of thermal expansion, and 9, 3in. x 3in. x 11.25in. prisms were cast for drying shrinkage evaluation. Hardened concrete testing followed the following ASTM standards:

- Compressive strength: ASTM C 39 (2010)
- Splitting Tensile strength: ASTM C 496 (2004)
- Static Modulus of Elasticity: ASTM C 469 (2010)
- Drying Shrinkage: ASTM C 157 (2008)

3.4 Experimental Testing Program

To evaluate each mixture design for cracking potential, a testing program was initiated to evaluate the stress development of a concrete mixture due to early-age volume changes under simulated environmental conditions. For each mixture, semi-adiabatic calorimetry, rigid cracking frame, free shrinkage frame, setting time and match-cured cylinder testing was performed. Figure 3.5 shows the order in which these tests were completed.

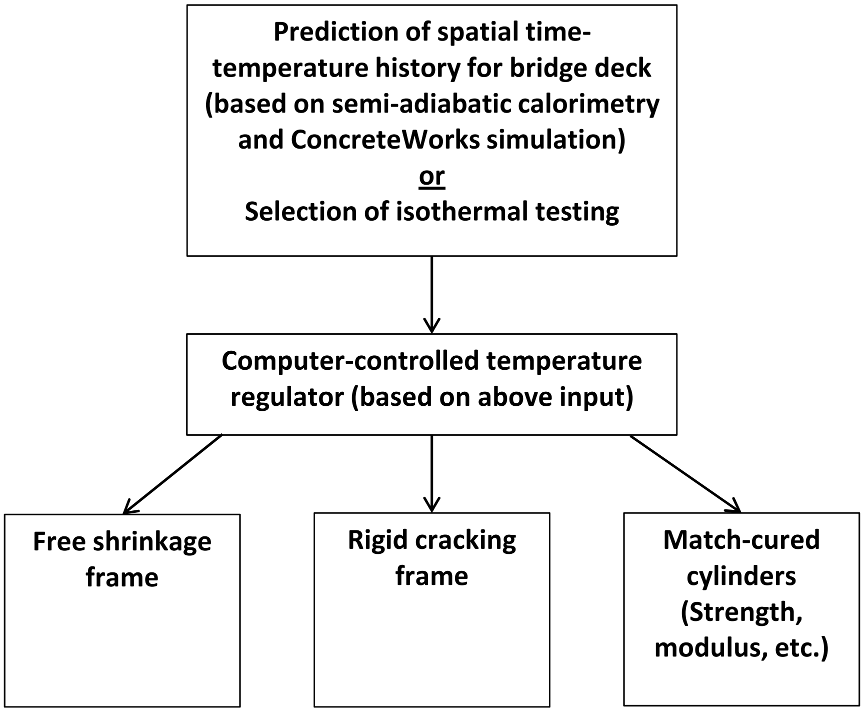

Figure 3.5: Testing process for rigid cracking frame.

3.4.1 Semi-Adiabatic Calorimetry

Before a rigid cracking frame test can be started for a mixture, the hydration parameters for that mixture must be calculated so that the simulated temperature development may be determined from ConcreteWorks. At least 7 days before the rigid cracking frame testing began, a

2 ft^3 concrete mixture was made to create one 6in. x 12in. cylinder and 12 ASTM C157 (2008) drying shrinkage prisms. The 2 ft^3 mixture size was determined based on the smallest allowable size mixture that was allowed by the concrete mixer. The 6in. x 12in. cylinder was made in three lifts, with rodding and tapping of the sides between each lift. The cylinder was then weighed, and placed in the Q-drum (Figure 3.6), marking how long after mixing had begun before the cylinder was placed in the Q-drum. The temperature of the concrete was measured using a Type K thermocouple inserted into the top of the concrete, and the heat flux through the insulated Q-drum was measured at the location of the logging box. After 120 hours had passed, the 6in. x 12in. cylinder was removed from the Q-drum, and the data were collected and processed.

Figure 3.6: Quadrel Q-drum.

3.4.2 Estimation of Bridge Deck Temperatures

Before the temperature profile could be created, several hydration parameters had to be determined for each mixture. The activation energy of the mixture (E_a) was determined using an empirical formula from Poole (2007), shown in Equation 3.2:

$$\begin{aligned} E_a = 41{,}230 + 1{,}416{,}000 * [(C_3A + C_4AF) * p_{Cement} * SO_3 * p_{Cement}] - 347{,}000 * Na_2O_{eq} \\ - 19.8 * Blaine + 29{,}600 * p_{Flyash} * p_{CaO-Flyash} + 16{,}200 * p_{GGBFS} - 51{,}600 \\ * p_{SF} - 3{,}090{,}000 * WRRET - 345{,}000 * ACCL \end{aligned} \tag{3.2}$$

The ultimate heat of hydration then had to be determined for the concrete mixture. This was done within the ConcreteWorks program, after inputting the concrete mixture design. Equation 3.3, found in Riding (2007), was used in the ConcreteWorks program to determine the ultimate heat of hydration.

$$H_u = H_{cem} * p_{Cem} + 461 * p_{GGBF-100} + 550 * p_{GGBF-120} + 1800 * p_{FA-CaO} * p_{FA} + 330 * p_{S.F.} \tag{3.3}$$

With the calculated activation energy and ultimate heat of hydration, the hydration parameters for the mixture could then be determined. Using the data gathered from the semi-adiabatic calorimetry testing, hydration parameters α, β, and τ for the concrete mixture were curve fit to match the values calculated from Equation 2.7 with those measured from the Q-drum. This process is described further in Riding (2007), Poole (2007), and Schindler and Folliard (2005).

With the hydration parameters calculated, a temperature profile could then be created in ConcreteWorks. Inputs for the ConcreteWorks program were the following:

- General Parameters
  - Placement Time = 10 A.M.
  - Placement Date:
    - Summer Pour = August 15, 2008
    - Winter Pour = February 17, 2008
  - Placement Location: Lubbock, TX
  - 8in. thick bridge deck with metal pan formwork
- Mixture proportions and aggregate types
- Cement Bogue values (determined with XRF testing)
- Hydration parameters: Ea, Hu, α, β, and τ
- Construction Inputs:
  - Summer Pour: 73^{o} placement temperature, blanket with 2.91 R-value
  - Winter Pour: 65^{o} placement temperature, blanket with 5.67 R-value

Inputs not specified were taken as the default values provided by ConcreteWorks. A sample report, which contains many of the inputs used, is provided in Appendix A.

After the ConcreteWorks temperature profile was created, the temperatures at approximately 4 in. below the concrete surface (mid-depth on the simulated bridge deck) were selected from the ConcreteWorks output as the temperature profile input for the rigid cracking frame mixture. Figure 3.7 shows sample summer and winter temperature profiles for a straight cement mixture (CH-RG) and a 35% Type C fly-ash replacement mixture (F4H-35RG).

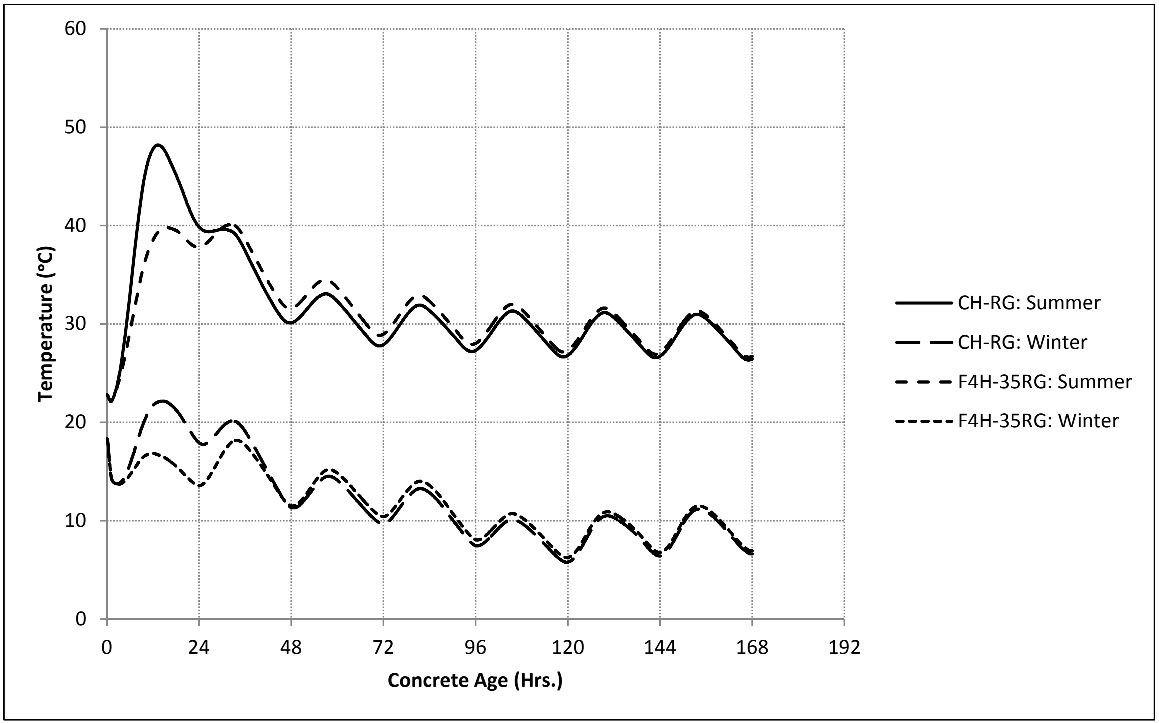

Figure 3.7: Simulated temperature profiles for summer and winter pours.

3.4.3 Rigid Cracking Frame

After the one week in which the semi-adiabatic calorimetry and drying shrinkage prisms were cast, a 5 ft^3 concrete mixture was made to supply concrete to the rigid cracking frame, free shrinkage frame, setting time specimens, and the match cured concrete cylinders.

Before being set into place on the cracking frame, the bottom and two side pieces of the formwork were covered with tight fitting plastic sheeting, which was taped into place using waterproof HVAC aluminum foil tape. The bottom and side pieces of formwork were then fit into place against the bottom of the cracking frame. After aligning the formwork, a combination of 'plumber's putty' and silicone were used to smooth and seal the gaps between the bottom crossbars, crossheads, and the gaps between the bottom and sides of the formwork.

Concrete was placed in two lifts in the rigid cracking frame, with a mechanical vibrator used after each lift to consolidate the concrete. Special attention was paid to the concrete placed inside the crossheads, to ensure that a good bond formed between the concrete and the teeth in the crosshead. Once the second lift was completed, a wooden trowel was used to smooth the concrete surface. The concrete was then covered with a plastic sheet and sealed with HVAC tape. The top crossbars were installed and torqued to specification, and then then top formwork was placed on top of the frame. Thermocouples were then inserted into the concrete through the top of the top formwork, and the hoses that connect the circulator, crossheads, and the formwork were connected. Finally, strain and temperature gauges were attached to the Invar side bars. A diagram of the rigid cracking frame is provided in Figure 3.8, and thorough discussion on the details of the rigid cracking frame can be found in Whigham (2005).

Six days after mixing, the concrete from the previous week's mixture was jackhammered out of the rigid cracking frame, and the crossheads were cleaned with a wire brush. The bottom and two sides of formwork pieces had the previously used plastic and silicone removed, and were then cleaned with a wire brush and oiled.

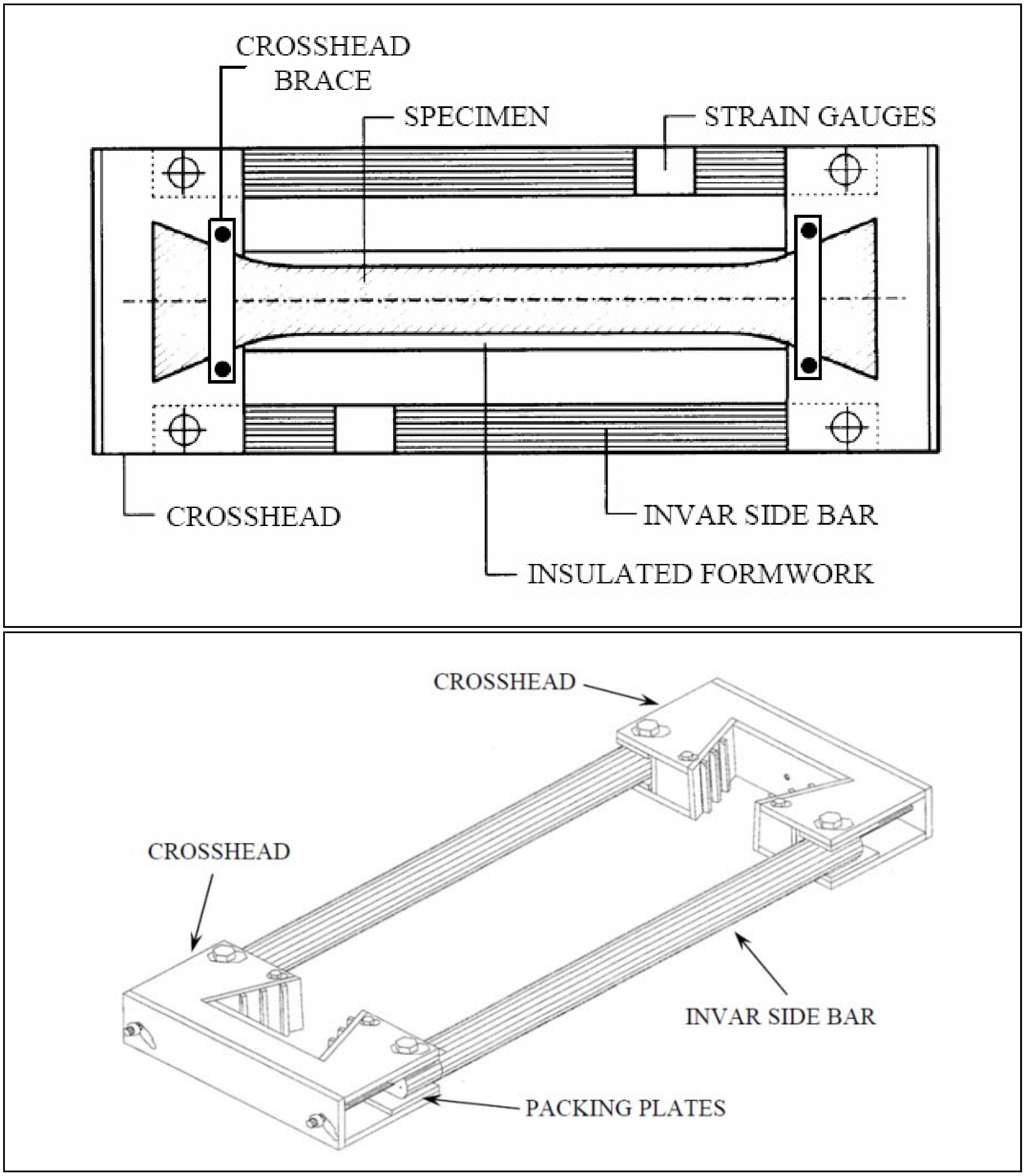

Figure 3.8: Rigid cracking frame drawings (Whigham, 2005; Meadows, 2007).

When simulating the summer and winter concrete pours, concrete in the rigid cracking frame, free shrinkage frame, and match cured cylinder bath were subjected to the ConcreteWorks-generated temperature profile for 96 hours. After this period, the concrete was cooled artificially at a rate of 1.8 1°F/hr. (1°C/hr.) to force cracking to occur. If cracking did not occur by 120 hours after mixing (24 hours of artificial cooling), the test was stopped. This time limit of 120 hours was chosen because past that time, the frame had usually reached the limit of its ability to lower the concrete temperature (due to the insulative properties of the frame, and temperature control in the testing room). If a concrete mixture was being tested isothermally, the rigid cracking frame, free shrinkage frame, and match cured cylinder bath were all kept at a temperature of 26.8°F (20°C) for 240 hours, after which the mixture was artificially cooled at 1.8 1°F/hr. Artificial cooling was allowed to run until approximately 260–300 hours after the start of mixing.

When the first test runs for the cold weather temperature profiles were placed in the cracking frame, it was found that the one water circulator that was used to control the rigid cracking frame and the free shrinkage frame had difficulty keeping the temperature on track during the first 8 hours, and had trouble reaching low temperatures during the artificial cooling phase of the test. This was due to the inadequate temperature control in the room used for testing during the summer months. To remedy the issue, cotton rags were wrapped around the brass fittings of the circulator hoses, and foam panels were taped against the sides of the crosshead that were exposed. The increased insulation proved to be effective in keeping a tighter tolerance between the concrete temperature and the temperature profile, and has also allowed the concrete to reach a lower temperature during the artificial cooling stage. Application of the additional insulation can be seen in Figure 3.9.

Figure 3.9: Rigid cracking frame with added insulation.

Before testing began on TxDOT Project 6332, the formwork that had been previously used for rigid cracking frame testing, shown in Figure 3.10, was replaced with formwork built by the author, shown in Figure 3.11. After many mixtures and years of testing, the previous wooden formwork had considerable distress, as shown in Figure 3.10, including rotting wood, separation of copper flashing, and fatiguing of the walls of the formwork. Fatigue of the sides of the formwork led to the sides shifting during concrete placement in the formwork, which later caused stress concentrations at the formwork-crosshead interface. The new formwork was built with a steel frame, and consists of three separate pieces. The new design was constructed to provide a greater ease of use, and to create formwork that would withstand the rigors of the set-up and removal procedure for many years. The new formwork is shown in Figure 3.11, with further construction pictures and information presented in Appendix C.

Figure 3.10: Old formwork for rigid cracking frame.

Figure 3.11: Rigid cracking frame with new formwork.

3.4.4 Free Shrinkage Frame

For each rigid cracking frame test, a free shrinkage frame test specimen was also cast. This specimen evaluates the unrestrained volume changes in the concrete under the same temperature conditions as the rigid cracking frame, such that creep parameters can be back calculated from the measured restrained stresses in the rigid cracking frame.

Before a mixture, the previous mixture was removed from the free shrinkage frame, and the frame and end plates were wiped clean. The endplates were bolted back onto the free shrinkage frame, and the inside of the frame was wiped down with oil. A layer of plastic was then set inside the frame and taped with painter's tape at the tops of the sides. Another layer of oil was then applied to the free shrinkage frame to decrease the resistance to concrete movement, and then another layer of plastic was placed in the frame, and secured at the top of the sides. Special care was taken to insure that the plastic fit completely into the frame, such that it did not reduce the specimen cross section. Two plastic sheet squares were then placed in front of the end plates, and threaded Invar rods were pushed through this sheet of plastic. On the exterior of the frame, the Invar rods were connected to LVDTs, and on the interior, connected to a 1in. x 1in. aluminum square that was screwed onto the end of the threaded rod. The Invar rod that was on the interior of the frame was then covered with a thick grease, to allow for safe removal of the rod after the test was completed.

On the mixing day, concrete was placed in the free shrinkage frame in two lifts, with mechanical vibration used after each lift to achieve proper consolidation. Special care was taken to insure that concrete was well consolidated between the aluminum squares and the steel end plates. While vibrating the second lift of the free shrinkage frame, the LVDTs were monitored and adjusted so that they were in an optimal location for measurement during the test, otherwise, inaccurate measurements would be taken if the LVDTs were positioned either too far 'in' or 'out' (National Instruments, 2006).

The end plates of the free shrinkage frame have interior plates that are able to move in and out of the inside of the free shrinkage frame. When fresh concrete is placed in the frame, bolts hold the plates so that they are further inside the frame. During the first few hours after mixing, these plates hold the concrete in place. Upon reaching initial set, as determined by a separate ASTM C403 (2008) test, bolts are tightened on the exterior of the free shrinkage frame that 'back-off' the plates, thereby leaving the concrete specimen free to expand and contract within the free shrinkage frame. The free shrinkage frame is shown in Figure 3.12 and Figure 3.13. The initial set time was recorded, and is presented on the individual graphs related to rigid cracking frame and free shrinkage frame testing in Appendix A. A table of setting time values is also presented in Section 4.9.

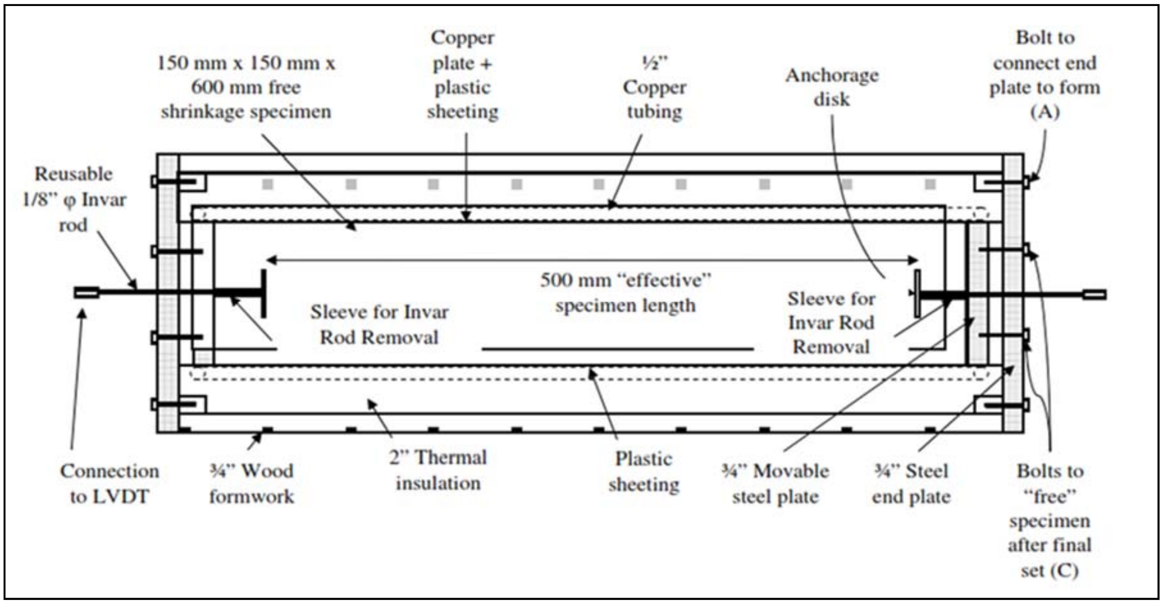

Figure 3.12: Plan view of free shrinkage frame (Meadows, 2007).

Figure 3.13: Free shrinkage frame after mix preparation.

3.4.5 Setting Time and Equivalent Age

For each concrete mixture, three time-of-set specimens were made in accordance with ASTM C 403 (2008). The specimens were cast in ink cans that were 5 in. high with a 6in. diameter. Approximately halfway through the testing for TxDOT 6332, the research team began including an iButton temperature measuring devices in the time-of-set cans (Maxim, 2011). iButtons, made by Dallas Semiconductor, consist of an onboard thermocouple, battery, and a memory chip capable of storing over 2,000 data points; iButtons are capable of logging temperature readings every 5 minutes for a period of 7 days. The time-of-set can with an iButton installed is shown in Figure 3.14. With that time-temperature and penetration resistance information, a substantial database of maturity and time-of-set data was created.

Figure 3.14: Temperature collection inside time-of-set can.

In addition to the two time-of-set cans that were cast and placed in a match-cured water bath under previous studies involving the free shrinkage frame (Riding, 2007; Rao, 2008; Whigham, 2005), another time-of-set specimen was cast with an iButton sensor, and allowed to cure in a room that was kept at 73°F and 50% RH (for use in drying shrinkage and length change measurements). This separate can, and separate temperature development, allowed the research team to further evaluate the prediction model proposed by Schindler (2004) for a given mixture design under different time-temperature histories. This temperature measurement, placed at the center of the time-of-set specimen, allowed the researcher to generate time-temperature histories for each time-of-set test that was performed.

3.4.6 Cylinder Match Curing System

For each rigid cracking frame that was tested, 26, 4in. x 8in. concrete cylinders were cast. Twenty-four of these cylinders were placed in a water bath that was driven by a circulator, and programmed to match the temperature of the middle of the rigid cracking frame. A Type K thermocouple was placed inside one of the cylinders at the beginning of the test to provide a feedback loop for the program that controlled the match-cure water bath. The match curing system is shown in Figure 3.15.

Figure 3.15: Cylinder match curing system.

For concrete mixtures undergoing hot weather simulations, cylinders were tested at 12 hours, 1 day, 2 day, 3 day, 7 day, and 28 days after mixing. Mixtures that were undergoing cold weather simulation were tested at 1 day, 2 day, 3 day, 4 day, 7 day, and 28 days after mixing. For each testing day, four cylinders were removed from the match cured water bath, and replaced with 'dummy' concrete cylinders. On the first set of testing (12 hours for hot simulations and 1 day for cold simulations), two cylinders were tested for splitting tensile strength, then one cylinder tested to determine compressive strength, then the last cylinder was tested for modulus of elasticity, using 0.4 x f'c from the previous test as an upper bound, then broken to obtain the compressive strength. On subsequent testing days, two cylinders were broken in splitting tension, and then the following two cylinders underwent both modulus and compression testing. The first cylinder that was tested for modulus of elasticity used an approximation for the 0.4 x f'c upper bound that was obtained from the percent load increase obtained from the splitting tensile cylinder tests. The second cylinder that was tested used an upper bound value that was calculated from the first cylinders compressive strength. This method of estimation for estimating the upper bound of the elastic modulus test was found to be quite accurate over the course of the project, and allowed the research team to conduct a greater number of modulus tests with the cylinders that were available for testing. Compression, splitting tension, and modulus of elasticity tests were performed according to ASTM standards (ASTM C39, 2010; ASTM C496, 2004; ASTM C469, 2010). The mechanical properties of the mixtures tested are presented in Chapter 4.

3.4.7 Drying Shrinkage Testing

As part of the 2 ft^3 concrete mix that was prepared for semi-adiabatic calorimetry, nine 3in. x 3in. x 11.25in. concrete prisms were prepared in accordance with ASTM C 157 (2008). Measurement of the drying shrinkage specimens followed a process similar to that presented in ASTM C 157, but with modifications to allow the research team to evaluate the effects of extended curing and hydration on drying shrinkage performance. After allowing the nine prisms to cure for 24 hours, the prisms were demolded, and then placed in 73°F lime-saturated water for approximately 1 hour. At the end of the hour, three of the prisms were removed from the lime-saturated water, gently dried of surface moisture, and measured and weighed. The remaining six prisms were allowed to continue curing in the lime-saturated water. At seven days after mixing, three more of the prisms were removed and measured, and at ten days after mixing, the last three prisms were removed, dried, and measured. Seven and ten days were selected, as these are close to the typical number of days (8 to 10 days) after mixing that curing blankets are removed from bridge decks in the field. For each set, the measurement that was taken immediately after the prisms were removed from the lime-saturated water was considered the initial measurement for the shrinkage calculations. For all prisms, after they were removed from the lime-saturated water, future measurements were taken at 4, 7, 14, 28, 56, 112, and 180 days after the removal from the lime-saturated water. Drying shrinkage prisms stored in the drying shrinkage room can be seen in Figure 3.16.

Figure 3.16: Drying shrinkage prisms.

Chapter 4. Laboratory Testing Program Results

The results obtained from the laboratory testing program are presented in this chapter. The fresh concrete properties and hydration parameters are presented first, followed by the mechanical strength development and drying shrinkage strains that were recorded for each mixture. In Section 4.3, models are also evaluated against the measured strength development and drying shrinkage strains. The remainder of the chapter involves the presentation and comparison of the temperature profiles, rigid cracking frame stresses, and free shrinkage frame strains for the mixtures evaluated. At the end of the chapter, a modified B3 creep model is evaluated for the mixtures tested. In post-processing of the results, the research team noted that erroneous hydration parameters were used in the generation of the temperature profiles for F1H-25RG, F4H-25RG, and U4L-RG. Ultimate degree of hydration, α_u, values were taken higher than 100% for these mixtures. While the results from these tests cannot be compared to the other mixtures, the mixtures have been included in this report for completeness.

4.1 Fresh Concrete Properties

Table 4.1 provides the fresh concrete properties measured by the research team, in accordance with the standards provided in Section 3.3.3.

Table 4.1: Fresh concrete properties.

Mixture Type	Mixture Name	Slump in.	Unit Weight lb/yd^3	Air %
Control Mixtures	CL-RG	5.00	149.6	3.4
	CL-RGC	5.50	148.0	3.3
	CL-RGI	3.25	148.8	2.3
	CH-RG	5.00	146.4	5.8
	CH-RGC	5.00	144.8	3.5
	CL-LS	3.25	146.8	2.4
	CL-LSC	6.75	147.2	2.5
Class-C Fly Ash Mixtures	*F3L-25RG	7.25	146.4	1.0
	*F3L-35RG	6.50	144.9	1.6
	F3L-35RGC	9.00	148.0	1.0
	F3L-35LS	9.00	145.6	1.0
	F3L-35LSC	8.50	146.4	2.2
	*F4L-25RG	8.50	147.6	1.5
	F4L-35RGC	9.25	146.0	1.6
	*F4H-25RG	3.50	146.4	2.1
	F4H-35RG	9.00	152.0	3.2
	F4H-35RGC	8.00	143.6	3.0
Other Mixtures	*U4L-35RG	9.00	147.3	0.7
	U4L-35RGC	10.50	146.8	1.0
	SL-RG	5.00	149.6	3.5
	SL-RGC	6.00	148.0	2.4
	SL-RGI	4.50	147.2	2.5
	OL-RG	1.50	148.4	2.0
	OL10-RG	0.50	147.7	2.0
Class-F Fly Ash Mixtures	*F1L-25RG	4.00	143.1	2.0
	F1L-25RGC	7.00	146	1.0
	*F1H-25RG	3.50	142.4	1.9
	F1H-25RGC	6.00	146.4	2.8
	*F2L-25RG	6.00	147.1	1.0
	F2L-25RGC	9.00	144.8	3.2
	*F2L-35RG	4.75	144.2	1.4
	F2L-35RGC	9.50	146	5.5
	F2H-25RG	8.50	146	3.8
	F2H-25RGC	8.25	142	4.1
GGBFS Mixtures	GL-35RG	3.50	146.4	4.0
	GL-35RGC	6.50	147.2	2.4
	GL-50RG	4.50	147.2	2.9
	GL-50RGC	7.00	147.2	2.0
	GH-50RG	4.00	147.6	3.9
	GH-50RGC	6.00	145.2	3.8
	GL-50LS	5.00	144	3.0
	GL-50LSC	9.25	146.8	2.5

* Denotes a mixture that was completed under IAC-FA

4.2 Semi-Adiabatic Calorimetry

Tables 4.2 through 4.6 provide the semi-adiabatic calorimetry results for the concrete mixtures tested. E_a, the activation energy, is calculated as shown in Equation 3.2; H_u, the ultimate heat of hydration, is calculated as shown in Equation 3.3; and α, β, and τ are curve fit using Excel Solver to match Equation 2.7 with the measured heat release from the Q-drum.

Table 4.2: Semi-adiabatic results for control mixtures.

Mixture Type	Mixture Name	E_a J/mol	H_u J/kg	α_u %	β	τ hrs.
Control Mixtures	CL-RG	32,119	468,839	0.747	1.011	14.44
	CL-RGC	32,119	468,838	0.747	1.011	14.44
	CL-RGI	32,119	468,839	0.747	1.011	14.44
	CH-RG	32,252	475,170	0.837	0.959	14.60
	CH-RGC	32,049	475,170	0.836	0.962	14.55
	CL-LS	32,129	468,839	0.774	1.103	15.55
	CL-LSC	32,129	468,839	0.774	1.103	15.55

* Denotes a mixture that was completed under IAC-FA

Table 4.3: Semi-adiabatic calorimetry results for Class C fly ash mixtures.

Mixture Type	Mixture Name	E_a J/mol	H_u J/kg	α_u %	β	τ hrs.
Class-C Fly Ash Mixtures	F3L-25RG*	26,499	410,919	0.828	0.729	25.66
	F3L-35RG*	26,650	410,168	0.817	0.914	20.71
	F3L-35RGC	30,339	448,133	1.000	0.718	34.75
	F3L-35LS	30,339	448,152	0.759	0.839	33.11
	F3L-35LSC	30,339	448,152	0.759	0.839	33.11
	F4L-25RG*	25,461	347,919	0.953	0.973	19.68
	F4L-35RGC	30,529	459,725	0.690	1.178	27.57
	F4H-25RG*	25,461	347,919	1.284	1.014	18.47
	F4H-35RG	29,886	468,757	0.904	0.789	26.93
	F4H-35RGC	29,846	468,286	0.904	0.790	26.91

* Denotes a mixture that was completed under IAC-FA

Table 4.4: Semi-adiabatic calorimetry results for Class F fly ash mixtures.

Mixture Type	Mixture Name	E_a J/mol	H_u J/kg	α_u %	β	τ hrs.
Class-F Fly Ash Mixtures	F1L-25RG*	25,000	309,368	0.896	0.934	14.67
	F1L-25RGC	29,119	356,975	0.862	0.974	15.75
	F1H-25RG*	25,461	347,919	1.074	0.796	14.42
	F1H-25RGC	28,588	369,091	0.941	0.907	16.25
	F2L-25RG*	27,102	447,461	2.773	2.769	28.22
	F2L-25RGC	30,163	423,193	0.702	1.091	17.92
	F2L-35RG*	25,461	347,919	0.787	1.028	16.86
	F2L-35RGC	29,631	404,934	0.570	1.242	19.87
	F2H-25RG	29,453	415,328	0.857	0.893	17.34
	F2H-25RGC	29,626	444,403	0.801	0.892	17.36

* Denotes a mixture that was completed under IAC-FA

Table 4.5: Semi-adiabatic calorimetry results for GGBFS mixtures.

Mixture Type	Mixture Name	E_a J/mol	H_u J/kg	α_u %	β	τ hrs.
GGBFS Mixtures	GL-35RG	33,651	497,245	0.812	0.713	24.53
	GL-35RGC	33,651	497,245	0.812	0.713	24.53
	GL-50RG	34,841	509,419	0.901	0.601	36.94
	GL-50RGC	34,841	509,419	0.901	0.601	36.94
	GH-50RG	33,871	512,585	0.831	0.709	28.72
	GH-50RGC	33,978	517,497	0.823	0.708	28.78
	GL-50LS	34,841	509,419	0.735	0.595	36.16
	GL-50LSC	34,841	509,419	0.735	0.595	36.16

* Denotes a mixture that was completed under IAC-FA

Table 4.6: Semi-adiabatic calorimetry results for other mixtures.

Mixture Type	Mixture Name	E_a J/mol	H_u J/kg	α_u %	β	τ hrs.
Other Mixtures	*U4L-35RG	27080	436268	1.436	0.668	32.84
	U4L-35RGC	30239	412841	0.675	1.284	30.76
	SL-RG	32129	468838	0.749	1.082	17.42
	SL-RGC	32129	468839	0.749	1.082	17.42
	SL-RGI	32129	468839	0.749	1.082	17.42
	OL-RG	32129	468839	0.782	1.087	15.60
	OL10-RG	32129	468838	0.795	1.023	14.83

* Denotes a mixture that was completed under IAC-FA

4.3 Hardened Concrete Properties

As previously discussed, mechanical testing was performed at various times throughout the course of a mixture. Additionally, a set of drying shrinkage specimens were cast for each mixture design and evaluated to obtain the drying shrinkage for that mixture with various curing times. The results of these tests are presented, and compared with existing prediction models.

4.3.1 Mechanical Properties

Tables 4.7 through 4.11 provide the mechanical testing results for the mixtures tested. For conciseness, f’c is used to abbreviate the compressive strength, f’st is used to abbreviate the splitting tensile strength, and E is used to abbreviate the elastic modulus of elasticity. Mixtures tested under IAC-FA are denoted with an asterisk before their name. All values are rounded and reported as specified by their respective ASTM specification.

Table 4.7: Mechanical properties for control mixtures.

CL-RG				
Time of Test	hrs.	f'c psi	f'st psi	E psi
12 Hr.	12.9	2,140	315	3,800,000
1 Day	24.7	3,670	445	4,500,000
2 Day	49.7	4,480	540	4,700,000
3 Day	73.0	4,790	540	5,250,000
7 Day	168.1	5,450	560	5,150,000
28 Day	677.0	6,120	590	5,850,000

CL-RGC				
Time of Test	hrs.	f'c psi	f'st psi	E psi
12 Hr.	14.8	680	100	1,800,000
1 Day	26.0	2,240	350	3,750,000
2 Day	52.4	3,830	555	4,450,000
3 Day	74.5	4,290	555	4,750,000
7 Day	166.3	5,580	560	5,050,000
28 Day	678.7	6,900	710	5,350,000

CL-RGI				
Time of Test	hrs.	f'c psi	f'st psi	E psi
24 Hr.	20.7	1,620	260	3,050,000
2 Day	49.1	3,630	490	4,500,000
3 Day	73.6	4,390	575	4,500,000
4 Day	97.9	4,580	600	4,900,000
7 Day	171.0	5,400	635	5,050,000
28 Day	675.9	6,140	660	5,450,000

CH-RG				
Time of Test	hrs.	f'c psi	f'st psi	E psi
12 Hr.	10.9	1,380	210	3,350,000
1 Day	25.2	2,840	380	4,550,000
2 Day	49.0	3,450	445	4,600,000
3 Day	73.5	3,560	480	4,650,000
7 Day	166.9	3,940	480	5,150,000
28 Day	669.7	4,480	520	5,300,000

CH-RGC				
Time of Test	hrs.	f'c psi	f'st psi	E psi
24 Hr.	22.5	1,740	270	3,500,000
2 Day	48.1	2,970	425	4,500,000
3 Day	75.0	3,380	415	4,500,000
4 Day	100.3	3,690	505	4,550,000
7 Day	167.4	4,240	510	4,600,000
28 Day	679.2	5,550	590	5,200,000

CL-LS				
Time of Test	hrs.	f'c psi	f'st psi	E psi
12 Hr.	12.4	1,210	180	2,600,000
1 Day	29.4	3,800	470	4,100,000
2 Day	51.6	5,080	515	4,550,000
3 Day	80.3	5,080	565	4,600,000
7 Day	172.6	5,410	605	4,700,000
28 Day	674.3	6,420	700	4,850,000

CL-LSC				
Time of Test	hrs.	f'c psi	f'st psi	E psi
24 Hr.	26.6	1,890	270	2,600,000
2 Day	48.8	3,530	445	3,350,000
3 Day	73.6	4,070	510	3,500,000
4 Day	99.5	4,360	545	4,000,000
7 Day	173.8	4,980	610	4,150,000
28 Day	679.9	6,240	675	5,100,000

* Denotes a mixture that was completed under IAC-FA

Table 4.8: Mechanical properties for Class C fly ash mixtures.

*F3L-25RG				
Time of Test hrs.		f'c psi	f'st psi	E psi
12 Hr.	10.5	280	35	1,450,000
1 Day	26.5	2,260	395	3,700,000
2 Day	52.0	3,460	520	4,650,000
3 Day	70.0	3,800	570	4,650,000
7 Day	171.0	3,850	645	5,350,000
28 Day	675.0	4,920	750	5,150,000

*F3L-35RG				
Time of Test hrs.		f'c psi	f'st psi	E psi
12 Hr.	11.0	210	30	1,400,000
1 Day	25.5	1,290	270	3,350,000
2 Day	48.0	2,570	430	4,050,000
3 Day	71.0	3,060	525	4,100,000
7 Day	170.8	3,670	600	4,200,000
28 Day	675.0	5,250	760	5,250,000

F3L-35RGC				
Time of Test hrs.		f'c psi	f'st psi	E psi
24 Hr.	30.9	600	90	2,200,000
2 Day	59.3	1,520	250	3,300,000
3 Day	77.1	2,000	325	3,550,000
4 Day	100.1	2,370	375	3,950,000
7 Day	176.7	3,930	465	4,500,000
28 Day	679.9	6,220	695	5,350,000

F3L-35LS				
Time of Test hrs.		f'c psi	f'st psi	E psi
12 Hr.	14.0	420	55	1,500,000
1 Day	28.9	1,770	250	3,100,000
2 Day	51.0	2,840	385	3,550,000
3 Day	77.4	3,660	450	4,100,000
7 Day	176.6	4,720	535	4,500,000
28 Day	677.8	6,020	635	4,850,000

F3L-35LSC				
Time of Test hrs.		f'c psi	f'st psi	E psi
24 Hr.	30.7	350	40	1,450,000
2 Day	57.5	1,330	185	2,850,000
3 Day	80.3	1,850	260	2,950,000
4 Day	99.9	2,210	330	3,050,000
7 Day	201.7	4,140	490	4,050,000
28 Day	682.6	5,970	670	4,800,000

*F4L-25RG				
Time of Test hrs.		f'c psi	f'st psi	E psi
12 Hr.	10.0	290	65	950,000
1 Day	25.8	2,330	430	4,350,000
2 Day	49.8	3,370	530	5,000,000
3 Day	70.0	3,960	625	4,700,000
7 Day	171.5	4,500	670	4,850,000
28 Day	676.0	5,910	740	5,900,000

F4L-35RGC				
Time of Test hrs.		f'c psi	f'st psi	E psi
24 Hr.	37.3	680	80	2,350,000
2 Day	63.8	1,830	295	3,700,000
3 Day	84.1	2,390	340	4,050,000
4 Day	109.3	2,740	405	4,350,000
7 Day	174.1	4,030	525	4,800,000
28 Day	677.9	6,960	680	4,850,000

*F4H-25RG				
Time of Test hrs.		f'c psi	f'st psi	E psi
12 Hr.	12.0	940	145	2,550,000
1 Day	28.0	2,500	390	4,050,000
2 Day	52.8	3,300	510	4,450,000
3 Day	81.8	3,550	555	4,750,000
7 Day	173.5	3,880	555	4,950,000
28 Day	679.7	5,040	690	5,350,000

F4H-35RG				
Time of Test hrs.		f'c psi	f'st psi	E psi
12 Hr.	13.3	580	80	2,500,000
1 Day	25.0	1,830	290	3,750,000
2 Day	49.4	3,070	415	4,150,000
3 Day	73.4	3,840	465	4,700,000
7 Day	170.4	4,370	515	4,900,000
28 Day	671.9	5,510	565	5,250,000

F4H-35RGC				
Time of Test hrs.		f'c psi	f'st psi	E psi
24 Hr.	23.3	530	75	2,200,000
2 Day	48.9	1,570	255	3,350,000
3 Day	75.6	2,270	325	3,650,000
4 Day	97.3	2,660	370	3,850,000
7 Day	172.8	4,160	495	4,500,000
28 Day	677.3	6,270	610	5,400,000

* Denotes a mixture that was completed under IAC-FA

Table 4.9: Mechanical properties for Class F fly ash mixtures.

*F1L-25RG				
Time of Test		f'c	f'st	E
	hrs.	psi	psi	psi
12 Hr.	9.0	160	25	850,000
1 Day	25.3	2,160	395	3,900,000
2 Day	51.0	2,990	480	4,400,000
3 Day	71.0	3,160	505	4,550,000
7 Day	171.0	3,670	600	4,200,000
28 Day	676.5	4,880	680	5,300,000

*F1H-25RG				
Time of Test		f'c	f'st	E
	hrs.	psi	psi	psi
12 Hr.	11.1	1,010	175	3,250,000
1 Day	29.3	1,980	325	3,450,000
2 Day	52.8	2,340	385	4,400,000
3 Day	76.3	2,630	385	4,400,000
7 Day	173.6	2,990	455	4,500,000
28 Day	678.4	3,800	625	4,950,000

*F2L-25RG				
Time of Test		f'c	f'st	E
	hrs.	psi	psi	psi
12 Hr.	9.0	180	25	700,000
1 Day	25.3	2,000	415	1,000,000
2 Day	50.5	2,790	485	4,550,000
3 Day	69.5	3,270	535	4,300,000
7 Day	171.0	3,960	670	4,400,000
28 Day	671.5	5,520	730	6,450,000

*F2L-35RG				
Time of Test		f'c	f'st	E
	hrs.	psi	psi	psi
12 Hr.	11.0	230	35	1,000,000
1 Day	25.8	1,720	310	3,300,000
2 Day	49.3	2,500	435	4,100,000
3 Day	69.0	2,720	475	4,200,000
7 Day	168.0	3,320	655	4,450,000
28 Day	673.7	4,560	710	5,400,000

F2H-25RG				
Time of Test		f'c	f'st	E
	hrs.	psi	psi	psi
12 Hr.	11.3	820	125	1,400,000
1 Day	25.4	2,370	325	4,000,000
2 Day	49.9	2,890	415	4,500,000
3 Day	73.4	3,190	385	4,550,000
7 Day	166.6	3,370	445	4,700,000
28 Day	669.9	4,840	555	4,950,000

*Denotes a mixture that was completed under IAC-FA

F1L-25RGC				
Time of Test		f'c	f'st	E
	hrs.	psi	psi	psi
24 Hr.	26.7	1,100	175	2,400,000
2 Day	49.6	2,020	295	3,600,000
3 Day	70.9	2,480	370	4,050,000
4 Day	98.4	3,010	425	4,100,000
7 Day	170.3	3,810	480	4,600,000
28 Day	680.9	5,460	660	5,200,000

F1H-25RGC				
Time of Test		f'c	f'st	E
	hrs.	psi	psi	psi
24 Hr.	22.0	1,100	180	2,700,000
2 Day	49.2	2,310	340	3,850,000
3 Day	71.7	2,750	380	4,000,000
4 Day	98.4	3,080	450	4,250,000
7 Day	170.0	3,840	480	4,750,000
28 Day	676.2	5,180	610	5,150,000

F2L-25RGC				
Time of Test		f'c	f'st	E
	hrs.	psi	psi	psi
24 Hr.	23.7	530	70	1,900,000
2 Day	48.0	1,670	265	3,500,000
3 Day	70.2	2,300	325	3,950,000
4 Day	97.3	2,580	390	4,100,000
7 Day	164.3	3,250	465	4,400,000
28 Day	681.8	5,660	665	5,200,000

F2L-35RGC				
Time of Test		f'c	f'st	E
	hrs.	psi	psi	psi
24 Hr.	32.9	480	65	1,300,000
2 Day	48.1	1,080	150	2,950,000
3 Day	76.8	1,870	250	3,800,000
4 Day	100.8	1,960	315	3,750,000
7 Day	171.9	2,800	420	4,550,000
28 Day	678.9	5,120	605	5,100,000

F2H-25RGC				
Time of Test		f'c	f'st	E
	hrs.	psi	psi	psi
24 Hr.	27.0	1,090	160	2,750,000
2 Day	50.3	2,060	305	3,400,000
3 Day	74.8	2,390	365	3,500,000
4 Day	101.4	2,680	415	3,600,000
7 Day	170.1	3,510	440	3,900,000
28 Day	670.4	5,090	565	4,350,000

Table 4.10: Mechanical properties for GGBFS mixtures.

GL-35RG				
Time of Test		f'c	f'st	E
	hrs.	psi	psi	psi
12 Hr.	13.5	1,250	180	2,900,000
1 Day	24.2	2,660	370	4,150,000
2 Day	50.9	4,110	475	4,700,000
3 Day	72.6	4,650	525	4,800,000
7 Day	166.3	5,170	525	5,000,000
28 Day	669.2	6,340	710	5,700,000

GL-35RGC				
Time of Test		f'c	f'st	E
	hrs.	psi	psi	psi
24 Hr.	30.3	900	135	2,350,000
2 Day	48.0	1,500	245	3,250,000
3 Day	79.2	2,080	320	3,700,000
4 Day	96.1	2,270	365	4,000,000
7 Day	172.4	3,450	460	4,500,000
28 Day	672.4	6,540	690	4,700,000

GL-50RG				
Time of Test		f'c	f'st	E
	hrs.	psi	psi	psi
12 Hr.	14.0	870	120	2,500,000
1 Day	24.7	1,980	315	3,300,000
2 Day	51.5	3,440	455	4,850,000
3 Day	73.4	4,240	510	5,350,000
7 Day	169.7	5,070	535	5,400,000
28 Day	674.2	6,000	600	5,500,000

GL-50RGC				
Time of Test		f'c	f'st	E
	hrs.	psi	psi	psi
24 Hr.	26.8	390	55	1,600,000
2 Day	46.3	840	135	2,350,000
3 Day	80.6	1,300	220	3,250,000
4 Day	100.2	1,450	235	3,300,000
7 Day	176.8	2,810	440	4,250,000
28 Day	676.6	6,880	740	5,850,000

GH-50RG				
Time of Test		f'c	f'st	E
	hrs.	psi	psi	psi
12 Hr.	11.6	570	75	2,800,000
1 Day	25.0	2,180	295	3,900,000
2 Day	48.2	3,440	450	4,600,000
3 Day	72.9	4,060	470	4,900,000
7 Day	166.9	4,510	545	5,050,000
28 Day	669.9	5,380	575	5,650,000

GH-50RGC				
Time of Test		f'c	f'st	E
	hrs.	psi	psi	psi
24 Hr.	28.5	510	65	1,700,000
2 Day	52.5	1,090	185	2,550,000
3 Day	73.5	1,390	230	2,800,000
4 Day	97.2	1,760	305	3,050,000
7 Day	168.9	3,410	500	3,650,000
28 Day	676.3	5,480	660	4,650,000

GL-50LS				
Time of Test		f'c	f'st	E
	hrs.	psi	psi	psi
12 Hr.	12.6	460	50	1,700,000
1 Day	28.8	1,640	235	3,250,000
2 Day	53.2	1,570	375	3,950,000
3 Day	79.1	3,820	475	4,200,000
7 Day	176.5	5,120	565	4,700,000
28 Day	681.0	6,760	730	4,950,000

Gl-50LSC				
Time of Test		f'c	f'st	E
	hrs.	psi	psi	psi
24 Hr.	30.7	660	95	1,850,000
2 Day	56.4	1,260	185	2,650,000
3 Day	74.6	1,440	215	2,700,000
4 Day	98.8	1,840	265	3,250,000
7 Day	177.6	3,080	425	4,000,000
28 Day	675.6	7,160	730	5,150,000

* Denotes a mixtures that was completed under IAC-FA

Table 4.11: Mechanical properties for other mixtures.

*U4L-35RG				
Time of Test hrs.		f'c psi	f'st psi	E psi
12 Hr.	11.9	490	70	1,750,000
1 Day	29.9	2,130	350	3,850,000
2 Day	52.3	3,200	500	4,500,000
3 Day	76.1	3,640	520	5,150,000
7 Day	171.9	4,510	615	5,050,000
28 Day	678.4	5,480	685	5,750,000

U4L-35RGC				
Time of Test hrs.		f'c psi	f'st psi	E psi
24 Hr.	35.3	140	20	450,000
2 Day	60.8	1,010	145	2,800,000
3 Day	82.1	1,360	210	3,350,000
4 Day	102.0	1,780	260	3,900,000
7 Day	173.0	3,360	430	3,950,000
28 Day	680.3	5,220	605	4,500,000

SL-RG				
Time of Test hrs.		f'c psi	f'st psi	E psi
12 Hr.	13.1	1,390	195	3,100,000
1 Day	26.3	3,340	435	4,650,000
2 Day	51.0	4,010	490	4,800,000
3 Day	74.7	4,390	545	5,250,000
7 Day	172.4	4,550	540	5,450,000
28 Day	676.7	6,050	635	5,500,000

SL-RGC				
Time of Test hrs.		f'c psi	f'st psi	E psi
24 Hr.	30.7	1,420	230	2,600,000
2 Day	56.2	2,990	425	3,650,000
3 Day	76.8	3,490	455	3,900,000
4 Day	103.2	3,930	530	3,950,000
7 Day	177.7	4,920	585	4,500,000
28 Day	679.8	5,860	685	5,350,000

SL-RGI				
Time of Test hrs.		f'c psi	f'st psi	E psi
24 Hr.	26.2	1,530	245	3,100,000
2 Day	47.9	2,980	430	4,250,000
3 Day	73.8	3,940	515	4,600,000
4 Day	97.9	4,330	550	4,800,000
7 Day	169.2	4,730	585	5,000,000
28 Day	674.8	6,480	655	5,450,000

* Denotes a mixture that was completed under IAC-FA

4.3.1.1 Mechanical Property Parameters

As discussed in Chapter 2, equations in the literature have shown an acceptable ability to capture the strength development profile for concrete mixtures. These formulations, coupled with equivalent age calculations, allow the research team to know the stress/strength throughout the course of a rigid cracking frame test. For the purposes of curve fitting the strength equations, Equation 2.15 is rewritten as Equation 4.1. The parameters for compressive strength, modulus of elasticity, and splitting tensile strength are presented in Tables 4.12 through 4.16.

$$E_c = {w_c}^{1.5} * A * {f'_c}^{B} \tag{4.1}$$

Table 4.12: Strength development parameters—Control mixtures.

Mixture	Compressive Strength			Elastic Modulus		Splitting Tensile Strength	
	fcult, psi	τ_s	β_s	A	B	l	m
CL-RG	6,653	24.970	0.729	86.080	0.410	3.535	0.591
CL-RGC	7,155	26.135	0.963	63.704	0.441	1.665	0.689
CL-RGI	6,395	25.268	0.982	73.427	0.425	1.941	0.674
CH-RG	4,806	23.024	0.738	112.102	0.390	0.892	0.761
CH-RGC	6,266	27.217	0.654	201.410	0.313	2.422	0.641
CL-LS	6,611	28.820	0.927	98.073	0.382	0.513	0.821
CL-LSC	6,471	24.636	0.924	11.643	0.626	0.825	0.772

*Denotes a mixture that was completed under IAC-FA

Table 4.13: Strength development parameters—Class C fly ash mixtures.

Mixture	Compressive Strength			Elastic Modulus		Splitting Tensile Strength	
	fcult, psi	τ_s	β_s	A	B	l	m
*F3L-25RG	4,969	35.029	1.028	49.749	0.488	0.244	0.946
*F3L-35RG	6,422	75.923	0.683	100.718	0.394	0.861	0.795
F3L-35RGC	7,701	79.238	0.745	133.956	0.355	1.151	0.733
F3L-35LS	7,729	77.939	0.705	67.941	0.428	0.779	0.772
F3L-35LSC	7,064	72.269	0.829	84.099	0.399	0.527	0.823
*F4L-25RG	6,440	57.952	0.657	75.815	0.429	0.511	0.850
F4L-35RGC	8,892	85.543	0.704	235.692	0.288	1.451	0.702
*F4H-25RG	6,123	50.318	0.581	68.055	0.448	0.490	0.854
F4H-35RG	6,169	53.779	0.817	166.403	0.328	1.280	0.713
F4H-35RGC	7,625	68.631	0.739	136.848	0.356	1.646	0.681

*Denotes a mixture that was completed under IAC-FA

Table 4.14: Strength development parameters—Class F fly ash mixtures.

Mixture	Compressive Strength			Elastic Modulus		Splitting Tensile Strength	
	fcult, psi	τ_s	β_s	A	B	l	m
*F1L-25RG	5,423	44.373	0.726	33.103	0.538	0.788	0.802
F1L-25RGC	6,476	46.440	0.669	70.780	0.437	0.723	0.792
*F1H-25RG	5,292	58.559	0.435	152.762	0.357	0.153	1.005
F1H-25RGC	5,874	36.452	0.713	85.782	0.414	1.030	0.748
*F2L-25RG	7,234	73.927	0.555	0.404	1.065	1.600	0.720
F2L-25RGC	7,559	75.994	0.577	92.696	0.408	0.685	0.800
*F2L-35RG	5,389	57.045	0.668	25.048	0.576	0.394	0.899
F2L-35RGC	7,727	106.800	0.578	60.018	0.466	0.487	0.839
F2H-25RG	6,251	53.752	0.493	19.643	0.600	0.673	0.795
F2H-25RGC	6,415	51.287	0.583	208.132	0.295	1.481	0.701

*Denotes a mixture that was completed under IAC-FA

Table 4.15: Strength development parameters—GGBFS mixtures.

Mixture	Compressive Strength			Elastic Modulus		Splitting Tensile Strength	
	fcult, psi	τ_s	β_s	A	B	l	m
GL-35RG	6,947	39.446	0.789	102.207	0.391	0.623	0.799
GL-35RGC	14,467	335.354	0.367	196.166	0.305	1.377	0.710
GL-50RG	6,708	49.190	0.838	75.081	0.434	1.749	0.675
GL-50RGC	57,576	15406.876	0.235	80.870	0.422	0.952	0.757
GH-50RG	5,714	39.504	0.920	192.339	0.321	0.599	0.805
GH-50RGC	6,763	82.051	0.798	119.124	0.358	0.929	0.766
GL-50LS	9,086	117.977	0.752	312.952	0.252	2.801	0.627
GL-50LSC	10,000	135.778	0.651	128.112	0.352	0.997	0.745

*Denotes a mixture that was completed under IAC-FA

Table 4.16: Strength development parameters—Other mixtures.

Mixture	Compressive Strength			Elastic Modulus		Splitting Tensile Strength	
	fcult, psi	τ_s	β_s	A	B	l	m
*U4L-35RG	6,884	75.082	0.720	66.860	0.451	1.042	0.757
U4L-35RGC	5,776	71.185	1.069	94.489	0.398	0.573	0.814
SL-RG	6,743	34.937	0.658	88.974	0.410	0.839	0.767
SL-RGC	6,063	31.259	1.105	33.191	0.512	0.997	0.753
SL-RGI	7,114	37.535	0.791	105.703	0.386	2.394	0.646

*Denotes a mixture that was completed under IAC-FA

4.3.2 Drying Shrinkage

As discussed in Chapter 3, drying shrinkage specimens were cast, cured, and measured to judge the effect of various curing regimes on the final drying shrinkage strain. As discussed in Chapter 2, many tests and models have been developed that attempt to capture drying shrinkage. Figure 4.1 shows what the input parameters are for some of the most commonly used drying shrinkage models. With the assistance of an undergraduate working on an independent study, the research team was able to evaluate the drying shrinkage strains that were recorded for the mixtures tested, against those that are predicted by the ACI 209, CEB 90, and B3 Models (ACI Committee 209, 2008; CEB-FIP Model Code '90, 1993; Bazant, 1995). Figure 4.2 displays the total drying shrinkage values at 180 days for all the mixtures tested under TxDOT Project 6332. Inputs that are required for the drying shrinkage modeling are labeled with an “S,” and inputs needed for creep modeling are labeled with a “C.” While many more mixtures were conducted, temperature effects were not considered in the drying shrinkage modeling, so only the unique mixture designs were evaluated.

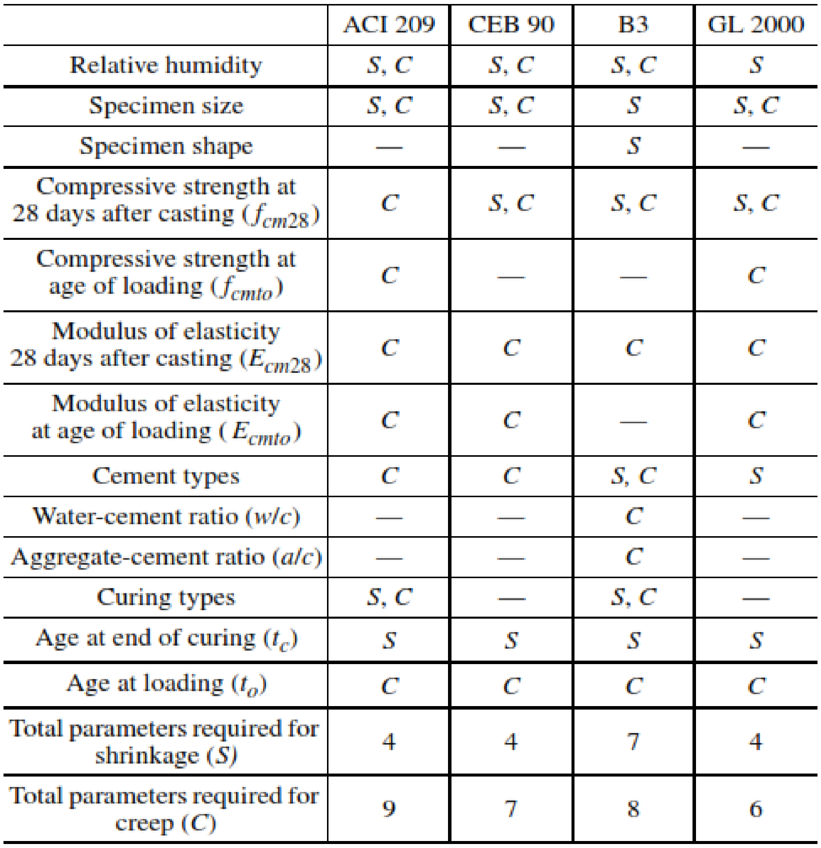

	ACI 209	CEB 90	B3	GL 2000
Relative humidity	*S*, *C*	*S*, *C*	*S*, *C*	*S*
Specimen size	*S*, *C*	*S*, *C*	*S*	*S*, *C*
Specimen shape	—	—	*S*	—
Compressive strength at 28 days after casting (f_{cm28})	*C*	*S*, *C*	*S*, *C*	*S*, *C*
Compressive strength at age of loading (f_{cmto})	*C*	—	—	*C*
Modulus of elasticity 28 days after casting (E_{cm28})	*C*	*C*	*C*	*C*
Modulus of elasticity at age of loading (E_{cmto})	*C*	*C*	—	*C*
Cement types	*C*	*C*	*S*, *C*	*S*
Water-cement ratio (w/c)	—	—	*C*	—
Aggregate-cement ratio (a/c)	—	—	*C*	—
Curing types	*S*, *C*	—	*S*, *C*	—
Age at end of curing (t_c)	*S*	*S*	*S*	*S*
Age at loading (t_o)	*C*	*C*	*C*	*C*
Total parameters required for shrinkage (*S*)	4	4	7	4
Total parameters required for creep (*C*)	9	7	8	6

Figure 4.1: Input factors for predicting shrinkage and creep (Al-Manseer & Lam, 2005).

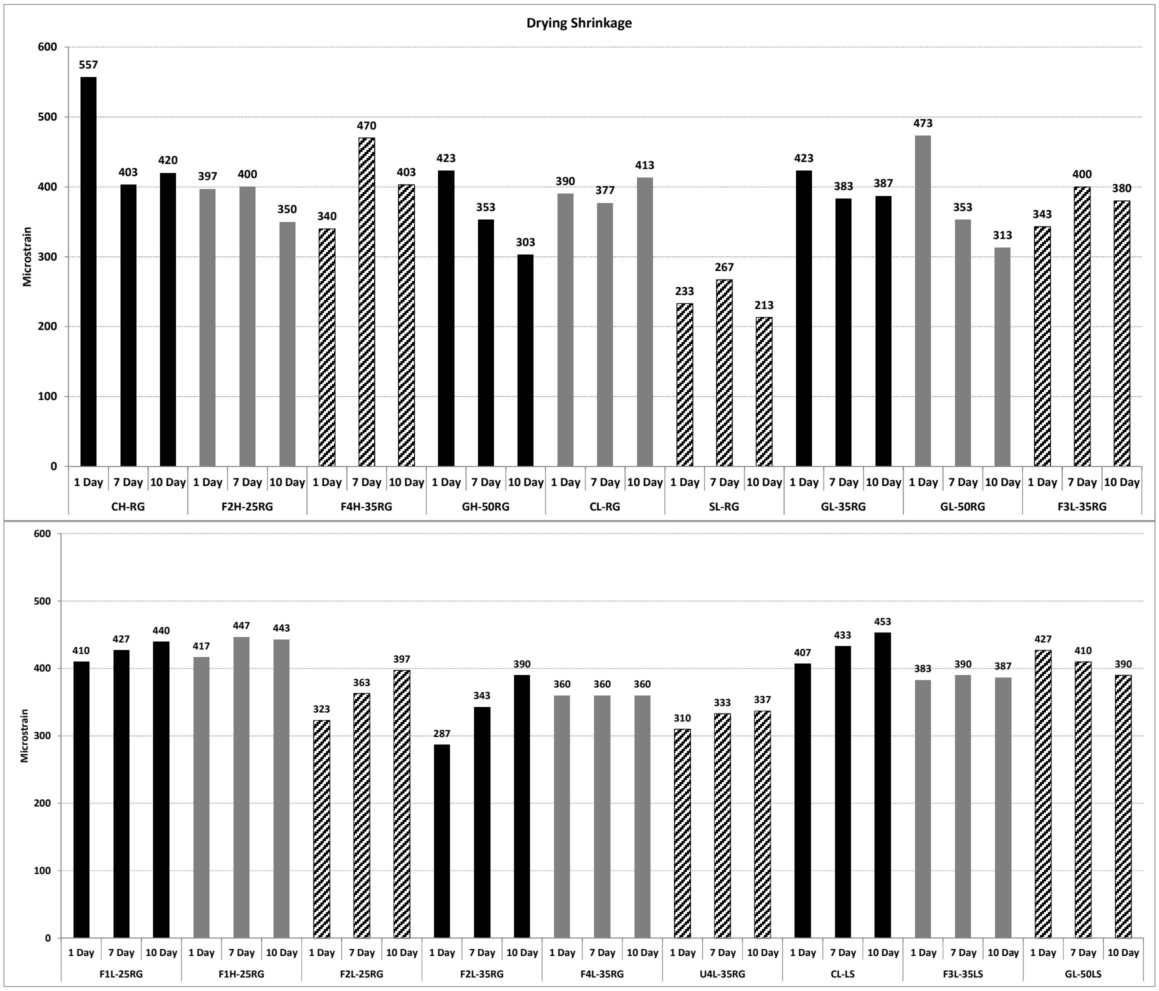

Figure 4.2: 180-day drying shrinkage strains.

Table 4.17 presents the measured versus the predicted 180-day drying shrinkage strains for the specimens that underwent the seven day curing regime. The research team was able to determine, using the measured values, that the effects of initial curing on the specimens tested was minimal on the final drying shrinkage strains. In addition, using the data set generated under TxDOT Project 6332, the B3 Model was chosen as the best for predicting drying shrinkage strains, and will be used in the future for the purposes of computer modeling of bridge deck systems.

Table 4.17: Measured vs. predicted drying shrinkage values for 7-day cure.

Mix ID		ACI 209R-92	B3 Bazant	CEB MC90-99	Measured Microstrain
CH-RG	Microstrain	666.8	466.0	560.9	-403.3
	% Error	65.3	15.5	39.1	
F2H-25RG	Microstrain	750.3	462.2	544.6	-400.0
	% Error	87.6	15.5	36.2	
F4H-35RG	Microstrain	766.6	455.8	515.2	-470.0
	% Error	63.1	-3.0	9.6	
GH-50RG	Microstrain	641.7	457.0	520.9	-353.3
	% Error	81.6	29.3	47.4	
CL-RG	Microstrain	666.8	450.8	489.8	-376.7
	% Error	77.0	19.7	30.0	
GL-35RG	Microstrain	629.4	449.1	480.9	-383.3
	% Error	64.2	17.2	25.4	
GL-50RG	Microstrain	654.3	451.7	494.5	-353.3
	% Error	85.2	27.8	39.9	
SL-RG	Microstrain	666.8	451.3	492.5	-256.7
	% Error	159.8	75.8	91.9	
F3L-35RG	Microstrain	766.5	450.0	485.8	-400.0
	% Error	91.6	12.5	21.5	
F1L-25RG	Microstrain	716.8	456.2	517.3	-426.7
	% Error	68.0	6.9	21.2	
F1H-25RG	Microstrain	691.8	458.8	529.5	-446.7
	% Error	54.9	2.7	18.5	
F2L-25RG	Microstrain	766.6	454.5	508.8	-363.3
	% Error	111.0	25.1	40.0	
F2L-35RG	Microstrain	779.0	459.4	532.0	-343.3
	% Error	126.9	33.8	54.9	
F4L-35RG	Microstrain	773.0	444.8	456.7	-360.0
	% Error	114.7	23.5	26.9	
U4L-35RG	Microstrain	803.9	458.4	527.6	-333.3
	% Error	141.2	37.5	58.3	
CL-LS	Microstrain	623.1	449.9	485.1	-433.3
	% Error	43.8	3.8	11.9	
F3L-35LS	Microstrain	766.6	451.9	495.7	-390.0
	% Error	96.6	15.9	27.1	
GL-50LS	Microstrain	666.8	443.5	449.3	-410.0
	% Error	62.6	8.2	9.6	
Average % Error		88.6	20.4	33.9	

4.4 Simulated Temperature Profiles

This section provides the simulated temperature profiles for the concrete mixtures tested. Figures 4.3 through 4.7 provide the simulated temperature profiles for the concrete mixture types, with individual temperature profiles presented in Appendix A. While the temperatures in the following graphs has been converted to °F, the individual temperature profiles Appendix A are presented in °C, as this was the convention used throughout the rigid cracking frame data processing programs. Semi-adiabatic calorimetry parameters, cement chemistry, mixture design, and location and specimen geometries were input into ConcreteWorks to generate the profiles presented. All profiles presented represent mid-depth on an 8in. thick concrete bridge deck. Figure 4.8, at the end of the section, displays the temperature profiles across various mixture types.

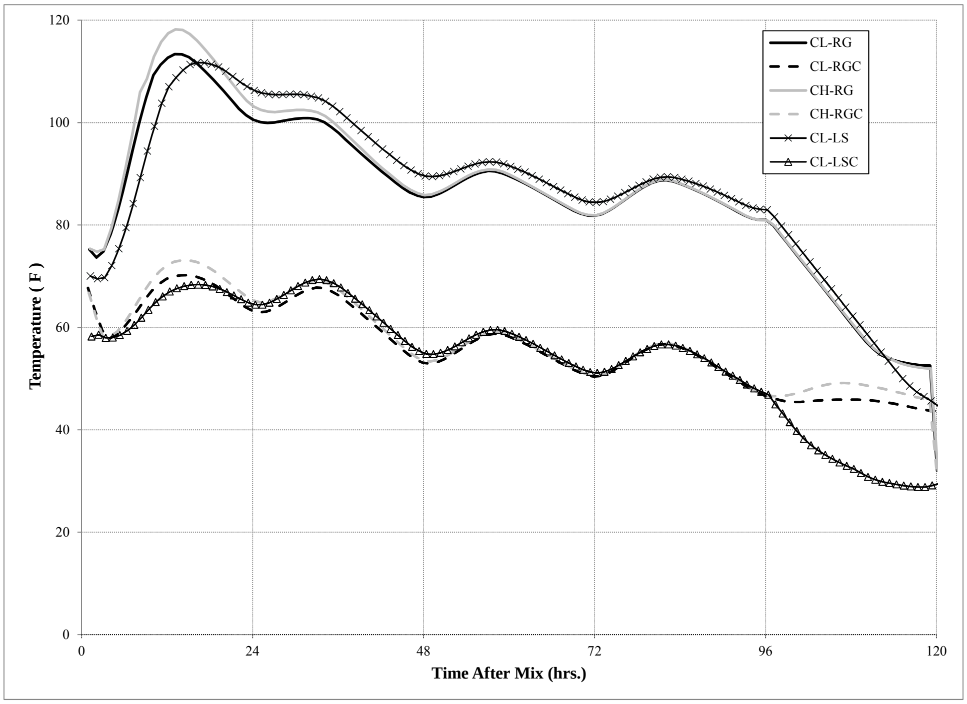

Figure 4.3: Temperature profiles for Control mixtures.

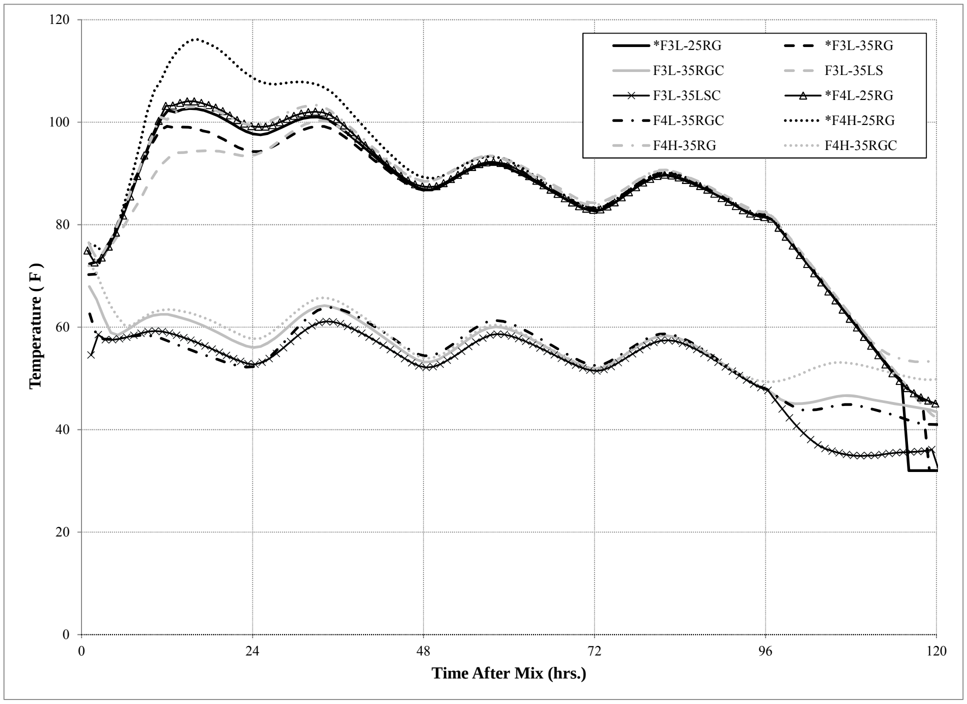

Figure 4.4: Temperature profiles for Class C fly ash mixtures.

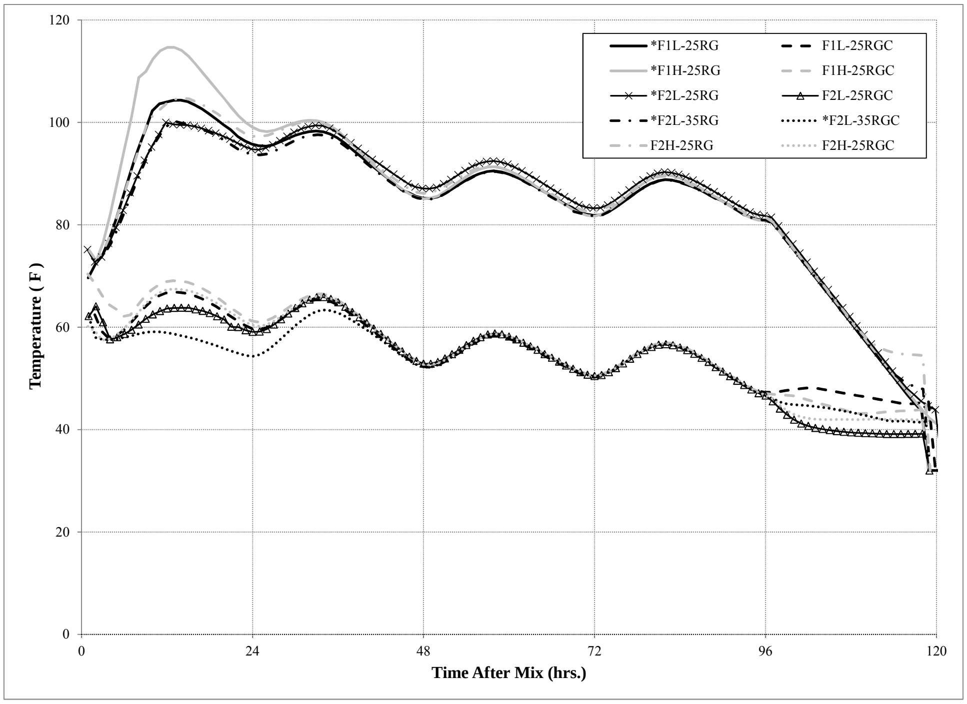

Figure 4.5: Temperature profiles for Class F fly ash mixtures.

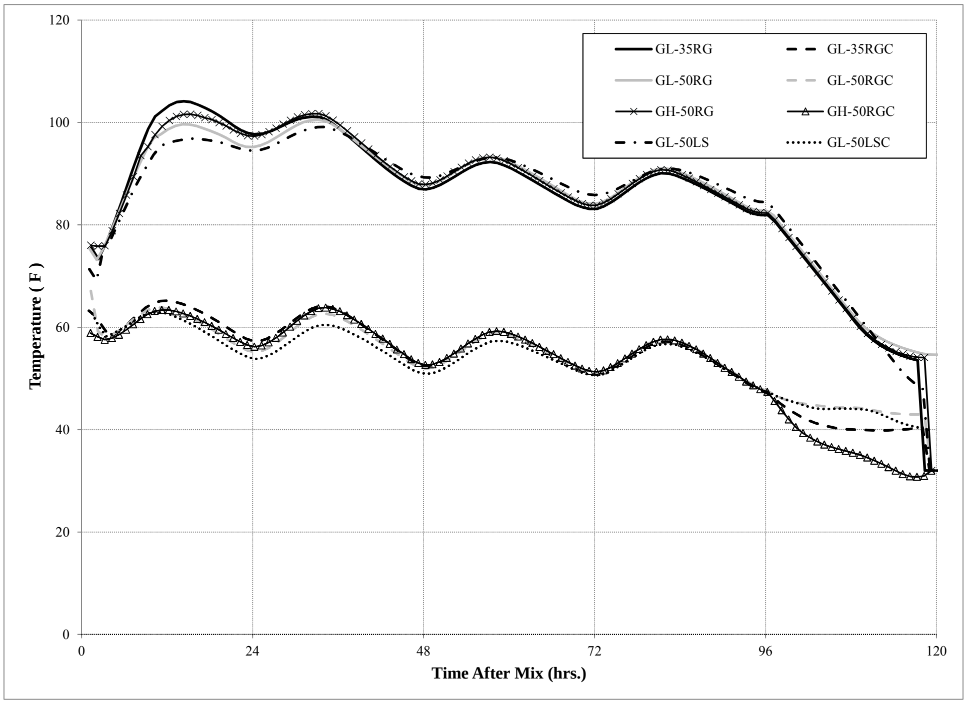

Figure 4.6: Temperature profiles for GGBFS mixtures.

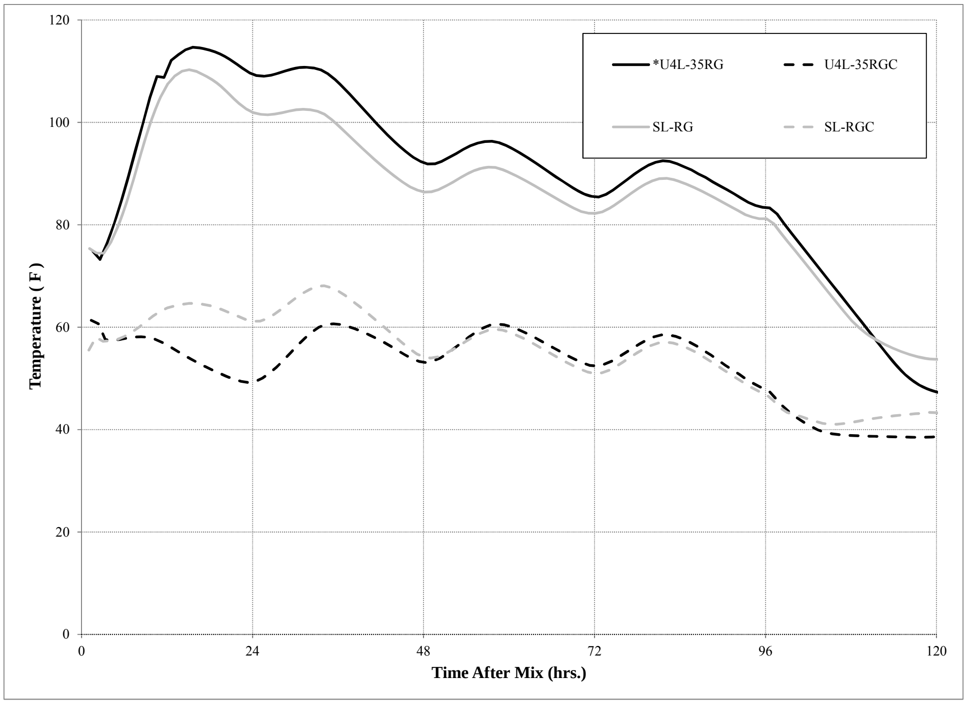

Figure 4.7: Temperature profile for Other mixtures.

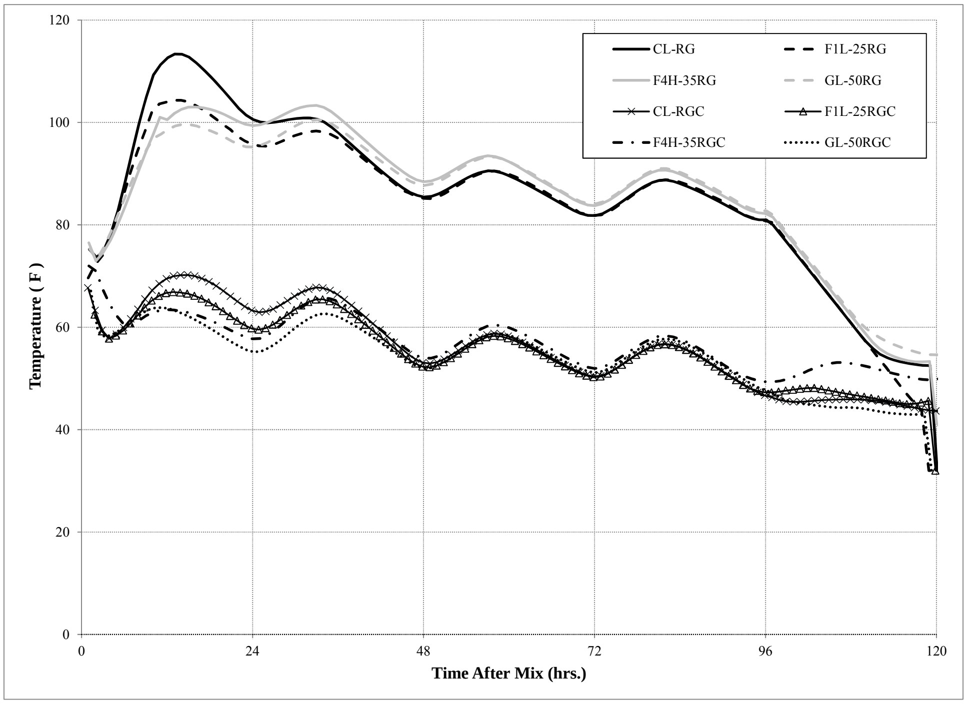

Figure 4.8: Temperature profile comparison across various mixture types.

4.5 Restrained Stress Development under Simulated Temperatures

This section provides the recorded stresses in the rigid cracking frame for the mixtures tested. The individual sections also provide some of the key points from each mixture. In the summaries, the ‘Δ Temp’ refers to the difference between the temperature at initial set and the temperature at the respective event. Under time of cracking, mixtures that cracked display the hour after mixing at which cracking occurred, while ‘NC’ denotes mixtures that did not crack. The various ‘ratios’ presented represent the stress in the rigid cracking frame divided by the curve-fit splitting tensile strength at the equivalent age corresponding to the respective event. The ‘Reserve’ ratio is the difference between the stress/strength at 96 hours after mixing compared to the ratio at the time of cracking. Section 4.5.6 compares some of the key points across all of the mixture types. The restrained stress development for individual mixtures can be found in Appendix A.

4.5.1 Control Mixtures

Figure 4.9 and Table 4.18 show the results of the rigid cracking frame testing for the control mixtures. Unlike most of the hot temperature profile mixtures, the CL-LS mixture did not crack, and had a considerably lower maximum stress during the 96 hour simulation. The high and low alkali mixtures were seen to perform quite similarly.

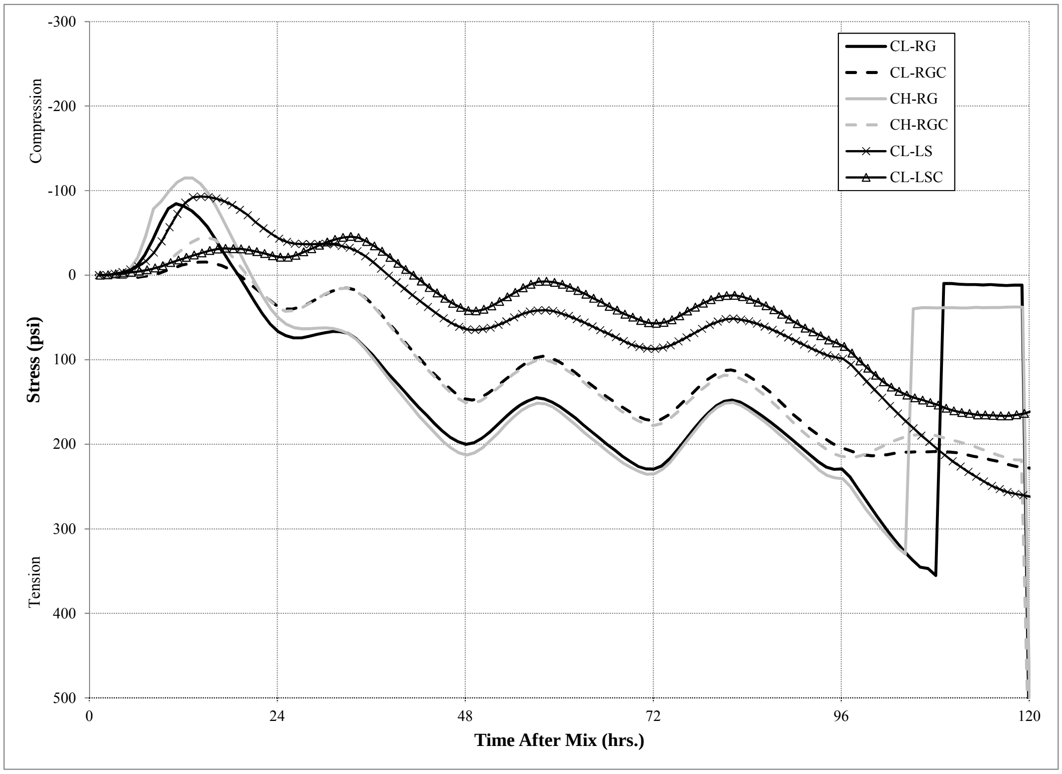

Figure 4.9: Rigid cracking frame stresses—Control Mixtures.

Table 4.18: Summary of rigid cracking frame results: Control Strength development parameters—Other mixtures.

Mix Name	CL-RG	CL-RGC	CH-RG	CH-RGC	CL-LS	CL-LSC	Averages
Time of Cracking	108.5	NC	105.0	NC	NC	NC	
Cracking Stress	354	--	334	--	--	--	344
Temperature at Initial Set	81.1	61.7	80.4	64.5	75.7	60.4	70.6
Cracking Temperature	60.0	--	66.2	--	--	--	63.1
ΔTemp at Cracking	21.1	--	14.2	--	--	--	17.6
Cracking Ratio	0.639	--	0.702	--	--	--	0.670
Reserve	0.219	--	0.192	--	--	--	0.205
ΔTemp at 96hr. Max Stress	0.1	15.0	-0.5	17.6	-7.3	13.2	6.4
Max 96hr Stress	231	70	241	214	98	82	156
Ratio at 96hr Max	0.421	0.177	0.510	0.463	0.165	0.154	0.315
Temperature at t_{max}	--	43.6	--	45.9	41.1	29.9	40.1
ΔTemp at t_{max}	--	18.1	--	18.6	34.6	30.5	25.4
Stress at t_{max}	--	228	--	219	266	159	218
Ratio at t_{max}	--	0.442	--	0.457	0.441	0.290	0.407

All stresses are in psi, all temperatures in °F

* Denotes a mixture that was tested under IAC-FA

4.5.2 Class C Fly Ash Mixtures

Figure 4.10 and Table 4.19 show the results of the rigid cracking frame testing for Class C fly ash mixtures. While the table was split between FA-3 and FA-4, the average column at the end of the bottom table is still an average of all Class C fly ash mixtures. In the results, FA-4 mixtures were seen to have slightly higher stresses and stress /strength ratios at the end of the 96 hour temperature simulation. Class C fly ash mixtures that utilized limestone coarse aggregate developed approximately half the stress at 96 hours that the respective river gravel mixture developed.

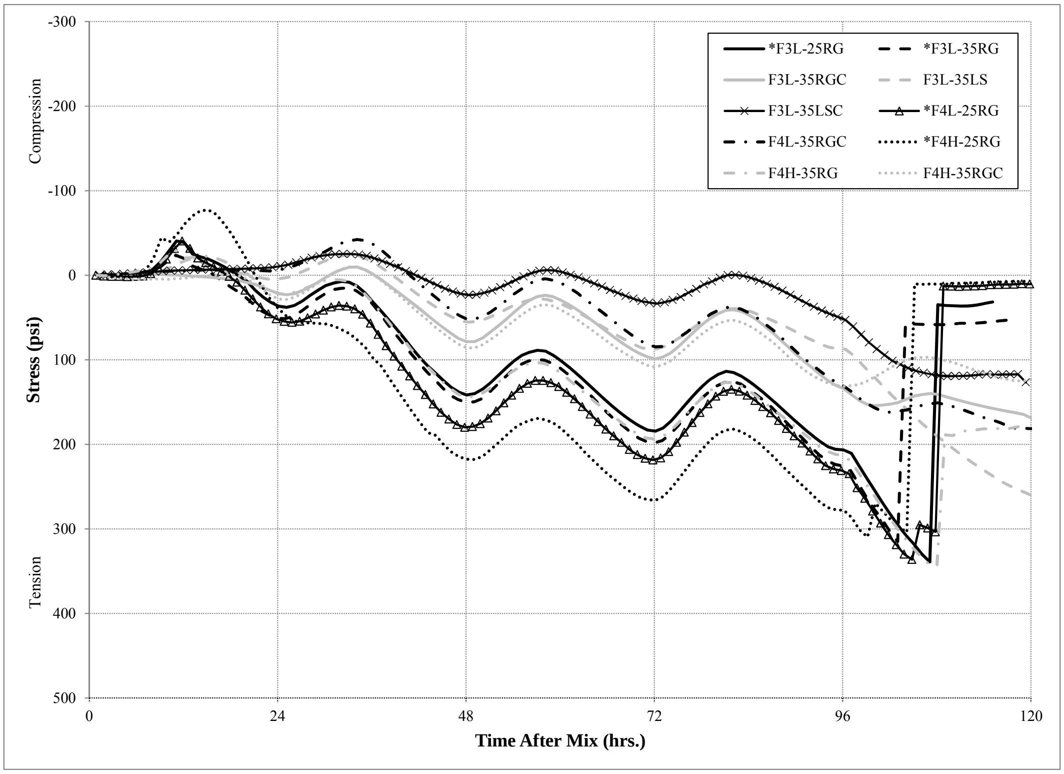

Figure 4.10: Rigid cracking frame stresses—Class C fly ash mixtures.

Table 4.19: Summary of rigid cracking frame results—Class C fly ash mixtures.

Mixture Name	*F3L-25RG	*F3L-35RG	F3L-35RGC	F3L-35LS	F3L-35LSC
Time of Cracking	107.4	103.7	NC	NC	NC
Cracking Stress	341	315	--	--	--
Temperature at Initial Set	87.3	89.0	62.0	87.6	57.4
Cracking Temperature	62.5	69.5	--	--	--
ΔTemp at Cracking	24.7	19.6	--	--	--
Cracking Ratio	0.541	0.562	--	--	--
Reserve	0.207	0.150	--	--	--
ΔTemp at 96hr. Max Stress	5.8	7.1	14.1	5.2	9.5
Max 96hr Stress	207	226	134	88	51
Ratio at 96hr Max	0.334	0.411	0.387	0.205	0.170
Temperature at t_{max}	--	--	43.2	39.5	36.1
ΔTemp at t_{max}	--	--	18.8	48.1	21.3
Stress at t_{max}	--	--	171	279	127
Ratio at t_{max}	--	--	0.447	0.552	0.382

Mixture name	*F4L-25RG	F4L-35RGC	*F4H-25RG	F4H-35RG	F4H-35RGC	Averages
Time of Cracking	108.8	NC	104.3	108.2	NC	5
Cracking Stress	303	--	304	344	--	321
Temperature at Initial Set	89.8	53.2	89.9	93.1	63.5	77
Cracking Temperature	60.0	--	68.1	61.9	--	64
ΔTemp at Cracking	29.8	--	21.8	31.1	--	25
Cracking Ratio	0.530	--	0.548	0.708	--	0.578
Reserve	0.116	--	0.040	0.261	--	0.155
ΔTemp at 96hr. Max Stress	8.3	5.2	8.2	10.9	14.1	9
Max 96hr Stress	231	130	278	213	132	169
Ratio at 96hr Max	0.414	0.365	0.508	0.447	0.368	0.361
Temperature at t_{max}	--	42.6	--	--	50.5	42
ΔTemp at t_{max}	--	10.6	--	--	13.0	22
Stress at t_{max}	--	160	--	--	116	170
Ratio at t_{max}	--	0.399	--	--	0.294	0.415

All stresses are in psi, all temperatures in ^{o}F

* Denotes a mixture that was completed under IAC-FA

4.5.3 Class F Fly Ash Mixtures

Figure 4.11 and Table 4.20 show the results of the rigid cracking frame testing for Class F fly ash mixtures. While the table was split between FA-1 and FA-2, the average column at the end of the bottom table is still an average of all Class F fly ash mixtures. The research team included F1H-25RGC only for completeness in this section. The abnormal results from this rigid cracking frame are likely an error with the connection of the strain gauges before the test equipment began recording. F1H-25RGC will be redone at a future date, and included in the final report for the project. No significant trends were seen in this mixture series.

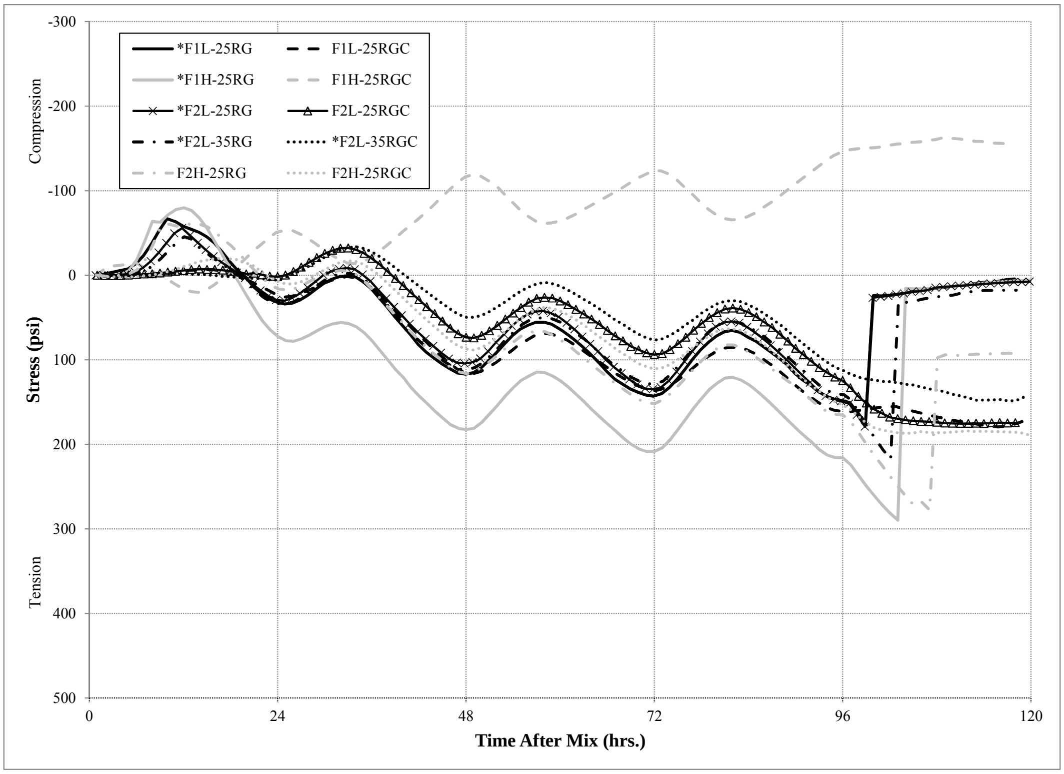

Figure 4.11: Rigid cracking frame stresses—Class F fly ash mixtures.

Table 4.20: Summary of rigid cracking frame results—Class F fly ash mixtures.

Mixture Name	*F2L-25RG	F2L-25RGC	*F2L-35RG	F2L-35RGC	F2H-25RG	F2H-25RGC
Time of Cracking	99.7	NC	102.2	NC	108.0	NC
Cracking Stress	185	--	214	--	274	--
Temperature at Initial Set	81.4	62.5	83.2	58.6	93.6	65.2
Cracking Temperature	76.5	--	71.2	--	61.4	--
ΔTemp at Cracking	4.9	--	12.1	--	32.2	--
Cracking Ratio	0.314	--	0.386	--	0.620	--
Reserve	0.059	--	0.126	--	0.238	--
ΔTemp at 96hr. Max Stress	-0.3	15.8	2.4	12.0	12.2	18.5
Max 96hr Stress	149	125	142	112	166	153
Ratio at 96hr Max	0.255	0.349	0.260	0.401	0.382	0.410
Temperature at t_{max}	--	39.2	--	41.9	--	41.2
ΔTemp at t_{max}	--	23.3	--	16.7	--	24.0
Stress at t_{max}	--	174	--	143	--	192
Ratio at t_{max}	--	0.457	--	0.430	--	0.487

Mixture name	*F1L-25RG	F1L-25RGC	*F1H-25RG	F1H-25RGC	Averages
Time of Cracking	99.1	NC	103.1	NC	5
Cracking Stress	152	--	289	--	223
Temperature at Initial Set	91.4	63.3	87.3	61.6	75
Cracking Temperature	76.6	--	69.9	--	71
ΔTemp at Cracking	14.8	--	17.5	--	16
Cracking Ratio	0.272	--	0.649	--	0.448
Reserve	0.005	--	0.155	--	0.117
ΔTemp at 96hr. Max Stress	10.6	16.0	6.6	14.5	11
Max 96hr Stress	148	162	217	-146	123
Ratio at 96hr Max	0.267	0.404	0.494	-0.351	0.287
Temperature at t_{max}	--	45.7	--	43.9	42
ΔTemp at t_{max}	--	17.6	--	17.7	20
Stress at t_{max}	--	172	--	-155	105
Ratio at t_{max}	--	0.403	--	-0.355	0.285

All stresses are in psi, all temperatures in °F

* Denotes a mixture that was completed under IAC-FA

4.5.4 GGBFS Mixtures

Figure 4.12 and Table 4.21 show the results of the rigid cracking frame testing for Class F fly ash mixtures. As seen in previous mixture series, the limestone coarse aggregate mixtures had considerably lower maximum 96 hours stresses than did their respective river gravel mixtures.

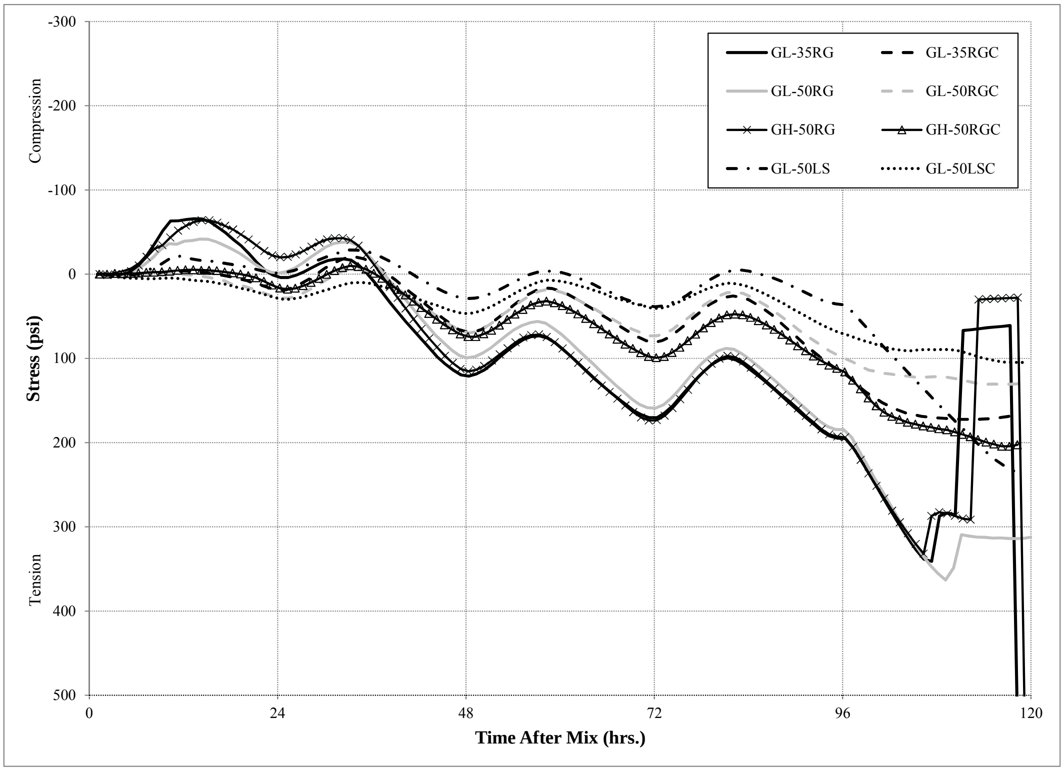

Figure 4.12: Rigid cracking frame stresses—GGBFS mixes.

Table 4.21: Summary of rigid cracking frame results—GGBFS Mixtures.

Mix Name	GL-35RG	GL-35RGC	GL-50RG	GL-50RGC	GH-50RG	GH-50RGC	GL-50LS	GL-50LSC	Averages
Time of Cracking	110.8	NC	110.0	NC	112.8	NC	NC	NC	3
Cracking Stress	284	--	368	--	290	--	--	--	314
Temperature at Initial Set	80.2	63.2	81.2	63.8	79.9	62.9	85.8	62.1	72
Cracking Temperature	57.8	--	59.9	--	56.3	--	--	--	58
ΔTemp at Cracking	22.4	--	21.3	--	23.6	--	--	--	22
Cracking Ratio	0.502	--	0.706	--	0.567	--	--	--	0.592
Reserve	0.151	--	0.344	--	0.181	--	--	--	0.225
ΔTemp at 96hr. Max Stress	-1.7	15.9	-1.5	16.1	-2.4	15.4	1.3	14.5	7
Max 96hr Stress	195	116	185	99	193	114	39	70	126
Ratio at 96hr Max	0.352	0.346	0.362	0.407	0.386	0.369	0.087	0.259	0.321
Temperature at t_{max}	--	40.5	--	43.3	--	30.8	46.2	39.5	40
ΔTemp at t_{max}	--	22.8	--	20.5	--	32.1	39.6	22.6	27
Stress at t_{max}	--	167	--	127	--	201	242	104	168
Ratio at t_{max}	--	0.467	--	0.472	--	0.585	0.460	0.337	0.464

All stresses are in psi, all temperatures in ^{o}F

* Denotes a mixture that was tested under IAC-FA

4.5.5 Other Mixtures

Figure 4.13 and Table 4.22 show the results of the rigid cracking frame testing for the “Other” mixtures. The shrinkage reducing admixture mixtures were shown to have lower stress/strength ratios and lower maximum stresses after 96 hours, most likely due to reduced contributions from chemical shrinkage.

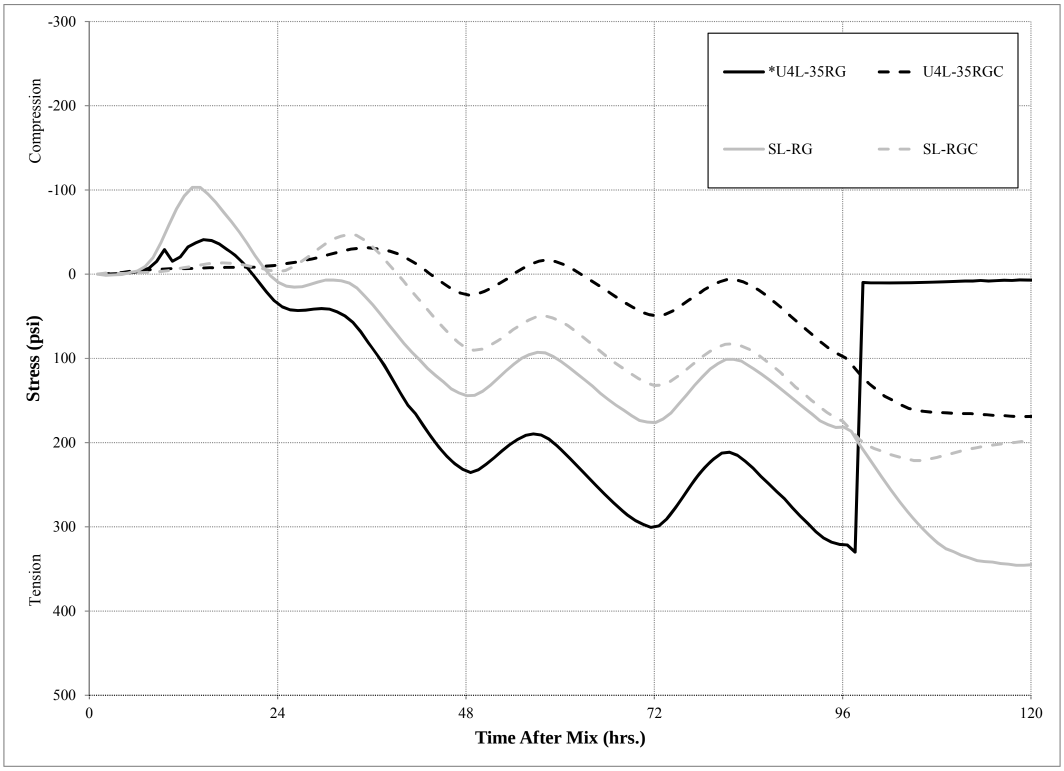

Figure 4.13: Rigid cracking frame stresses—Other mixtures.

Table 4.22: Summary of rigid cracking frame results—Other mixtures.

Mix Name	*U4L-35RG	U4L-35RGC	SL-RG	SL-RGC	Averages
Time of Cracking	98.3	NC	NC	NC	1
Cracking Stress	338	--	--	--	338
Temperature at Initial Set	96.3	50.8	87.3	61.6	74
Cracking Temperature	80.7	--	--	--	81
ΔTemp at Cracking	15.6	--	--	--	16
Cracking Ratio	0.607	--	--	--	0.607
Reserve	0.028	--	--	--	0.028
ΔTemp at 96hr. Max Stress	12.9	2.9	6.1	14.6	9
Max 96hr Stress	321	97	184	175	194
Ratio at 96hr Max	0.579	0.386	0.339	0.346	0.413
Temperature at t_{max}	--	38.6	51.7	43.6	45
ΔTemp at t_{max}	--	12.2	35.6	18.0	22
Stress at t_{max}	--	168	331	196	232
Ratio at t_{max}	--	0.576	0.595	0.367	0.513

All stresses are in psi, all temperatures in °F

* Denotes a mixture that was tested under IAC-FA

4.5.6 Comparison of All Mixture Types

Figure 4.14, Figure 4.15, and Table 4.23 show a comparison of selected rigid cracking results from various mixture types. Table 4.23 was created by taking the average of all the values in a mixture category for the given criteria. Due to the fewer number of mixtures performed within the “Other” mixtures category, they are only intermittently presented in the following figures. However, the results from the Other mixtures are presented in Table 4.23 for comparison with the other mixture types. Evaluation of these graphs show that, generally, the control mixtures generate the highest early stress peaks, with GGBFS generating the lowest; and control mixtures and shrinkage-reducing admixture mixtures generate the highest 96 hours stresses, with GGBFS and Class F fly ash mixtures producing the lowest maximum 96 hour stresses. It is believed that the shrinkage reducing admixture mixture generated stresses similar to the control mixture due to the lack of autogenous and drying shrinkage. Figure 4.16 through Figure 4.18 further compare aspects of average cracking and maximum 96 hours stresses, stress/strength ratios, reserve strength ratios, 96 hours maximum stress ratios, and temperatures and temperature differences at cracking. ‘D Temp’ denotes the difference between the temperature at cracking and that at initial set.

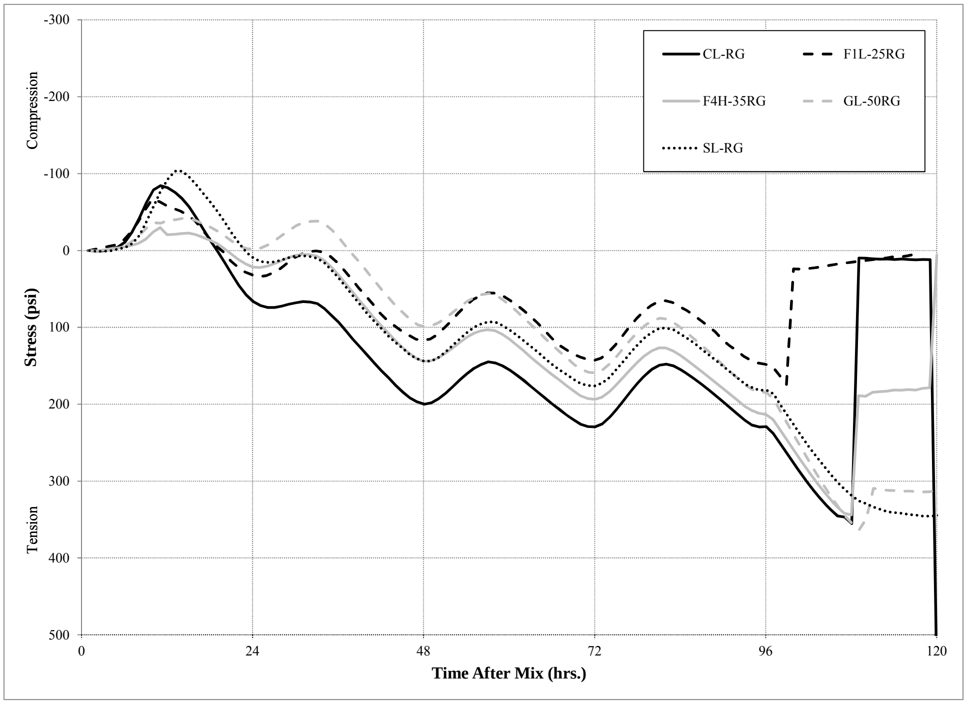

Figure 4.14: Hot weather rigid cracking frame stresses—All mixture types.

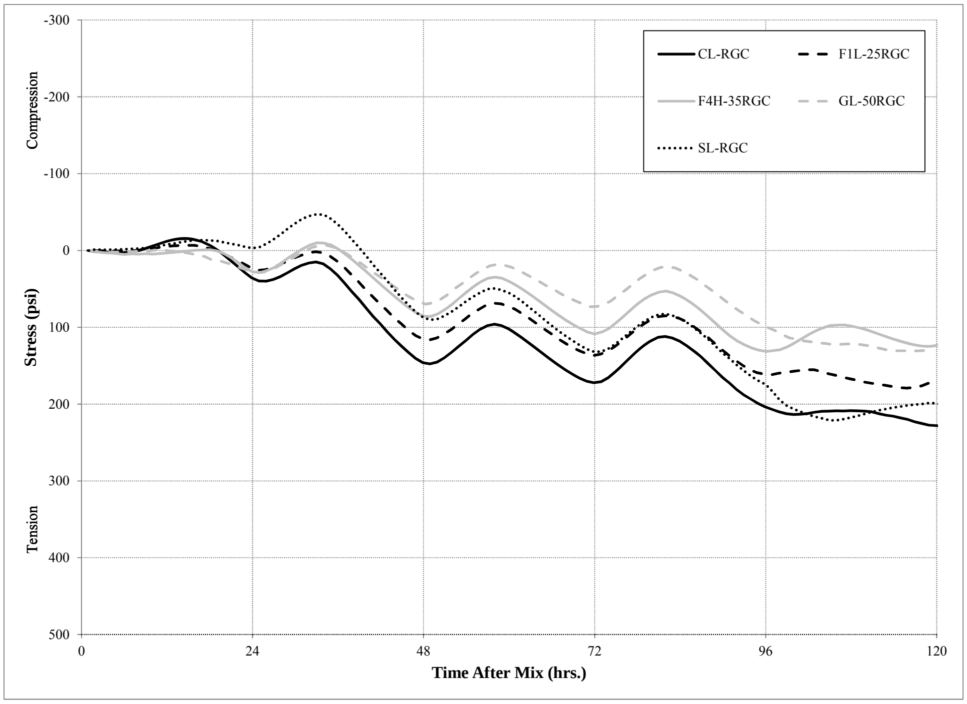

Figure 4.15: Cold weather rigid cracking frame stresses—All mixture types.

Table 4.23: Summary of rigid cracking frame results—All mixture types.

Mixtures	Control Mixtures	Class C Fly Ash	Class F Fly Ash	GGBFS Mixtures	Other Mixtures
Number of Mixes Cracked	2	5	5	4	1
Cracking Stress	344	321	223	260	338
Temperature at Initial Set	70.6	77	75	72	74
Cracking Temperature	63.1	64	71	55	81
ΔTemp at Cracking	17.6	25	16	21	16
Cracking Ratio	0.670	0.578	0.448	0.545	0.607
Reserve	0.205	0.155	0.117	0.168	0.028
ΔTemp at 96hr. Max Stress	6.4	9	11	7	9
Max 96hr Stress	156	169	123	126	194
Ratio at 96hr Max	0.315	0.361	0.287	0.321	0.413
Temperature at t_{max}	40.1	42	42	39	45
ΔTemp at t_{max}	25.4	22	20	29	22
Stress at t_{max}	218	170	105	178	232
Ratio at t_{max}	0.407	0.415	0.285	0.462	0.513

All stresses are in psi, all temperatures in ° F

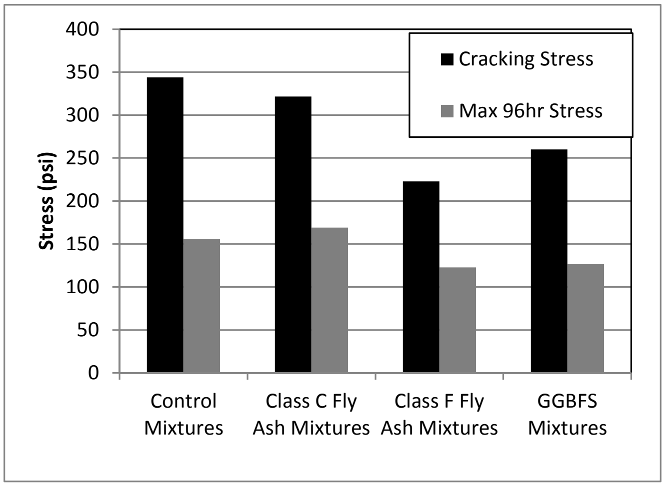

Figure 4.16: Comparison of stresses for mixture types.

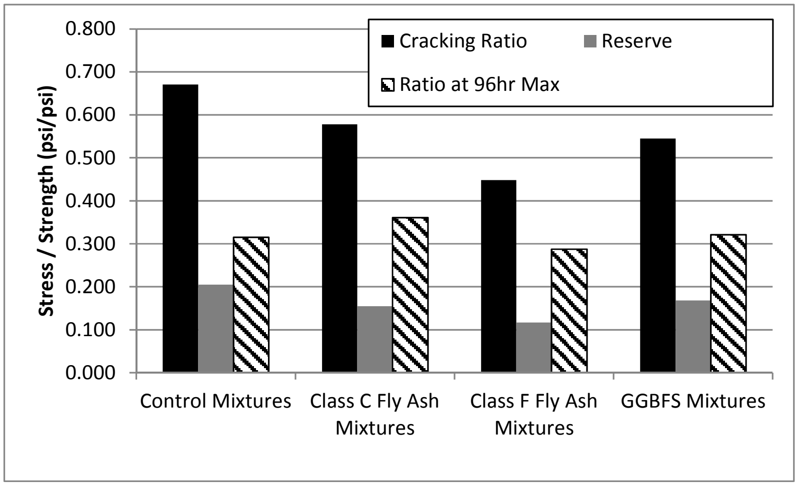

Figure 4.17: Comparison of stress/strength ratios for mixture types.

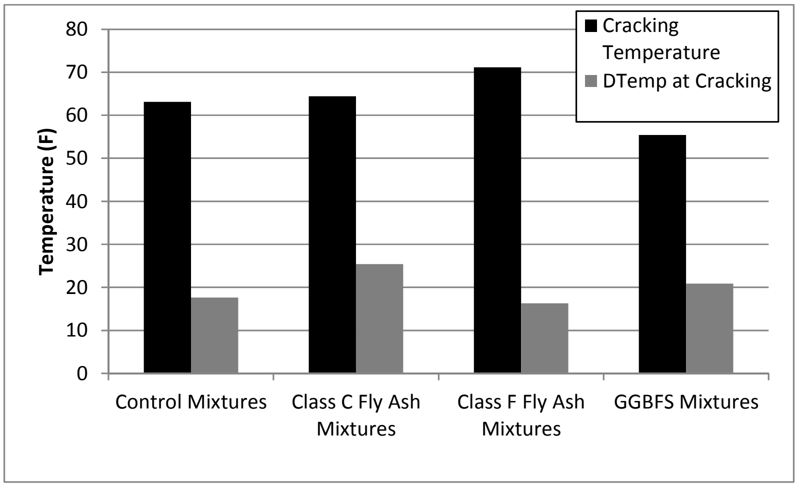

Figure 4.18: Comparison of temperatures for mixture types.

4.6 Free Deformation under Simulated Temperatures

This section presents the results of the free shrinkage frame testing performed under this project. It should be noted that 12 of the 32 mixtures did not produce satisfactory free shrinkage frame data. This problem was usually caused by one of the LVDTs not measuring throughout the test because the rod was hung up in the hole in the end plates. This typically resulted in only one of the two LVDTs recording quality data over the course of the test. Four of the bad shrinkage frame results were re-run and those corrected data are presented in this report. To the best of the research team's knowledge, the following mixtures have poor free shrinkage frame data: CL-RGC, F4L-35RGC, F4H-35RGC, GL-35RG, GL-50RG, GH-50RGC, GL-50LSC. See Figures 4.18 through 4.23.

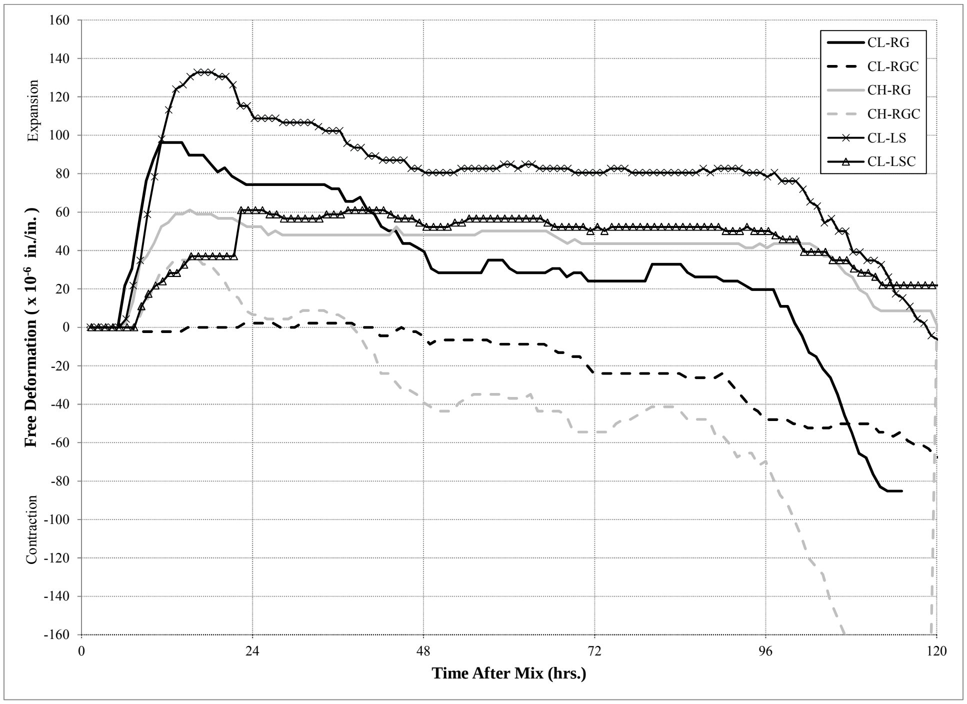

Figure 4.19: Free shrinkage frame strains—Control mixtures.

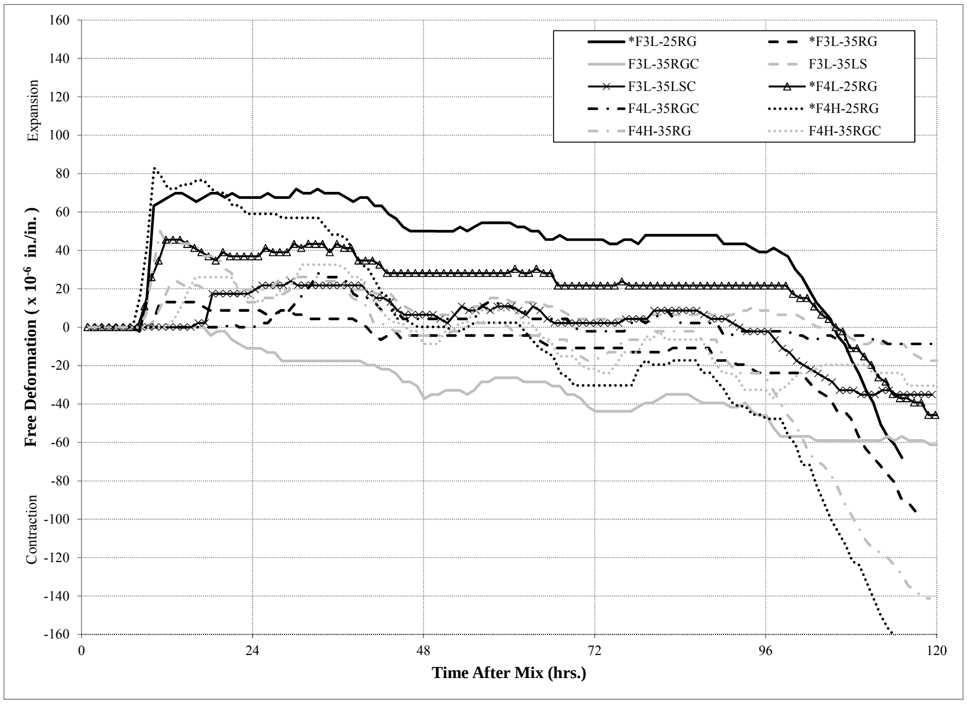

Figure 4.20: Free shrinkage frame strains—Class C fly ash mixtures.

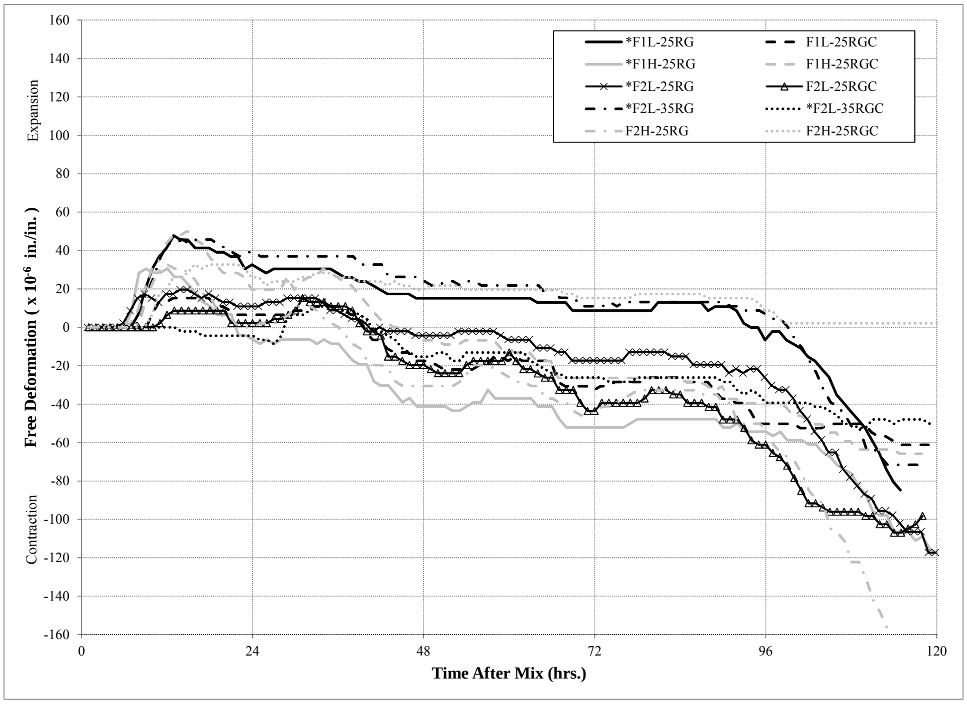

Figure 4.21: Free shrinkage frame strains—Class F fly ash mixtures.

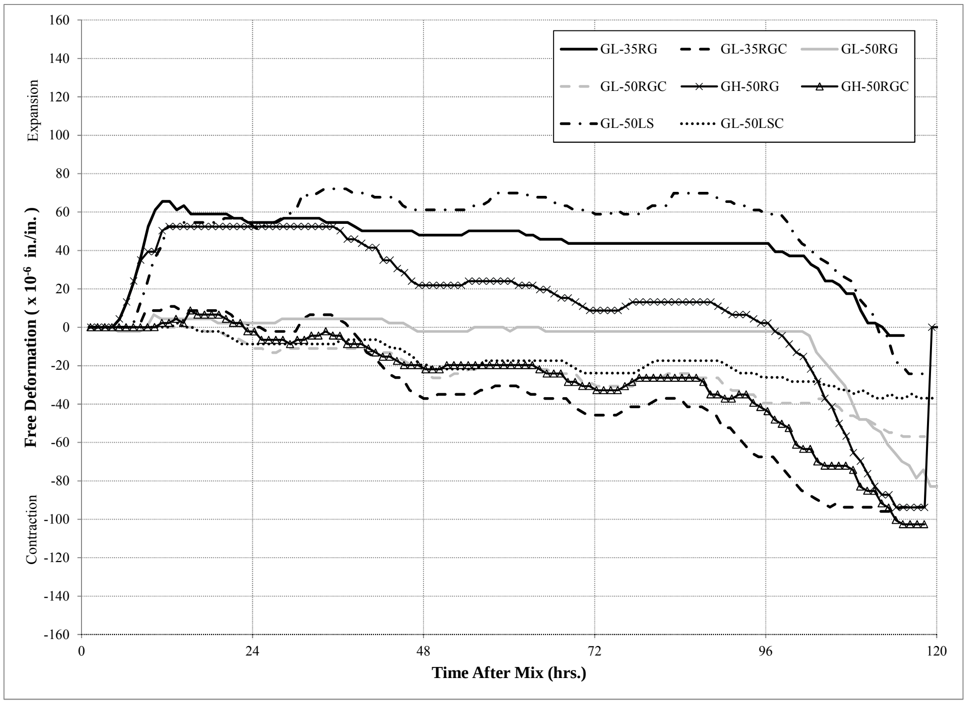

Figure 4.22: Free shrinkage frame strains—GGBFS mixes.

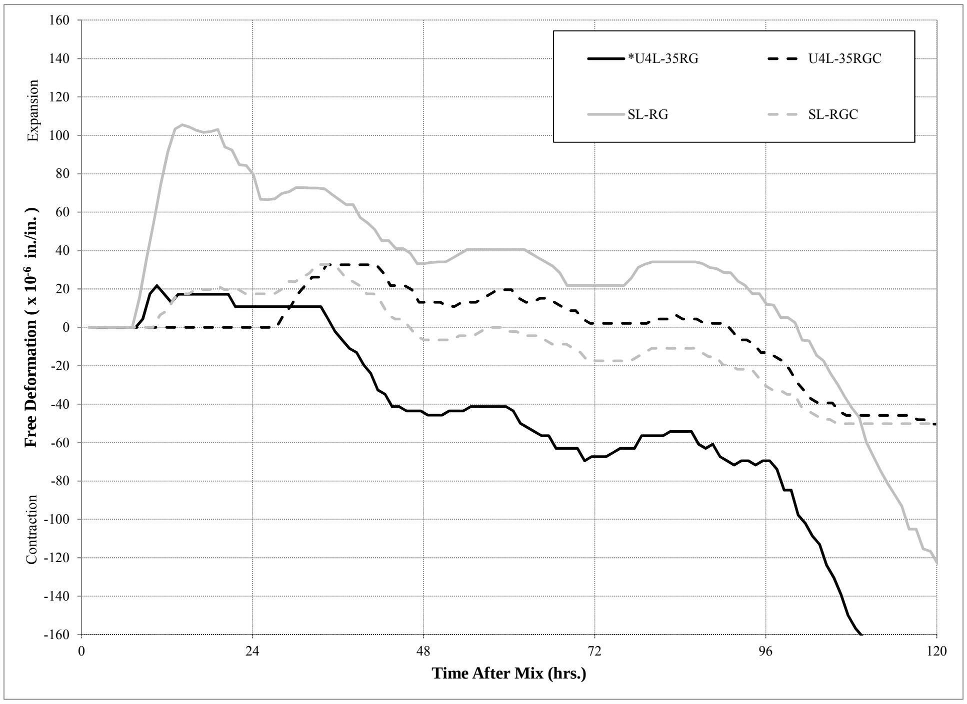

Figure 4.23: Free shrinkage frame strains—Other mixtures.

4.7 Restrained Stress Development under Isothermal Conditions

Figure 4.24 provides the results from the rigid cracking frame for the isothermally cured mixtures. While the shrinkage-reducing admixture appears to lower the stresses in the cracking frame at earlier ages, by the end of the test (10 days), the mixtures appear to have the same level of stress.

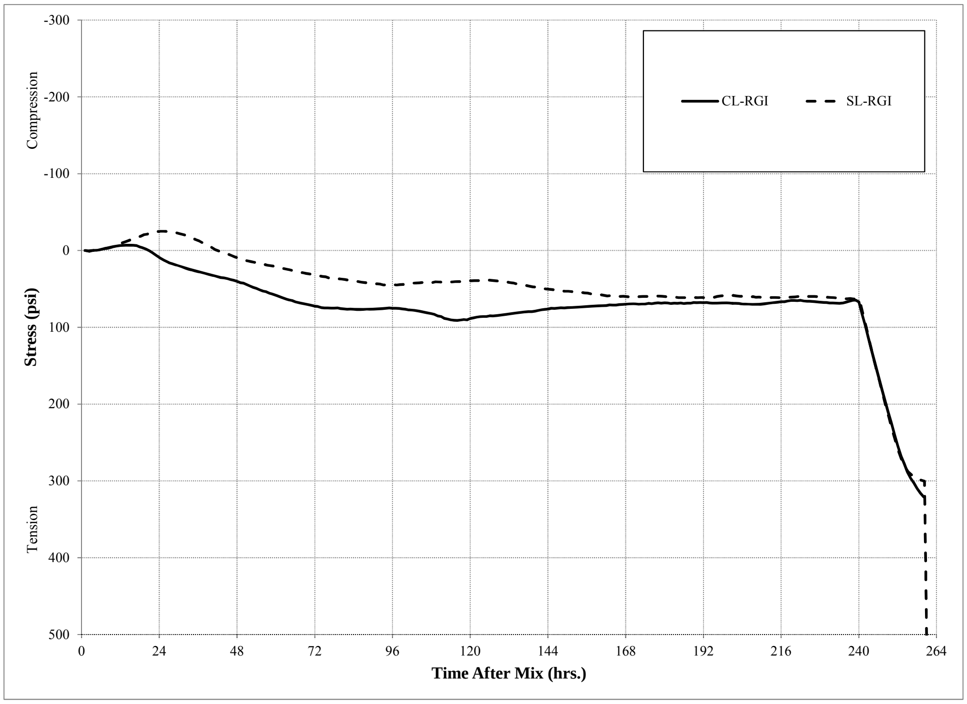

Figure 4.24: Rigid cracking frame stresses—Isothermal mixtures.

4.8 Free Deformation under Isothermal Conditions

Figure 4.25 displays the free shrinkage frame results for the isothermally cured mixtures. As is apparent in the graph, the shrinkage reducing admixture was effective in minimizing the shrinkage strains in the concrete. Strains in SL-RGI were approximately zero at the end of the 10-day test.

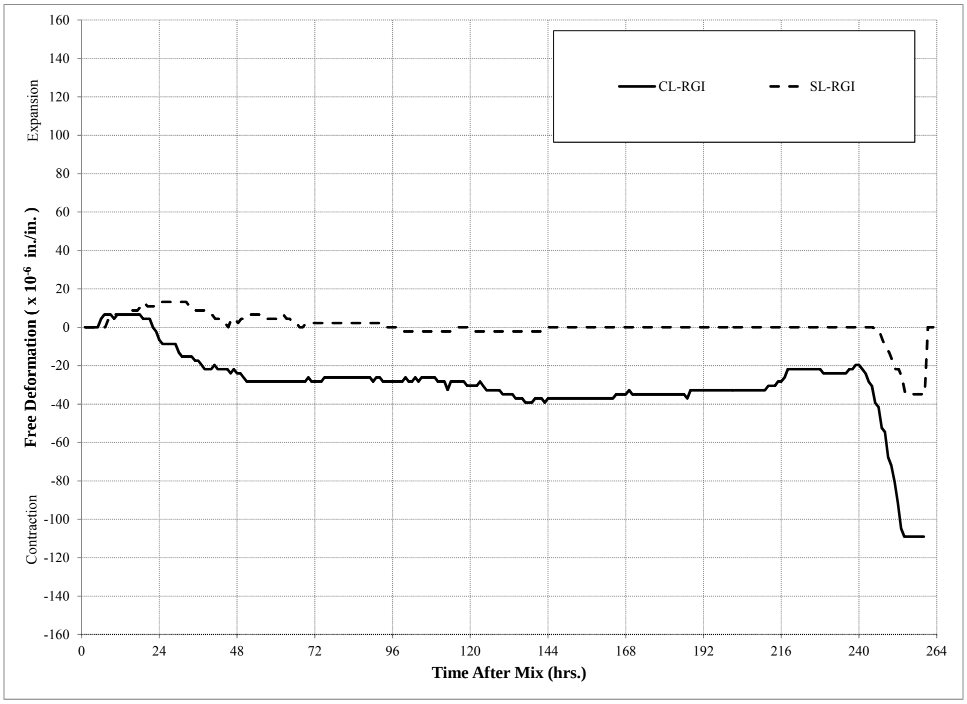

Figure 4.25: Free shrinkage frame strains—Isothermal mixtures.

4.9 Setting Times

Table 4.24 presents the setting times for the concrete mixtures evaluated. The research team, approximately halfway through the TxDOT 6332 test matrix, began instrumenting time-of-set specimens with iButton temperature data loggers, and for each mixture tested, placed time-of-set cans in a temperature controlled room, in a room that had a high air temperature, and in the match cured water bath. In Table 4.24, Hot Air Cure specifies that a time-of-set specimen was left inside a testing room where the ambient air temperature was approximately 90 °F. Hot and Cold Mix Profile are time-of-set specimens that were kept inside the match cured water bath that matched the temperature of the rigid cracking frame for that mixture under either hot or cold temperature simulation. DS Room Cure specimens were placed inside the same room that was used in evaluating concrete drying shrinkage. The DS Room was kept at 73 °F. As noted in the table, in the mixtures marked with an asterisk, the time-of-set data for the Hot Mix Profile was obtained from the hot weather rigid cracking frame test performed under IAC-FA.

The research team, in collaboration with Auburn University, is attempting to use the data collected in Table 4.24, along with the time-temperature history for each of the tests, to generate equivalent age setting times for the different mixture designs. When the equivalent age of initial and final set is found for the mixtures, the degree of hydration at initial and final set may also be determined. The research team, in doing this, hopes to use the data collected under this project, as well as previous TxDOT funded projects, to generate general degrees of hydration that can be associated with initial and final set for any mixture. Previous work by Schindler (2004) and Edson (2007) have shown that this is possible for mixtures with a variety of SCMs, admixtures, and time-temperature histories.

Table 4.24: Setting times of concrete mixtures.

Mixture Name		Hot Air Cure		Hot Mix Profile		Cold Mix Profile		DS Room Cure	
		Initial Set	Final Set	Initial Set	Final Set	Initial Set	Final Set	Initial Set	Final Set
Control Mixtures	CL-RG	--	--	4.6	6.0	6.5	9.1	--	--
	CH-RG	4.7	5.8	4.3	5.5	6.7	9.4	--	--
	CL-LS	--	--	5.0	6.7	7.0	9.9	5.5	7.4
Class C Fly Ash Mixtures	F3L-35RG*	8.1	9.5	7.5	8.8	13.3	16.0	10.1	13.0
	F3L-35LS	--	--	9.1	11.3	14.9	19.2	9.2	11.4
	F4L-35RG	--	--	--	--	20.7	34.7	12.0	14.6
	F4H-35RG	7.1	8.2	7.9	9.7	12.3	14.0	--	--
Class F Fly Ash Mixtures	F1L-25RG*	5.5	7.5	4.9	6.3	8.5	11.5	6.5	8.3
	F1H-25RG*	4.6	5.8	4.6	5.8	6.4	8.4	5.9	7.3
	F2L-25RG*	--	--	5.4	7.0	10.0	13.6	8.0	9.8
	F2L-35RG*	--	--	6.4	7.9	13.6	19.0	9.5	11.7
	F2H-25RG	--	--	5.2	6.5	9.1	11.5	6.6	8.3
GGBFS Mixtures	GL-35RG	--	--	4.5	5.9	8.3	10.8	6.7	8.9
	GL-50RG	--	--	4.7	6.4	10.1	13.0	--	--
	GH-50RG	--	--	4.5	6.1	9.1	11.8	7.0	9.1
	GL-50LS	--	--	5.3	7.0	8.0	11.1	6.1	8.4
Other Mixtures	U4L-35RG*	--	--	7.7	10.0	25.4	31.6	15.5	18.1
	SL-RG	--	--	5.9	7.2	9.0	12.8	6.5	8.6
	OL-RG	--	--	5.0	6.7	--	--	5.0	7.0

* Denotes a mixture whose Hot Profile was a mixture completed under IAC-FA

All values presented are in hours after start of mix.

4.10 Evaluation of Modified B3 Creep Model

In collaboration with Auburn University, a modified version of the B3 Model developed by Byard (2011) has been evaluated against the results of the rigid cracking frame testing conducted under TxDOT 6332. The Modified B3 Model aims to better capture the early-age behavior of the concrete by modifying the ageing viscoelastic term and the elastic modulus to obtain a closer approximation of early-age concrete behavior. The modification to the q_2 term is seen in Equation 4.2, with the addition of the term including q_5. q_5 is intended to be an equivalent age 'modified set time' at which the concrete begins to gain strength.

$$q_2 = \left[86.814 * 10^{-6} * c^{0.5} * f_{cm}{}^{-0.9}\right] * \frac{t_o}{t_o - q_5} \tag{4.2}$$

While Bazant recommended the use of the 28-day elastic modulus in the calculation of q_1, it is well known that the modulus of elasticity rapidly increases at early ages. The use of a hyperbolic modulus curve captures this early-age change. In the hyperbolic modulus curve, S_u, k_T, and t_0 are curve fit to match values from cylinder testing. The Modified B3 Model further adjusts the early-age modulus to better characterize the instantaneous strain at early ages. In Equation 4.4, t_e and q_6 are in units of equivalent age days.

$$Hyperbolic\ Modulus = S_u * k_T * \frac{t - t_0}{(1 + k_T * [t - t_0])} \tag{4.3}$$

$$Modified\ Modulus = \left[S_u * k_T * \frac{t - t_0}{(1 + k_T * [t - t_0])}\right] * \frac{t_e - q_6}{t_e} \tag{4.4}$$

In evaluating this creep model against the mixtures, the research team evaluated the R^2 of the models prediction against a default 0.2 for both q_5 and q_6. The values of q5 and q6 were then curve fit to maximize the R^2 value for that specific mixture using Excel Solver. For each set of mixtures evaluated, only the mixtures that provide R^2 values greater than 70% will be used in the final model to be implemented into ConcreteWorks. Mixtures that perform below this standard will be highlighted in Tables 4.25 through 4.29. As discussed previously, some of the free shrinkage frame tests failed to record desirably. While these mixes were included in the following tables for completeness, only the mixtures that are NOT highlighted will be used in averaging R^2 values and q_5 and q_6 terms.

Table 4.25: Modified B3 Model performance—Control mixtures.

Mixture	Original Terms R^2	New Terms R^2	New q_5	New q_6
CL-RG	0.741	0.880	0.334	0.200
CL-RGC	0.659	0.537	1.052	0.127
CL-RGI	0.959	0.966	0.003	0.134
CH-RG	0.355	0.463	0.287	0.200
CH-RGC	0.961	0.964	0.939	0.156
CL-LS	0.702	0.818	0.294	0.001
CL-LSC	-0.686	0.500	0.513	0.001
Average	0.841	0.907	0.393	0.123

*Denotes a mixture that was completed under IAC-FA

Table 4.26: Modified B3 Model performance—Class C fly ash mixtures.

Mixture	Original Terms R^2	New Terms R^2	New q_5	New q_6
*F3L-25RG	-0.439	0.714	0.925	0.146
*F3L-35RG	0.387	0.402	0.001	0.001
F3L-35RGC	0.927	0.928	0.138	0.144
F3L-35LS	0.604	0.784	0.672	0.201
F3L-35LSC	0.806	0.876	0.404	0.145
*F4L-25RG	0.118	0.817	1.332	0.202
F4L-35RGC	0.608	0.622	0.272	0.200
*F4H-25RG	0.193	0.828	0.864	0.182
F4H-35RG	0.751	0.883	0.692	0.202
F4H-35RGC	0.847	0.944	0.593	0.086
Average	0.476	0.847	0.703	0.163

*Denotes a mixture that was completed under IAC-FA

Table 4.27: Modified B3 Model performance—Class F fly ash mixtures.

Mixture	Original Terms R^2	New Terms R^2	New q_5	New q_6
*F1L-25RG	0.202	0.736	0.696	0.199
F1L-25RGC	0.908	0.981	0.001	0.452
*F1H-25RG	0.593	0.632	0.331	0.200
F1H-25RGC	-1.324	-1.041	0.001	0.136
*F2L-25RG	0.410	0.742	1.031	0.198
F2L-25RGC	0.898	0.940	0.504	0.177
*F2L-35RG	-0.222	0.779	0.974	0.199
F2L-35RGC	0.927	0.933	0.368	0.149
F2H-25RG	0.955	0.974	0.001	0.001
F2H-25RGC	0.423	0.823	0.748	0.219
Average	0.563	0.864	0.540	0.199

*Denotes a mixture that was completed under IAC-FA

Table 4.28: Modified B3 Model performance—GGBFS mixtures.

Mixture	Original Terms R^2	New Terms R^2	New q_5	New q_6
GL-35RG	0.490	0.632	0.287	0.200
GL-35RGC	0.723	0.864	0.497	0.174
GL-50RG	0.546	0.862	0.001	0.414
GL-50RGC	0.911	0.919	0.056	0.216
GH-50RG	0.847	0.873	0.284	0.200
GH-50RGC	0.952	0.968	0.001	0.001
GL-50LS	-3.587	0.293	0.458	0.160
GL-50LSC	0.813	0.826	0.104	0.437
Average	0.799	0.885	0.157	0.240

*Denotes a mixture that was completed under IAC-FA

Table 4.29: Modified B3 Model performance—Other mixtures.

Mixture	Original Terms R^2	New Terms R^2	New q_5	New q_6
*U4L-35RG	0.437	0.446	0.276	0.001
U4L-35RGC	0.559	0.778	0.570	0.110
SL-RG	0.802	0.902	0.397	0.203
SL-RGC	0.883	0.907	0.650	0.200
SL-RGI	0.783	0.791	0.216	0.001
OL-RG	--	--	--	--
OL10-RG	--	--	--	--
Average	0.757	0.845	0.458	0.129

*Denotes a mixture that was completed under IAC-FA

A relatively good fit was found for the majority of the mixtures that were evaluated against this model. The mixtures that were found to not have a good fit typically had poor free shrinkage frame data, a key input in the Modified B3 Model. While a good fit is shown for the mixtures at The University of Texas, a more thorough evaluation took place at Auburn University and is shown in Chapter 5.

Chapter 5. Modeling Early-Age Stress Development of Restrained Concrete

5.1 Introduction and Background

Concrete at early ages behaves much differently than mature concrete. Immediately after setting, concrete undergoes a rapid change in mechanical properties. Early-age concrete has significantly different elastic and viscoelastic behavior than matured concrete Emborg, 1989; Gutch and Rostásy, 1995; Westman, 1999. For concrete placed in restrained conditions such as bridge decks, culverts, tunnels, retaining walls, and tanks, the early-age elastic and viscoelastic responses of concrete are essential to quantify so that designers can accurately model stress and minimize early-age cracking. By minimizing early-age cracking, the service life of structures can be extended (Darwin and Browning, 2008).

The objectives of the work documented in this chapter are to

1. Assess the accuracy of the B3 Model to estimate the development of early-age concrete stress,
2. Model early-age stresses by modifying the B3 Model to improve its ability to predict the development of concrete stresses from setting onward, and
3. Assess the accuracy of the modifications made to the B3 Model to estimate the development of concrete stress at early ages.

5.1.1 Cracking

Darwin and Browning (2008) reported that "by controlling early age cracking, the amount of cracking at later ages should remain low," and that early-age cracking can significantly increase the rate and amount of chloride penetration (from deicing salts), which may accelerate the corrosion rate of embedded reinforcing exposed to chlorides. Transverse bridge deck cracking occurrence is a common problem for many bridge types in diverse regions (Krauss and Rogalla, 1996). The National Cooperative Highway Research Program (NCHRP) Report 380 (1996) reported the results of a survey sent to all U.S. Departments of Transportation (DOTs) and several transportation agencies overseas to evaluate the extent of deck cracking. Sixty-two percent of the responding agencies considered early-age transverse cracking to be problematic (Krauss and Rogalla, 1996). In addition, their research showed that more than 100,000 bridges suffer from early-age cracking (Krauss and Rogalla, 1996). Given the abundance of cracking observed in bridge decks and other large concrete structures, and the impact of early-age cracking on long-term performance and durability, it is imperative that concrete be proportioned and placed to minimize early-age cracking.

Cracking of hardening concrete occurs when the induced tensile stress exceeds the tensile strength of the concrete. The development of in-place stress is affected by the shrinkage, coefficient of thermal expansion, setting characteristics, restraint conditions, elastic modulus development, stress relaxation, capillary stresses, and temperature history of the hardening concrete. The tensile strength (and strain capacity) increases as the hydration of the cementitious system progresses. The tensile strength is impacted by the cementitious materials content and type, the water-cementitious materials ratio, the aggregate type, gradation, and texture, the degree of curing (internal/external) provided, and the temperature history of the hardening concrete. Quantification of many of the mechanisms mentioned above is quite complicated at early ages, and many of these variables have complex interactions.

5.1.2 The Maturity Method

The curing temperature affects the rate of hydration of the cementitious materials. Therefore, setting and strength gain are functions of both time and temperature (Pinto and Hover, 1999). Several functions can be used to account for the effects of time and temperature; however, the Freiesleben, Hansen, and Pedersen (1977) function, based on the Arrhenius equation (shown in Equation 5.1) has been found to be more representative of the time-temperature effects of the strength development of concrete than other functions (Carino, 2004).

$$t_e = \sum e^{-\frac{E}{R}\left[\frac{1}{T_c}-\frac{1}{T_r}\right]}\Delta t \qquad (5.1)$$

where t_e = equivalent age at reference temperature (hours),
E = activation energy (J/mol),
T_c = average temperature of concrete during time interval Δt (K),
T_r = specified reference temperature (K),
Δt = time interval (hours), and
R = universal gas constant (J/[mol K]).

The activation energy determines the overall effect of temperature within the maturity function (Carino, 2004). The activation energy can be estimated from the total content of the cement Bogue compounds, the cement fineness, and the type and amount of supplementary cementing materials (Schindler, 2004), and chemical admixtures (Riding et al., 2011). The reference temperature is generally taken as 296 K (73°F) for work performed in the United States.

5.1.3 Time-Dependent Behavior of Concrete

When concrete is loaded, there is an immediate elastic response. If the load is maintained, additional time-dependent response will occur. This additional response is due to the viscoelastic and viscoplastic nature of concrete. Creep is a time-dependent increase in strain under constant stress, whereas relaxation is a time-dependent reduction in stress under a constant strain. For early-age cracking, relaxation effects can be beneficial in delaying the cracking time by reducing the tensile stress development (Mehta and Monteiro, 2006). Reducing the early-age stress can significantly increase the time to cracking, lead to reduced crack widths, or prevent cracking all together.

The time-dependent response can be expressed in terms of *compliance*, which has the units of MPa^{-1} (psi^{-1}), or as a ratio of the elastic deformation, which is known as a *creep coefficient* (ACI 209.2R, 2008). Compliance is a unit strain per stress as show in Equation 5.2. An illustration of creep in terms of a compliance function and in terms of a creep coefficient is shown in Figure 5.1. The compliance term encompasses both the elastic deformations and time-dependent, whereas the creep coefficient term captures only the time-dependent deformation.

$$J(t,t_0) = \varepsilon(t)/\sigma_0 \qquad (5.2)$$

where $J(t,t_0)$ = compliance as a function of time (t) and loading age (t_0), 1/MPa (1/psi),
$\varepsilon(t)$ = strain at time t, mm/mm (in./in.), and

σ_0 = stress applied at age t_0, MPa (psi).

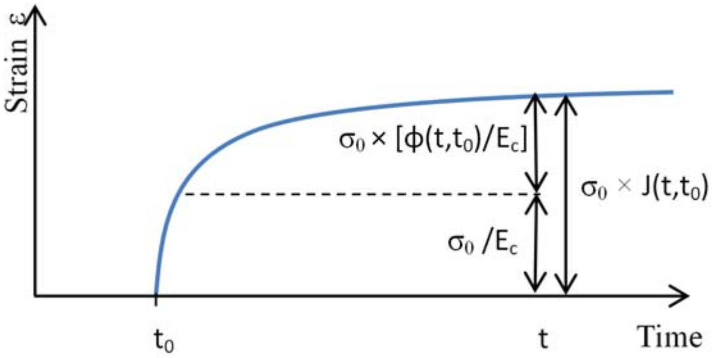

Figure 5.1: Stress behavior described with compliance and creep coefficient functions.

5.1.4 The B3 Model

Many models in literature estimate the compliance of mature concrete, including the B3 Model (Bažant and Baweja, 2000). This model was calibrated with mature, well-hardened concrete. Because of this, the initial loading age that this model was calibrated for is 1 day or later. The B3 Model is based on solidification theory. Solidification theory is a physically justified model for concrete as it describes the cement hydration as growth of a load-bearing volume fraction [Bažant and Baweja, 1989a; and Bažant and Prasannan, 1989b]. The B3 Model is a simpler and more theoretically justified compliance model than previous models proposed by Bažant and his co-workers (2000). The B3 Model is based on the solidification of hardening cement modeled with a Kelvin chain and linear spring. Compliance is calculated using Equation 5.3, where the q_1 term is the elastic response, $C_0(t,t_0)$ is the basic-creep term, and $C_d(t,t_c)$ is the drying-creep term. The basic-creep term is determined as shown in Equation 5.4. The constants in this model were calibrated using the inch-pound system; thus the inputs must be in psi or lb/yd^3. However, the result of the compliance calculation can be converted using (1 psi)$^{-1}$ = (6,895 Pa)$^{-1}$.

$$J(t,t_0) = q_1 + C_0(t,t_0) + C_d(t,t_c) \tag{5.3}$$

$$C_0(t,t_0) = q_2 Q(t,t_0) + q_3 \ln[1 + (t - t_0)^n] + q_4 \left(\frac{t}{t_0}\right) \tag{5.4}$$

where

$q_1 = \left(\frac{0.6}{E_{c,28}}\right)\frac{1}{psi}$ (5.5)

$q_2 = 86.814 \times 10^{-6} \times c^{0.5} f_{c,28}^{-0.9}$,

$q_3 = 0.29\,(w/c)^4\, q_2$,

$q_4 = 0.14 \times 10^{-6}\,(a/c)^{-0.7}$,

$Q(t,t_0) = Q_f(t_0)\left[1 + \left(\frac{Q_f(t_0)}{Z(t,t_0)}\right)^{r(t_0)}\right]^{-1/r(t_0)}$,

$Q_f(t_0) = \left[0.086(t_0)^{2/9} + 1.21(t_0)^{4/9}\right]^{-1}$,

$Z(t,t_0) = (t_0)^{-m} \times \ln[1 + (t - t_0)^n]$,

$r(t_0) = 1.7(t_0)^{0.12} + 8$,

$E_{c,28}$ = 28-day modulus of elasticity (lb/in^2)
$f_{c,28}$ = 28-day compressive strength (lb/in^2)
n = 0.1,
m = 0.5,
a/c = aggregate-cement ratio by mass,
w/c = water-cement ratio by mass,
a = total aggregate content (lb/yd^3), and
c = cement content (lb/yd^3).

Because the formulation of the B3 Model was based on physical phenomena, each term has a physical meaning and is therefore easier to comprehend than other compliance models. The physical meanings of each term in Equations 5.4 and 5.5 are provided here as defined by (Bažant and Baweja, 2000):

$q_1 \longrightarrow$ Elastic compliance component, 1/Pa (1/psi),
$q_2 Q(t, t_0) \longrightarrow$ Aging viscoelastic compliance component, 1/Pa (1/psi),
$q_3 \ln[1 + (t - t_0)^n] \longrightarrow$ Non-aging viscoelastic compliance component, 1/Pa (1/psi), and
$q_4 \left(\frac{t}{t_0}\right) \longrightarrow$ Plastic flow compliance component, 1/Pa (1/psi).

The aging viscoelastic term represents an age dependent viscoelasticity and the non-aging viscoelastic term is an age independent viscoelasticity. A graphical illustration of the magnitude and contribution of each term separately versus the total compliance is provided in Figure 5.2 for a bridge deck mixture loaded at one day. The results shown in this figure illustrate that the total compliance is initially dominated by the aging viscoelastic and elastic compliance components. Over time, the plastic flow compliance component begins to significantly contribute to the overall behavior. For this mixture, the non-aging viscoelastic compliance component is negligible.

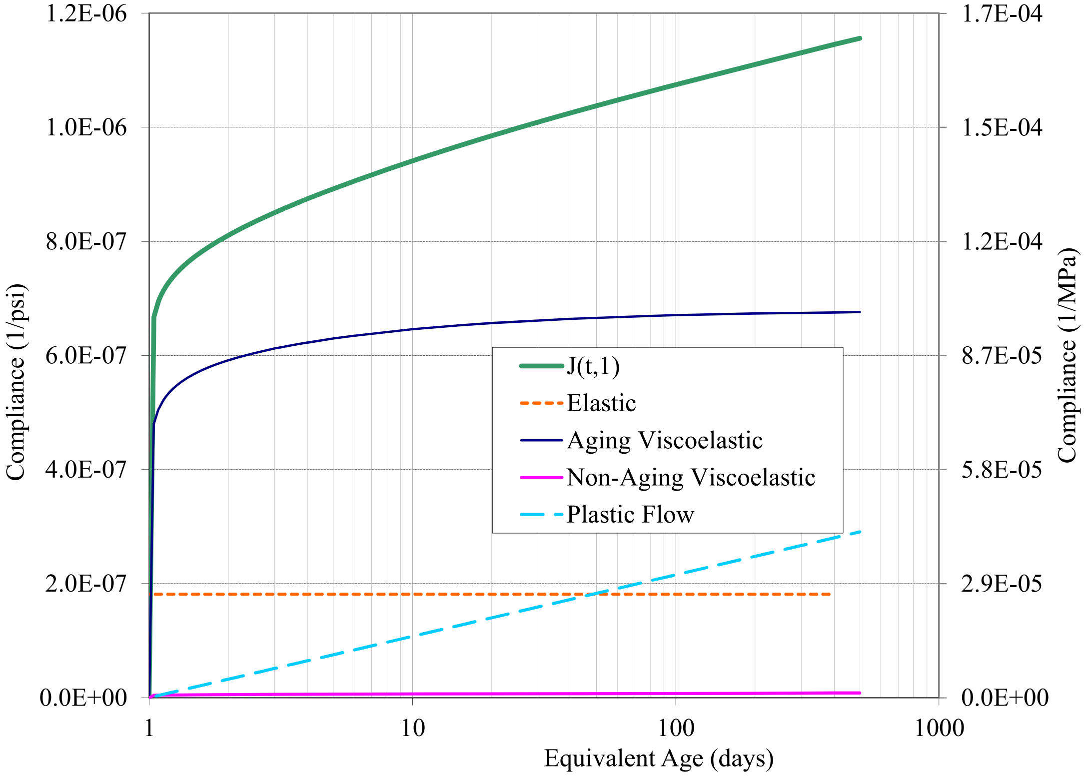

Figure 5.2: Illustration of component of B3 Model.

As shown in Equation 5.5, the modulus used in the B3 Model is an asymptotic modulus, which Bažant and Baweja (2000) require to be determined by taking the measured 28-day modulus divided by 0.6. Unlike other creep models, the elastic compliance component of the B3 Model is treated as a constant with respect to age. Since the elastic response is the immediate strain under very short load durations (1 μs), Bažant and Prasannan (1989a) state that the results from standardized *elastic modulus tests* inherently contain both elastic and time-dependent behavior. Because of this Bažant and Prasannan (1989a) state the following: "We nevertheless take the view that age-dependence of E(t) is a complication that is both unnecessary and thermodynamically objectionable."

5.1.5 Modification of the Early-Age Viscoelastic Compliance Component

The B3 Model was not calibrated or designed to account for the behavior of concrete loaded before one day. However, for crack prediction modeling, it is necessary to determine the amount of relaxation that occurs from the onset of setting. The B3 Model does not accurately predict the relaxation behavior of concrete loaded prior to one day due to a lack of viscoelastic response (Østergaard et al., 2001). This lack of early-age viscoelastic response was corrected by Østergaard et al. (2001) with a modified q2 term as shown in Equation 5.6. The q5 term is referred to as the structural set time, and should correspond to the transition from liquid viscoelastic to solid viscoelastic response (Østergaard et al., 2001). If q5 is set equal to the age at loading (t_0) then the modified q2 approaches infinity; therefore, q5 must always be less than t_0.

$$q'_2 = q_2\left(\frac{t_0}{t_0 - q_5}\right) \tag{5.6}$$

where q_5 = structural setting time (days).

The advantage of a correction in the form of Equation 5.6 is that the effect is quickly diminishing, which leaves the B3 Model virtually unmodified at later ages as shown in Figure 5.3. The early-age viscoelastic response will be increased greatly by the q_2 modification, but after two days the modified q_2 is virtually the same as the unmodified q_2 as illustrated in the figure.

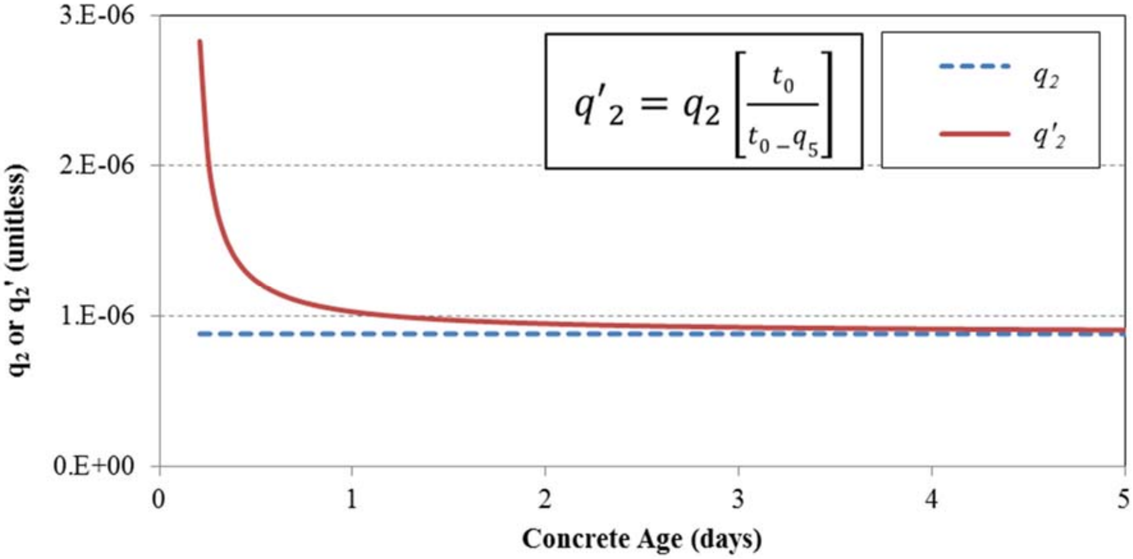

Figure 5.3: Effect of q_2 modification (with q_5 = 0.25 days).

5.1.6 Superposition

Concrete behavior can be approximated as linear-elastic at low stress levels (Mehta and Monteiro, 2006). This approximation applies to viscoelastic behavior also. If the concrete is loaded within the linear viscoelastic range, then creep strain is proportional to the applied stress. With the principle of superposition, the sum of incremental creep responses of individual stress increments can be added to determine the strain of an element with the same stress history (McHenry, 1943). There is a limit at which concrete starts behaving with non-linear elastic and viscoelastic response. At that point, the principle of superposition becomes invalid, because the behavior becomes non-proportional. There is some uncertainty as to what the upper limit of proportional behavior is—it is generally at stress-strength ratios of 40 to 60% for most mixtures, but can be as high as stress-strength ratios of 85% (Neville et al, 1983).

5.2 Experimental Plan and Test Methods

5.2.1 Restrained Stress Development

The rigid cracking frame (RCF), shown in Figure 5.4, consists of a 150 × 150 × 1300 mm (6 × 6 × 50 in.) dog-bone-shaped formwork and a restraining frame. Fresh concrete is placed inside plastic-lined formwork and is sealed on all sides. The formwork is constructed so that the curing temperature of the concrete specimen can be controlled. Length changes that occur within the concrete after set are restrained by the RCF, and the uniaxial stress development in the concrete is measured. The RCF test setup was adapted from the configuration developed by Dr. Rupert Springenschmid and documented by the RILEM Technical Committee 119 (1998). Because the formwork is sealed, no moisture is lost, and drying shrinkage effects do not develop. Because of this, the drying-creep term in the B3 Model is not used in this study. A detailed description of the RCF test setup used for this project can be found elsewhere (RILEM Technical Committee 119, 1998).

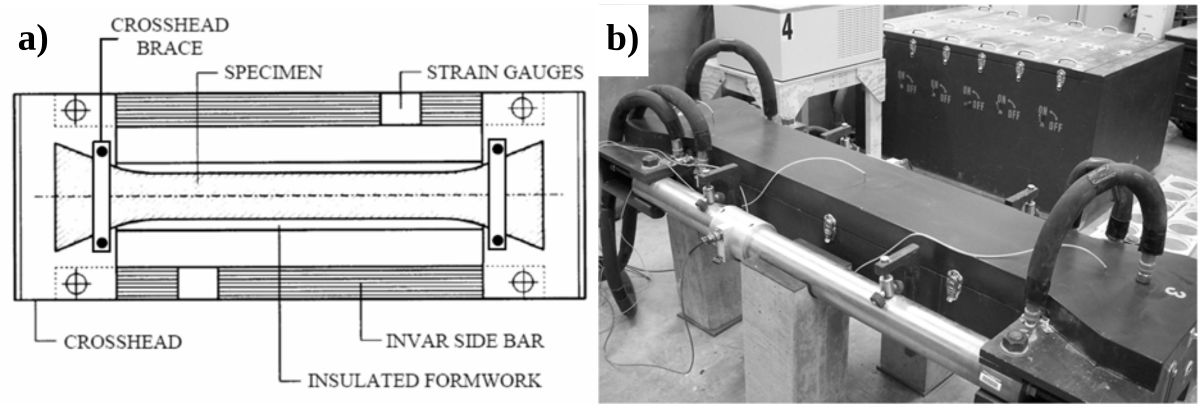

Figure 5.4: Rigid cracking frame test: a) schematic diagram and b) actual equipment.

5.2.2 Development of Mechanical Properties

Companion 150 × 300 mm (6 × 12 in.) cylindrical specimens were made to assess the development of the splitting tensile strength, compressive strength, and modulus of elasticity as per ASTM C 496 (2004), ASTM C 39 (2005), and ASTM C 469 (2002), respectively. Immediately after being cast, the mechanical property specimens were placed in a temperature-controlled box and cured to the same temperature profile as the RCF until cracking occurred in the specimen. The temperature-controlled box can be seen in the background of Figure 5.4b. After cracking occurred in the RCF specimen, the mechanical property specimens were moved and placed in a moist curing room for standard curing as per ASTM C 192 (2007). The mechanical properties were tested at ages of 0.5, 1, 2, 3, 7, and 28 days and their temperature recorded to allow the equivalent age at testing to be determined.

5.2.3 Setting

Initial and final set times were determined from penetration resistance testing as per ASTM C 403 (2008). The mortar sample for this test was obtained by wet sieving the concrete over a 4.75 mm (No. 4) sieve. The mortar sample for setting was also match cured to the temperature history.

5.2.4 Mixtures

Seventy-two combinations of mixture proportions and curing conditions were used to collect data to develop an early-age stress prediction model. Mixture proportions are provided in Table 5.1.

Table 5.1: Mixture proportions and selected target properties.

Mixture ID	Cement	SCM 1	SCM 1 %	SCM 2	SCM 2 %	Cement + SCM lb/yd^3	w/cm	CA Type	FA/ (FA + CA)	Chemical Admixtures Used
1	IA	-	-	-	-	564	0.42	SRG	0.40	MRWR
2	IA	-	-	-	-	564	0.42	SRG	0.40	LRWRR
3	I/IIA	-	-	-	-	564	0.42	SRG	0.40	LRWRR
4	I/IIA	-	-	-	-	564	0.42	SRG	0.40	LRWRR, AEA
5	V	-	-	-	-	559	0.44	SRG	0.45	MRWR
6	I/IIB	S2	48	-	-	583	0.41	SGR	0.44	HRWR-N, AEA
7	I/IIC	FF3	30.9	-	-	610	0.35	SRG	0.38	LRWR, MRWR
9	IB	-	-	-	-	564	0.42	L	0.40	HRWR-PC
12	IB	-	-	-	-	564	0.42	SRG	0.40	LRWRR
14	IB	FF2	20	-	-	564	0.42	SRG	0.40	LRWRR
15	IB	FF2	30	-	-	564	0.42	SRG	0.40	LRWRR
16	IB	FF1	20	-	-	564	0.42	SRG	0.40	LRWRR
17	IB	FF1	30	-	-	564	0.42	SRG	0.40	LRWRR
19	IB	FC1	20	-	-	564	0.42	SRG	0.40	LRWRR
20	IB	FC1	30	-	-	564	0.42	SRG	0.40	LRWRR
21	IC	FC2	30	-	-	564	0.42	SRG	0.40	LRWRR
21	IB	FC2	20	-	-	564	0.42	SRG	0.40	LRWRR
22	IC	FC2	20	-	-	564	0.42	SRG	0.40	LRWRR
23	IC	Sl	30	-	-	564	0.42	SRG	0.40	LRWRR
24	IB	S1	50	-	-	564	0.42	SRG	0.40	LRWRR
25	IC	FC1	25	SF	6	564	0.42	SRG	0.39	LRWRR
26	IC	FF2	25	SF	6	564	0.42	SRG	0.39	LRWRR
27	IC	FF2	30	S1	30	564	0.42	SRG	0.40	LRWRR
29	IB	-	-	-	-	657	0.32	SRG	0.40	LRWRR, HRWR-PC
31	IB	-	-	-	-	517	0.48	SRG	0.40	
32	IB	-	-	-	-	470	0.53	SRG	0.40	
33	III	-	-	-	-	564	0.42	SRG	0.40	LRWRR
34	IC	-	-	-	-	564	0.42	SRG	0.40	AEA
40	V	-	-	-	-	564	0.44	SRG	0.40	MRWR
41	I/IID	FF5	25	-	-	585	0.45	dolomite	0.40	LRWRR, AEA
42	I/IID	FF5	25	-	-	585	0.45	SRG	0.40	LRWRR, AEA
46	IC	-	-	-	-	561	0.42	L	0.40	HRWR-PC
47	I/IIA	-	-	-	-	564	0.42	SRG	0.40	LRWRR

Concretes were evaluated with siliceous river gravel (SRG), limestone (L), and dolomite (D) coarse aggregates. Three ASTM C 150 Type I, four Type I/II, one Type III, and one Type V cements were used. Also, five ASTM C 618 Class F fly ash, three Class C fly ash, two GGBFS, and one silica fume were used in the mixtures. The chemical composition of each of the cements and SCMs can be found in Tables 5.2 and 5.3, respectively. The mixtures also utilized air-entraining admixtures (AEA), low-range water reducers (LRWR), mid-range water reducers (MRWR), and high-range water reducers (HRWR) in the form of polycarboxylate (PC) or naphthalene (N) bases. All of the mixtures were normal weight mixtures intended for use in bridge decks or mass concrete applications.

Table 5.2: Cement properties.

Property	IA	IB	IC	I/IIA	I/IIB	I/IIC	I/IID	III	V
SiO_2	19.2	20.5	21.3	20.8	21.0	20.5	21.3	20.2	21.6
Al_2O_3	5.3	5.4	5.3	3.9	4.1	4.9	5.0	5.0	4.0
Fe_2O_3	2.3	2.0	1.9	3.7	3.8	3.3	3.3	3.7	5.3
CaO	63.2	64.5	63.6	64.5	63.4	64.4	62.0	62.5	63.1
MgO	1.1	1.2	1.3	1.0	1.3	1.5	2.0	1.0	0.8
Na_2O	0.1	0.1	0.1	0.2	0.1	0.2	0.2	-	0.3
K_2O	1.0	0.6	0.6	0.6	0.6	0.4	0.4	-	0.2
$Na_2O+0.658*K_2O$	0.8	0.5	0.5	0.6	0.5	0.5	0.5	0.3	0.4
TiO_2	0.3	0.3	0.2	0.2	0.2	0.2	0.3	-	0.2
MnO_2	0.0	0.0	0.0	0.0	0.6	0.4	0.4	-	0.1
P_2O_5	0.2	0.2	-	0.0	0.2	0.1	0.1	-	0.0
SrO	0.1	0.1	-	0.0	0.2	0.1	0.0	-	0.1
BaO	0.0	0.0	-	0.0	0.0	0.0	0.0	-	0.0
SO_3	3.2	3.4	3.6	2.4	3.0	2.8	2.6	4.6	2.7
LOI	4.1	1.8	-	2.7	1.5	1.4	2.4	1.9	1.6
Free CaO	0.0	0.0	0.0	0.0	0.0	0.6	0.5	-	0.0
ASTM C 150 Bogue Compounds									
C_3S	63.1	58.3	49.0	66.5	56.5	60.7	45.2	48.8	49.9
C_2S	7.4	14.7	24.0	9.4	17.7	12.9	26.9	21.1	24.4
C_3A	10.3	11.0	10.9	4.0	4.6	7.5	7.5	7.0	1.8
C_4AF	7.0	6.1	5.7	11.4	11.5	10.0	10.1	11.4	16.1

Table 5.3: Supplementary cementing materials properties.

	Class F Fly Ashes					Class C Fly Ashes			Slag Cement		Silica Fume
	FF1	**FF2**	**FF3**	**FF4**	**FF5**	**FC1**	**FC2**	**FC3**	**S1**	**S2**	**SF**
SiO2	56.6	51.7	46.7	49.5	NA	37.8	33.1	37.4	34.5	34.0	94.3
Al2O3	30.7	24.8	19.7	17.6	NA	19.8	18.4	17.7	11.4	11.4	0.0
Fe2O3	4.9	4.2	5.1	5.5	NA	6.2	5.4	5.9	0.7	1.2	0.1
CaO	0.7	13.1	18.4	19.5	NA	23.1	28.9	25.9	41.7	41.7	0.5
MgO	0.7	2.3	3.0	2.8	NA	4.6	5.3	5.2	7.3	8.3	0.6
Na2O	0.1	0.2	1.8	0.6	NA	1.7	1.6	1.6	0.1	0.2	0.1
K2O	2.3	0.8	0.9	1.0	NA	0.1	0.4	0.6	0.4	0.3	1.0
Na2O+0.658*K2O	1.6	0.7	2.3	1.2	NA	1.8	1.9	2.0	0.4	0.4	0.7
SO3	0.0	0.5	0.8	1.1	NA	1.5	2.3	1.8	1.9	1.2	0.2
LOI	2.1	0.2	0.4	0.4	NA	0.7	0.3	0.5	0.8	0.8	3.1
Blaine	147	166	420	296	NA	348	300	588	332	320	20000

Note: N.A.= No data available

5.2.5 Compliance Modeling using Results of the Rigid Cracking Frame and Thermal Strain

The thermal strain was determined using the coefficient of thermal expansion and temperature change as expressed in Equation 5.7. This method neglects autogenous strain. However, all but two of the mixtures had w/cm of 0.41 or greater; therefore, autogenous strain is negligible. From Equation 5.2 stress can be calculated as shown in Equation 5.8. Because the RCF does not provide full restraint, the RCF concrete specimen experiences some strain and this strain is captured by the strain gauges on the RCF side bars. Because the RCF does deform somewhat, the strain must be accounted for as shown in Equation 5.8. In Equation 5.8 ε_{RCF} is negative because it reduces the strain that causes stress development.

$$\varepsilon_T = \alpha \Delta T \tag{5.7}$$

where

ε_T = strain due to thermal effects, mm/mm (in./in.),,
α = Coefficient of thermal expansion, mm/mm/ °C (in./in./°F), and
ΔT = temperature change, °C (°F).

$$\sigma = \frac{\varepsilon_T - \varepsilon_{RCF}}{J(t,t_0)} \tag{5.8}$$

where

σ = calculated stress development, Mpa (psi), and
ε_{RCF} = strain of the rigid cracking frame specimen, mm/mm (in./in.).
$J(t, t_0)$ = compliance function, 1/Mpa (1/psi).

Starting at initial set, thermal strain results were calculated over one-hour time steps using the temperature profile of each mixture ($\Delta\varepsilon_T$). The strain of RCF concrete specimen measured from the side bar strain gages were also determined over the same one-hour time step ($\Delta\varepsilon_{RCF}$). The total change in strain over the one-hour time step is the change in the thermal strain ($\Delta\varepsilon_T$) minus the change in RCF strain ($\Delta\varepsilon_{RCF}$), as expressed in Equation 5.9. The strain change increments were divided by the compliance function for that age and loading age, to determine the stress response as a function of time for each strain increment. Using the principle of superposition, the response of all the strain increments were calculated by summing the response of the strain increments at a time and those previously as illustrated in Figure 5.5 and expressed in Equation 5.10.

$$\Delta\varepsilon(t_0) = \Delta\varepsilon_T - \Delta\varepsilon_{RCF} \tag{5.9}$$

$$\sigma(t_n) = \sum\left[\frac{\Delta\varepsilon(t_{0,1})}{J(t_n,t_{0,1})} + \frac{\Delta\varepsilon(t_{0,2})}{J(t_n,t_{0,2})} + \cdots + \frac{\Delta\varepsilon(t_{0,n})}{J(t_n,t_{0,n})}\right] \tag{5.10}$$

where $\sigma(t_n)$ = stress at time n, Mpa (psi),
$J(t_n, t_{0,1})$ = compliance function at time *n* for loading at time one, 1/Mpa (1/psi), and
$\Delta\varepsilon(t_{0,1})$ = one hour strain increment at time one mm/mm (in./in.).

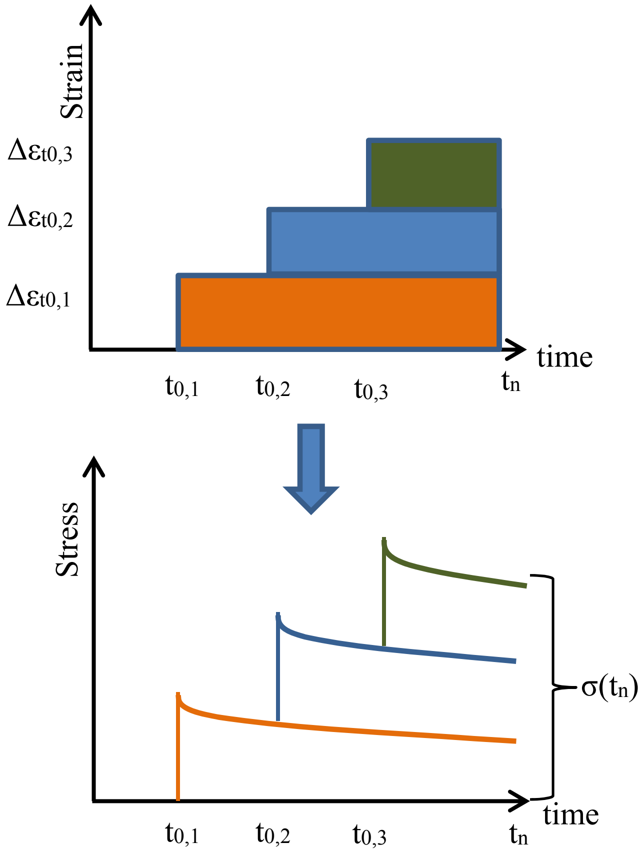

Figure 5.5: Illustration of superposition of stress relaxation.

5.2.6 Early-Age Compliance Modeling with the B3 Model

Using the equivalent-age maturity function and the modeled temperature history the equivalent age of rigid cracking frame and mechanical property results were determined. The activation energy was calculated for the cement and SCM combination used (Schindler, 2004) and a reference temperature of 276 °K (73°F) were used as maturity function constants.

The stress development from the B3 compliance model using the calculated thermal stress data and the measured stress development in terms of equivalent age for the 12E mixture are shown in Figure 5.6. The splitting tensile strength development was scaled by a factor equal to the ratio of measured stress at cracking to the cylinder splitting tensile strength at the same equivalent age. This was done so that the stress development and strength development coincide at cracking. For example, the cracking stress for the 12E mixture was 2.2 MPa (321 psi) at 8.6 days of equivalent age. The splitting tensile strength at 8.61 days of equivalent age was 4.2 MPa (606 psi). Thus, the splitting tensile strength development was scaled by 0.53 to determine the tensile strength development relative to the stress at cracking. The scaled tensile strength development is shown in Figure 5.6. The modeled stress development was truncated when the measured stress development reached a scaled stress-to-strength ratio of 70% as illustrated in Figure 5.6. This approach was use as above a stress-to-strength ratio of 70% the principle of superposition may not be applicable to compliance modeling.

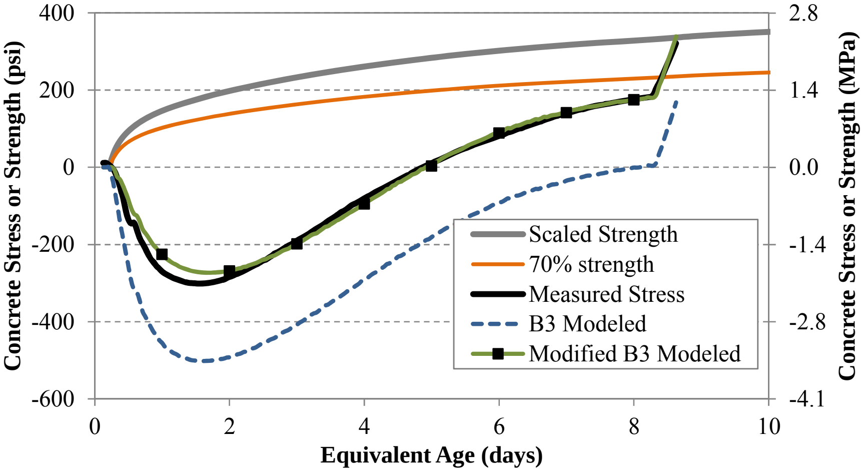

Figure 5.6: Typical measured and B3 modeled stress development with scaled strength development.

5.2.7 Statistical Assessment

The coefficient of determination (R^2) of the modeled versus measured stress development was calculated for each mixture. The coefficient of determination is expressed in Equation 5.11 (Scheaffer et al., 2010). The coefficient of determination is a way to quantify the goodness of fit of a predicted data set to a measured data set, where 1.0 is a perfect fit. The unbiased estimate of the standard deviation of the absolute error (S_j), shown in Equation 5.12 (McCuen, 1985), was also calculated for the measured stress versus predicted stress.

$$R^2 = 1 - \frac{SS_{err}}{SS_{tot}} \tag{5.11}$$

where R^2 = coefficient of determination (unitless),

SS_{err} = sum of the squared error $= \sum(y_i - f_i)^2$,

SS_{tot} = sum of squares total $= \sum(y_i - \bar{y})^2$,

y_i = predicted value,

$\bar{y}$ = mean observed data, and
f_i = observed data.

$$S_j = \sqrt{\frac{1}{n-1}\sum_i^n \Delta_i^2} \tag{5.12}$$

where S_j = unbiased estimate of the standard deviation, MPa (psi),
n = number of data points (unitless), and
Δ_i = absolute error, MPa (psi).

5.3 Results and Discussion

5.3.1 B3 Model Results and Discussion

Stress development was measured using RCFs at the University of Texas and Auburn University. In some instances, mixtures were evaluated with multiple temperature scenarios for summer, fall, and winter placements, and varying member dimensions. If the same mixture proportions were evaluated under varying temperature scenarios, the results are denoted with upper case letters after the mixture number.

Figure 5.7 illustrates typical B3 Model stress prediction results compared to measured stress development. The mixtures utilize a) Type I, b) Type I + 50% GGBFS, c) Type I + 20% Class F ash, and d) Type V cementitious materials to illustrate the model's effectiveness with varying cementitious compositions. The measured stress development versus B3 Model stress development for all mixtures at one-hour increments are plotted in Figure 5.8, where a negative value is a compressive stress and a positive value is a tensile stress. Because concrete starts behaving nonlinearly at higher stress-to-strength ratios, the data points that were above a stress-to-scaled strength ratio of 70% were omitted from Figure 5.8. Figures 5.6, 5.7, and 5.8 indicate that the B3 Model generally overpredicts the early-age *compressive* stress development and underpredicts the tensile stress. This result from the B3 Model is expected because it was not calibrated or designed to predict the behavior of concrete loaded immediately after setting, which is the period where the modulus of elasticity is rapidly changing and the concrete behavior is highly viscoelastic. This lack of calibration at early ages leads to an inaccurate predictions of early-age elastic and viscoelastic compliance components. The lack of the B3 Model's ability to account for early-age compressive stress led to higher-than-measured compressive stress development, and this in turn caused a delay in the predicted time at zero-stress and lower tensile stress development.

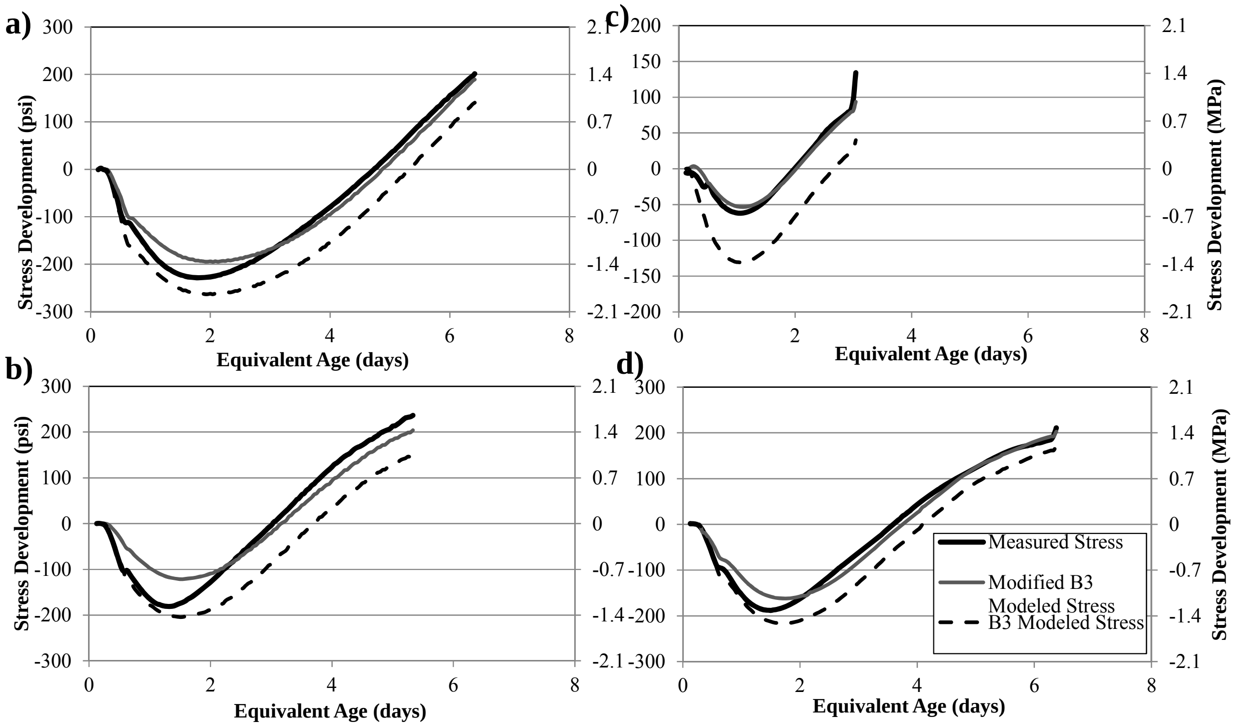

Figure 5.7: B3 model and Modified B3 Model stress development results for a) 12A: Type IB, b) 24B: Type IB+50%S1 c) 14: IB +20%FF2, and d) 5C: Type V.

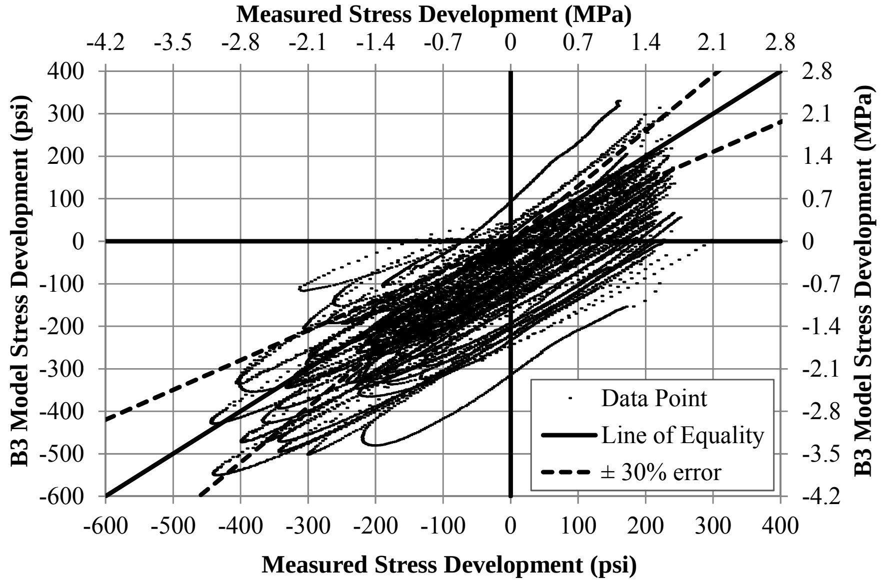

Figure 5.8: Measured vs. B3 modeled stress development.

The R^2 and S_j values for the B3 Model's predicted versus measured stress for each mixture is presented in Table 5.2. The R^2 and S_j of all the unmodified B3 Model predictions compared to the measured data points considering all data is 0.59 and 0.78 MPa (113 psi), respectively. The R^2 and S_j of all of the data collected give a measure of how well the B3 Model predicts the measured stress. The R^2 value suggests that 59% of the error in data is explained by the model.

5.3.2 Early-Age Compliance Modeling with the Modified B3 Model

The B3 Model overestimates the measured initial compressive stress (i.e., too high elastic modulus) and underestimates early-age tensile stress (i.e., too little early-age relaxation), as illustrated in Figures 5.6, 5.7, and 5.8. Østergaard et al. (2001) have shown that the B3 Model underestimates the amount of early-age stresses relaxation, which was attributed to a lack of early-age viscoelastic response. However, early-age concrete exhibits both high viscoelastic properties and rapidly changing elastic properties (Emborg, 1989; Westman, 1999). The elastic response of the B3 Model is treated as a constant equal to the asymptotic modulus of elasticity (E_0), which Bažant and Baweja (2000) determine as the 28-day modulus of elasticity divided by 0.6 as shown in Equation 5.5. This may be acceptable for sufficiently hardened concrete; however the modulus of elasticity at early ages is changing rapidly (Emborg, 1989; Westman, 1999). The elastic modulus for a mixture is shown versus the asymptotic modulus used in the B3 Model in Figure 5.9. Using the asymptotic modulus of elasticity leads to very high early-age stress predictions because the actual elastic response is much less. Because of this, the function developed by Østergaard et al. (2001) was used to adjust the B3 Model's lack of viscoelastic response and a correction of the same mathematical form was used to modify the very early-age modulus of elasticity. The early-age viscoelastic modification developed by Østergaard et al. (2001) and the proposed early-age elastic modification are shown in Equations 5.7 and 5.15, respectively. The early-age elastic modifier and the proposed time-dependent E_0 is shown in Figure 5.9.

$$q_1' = q_1\left[\frac{t_0}{t_0-q_6}\right] = \frac{0.6}{E_{c,28}}\left[\frac{t_0}{t_0-q_6}\right] \qquad (5.13)$$

where q_1' = modified elastic compliance (1/psi),

q_6 = factor for early-age elastic behavior (days).

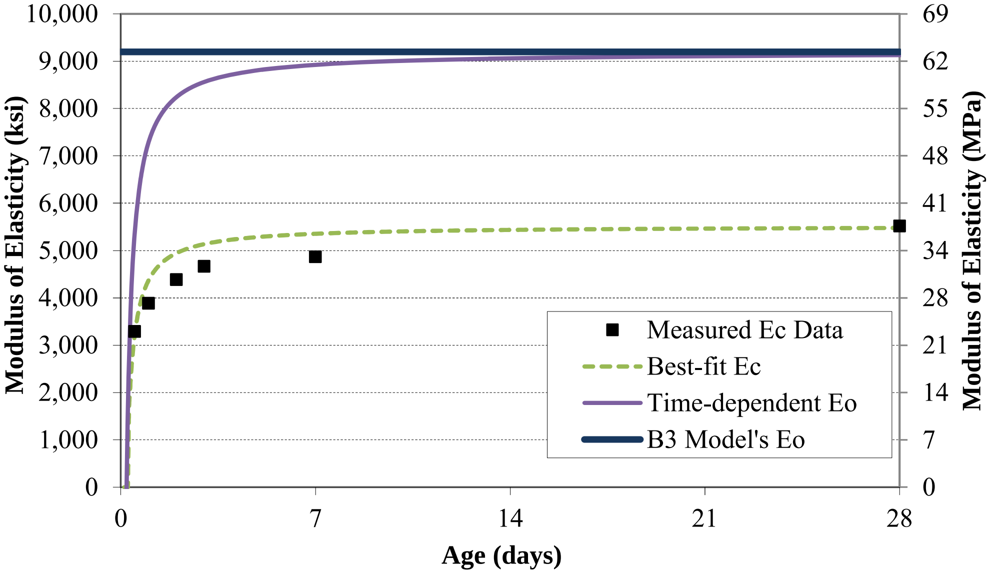

Figure 5.9: Illustration of modifications made to the elastic behavior of the B3 Model.

The use of these two modifications will decrease the modeled compressive stress development that results from loading at early ages; however, these modifications will have little to no impact on loads applied after an equivalent age of 2 days. Similar to q_5, q_6 cannot be greater than the setting time because the response approaches infinity when the loading age (t_0) equals q_6. A modification in the form of Equations 5.7 and 5.15 quickly diminishes, leaving the model virtually unchanged at later ages. If the elastic and creep terms of the B3 Model as expressed in Equations 5.4 and 5.5 are combined and drying effects are omitted, then the B3 Model can be expressed as shown in Equation 5.14. When the modifications are substituted into Equation 5.14, then the Modified B3 Model can be expressed as shown Equation 5.15.

$$J(t,t_0) = q_1 + q_2 Q(t,t_0) + q_3 \ln(1 + (t - t_0)^n) + q_4 \left(\frac{t}{t_0}\right) \tag{5.14}$$

$$J(t,t_0) = q_1 \left[\frac{t_0}{t_0 - q_6}\right] + q_2 \left[\frac{t_0}{t_0 - q_5}\right] Q(t,t_0) + q_3 \ln(1 + (t - t_0)^n) + q_4 \left(\frac{t}{t_0}\right) \tag{5.15}$$

where q_5 = age factor for early-age viscoelastic behavior in equivalent age (days), and

q_6 = age factor for early-age elastic behavior in equivalent age (days).

5.3.3 Effect of the Modifiers Added to the B3 Model

The effect of increasing q_6 on the elastic component of compliance (q_1') is shown in Figure 5.10. Increasing q_6 results in a greater elastic component of compliance at early ages; at later ages (approximately 2 days), the unmodified elastic compliance component is approached. The stress predicted from increased elastic component of compliance will be reduced compared to the unmodified B3 Model's elastic compliance component. The effect of increasing q_5 on the modified age-dependent viscoelastic component of compliance [$q_2' \, Q(t,t_0)$] is shown in Figure 5.11. Increasing q_5 leads to increased viscoelastic response, which leads to more stress relaxation and reduced early-age predicted stress when compared to the unmodified viscoelastic response of the B3 Model.

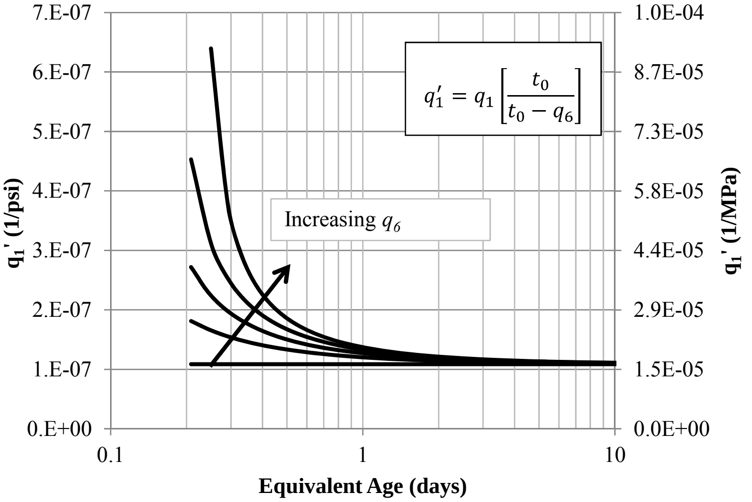

Figure 5.10: Effect of increasing q_6 on modified elastic response.

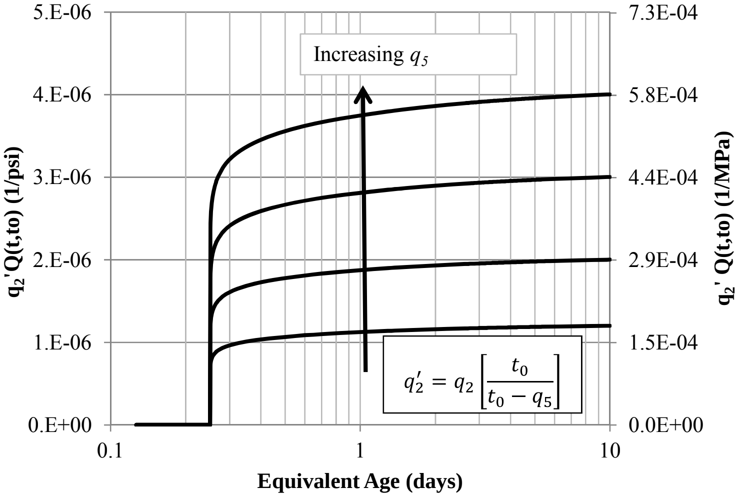

Figure 5.11: Effect of increasing q_5 on the modified viscoelastic response.

The effect of the q_1' and q_2' on compliance [$J(t,t_0)$] as predicted with the Modified B3 Model is shown in Figure 5.12. The unmodified B3 Model's compliance at a loading age of 0.25 days [$J(t,0.25)$] and 2.0 days [$J(t,2.0)$] as a function of equivalent age are also shown in this figure. For this illustration, the modifiers q_5 and q_6 were both set equal to the time just before initial set in equivalent age, which is their maximum value. The effect on compliance of applying only the viscoelastic modified (q_2') and then applying simultaneously the viscoelastic (q_2') and elastic modifications (q_1') are shown. At the 0.25-day loading age, the modifications added to the Modified B3 Model have a significant effect on the modeled compliance, whereas the effect on the 2-day loading is insignificant as shown in Figure 5.12. The change in response provided by the q_1' adjustment decreases the early-age elastic stress development. The change in response provided by the q_2' adjustment increases the magnitude of early-age stress relaxation.

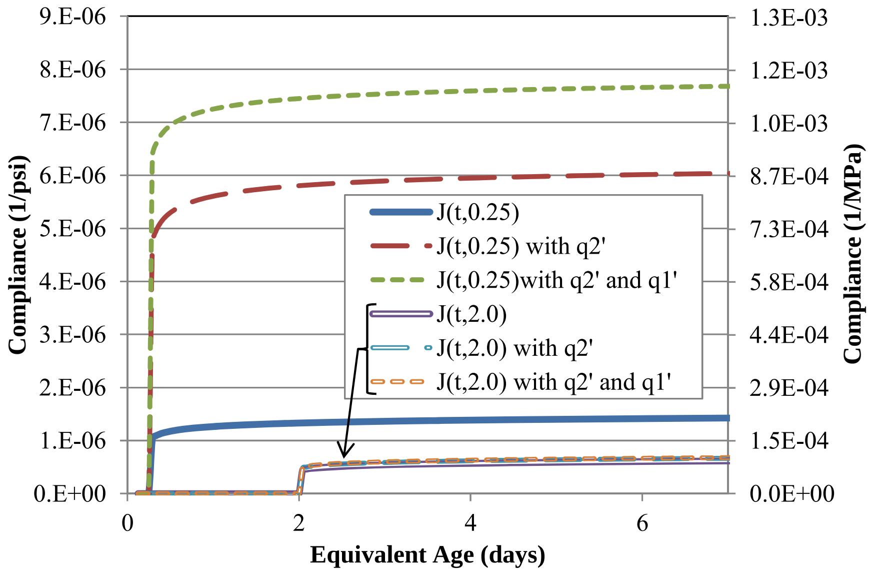

Figure 5.12: Effect of q1' and q2' correction on calculated compliance.

To solve for the most appropriate q_5 and q_6 values for each concrete tested, the measured stress and modulus of elasticity values were used. The analysis to determine the most appropriate modifying terms was conducted in terms of equivalent age (t_e), solving for the q_5 and q_6 terms separately. The elastic modifier was solved for first to uniquely account for the time-dependent development of early-age modulus of elasticity. Figure 5.9 illustrates the modulus modification, showing discrete data points and the best-fit modulus data. The best-fit modulus was determined using a least-squares regression analysis to minimize the error between the discrete data points, and the modifying equation expressed in Equation 5.13 using the measured 28-day modulus. This result was then scaled by a factor of 0.6^{-1} to determine the time-dependent asymptotic modulus (E_0), so that the later-age results adhere to the approach developed by Bažant and Baweja (2000). The unmodified E_0 is also shown for comparison. The time-dependent E_0 approaches the unmodified E_0 at later ages (as illustrated in Figure 5.9).

The q_5 term was then solved for by least-squares regression analysis to minimize the error between stress development of the elastic Modified B3 Model results and the measured stress development. The maximum allowable value of q_5 and q_6 was set equal to the equivalent age just before initial set as measured by ASTM C 403 (2008). Only the data with a stress-to-scaled strength ratio of less than 70% were used to determine the best-fit value of q_5.

5.3.4 Modified B3 Model Results and Discussion

The R^2 and S_j of all the Modified B3 Model predictions compared to the measured stress development are provided in Table 5.4. The early-age stress developments predicted with the Modified B3 Model were illustrated earlier in Figure 5.6 and Figure 5.7. Figure 5.7 illustrates some typical measured, B3 Model results and Modified B3 Model results. All measured stress versus Modified B3 Model's predicted stress developments are plotted in Figure 5.13. The early-age viscoelastic and elastic modulus modifiers effectively combine to improve the predicted early-age compressive stress development due to greater viscoelastic relaxation and reduced elastic stress development. The increased viscoelastic response causes more stress to be relaxed and the decreased elastic stress was due to the reduced early-age modulus of elasticity causing less stress per unit of strain. Both the viscoelastic response and elastic response combine to reduce the early-age compressive stress.

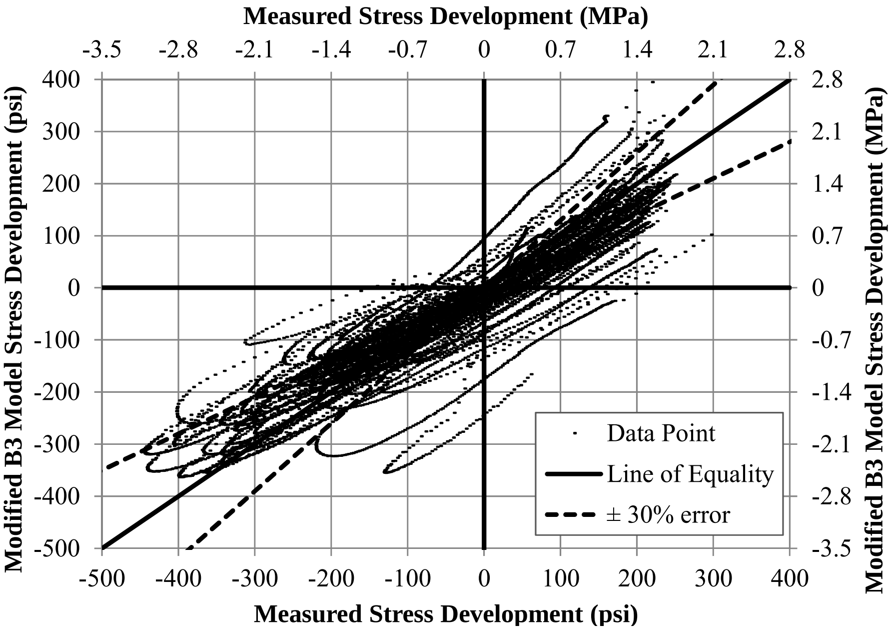

Figure 5.13: Measured vs. Modified B3 modeled stress development.

The later-age tensile stress prediction from the Modified B3 Model was also improved. The increased early-age compressive stress response decreased the time to zero stress—which causes modeled tensile stresses to develop earlier—and provide a much improved estimate of the later-age tensile stress development. The improvement in goodness of fit between the Modified B3 Model as compared to the unmodified B3 Model is quantified in Table 5.4. The R2 of the whole data set improved from 0.59 to 0.80 and the Sj from all the data improved from 0.78 MPa (113 psi) to 0.42 MPa (60 psi). This improvement in R2 and Sj quantifies that the Modified B3 Model provides an improved fit to the measured data when compared to the original B3 Model.

The viscoelastic and elastic correction factor constants q5 and q6 are plotted versus the initial setting time in equivalent age in Figure 5.14. The values of these constants were generally similar to the initial setting time as illustrated in the figure. When the viscoelastic and elastic correction factor constants are near setting, their responses are the highest possible and these values seem to accurately account for the modifications required to the B3 Model. If testing cannot be performed to determine the best-fit values for q5 and q6, then the equivalent age at initial set could be used to apply the Modified B3 Model to estimate the stress development (Byard, 2011).

Table 5.4: Coefficient of determination (R^2) and unbiased estimation of standard deviation (S_j) for the B3 Model and Modified B3 Model.

Mixture	R^2		S_j psi, (MPa)		q_5 (eq days)	q_6 (eq days)	Initial Set (eq days)	Final Set (eq days)
	ModifiedB 3 Modeled	B3 Modeled						
University of Texas at Austin								
1	0.74	0.69	47	61	0.17	0.26	0.26	0.35
2	0.31	0.31	55	94	0.35	0.38	0.42	0.50
3A	0.91	0.95	38	29	0.00	0.21	0.21	0.26
3C	0.17	0.22	119	115	0.05	0.16	0.21	0.26
4	0.85	0.87	40	39	0.04	0.18	0.21	0.27
5A	0.58	0.33	44	85	0.28	0.28	0.28	0.38
5B	0.88	0.55	31	87	0.28	0.28	0.28	0.35
5C	0.98	0.89	18	43	0.15	0.28	0.28	0.34
6	0.84	0.91	23	17	0.00	0.26	0.26	0.39
7	0.40	0.22	61	115	0.26	0.26	0.26	0.33
9A	0.93	0.94	31	28	0.00	0.15	0.21	0.30
9B	0.91	0.49	30	108	0.21	0.21	0.21	0.30
9C	0.63	0.64	108	107	0.00	0.21	0.21	0.30
12Aa	0.96	0.81	22	58	0.15	0.17	0.21	0.28
12Ab	0.92	0.89	38	50	0.06	0.20	0.20	0.26
12B	0.23	0.15	71	138	0.21	0.21	0.21	0.28
12C	0.79	0.81	82	75	0.00	0.21	0.18	0.26
12D	0.99	0.97	20	32	0.06	0.17	0.21	0.27
12E	0.99	0.46	16	189	0.21	0.21	0.21	0.30
14	0.88	0.72	36	69	0.23	0.20	0.23	0.30
15	0.41	0.27	51	96	0.27	0.27	0.27	0.30
15A	0.44	0.47	81	79	0.00	0.21	0.21	0.26
15B	0.31	0.23	33	68	0.27	0.25	0.27	0.30
15C	0.57	0.62	52	55	0.14	0.27	0.27	0.33
15D	0.94	0.53	29	124	0.26	0.26	0.26	0.32
15E	0.54	0.13	51	204	0.27	0.27	0.27	0.30
16	0.96	0.81	22	58	0.15	0.17	0.21	0.28
16	0.91	0.56	30	95	0.26	0.21	0.26	0.30
17	0.92	0.76	30	60	0.21	0.21	0.21	0.28
19	0.85	0.62	41	84	0.21	0.21	0.21	0.26
20A	0.92	0.96	38	28	0.00	0.21	0.21	0.28
20C	0.50	0.33	66	109	0.21	0.21	0.21	0.28
20D	0.38	0.21	102	179	0.21	0.21	0.21	0.28
20E	0.27	0.12	152	288	0.21	0.21	0.21	0.28
21A	0.76	0.98	50	21	0.25	0.25	0.25	0.31

Mixture	**R^2**		**S_j psi, (MPa)**		**q_5 (eq days)**	**q_6 (eq days)**	**Initial Set (eq days)**	**Final Set (eq days)**
	ModifiedB3 Modeled	**B3 Modeled**						
40C	0.92	0.87	34	44	0.00	0.29	0.29	0.40
40D	0.92	0.88	39	52	0.18	0.21	0.21	0.27
40E	0.94	0.65	29	91	0.15	0.15	0.15	0.18
41	0.83	0.80	20	25	0.21	0.21	0.21	0.26
42	0.67	0.62	35	45	0.26	0.26	0.26	0.38
46	0.99	0.97	12	19	0.01	0.21	0.21	0.29
47A	0.90	0.67	30	73	0.20	0.21	0.21	0.26
47B	-0.01	0.03	100	141	0.15	0.15	0.15	0.18
Auburn University								
12a	0.91	0.83	38	60	0.12	0.16	0.16	0.23
12B	0.18	0.09	110	209	0.16	0.15	0.16	0.23
12C	0.80	0.89	85	61	0.16	0.16	0.16	0.23
12D	0.97	0.87	35	87	0.16	0.16	0.16	0.23
12E	0.94	0.50	45	181	0.16	0.11	0.16	0.23
21	0.03	0.08	81	163	0.37	0.22	0.37	0.50
22	0.33	0.16	62	162	0.33	0.17	0.33	0.42
23A	0.79	0.43	42	109	0.26	0.19	0.26	0.34
23C	0.84	0.95	53	30	0.25	0.25	0.25	0.44
23D	0.89	0.68	48	102	0.25	0.17	0.25	0.37
23E	0.82	0.41	66	188	0.26	0.20	0.26	0.34
24A	0.40	0.20	46	109	0.32	0.32	0.32	0.42
24B	0.96	0.37	9	64	0.23	0.32	0.32	0.42
24C	0.80	0.68	46	68	0.32	0.32	0.32	0.42
24D	0.85	0.43	43	135	0.32	0.32	0.32	0.42
24E	0.62	0.23	57	165	0.36	0.33	0.37	0.47
25	0.30	0.11	64	187	0.41	0.41	0.41	0.69
26	0.61	0.33	45	109	0.33	0.31	0.33	0.41
27	0.13	0.32	215	100	0.44	0.43	0.65	0.84
29	0.97	0.69	31	120	0.15	0.10	0.15	0.28
31	0.73	0.69	50	64	0.16	0.15	0.16	0.24
32	0.82	0.55	37	78	0.18	0.18	0.18	0.24
33A	0.59	0.74	93	75	0.16	0.16	0.16	0.23
33B	0.15	0.11	108	206	0.16	0.16	0.16	0.23
33C	0.86	0.86	46	48	0.16	0.16	0.16	0.23
33D	0.85	0.89	71	63	0.16	0.16	0.16	0.23
33E	0.91	0.54	55	180	0.16	0.16	0.16	0.23
All Data Points	0.80	0.59	60 (0.42)	113 (0.78)	-	-	-	-

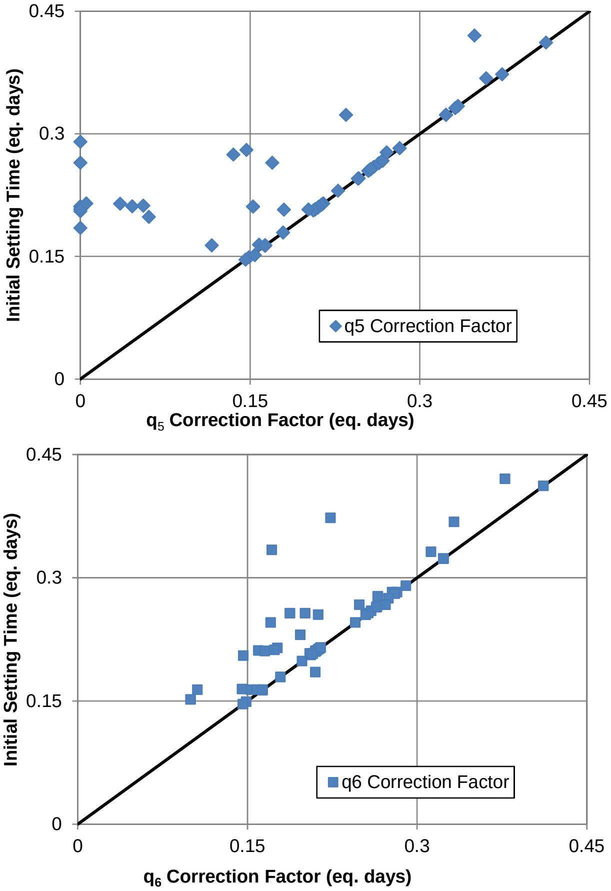

Figure 5.14: a) Viscoelastic and b) elastic correction factor constantans versus initial setting time in equivalent age.

5.4 Conclusions

Early-age compliance modeling of concrete was examined in this chapter. This was accomplished by measuring the early-age stress development of concrete with varying cementing materials, aggregate types, water-cement ratios, and temperature histories. The measured stress development was compared to the stress development predicted by the B3 compliance model (Bažant and Baweja, 2000). The B3 compliance model did not adequately predict the response of the concrete at early ages due to a lack of viscoelastic response and much too high elastic stress development estimated by the model. Modifications were made to the B3 Model to better account for the early-age viscoelastic and elastic response typical for concrete at early ages. The results presented in this chapter support the following conclusions:

- The B3 Model underestimates the early-age relaxation response.
- A viscoelastic modifying term (q_5), introduced by Østergaard et al. (2001) and shown in Equation 5.6, more accurately accounts for the high amount of relaxation of concrete at early ages.
- The constant asymptotic modulus of the B3 Model leads to high early-age elastic stress development compared to measured stress development. A proposed elastic

response modifying term (q_6), shown in Equation 5.5, more accurately accounts for the changing stiffness of early-age concrete.

- The early-age modifications recommended in the Modified B3 Model have diminishing effectiveness with time and the later-age predictions are virtually unchanged with regards to the original B3 Model.
- The contribution of the elastic and viscoelastic components of the Modified B3 Model provides a better fit, increases the coefficient of determination from 0. 59 to 0.8, and decreases the unbiased estimation of standard deviation of absolute error from 0.78 MPa (113 psi) to 0.42 MPa (60 psi) for the complete data set when compared to measured stress development at early ages.

Chapter 6. Evaluation of Early Tensile Strength of Concrete

6.1 Introduction

Predicting early-age tensile strength of concrete is important in determining whether tensile stresses due to plastic shrinkage will cause cracking. These experiments investigate the effect of w/c, SCMs, and aggregate type on the tensile strength of concrete from initial set of concrete up to 28 days.

6.2 Tensile Testing Setup

The tensile testing setup used in this experiment is based off of same device used by Abel and Hover (1998). The apparatus consists of a two-part mold used to test the tensile capacity of early-age concrete. Figure 6.1 shows the mold used for the direct tension testing. A few modifications to the original setup by Abel and Hover are explained in this section.

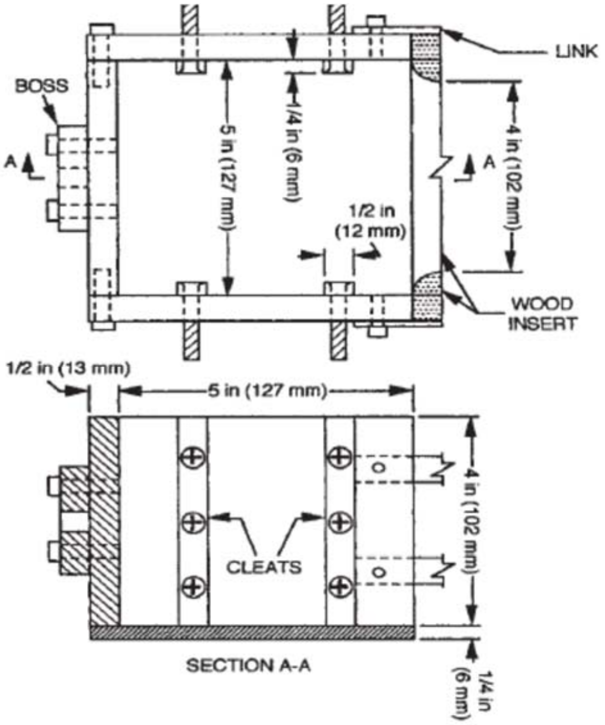

Figure 6.1: Mold used for direct tension.

Abel and Hover originally used wooden dowels to reduce the cross section; however for this experiment we needed early-age tensile strength data up to 24 hours after mixing. Therefore, a larger PVC dowel was used to decrease the cross section and allow for higher stresses to be achieved (shown in Figure 6.2).

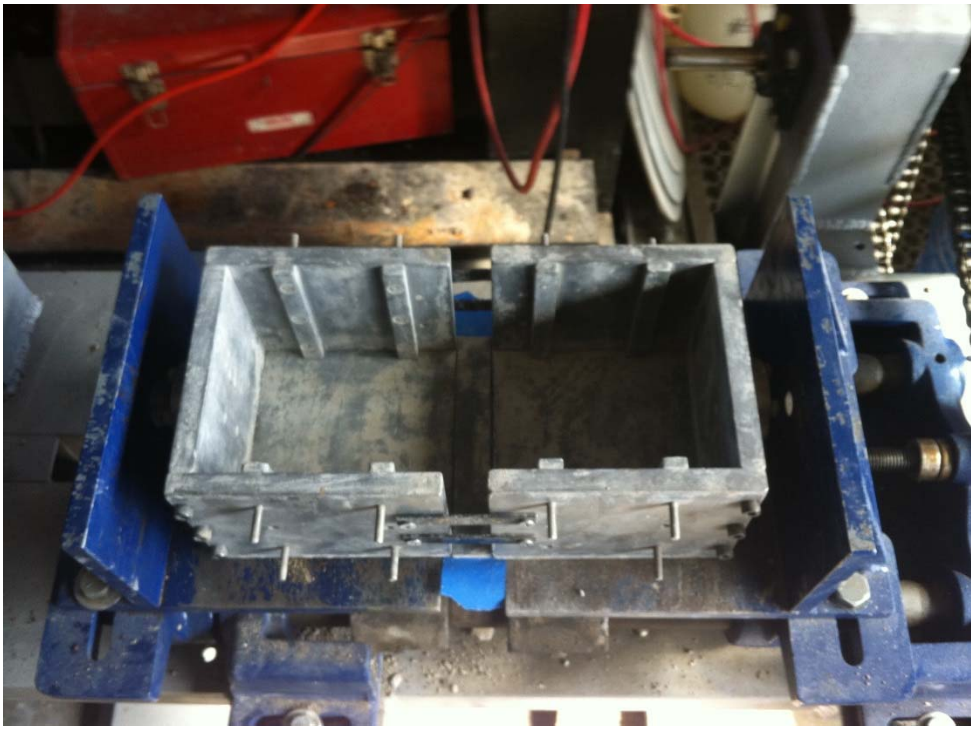

Figure 6.2: Direct tensile mold with PVC dowels.

Additionally, Abel and Hover’s load frame was modified to include an automated motor. This automated motor displaces the mold halves at a constant rate of 0.03 in. per minute. During Abel and Hover testing, testing loads of more than 1.4 kips were captured, which caused the longitudinal supports to tilt, further causing a moment on the concrete specimen. The new tensile setup eliminated this problem by adding vertical bracing to the longitudinal supports. A brass bearing is placed under the vertical support to help reduce friction. The remaining aspects of Abel and Hover’s tensile testing rig remained unchanged. The new tensile testing setup is shown in Figure 6.3.

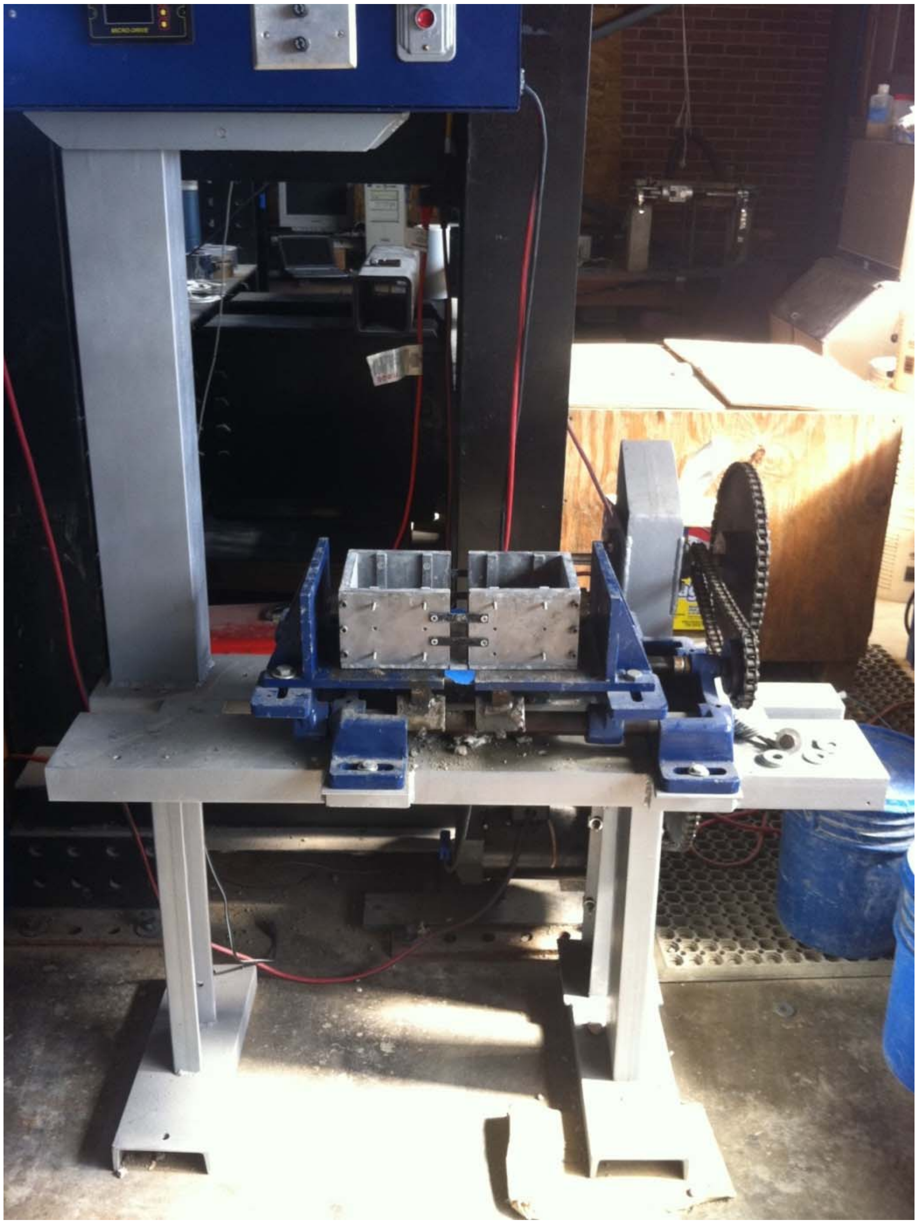

Figure 6.3: Tensile testing rig.

6.3 Concrete Mixture Design

A wide range of concrete mixtures were designed to evaluate the performance of w/cm, SCMs, and aggregate type on the prediction of early tensile strength. Table 6.1 provides the mixture designs.

Table 6.1: Concrete mixture proportions.

Mix ID	Cement (pcy)	SCM (pcy)	Water (pcy)	Coarse Aggregate (pcy)	Fine Aggregate (pcy)	SCM Tyoe	Coarse Aggregate Type	Fine Aggregate Type
C1L-RG	564	-	254	1941	1232	-	SRG	SNS
C1L-RG 0.4w/c	611	-	254	1941	1232	-	SRG	SNS
F1L-25RG	423	141	254	1914	1215	F	SRG	SNS
F1L-35RG	367	197	254	1923	1220	F	SRG	SNS
F4L-25RG	423	141	254	1920	1219	C	SRG	SNS
GL-35RG	367	197	254	1932	1226	GGBFS	SRG	SNS
GL-50RG	282	282	254	1928	1223	GGBFS	SRG	SNS
C1L-LS	564	-	254	1922	1220	-	CL	SNS

- GGBFS = Ground Granulated Blast Furnace Slag
- F = ASTM C 618 Class F Fly Ash
- C = ASTM C 618 Class C Fly Ash
- SRG = Siliceous River Gravel
- SNS = Siliceous Natural Sand
- CL = Crushed Limestone

6.4 Testing Procedure

Prior to mixing, materials and molds were stored at laboratory ambient conditions for 24 hours.

6.4.1 Concrete Placement and Testing

After the concrete was mixed, the fresh concrete was placed in two lifts using 25 rods on each lift into the early tensile mold. The concrete was struck off using wooden float and the PVC dowels were checked to ensure they were vertical. For each concrete mixture, seven early-age molds were cast and tested. In addition 10, 4 x 8in. cylinders were cast for after initial set splitting tensile testing. The specimens were stored under a plastic sheet at ambient laboratory conditions. To determine when the first early age specimen would be tested, a time-of-set can was used to determine initial and final set times. When initial set was reached, the first specimen was loaded onto the frame and a load cell was attached, and the machine was turned on to begin operation. It ran until a peak load was reached. At final set another specimen was tested. Four specimens were tested approximately every hour after final set. For lower strength specimens a 500 lb capacity load cell was used. For higher strength specimens a 5,000 lb capacity load cell was used. The final seventh mold was tested at 24 hours along with two splitting tensile cylinders. The splitting tensile testing took place at 1, 3, 5, 7, and 28 days.

6.5 Test Results

Results from the tensile strength tests are plotted in Figures 6.4 through 6.6. The plots show tensile strength development versus time after mixing. The overall tensile strength development occur the quickest in mixtures without any SCM's. There is not a significant difference in early tensile strength development between aggregate types. The limestone aggregate mixture has a slightly higher strength development.

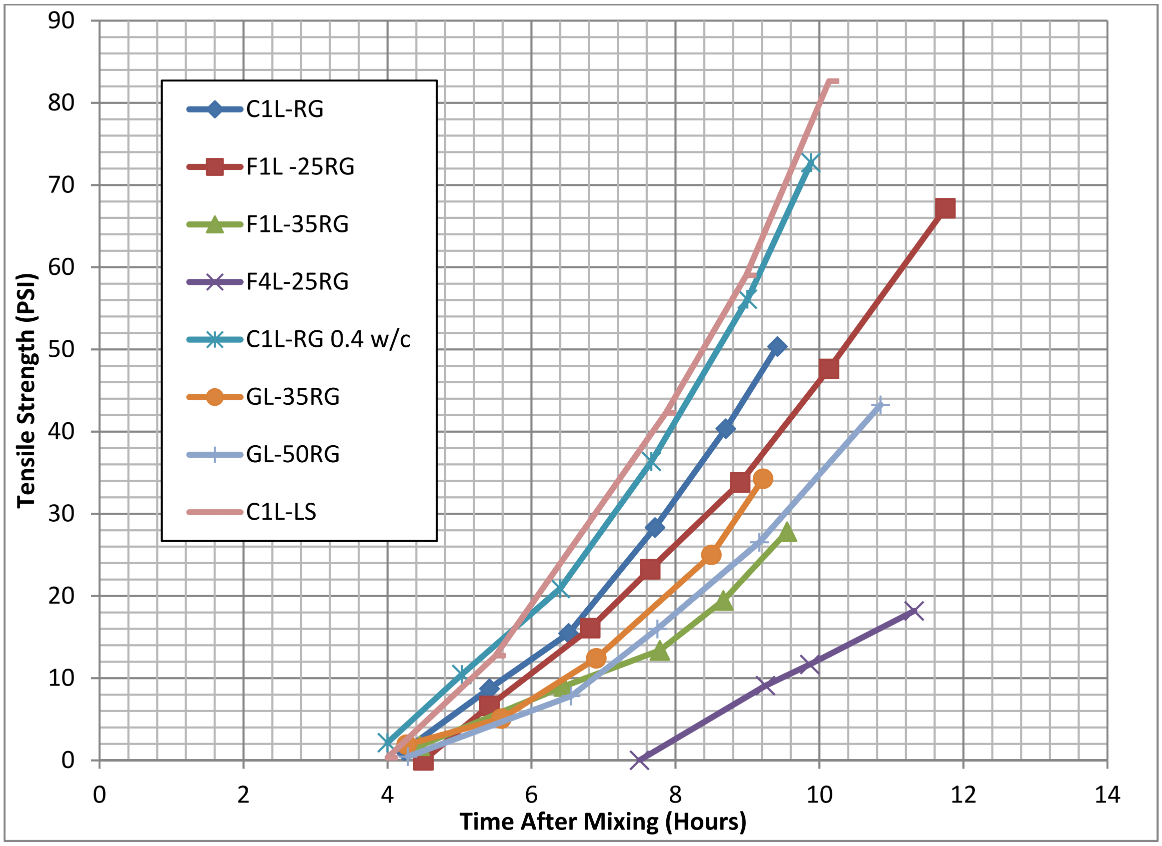

Figure 6.4: Tensile strength results up to 12 hours.

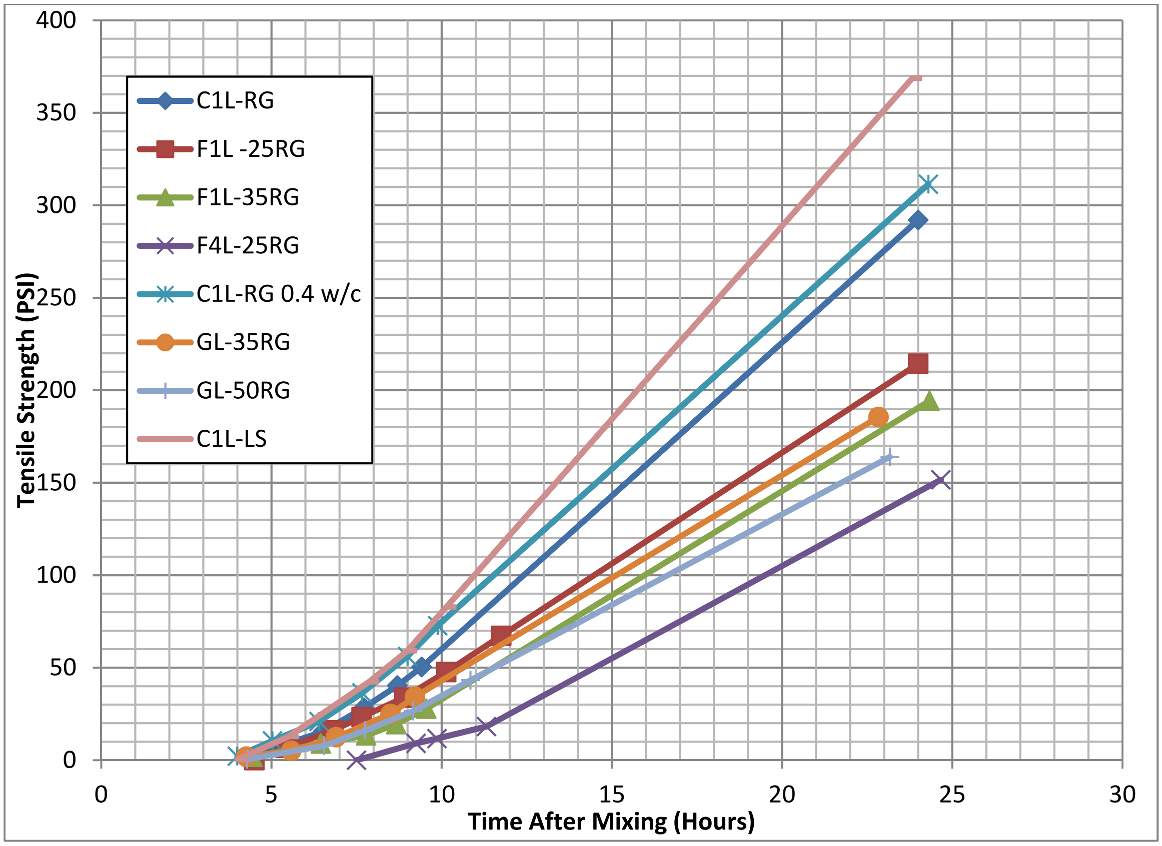

Figure 6.5: Tensile strength results up to 24 hours.

At 24 hours splitting tensile tests were conducted, Figure 6.6 shows the comparison between 24-hour direct tension and splitting tensile testing. A good correlation occurs between both testing methods at 24 hours. A larger error does occur for higher tensile strength mixtures at 24 hours. The failure type between direct tension specimens changed with strength development. During the first two breaks, the specimen usually exhibited ductile like behavior. The crack development in the specimen could be observed and generally failed along the aggregates. Later-age specimens typically failed at the PVC cross section. Inspection of later-age specimens after peak load was reach also revealed failure around the aggregates, at 24 hours the specimens were shown to fail through the aggregates.

Straight cement mixtures experienced quicker strength gain than SCM mixtures. C1L-LS had the quickest strength gain followed by the C1L-RG 0.4 w/c. The F1L-25RG preformed best out of the SCM mixtures. F4L-25RG had the worst early-age strength development. Splitting tensile testing was conducted at 1, 3, 5, 7, and 28 days and shown in Figure 6.7 and 6.8.

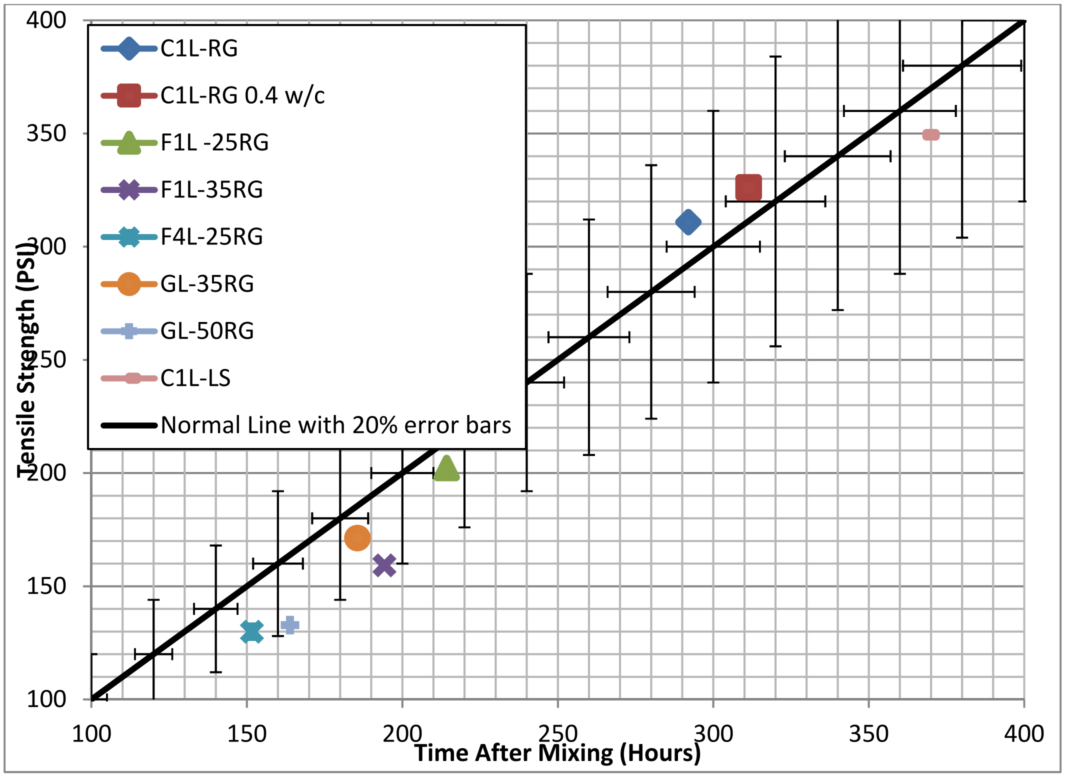

Figure 6.6: Tension versus splitting tensile comparison.

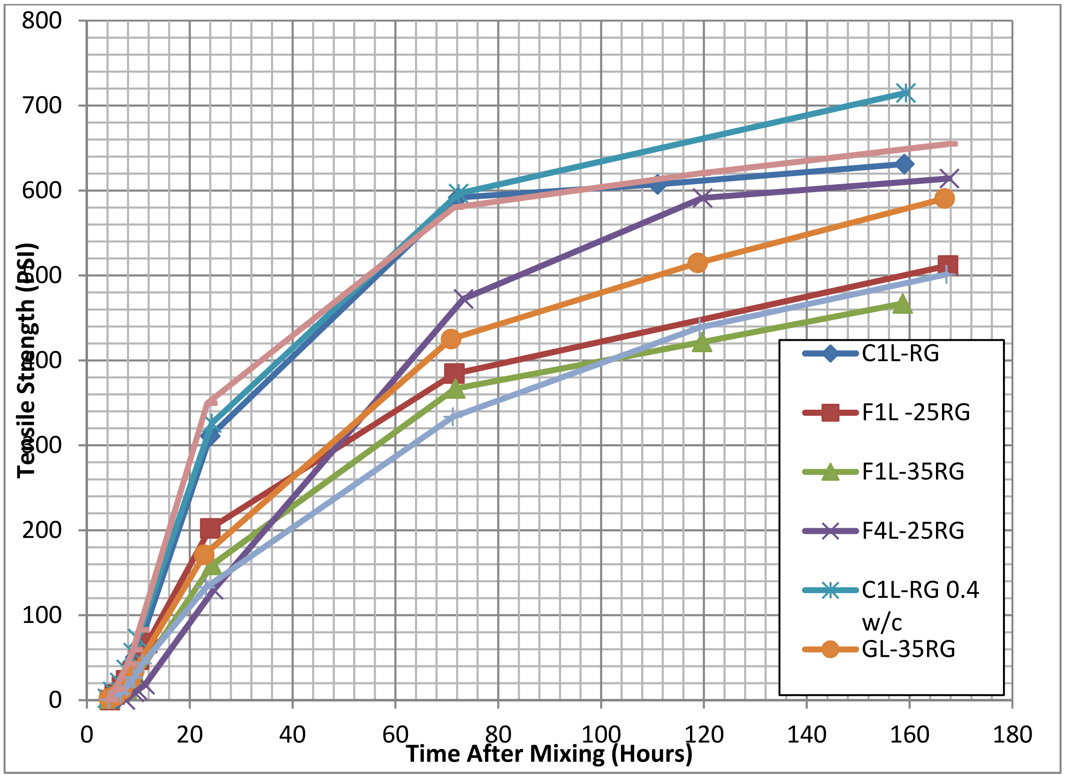

Figure 6.7: Tensile strength development up to 7 days.

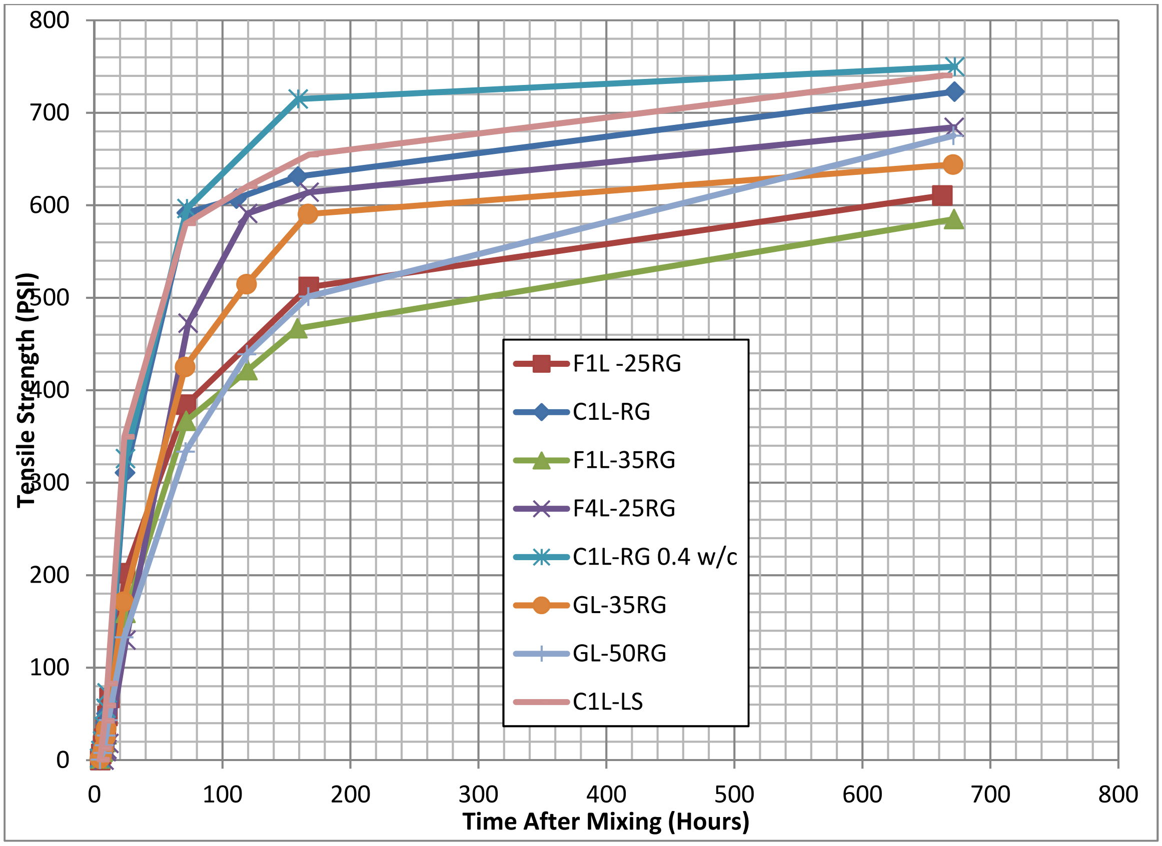

Figure 6.8: Tensile strength development up to 28 days.

Chapter 7. Field Testing Program

Chapter 7 covers the six Texas bridge decks that the research team instrumented. At each pour, multiple temperature sensors were placed in the concrete, semi-adiabatic testing was conducted on the field concrete, and mechanical testing specimens were collected. After the pours were completed, the research team evaluated the performance of their testing procedures, and made adjustments to ensure better data collection in the future.

7.1 San Antonio Bridge Deck

The first bridge deck that the research team instrumented was in San Antonio at Ingram Road and Interstate 410. The bridge deck consisted of 8 in. of cast-in-place concrete on metal pan formwork, supported by steel beams. The pour began on July 19, 2009 at 9:40 p.m., and ended on July 20, 2009 at 1:40 a.m. Information gained from this field instrumentation included temperature data from July 19 to July 31, two sets of semi-adiabatic calorimetry data, and mechanical testing results.

7.1.1 Structural Plans for San Antonio Bridge Deck

The San Antonio bridge deck was an 8in. cast-in-place concrete bridge deck, formed with steel pans, and supported by steel beams. A typical cross section and the elevation of the bridge deck are presented in Figure 7.1 and Figure 7.2. Additional structural plans, specifically those that detail the span lengths and widths, can be found in Appendix B.

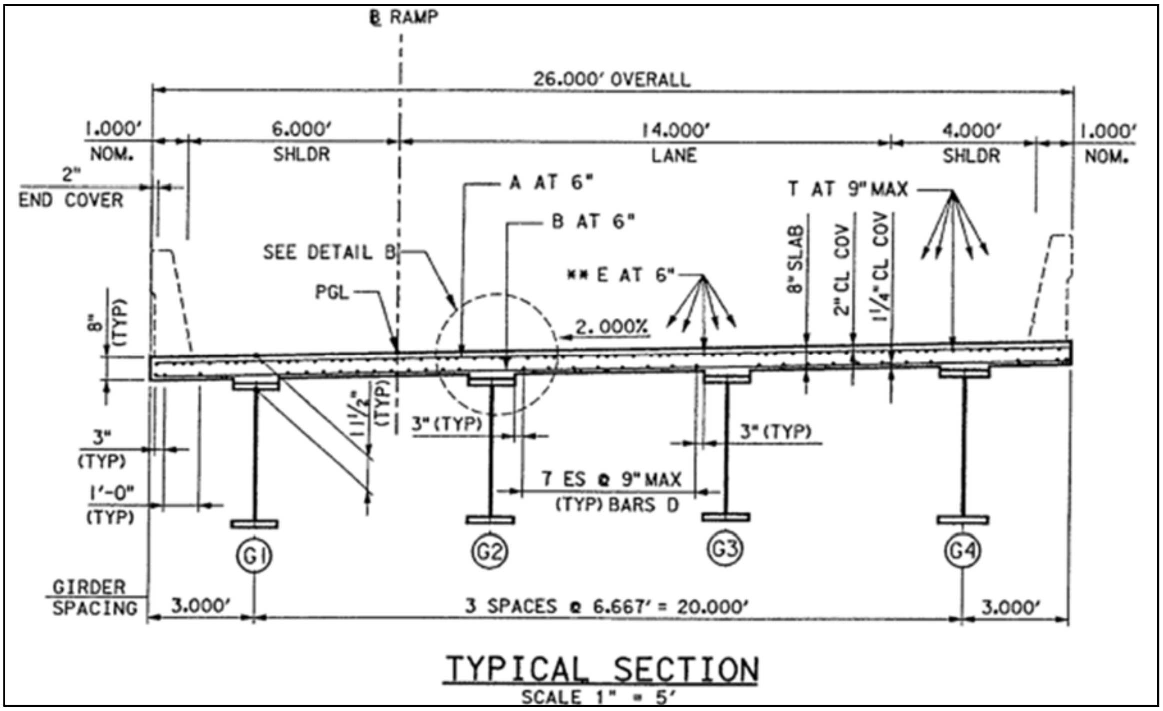

Figure 7.1: San Antonio bridge deck typical section.

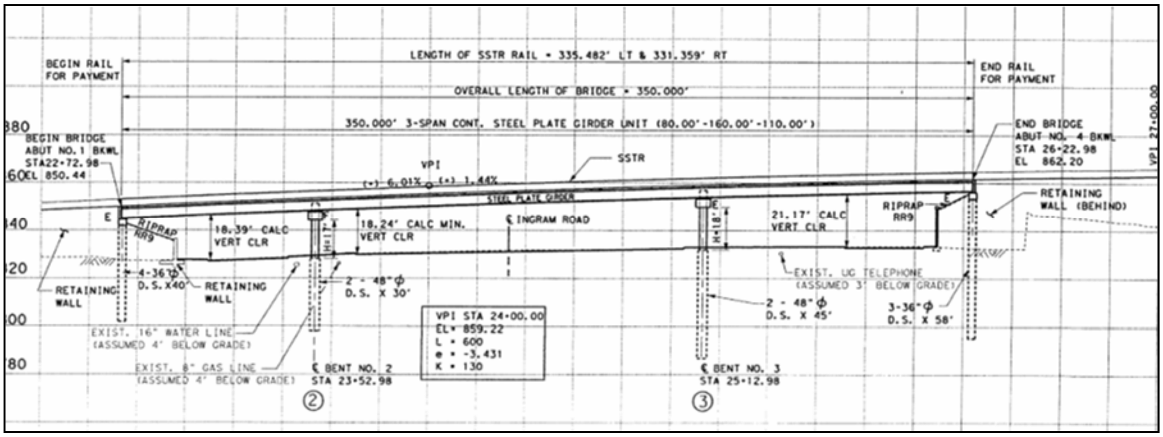

Figure 7.2: Elevation of San Antonio bridge deck.

7.1.2 Materials and Mixture Design of San Antonio Bridge Deck

The mixture design for the San Antonio bridge deck is presented in Table 7.1. The mixture designs were acquired from the batch tickets that were collected throughout the pour. Information was not collected on the cement or fly ash type. The San Antonio bridge deck pour used approximately 1in. maximum-size-aggregate (MSA) limestone. Information from the batch ticket indicates that this was most likely a TxDOT Gr. 4 coarse aggregate. River sand was used as the fine aggregate.

Table 7.1: Mixture design for San Antonio bridge deck.

	Cement lb/yd^3	Fly Ash lb/yd^3	Water lb/yd^3	Ice lb/yd^3	Coarse lb/yd^3	Fine lb/yd^3	WR2 oz/yd^3
First Truck	489	122	188	80	1822	1330	23
Mid Mix	489	122	188	100	1822	1330	19
End of Mix	489	122	188	100	1822	1330	15

7.1.3 Instrumentation and Testing of San Antonio Bridge Deck

The layout of the iButton instrumentation is provided in Figure 7.3 and Figure 7.4. Strands A and D were used to evaluate the difference in temperature development at the beginning of the pour with that at the end of the pour. Strands B and C had buttons strings that were located in the middle of width of the deck, on the deck overhang, and over the girders on the bridge deck. Further information on the iButton locations and depths can be found in Appendix B.

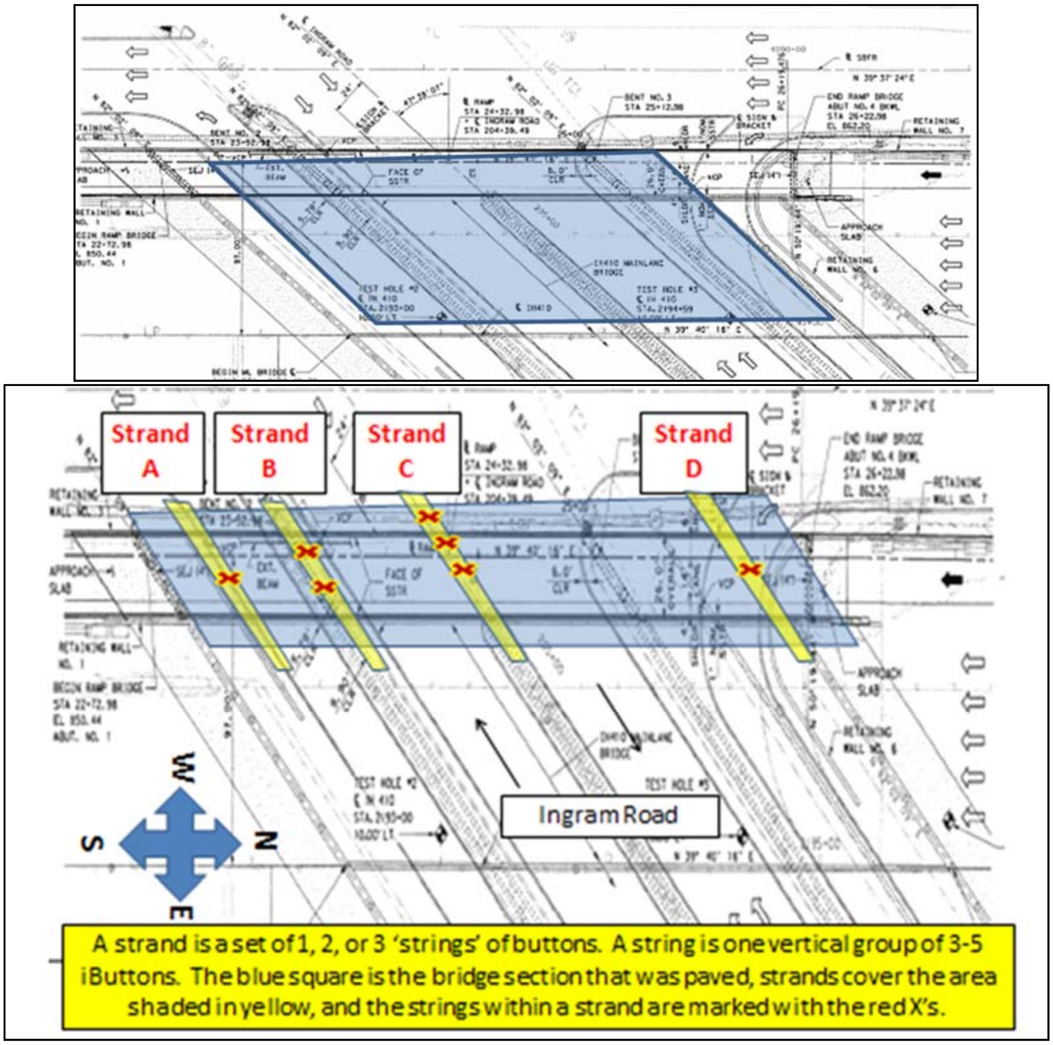

A strand is a set of 1, 2, or 3 'strings' of buttons. A string is one vertical group of 3-5 iButtons. The blue square is the bridge section that was paved, strands cover the area shaded in yellow, and the strings within a strand are marked with the red X's.

Figure 7.3: iButton strand layout for San Antonio bridge deck.

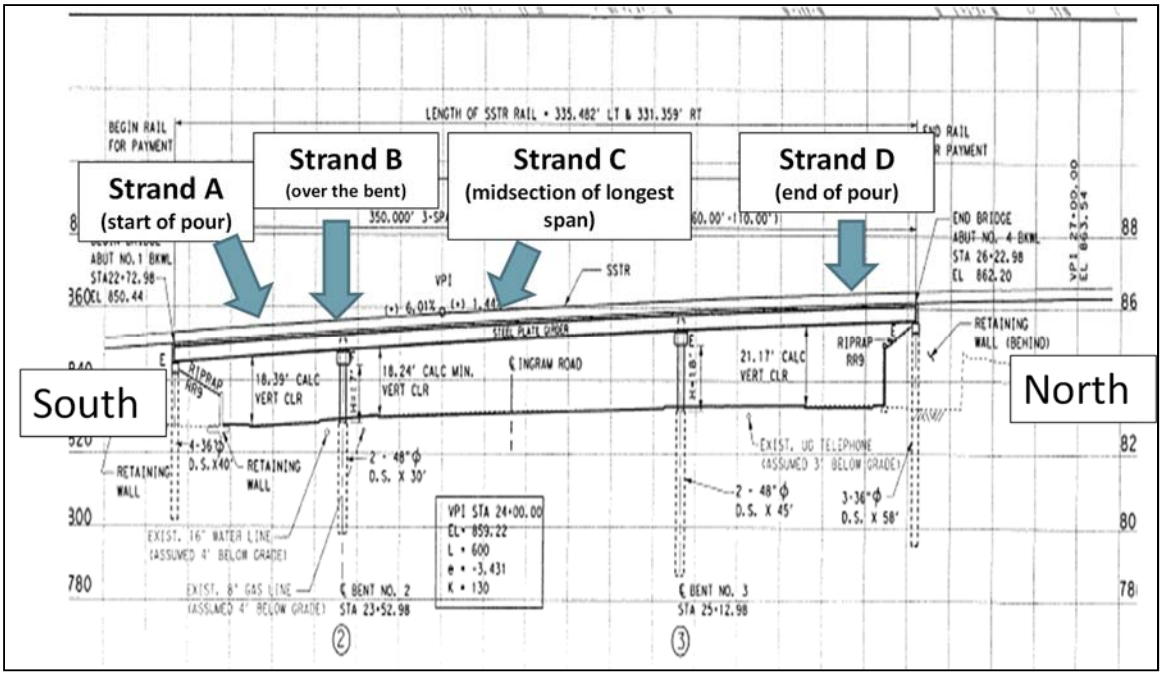

Figure 7.4: iButton strand layout for San Antonio bridge deck.

The San Antonio bridge deck provided the research team with their first experience at instrumentation using iButtons embedded in concrete for extended periods. To ensure that the iButtons would not be corrupted, they had to be sealed before they could be embedded in concrete. This was accomplished by covering the iButtons in a two-part epoxy before they were attached with plastic ties to the plastic rod. In addition, to reduce the number of wires that would be required to collect data from the iButtons, a single two-conductor wire was soldered to each iButton, connecting all the iButtons on a given string. The wires were then run transversely across the deck, and labeled for later data collection. A typical four-button iButton string for the San Antonio bridge deck is shown in Figure 7.5.

Figure 7.5: iButton strings for San Antonio bridge deck.

Approximately 12 hours after the pour began, the research team returned to the bridge deck for the first set of data collection. At this point, the iButtons were reset to have a longer time interval between measurements, and the buttons were left to continue recording. It was noted at this point that the curing method that was in place was black plastic sheeting directly on top of the concrete, as shown in Figure 7.6. In later discussions, TxDOT reported that the practice of using black plastic was no longer allowed, but that due to the early date at which the construction contract was granted, the construction firm was not forbidden from using black plastic. The use of black plastic during the summer, combined with the placement time of the concrete, led to substantially high temperatures in the first temperature peak. This can be seen further in the temperature data in the next section.

Figure 7.6: Curing method for San Antonio bridge deck.

Two more trips were made to the bridge deck to collect data later. On the last data collection trip, the research team inspected the bridge deck to see if any early-age cracking could be found. While some "crack-like" lines were found at regularly spaced intervals running transversely across the bridge deck between tining grooves, shown in Figure 7.7, it could not be concluded that they were in fact early-age cracking. The research team reasoned that these "cracks" were more likely the effect of a twisted or broken tine on the tining rake.

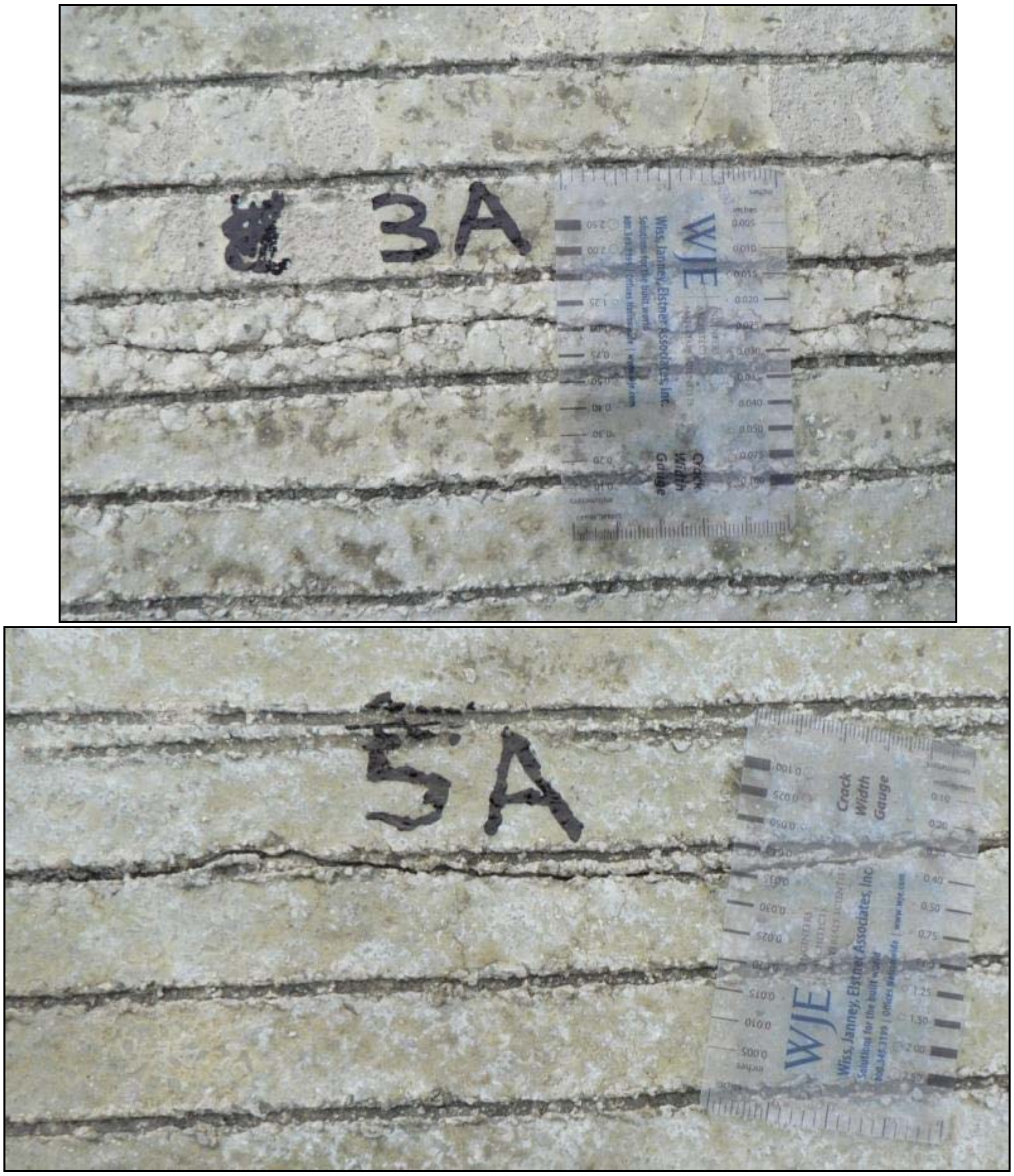

Figure 7.7: Crack-like lines on San Antonio bridge deck.

7.1.4 San Antonio Bridge Deck Results

San Antonio Bridge Deck Recorded Temperatures

This section presents temperature data from the middle of the pour, in the middle of the bridge deck, for the bridge decks that were instrumented. A complete set of temperature data is in Appendix B—the graphs are titled with the bridge deck that was instrumented, the button string being displayed, and the duration of data being presented. Figure 7.8 and Figure 7.9 display the recorded bridge deck temperatures in the middle of the San Antonio bridge deck. The gradient defines the temperature difference between the top and bottom of the bridge deck pour. The San Antonio bridge deck had the highest first peak temperatures of all the mixtures evaluated, likely due to the time of placement and the use of black plastic for curing. The research team was not able to clearly determine, through the data or through communication with the contractor, when the curing plastic was removed from the bridge deck. However, a best guess based on correspondence between the ambient air temperature and the top iButton temperature led to the assumption that the curing plastic was removed on July 29, 2009.

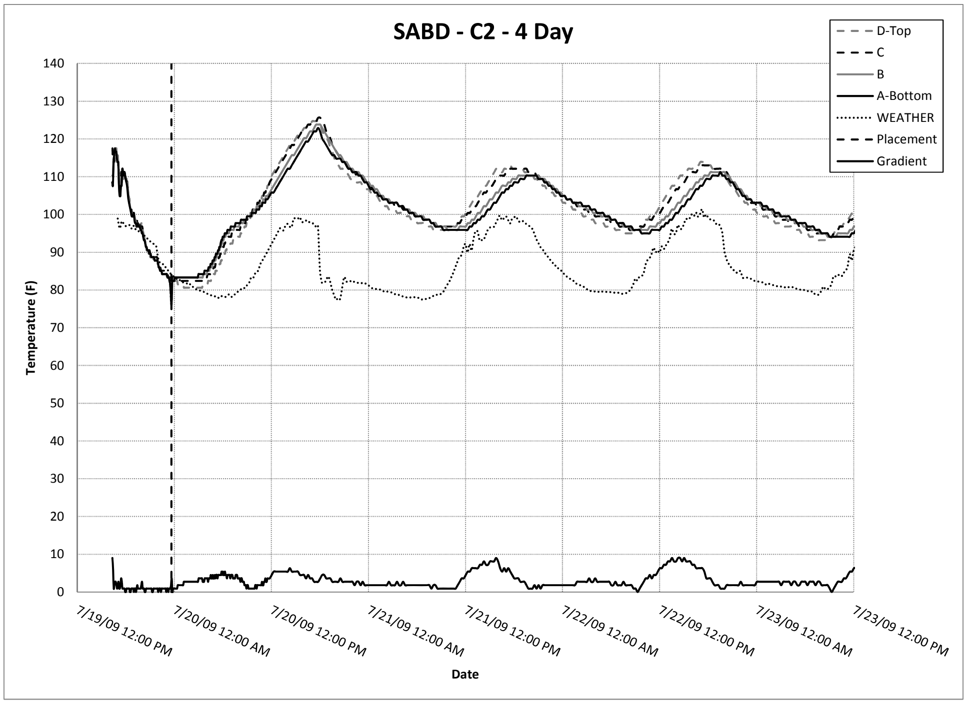

Figure 7.8: Four-day temperature data: SABD—C1.

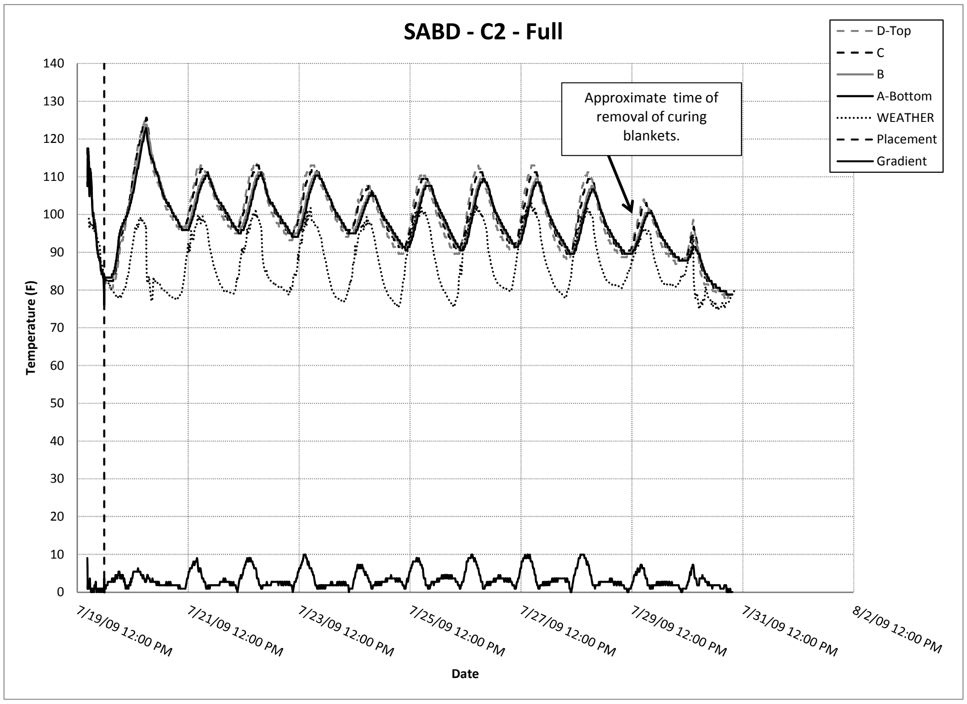

Figure 7.9: Full temperature data: SABD—C1.

Fresh Concrete Properties

Table 7.2 provides the fresh concrete properties that were measured by the research team during casting at the field instrumentation site in San Antonio. All values were confirmed by tests conducted concurrently by a certified TxDOT inspector.

Table 7.2: Fresh concrete properties—San Antonio bridge deck.

Strand	Slump in.	Air Content %
A	2.5	2.4
B	5.5	1.7

Chemical Analyses of Field Testing Materials

Due to safety concerns from the producer, cement, fly ash, admixture, and aggregates were unable to be collected from the San Antonio pour. XRF and Bogue calculation results are presented for the cements and SCMs. Dosages from the batch tickets and physical properties from producer information sheets are provided for the concrete admixtures.

Mechanical Strength Development

Table 7.3 provides the mechanical strength development for the bridge deck mixtures. The choice as to where and when to take cylinders from the field site varied for each site due to decisions made from previous pours, limitations from the contractor, and limitations on what could be transported back to the laboratory.

Table 7.3: Mechanical properties for San Antonio bridge deck.

Test		Strand A	Strand B
12 Hr.	f'c	1,152	1,225
	f'st	--	--
	E	--	--
24Hr.	f'c	2,887	2,887
	f'st	403	403
	E	--	--
2 Day	f'c	3,621	3,375
	f'st	507	506
	E	--	--
3 Day	f'c	--	4,730
	f'st	--	593
	E	--	--
7 Day	f'c	5,968	5,599
	f'st	--	721
	E	--	--
28 day	f'c	7,463	7,676
	f'st	816	843
	E	--	5,025,873
1 Year	f'c	--	8,035
	f'st	--	807
	E	--	5,744,161

All values in psi.

7.2 Georgetown Bridge Deck: Summer Pour

The research team's second bridge deck instrumentation was located in Georgetown, at College Street over the San Gabriel River. The bridge deck consisted of 4in. cast-in-place concrete on top of 4-in. precast, prestressed concrete panels, supported by precast, prestressed concrete girders. The pour began on August 19, 2009 at 4:00 a.m., and concluded at approximately August 19 at 7:00 a.m. Information gathered from this instrumentation included temperature data from August 19 to either August 25 or September 2, depending on when the contractor cut the iButton collection lines, two sets of semi-adiabatic calorimetry data, and mechanical testing results.

7.2.1 Structural Plans for Georgetown Bridge Deck

The Georgetown bridge deck was a 4in. cast-in-place concrete bridge deck, with 4in. precast, prestressed concrete panels supported by precast, prestressed concrete girders. A typical cross section and the elevation of the bridge deck can be seen in Figure 7.10 and Figure 7.11. Additional structural plans, specifically those that detail the span lengths and widths, can be found in Appendix B.

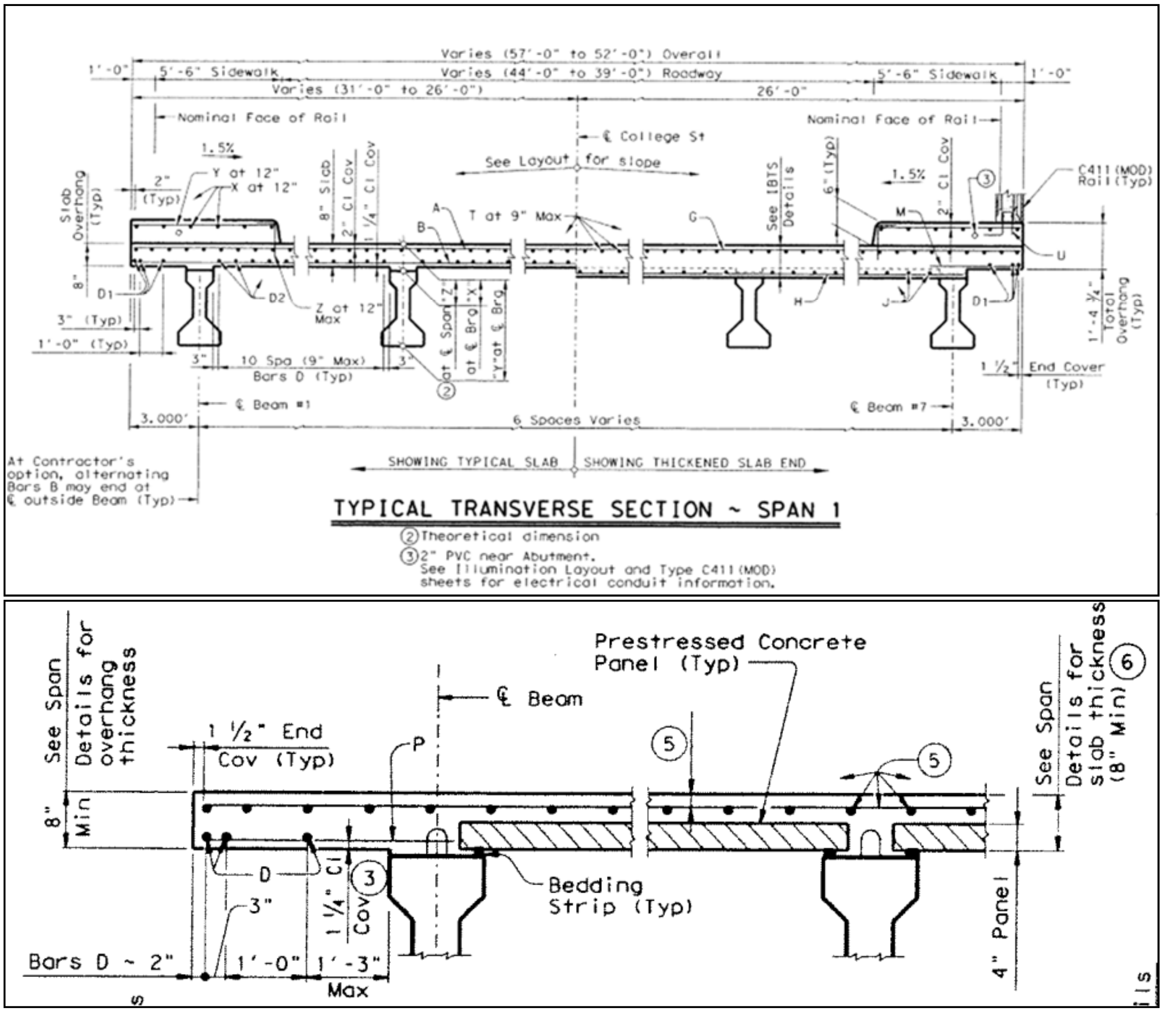

Figure 7.10: Cross section of Georgetown bridge deck: summer pour.

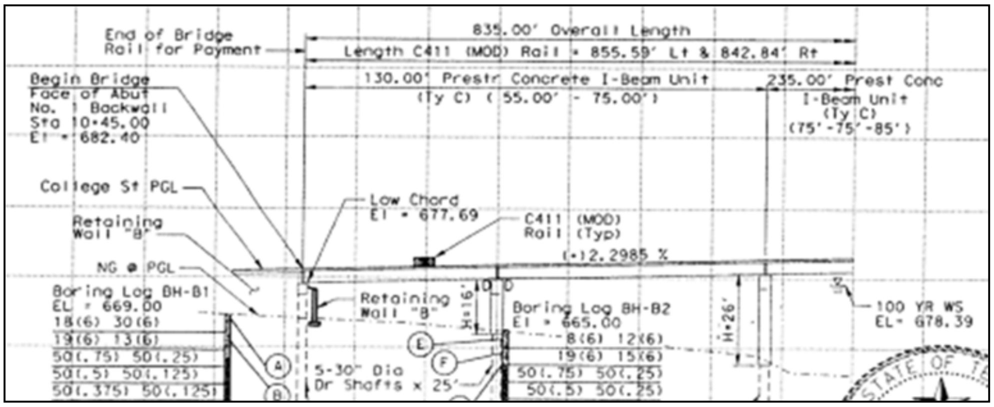

Figure 7.11: Elevation of Georgetown bridge deck: summer pour.

7.2.2 Materials and Mixture Design of Georgetown Bridge Deck

The mixture design, acquired from the batching tickets, for the Georgetown bridge deck summer pour is shown in Table 7.4. A low-alkali cement, ASTM C 618 Class C fly ash, approximately 1in. MSA limestone coarse aggregate, and river sand were used for this mixture design. The research team also noted that approximately halfway through the pour, the use of 70 lb/yd^3 of ice was used (replacing mixture water). It is unknown whether the ice was used at the beginning of the pour as well, or only during the second half. Table 7.4 shows only one mixture design, as no changes were made to the mixture design throughout the pour.

Table 7.4: Mixture design for Georgetown bridge deck summer pour.

Cement lb/yd^3	Fly Ash lb/yd^3	Water lb/yd^3	Coarse lb/yd^3	Fine lb/yd^3	AE oz/yd^3	WR3 oz/yd^3
430	143	257	1758	1267	2.2	22

7.2.3 Instrumentation and Testing of Georgetown Bridge Deck

The layout of the iButton instrumentation is provided in Figure 7.12 and Figure 7.13. Once again, Strands A and D were used to capture changes between the first trucks to arrive to the site, and the last trucks to arrive. Strand B was used to capture temperature data on the middle and East side of the bridge deck, and Strand C was used to capture data on the middle and West side of the bridge deck. In order to better understand the heat transfer between the bridge deck and the underside of the bridge deck, the research team decided to place iButtons underneath the precast panels, and at the middle of the precast panel. iButtons were placed in the middle of the panel by drilling a hole at a 45° into the precast panel, placing the iButton in the middle, then epoxying the hole shut. Both Strand B and C had iButtons located under the bridge deck panels, inside the bridge deck panels, above the panels, above the girders, and above the falsework on the edge of the deck. Further information on the iButton locations and depths can be found in Appendix B.

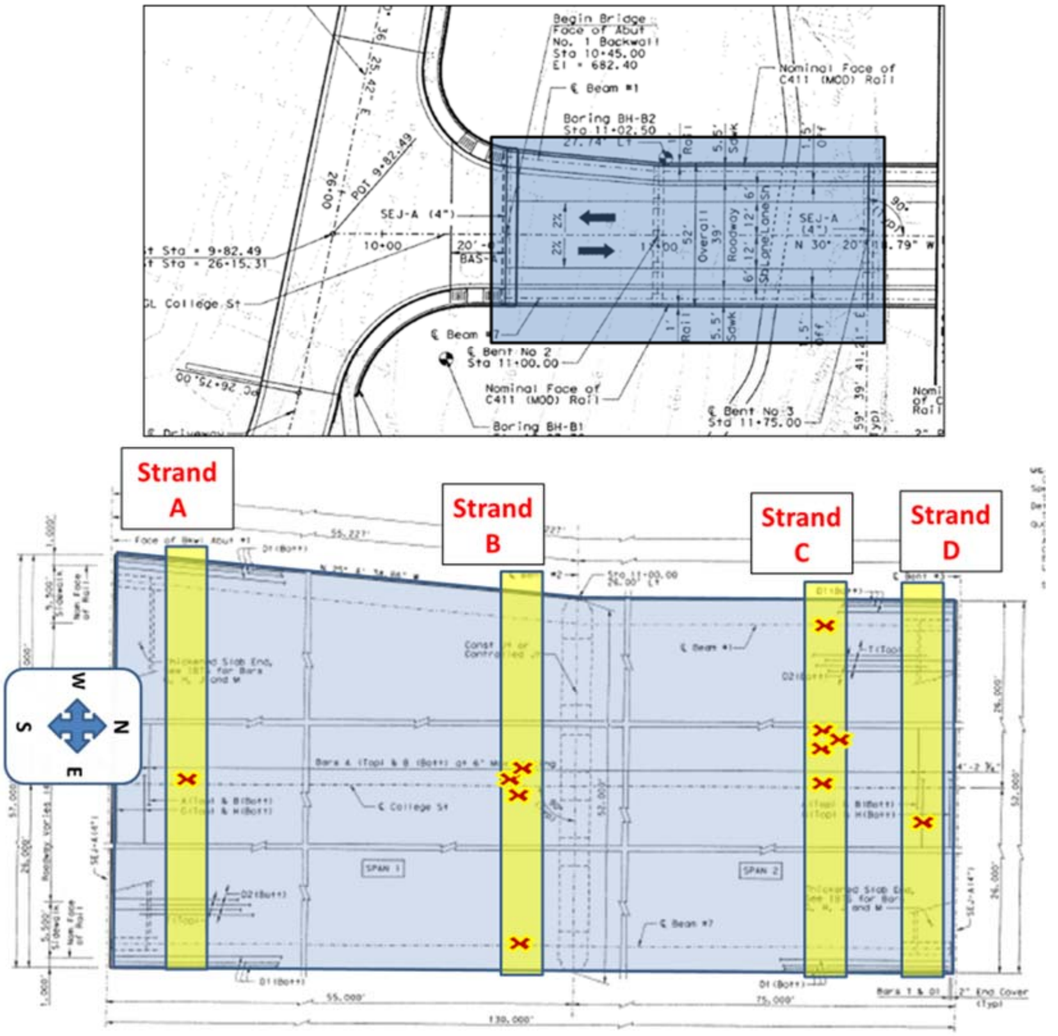

Figure 7.12: iButton string layout for Georgetown bridge deck summer pour.

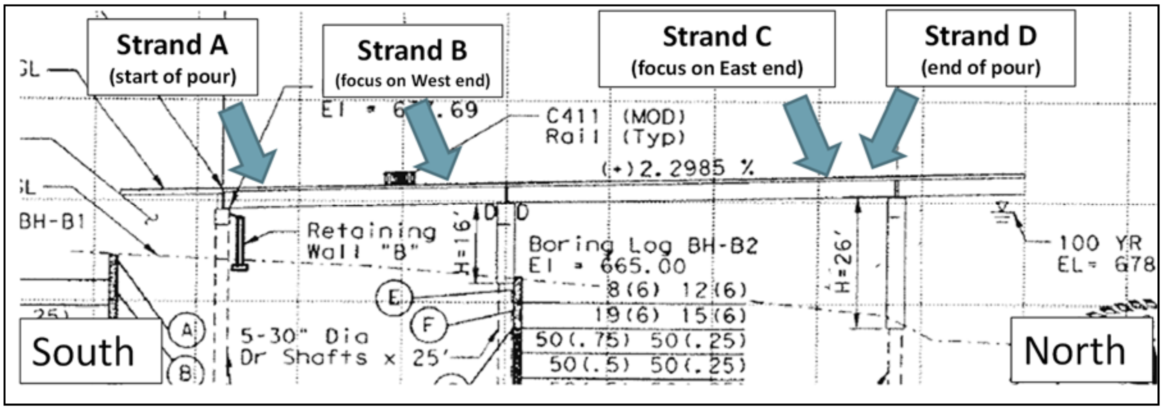

Figure 7.13: iButton strand layout for Georgetown bridge deck summer pour.

On the Georgetown bridge deck summer pour, the research team made some slight modifications to their iButton preparation procedures. As before, a single two-conductor wire was soldered to a string of iButtons, allowing multiple iButtons to be read from one string. A hollow plastic rod had a space cut into it, and then the iButtons were placed into the rod, and held in place with a plastic tie. Two part epoxy was then used to waterproof and protect the iButtons, and to seal the hole at the top of the plastic rod. Rather than floating the iButton plastic rod in the reinforcement cage, as was done in San Antonio, a ¾” hole was drilled into the precast panels, and the bottom of the plastic rod was epoxied into this hole. This method was to prevent the iButton string from twisting out of a vertical orientation, and to provide a more accurate knowledge of the depth of the iButtons after concrete was placed around them. The wires for the iButtons were run transversely across the deck, and over the top of the side formwork. iButton strings from the Georgetown bridge deck summer pour are shown in Figure 7.14.

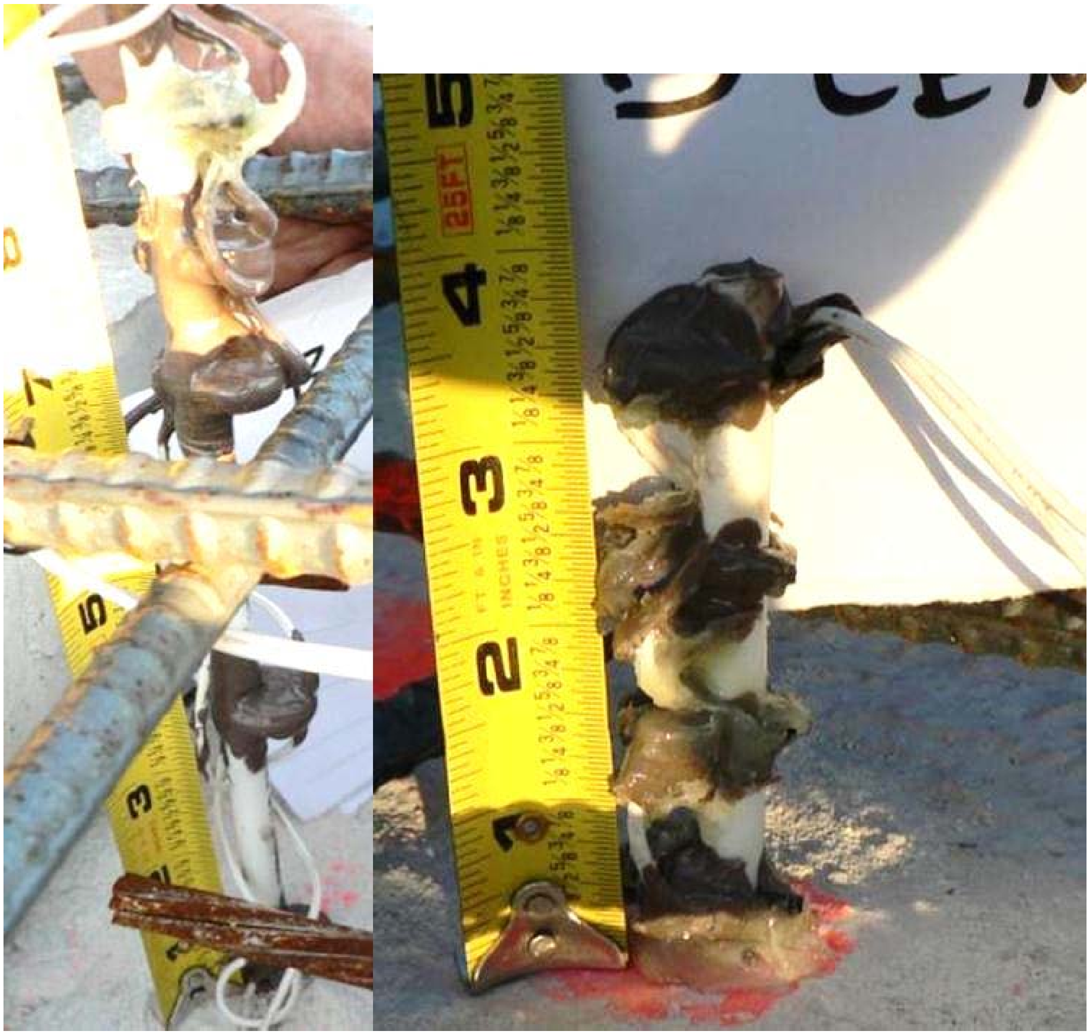

Figure 7.14: iButton strings on Georgetown bridge deck summer pour.

Two days after the pour, the research team returned to the bridge deck for the first data collection. The research team downloaded the data from the last two days, and reset the iButtons with a longer time interval between recordings. The research team also discovered that three of their eight iButton strings, including both of the six-button strings that were placed in the deeper sections over the girder, had been corrupted and could not be read. The research team, after considering various options, deemed that the use of a single two-conductor wire, coupled with having a button wedged against the precast panels, was the culprit in the iButton failures. The bottom button, more than likely, was damaged during the pour. Because the iButtons were connected in series, the failure of one iButton resulted in the inability to collect data from any of the iButtons on that string. The research team decided, for future pours, that a parallel wiring scheme would be used. Each iButton was wired with an independent jumper that went to the common ground wire, and with a separate, individual wire. Using this method, if one iButton were corrupted, either by moisture intrusion or damaging of the solder connection, the rest of the iButton data on the string could still be acquired. The research team also used a naming scheme on all the wiring, such that specific colors were always placed in the same order (silver for ground, red on bottom button, brown on the button above, etc.) to reduce confusion when downloading data from the iButtons. The wiring scheme and examples of the iButton strings are shown in Figure 7.15 and Figure 7.16.

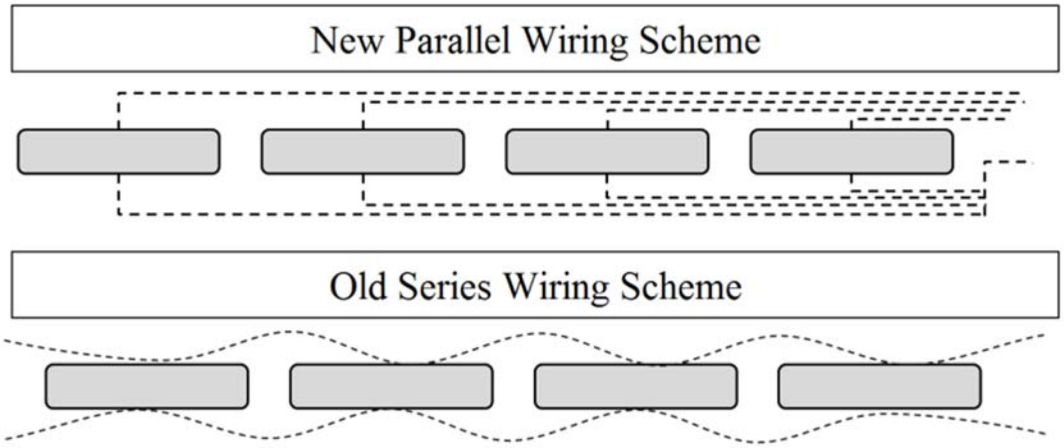

Figure 7.15: New and old iButton wiring schemes.

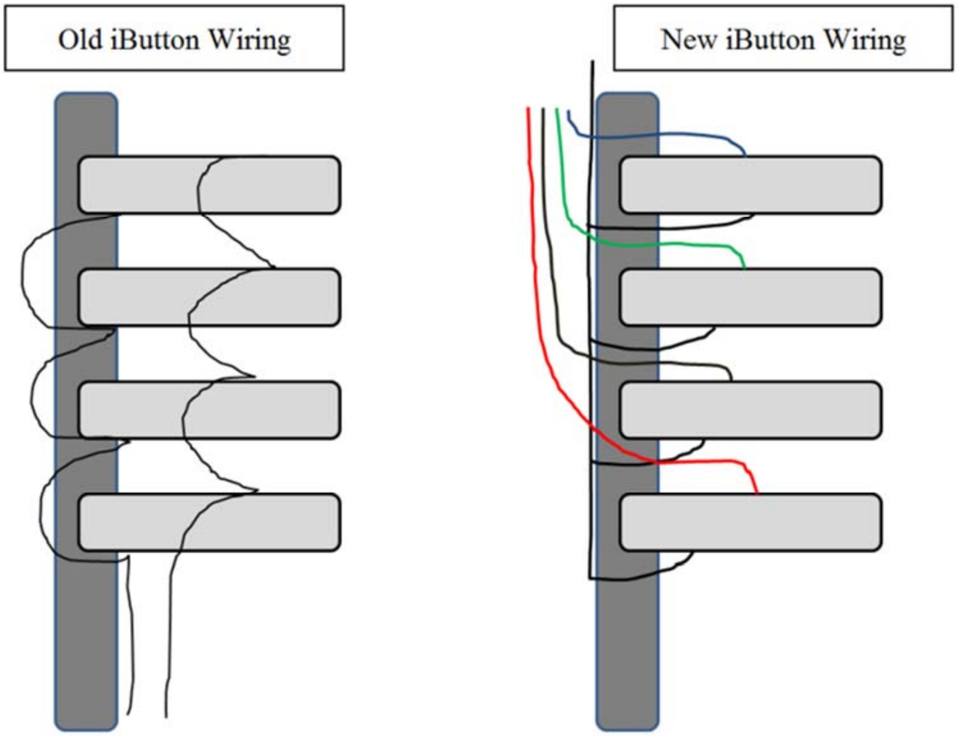

Figure 7.16: iButton string wiring configurations.

On the first return trip, and the following two data collection trips, the research team took note of the curing method that was used by the contractors. For this pour, moist cotton curing blankets were placed on top of the concrete, and were covered by a sheet of black plastic. The plastic was in place to prevent evaporation from the curing blankets below. While having the plastic separated from the concrete by a curing blanket, it was reasoned that the use of black plastic, rather than white or clear, was probably a poor choice in the summer time, and contributed to a higher daily peak temperature in the concrete than would have been seen with a white or clear plastic. Unfortunately, the research team did not take any pictures of the curing methods that were used on the Georgetown bridge deck for the summer pour.

On the last of the return trips to the Georgetown bridge deck summer pour, the research team inspected the bridge deck in an attempt to find early-age cracking. In the section that was available for the research team to inspect, no early-age cracking could be found.

7.2.4 Georgetown Bridge Deck Results: Summer Pour

Georgetown Bridge Deck Recorded Temperatures

Figure 7.17 and Figure 7.18 display the temperature data for the middle of the bridge deck cast in the Georgetown summer pour. In this bridge deck, as well as in the winter pour, the research team was able to place iButtons underneath the bridge deck panels, as well as inside the middle of bridge deck panels. This provided the team with a better understanding of the heat transfer occurring between the existing superstructure and the newly cast bridge deck concrete.

While not as high as those seen in San Antonio, the Georgetown summer pour did have some high temperatures in the first few temperature peaks, partially due to the use of black plastic on top of the curing blankets during very high summer time temperatures. The research team was able to determine the cause for the high temperatures by examining the temperatures in the bridge deck following the removal of the curing blankets and plastic on August 8, 2009.

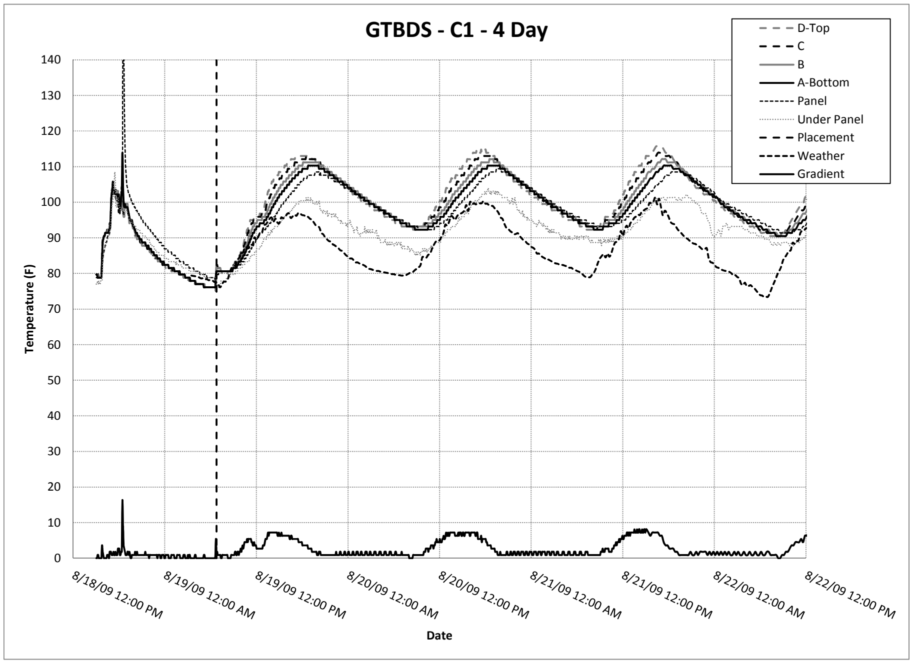

Figure 7.17: Four-day temperature data: GTBDS—C1.

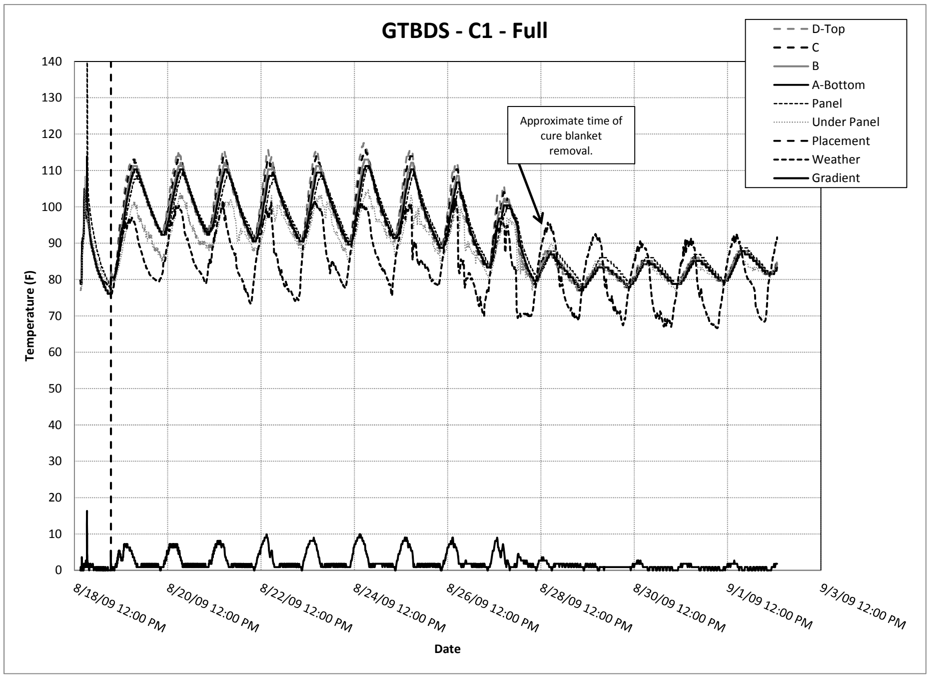

Figure 7.18: Full temperature data: GTBDS—C1.

Fresh Concrete Properties

Table 7.5 provides the fresh concrete properties that were measured by the research team during casting for the summer field instrumentation site in Georgetown. All values were confirmed by tests conducted concurrently by a certified TxDOT inspector.

Table 7.5: Fresh concrete properties—Georgetown summer pour.

Strand	Time	Slump in.	Air %	Temperature ^{o} F
A	4:31 AM	5.0	4.6	86
B	5:22 AM	5.0	4.9	82
C	6:40 AM	4.3	4.7	83
D	7:19 AM	4.5	4.7	82

Chemical Analyses of Field Testing Materials

Cement, fly ash, and admixtures were acquired from the ready mix producers for the Georgetown bridge deck field instrumentation project. Table 7.6 presents the results of XRF and Bogue calculated cement phases.

Table 7.6: XRF and Bogue results for field materials.

		GTBD Cement	GTBD Fly Ash	LBD Cement	LBD Fly Ash
XRF Results	SiO_2	20.5	47.1	20.7	33.1
	Al_2O_3	4.3	15.4	4.4	18.7
	Fe_2O_3	3.0	5.2	5.0	6.3
	CaO	63.4	28.7	62.8	25.0
	MgO	1.6	2.4	0.8	4.6
	SO_3	2.8	0.9	2.9	1.2
	Na_2O	0.18	0.31	0.24	1.21
	K_2O	0.46	1.05	0.24	0.27
	Na_2Oe	0.48	1.00	0.39	1.39
Cement Phases	C_3S	61.3	--	53.9	--
	C_2S	12.4	--	18.6	--
	C_3A	6.4	--	3.3	--
	C_4AF	9.2	--	15.1	--

All values are in % by weight.

* Na_2Oe equivalent alkali content

GTBD = Georgetown bridge deck; LBD = Lubbock bridge deck.

Admixtures

The properties of the admixtures used at the Georgetown bridge deck pour is provided in Table 7.7. AE and WR3 refer to the air-entraining and water reducing admixtures used at the Georgetown summer pour.

Table 7.7: Onsite admixtures used for field sites.

Admixture	Dosage	Specific Gravity	% Solids
AE	0.38 oz./cwt	1.01	6%
WR3	3.8 oz./cwt	1.2	41%
AE2	1.28 oz./cwt	1.01	13%
WR4	10 oz./cwt	1.27	43%
Fibers	1.5 lb./yd^3	0.91	--

Mechanical Strength Development

Table 7.8 provides the mechanical strength development for the bridge deck mixtures. The choice as to where and when to take cylinders from the field site varied for each site due to decisions made from previous pours, limitations from the contractor, and limitations on what could be transported back to the laboratory.

Table 7.8: Mechanical properties for Georgetown summer pour.

Test	(psi)	String A	String B	String D
12Hr.	f'c	1,243	1,101	1,176
	f'st	--	179	--
	E	--	--	--
24Hr.	f'c	2,023	1,922	1,924
	f'st	339	295	298
	E	--	2,728,880	--
2 Day	f'c	2,811	2,646	2,800
	f'st	395	415	410
	E	--	3,165,204	--
3 Day	f'c	--	2,986	--
	f'st	--	424	--
	E	--	3,349,360	--
7 Day	f'c	--	3,828	--
	f'st	--	516	--
	E	--	3,538,608	--
14 Day	f'c	--	4,227	--
	f'st	--	526	--
	E	--	3,830,903	--
28 day	f'c	5,112	5,175	5,529
	f'st	574	564	582
	E	4,350,670	4,093,487	4,187,861
1 Year	f'c	--	5,792	--
	f'st	--	608	--
	E	--	--	--

All values in psi.

Semi-Adiabatic Calorimetry

Table 7.9 presents the semi-adiabatic calorimetry results from the field pours. In this table, GTBDS represents the summer Georgetown bridge deck pour and GTBDW represents the winter Georgetown bridge deck pour. While the research team was able to collect Q-drum data from the San Antonio pour, the inability to acquire a sample of the cement and fly ash resulted in an inability to determine the activation energy and ultimate heat of hydration—parameters that are required in the semi-adiabatic calorimetry data analysis for determining the hydration parameters α, β, and τ. As described in Chapter 3, activation energy, Ea, and ultimate heat of hydration, Hu, are calculated using empirical equations from previous work done by members of the research team. The hydration parameters α, β, and τ are found using curve fitting to match the heat generated within the Q-drum with that predicted by Equation 2.7.

Table 7.9: Semi-adiabatic calorimetry results for field pours.

Qdrum Recording	E_a J/mol	H_u J/kg	α_u %	β	τ hrs.
GTBDS-Strand A	34,771	484,154	0.801	0.561	22.81
GTBDS-Strand B	34,771	484,154	0.788	0.569	23.07
GTBDW-Strand B	34,771	484,154	0.754	0.678	17.49
GTBDW-Strand C	34,771	484,154	0.863	0.792	16.19
LBD- Strand B	35,023	446,253	0.795	0.657	30.57

GTBDS = summer Georgetown bridge deck pour
GTBDW = winter Georgetown bridge deck pour
LBD = Lubbock bridge deck pour

7.3 Georgetown Bridge Deck: Winter Pour

In November of 2009, the research team returned to the Georgetown bridge deck to instrument the last span of the bridge. Prior to this instrumentation, and following the first span that was poured, contractors had completed two separate pours to cross the midspan of the bridge. As before, the bridge deck consisted of 4 in. of cast-in-place concrete on top of 4in. precast, prestressed concrete panels that were supported by precast, prestressed concrete girders. The pour began on November 19, 2009 at 8:00 a.m., and concluded on November 19, 2009 at approximately 12:00 p.m. Information gained from this field instrumentation included temperature data from November 19 to either December 10 or January 8, depending on when the contractors cut the remaining iButton collection lines, two sets of semi-adiabatic calorimetry data, and mechanical testing results.

7.3.1 Structural Plans for Georgetown Bridge Deck

The Georgetown bridge deck winter pour consisted of 4in. cast-in-place concrete over 4in. precast, prestressed concrete panels, supported by precast, prestressed concrete girders. A typical cross section was shown in Figure 7.10; Figure 7.19 shows the elevation for the winter pour.

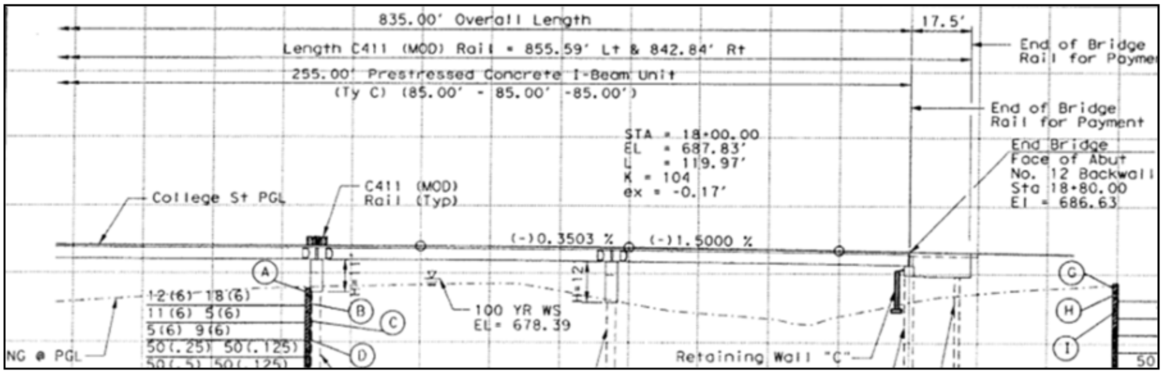

Figure 7.19: Elevation of Georgetown bridge deck for the winter pour.

7.3.2 Materials and Mixture Design of Georgetown Bridge Deck

The mixture design for the Georgetown bridge deck winter pour is presented in Table 7.10. A low-alkali cement, ASTM C 618 Class C fly ash, approximately 1in. MSA limestone coarse aggregate, and river sand were used for this mixture design. The mixture design information was acquired from batch tickets that were collected throughout the pour. The mixture design was not seen to change over the course of the Georgetown bridge deck winter pour.

Table 7.10: Mixture design for Georgetown bridge deck winter pour.

Cement lb/yd^3	Fly Ash lb/yd^3	Water lb/yd^3	Coarse lb/yd^3	Fine lb/yd^3	AE oz/yd^3	WR3 oz/yd^3
430	143	252	1776	1254	2.2	22

7.3.3 Instrumentation and Testing of Georgetown Bridge Deck

The layout for the Georgetown bridge deck winter pour is provided in Figure 7.20 and Figure 7.21. Strands A and D were used to capture the changes between the beginning and end of the pour, and Strands B and C were used to capture data throughout the middle of the pour. As before, iButtons were placed both under and inside the precast panels on Strings B and C. On this pour, due to results seen from previous instrumentation, no procedures were taken to evaluate one side of the deck relative to the other (i.e., east vs. west). Further information on the layout and position of the iButtons can be found in Appendix B.

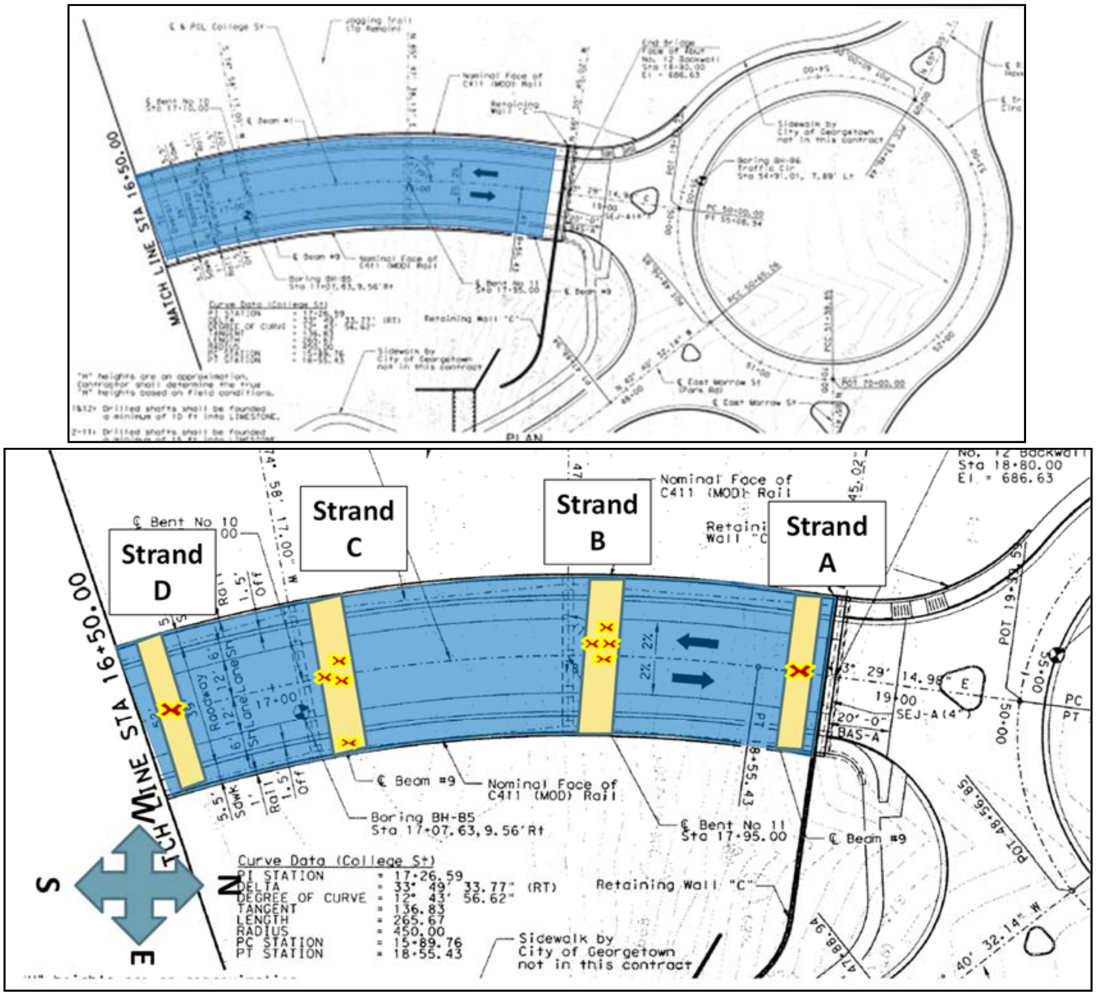

Figure 7.20: iButton string layout for Georgetown bridge deck winter pour.

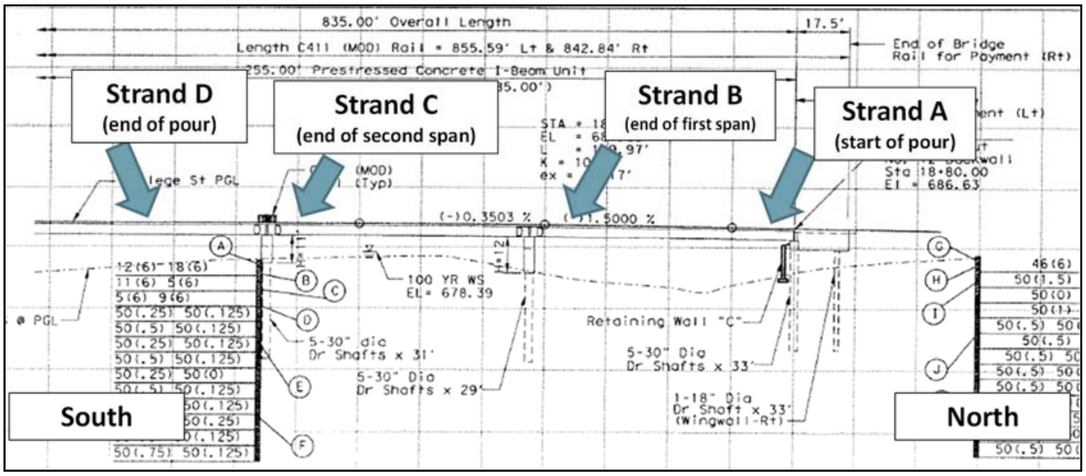

Figure 7.21: iButton strand layout for Georgetown bridge deck winter pour.

On their third bridge deck, the research team made modifications to their iButton preparation from lessons that had been learned from failures in previous bridge decks. The iButton strings now consisted of a solid, slightly flexible piece of plastic rod that had gaps cut out for iButtons. iButtons were soldered to six-conductor wire, this time in parallel, and then connected to the plastic rod with plastic ties. Two part epoxy was then used to cover the iButtons. Once again, a hole was drilled into the precast panel, and the bottom of the plastic rod was epoxied into this hole. The wires for the iButtons were run transversely across the deck, and with the foreman's permission, were run through a small hole that was drilled into the side formwork for the deck. It should be noted that the long duration of temperature measurements that the research team collected was due largely in part to the cooperation of the foreman of the contracting crew. By the time the winter pour was completed, the research team had built a good communication system with the foreman, and he worked to keep the iButton wires in readable condition in the months following the pour. Data collection ended with the pouring of the sidewalks on the bridge deck, which covered the remaining iButton collection wires. iButton strings from the Georgetown bridge deck winter pour can be seen in Figure 7.22.

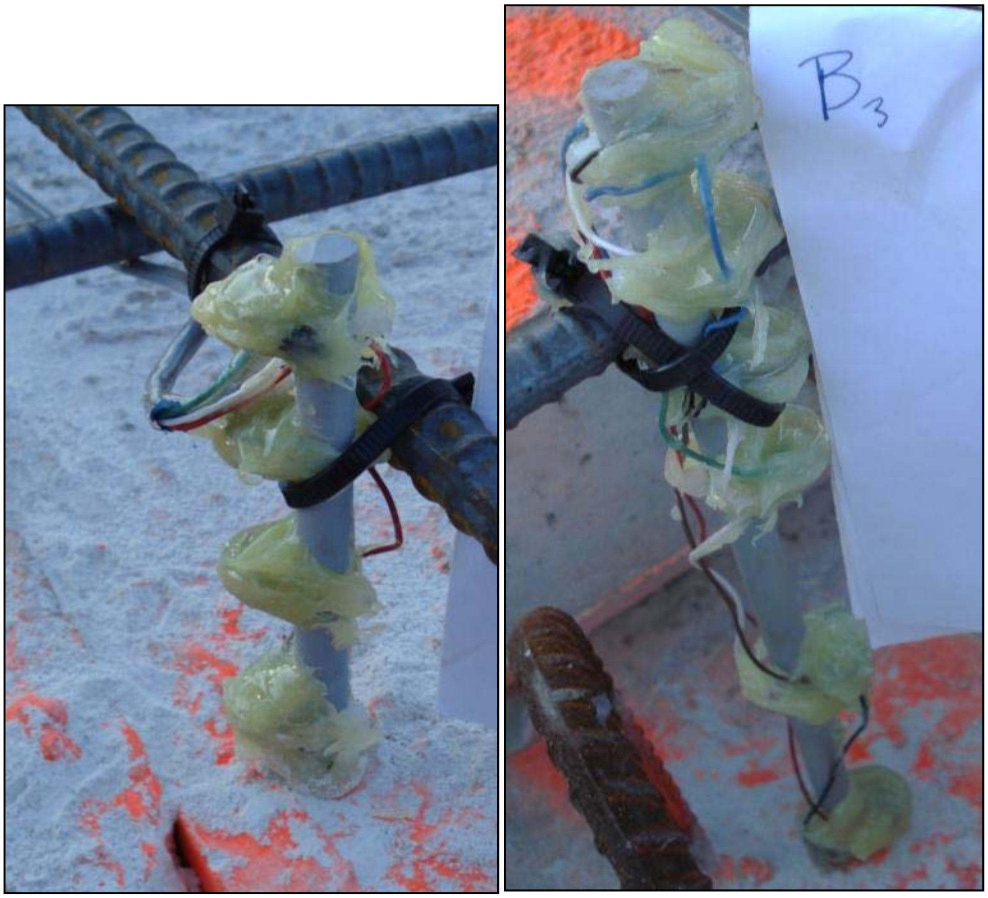

Figure 7.22: iButton strings for Georgetown bridge deck winter pour.

The research team returned to the bridge deck for the first data collection three days after the day of the pour. The iButtons were reset at this point for a longer collection interval, and data from the first three days was downloaded. The research team noted that for curing, the contractors had placed black plastic on top of the concrete, and then covered the black plastic with curing blankets. Later conversations with the contractor and TxDOT employees revealed that this method, in the freezing temperatures that prevailed in the days after the pour, helped protect the concrete from frost damage during the first days after casting. The curing method can be seen in Figure 7.23 and Figure 7.24.

Figure 7.23: Curing method for Georgetown bridge deck winter pour.

Figure 7.24: Black plastic under curing blanket at Georgetown winter pour.

Two more trips were made to the bridge deck to collect data from the iButtons, and to inspect the deck for early-age cracking. While no true early-age cracking was found, there were minor cracks located above the plastic "zip strip." The cracking above the plastic strips is shown in Figure 7.25.

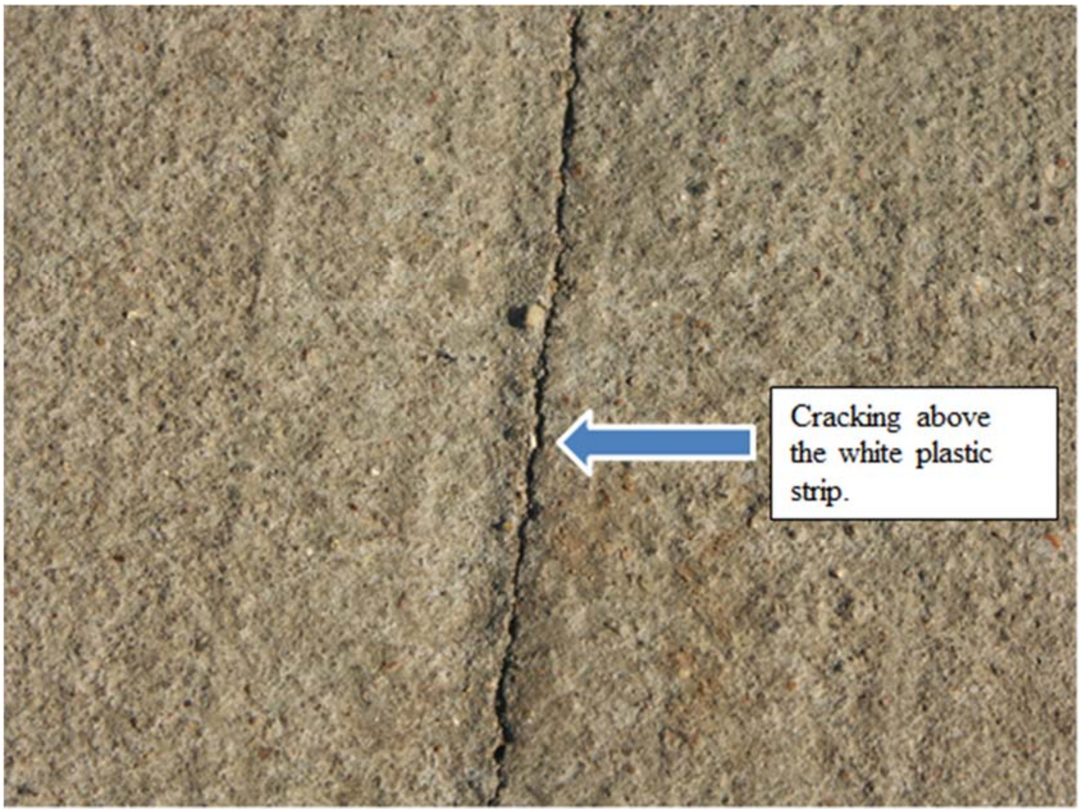
Cracking above the white plastic strip.

Figure 7.25: Cracking above plastic strip on bridge deck.

Cracking was also seen longitudinally between the sidewalk-bridge deck interface and in the transversely in the sidewalk at the line where the plastic strip was located in the bridge deck. The sidewalks were cast several months after the casting of the bridge deck. Cracks in the sidewalk can be seen in Figure 7.26 and Figure 7.27.

Figure 7.26: Cracking between bridge deck and sidewalk concrete.

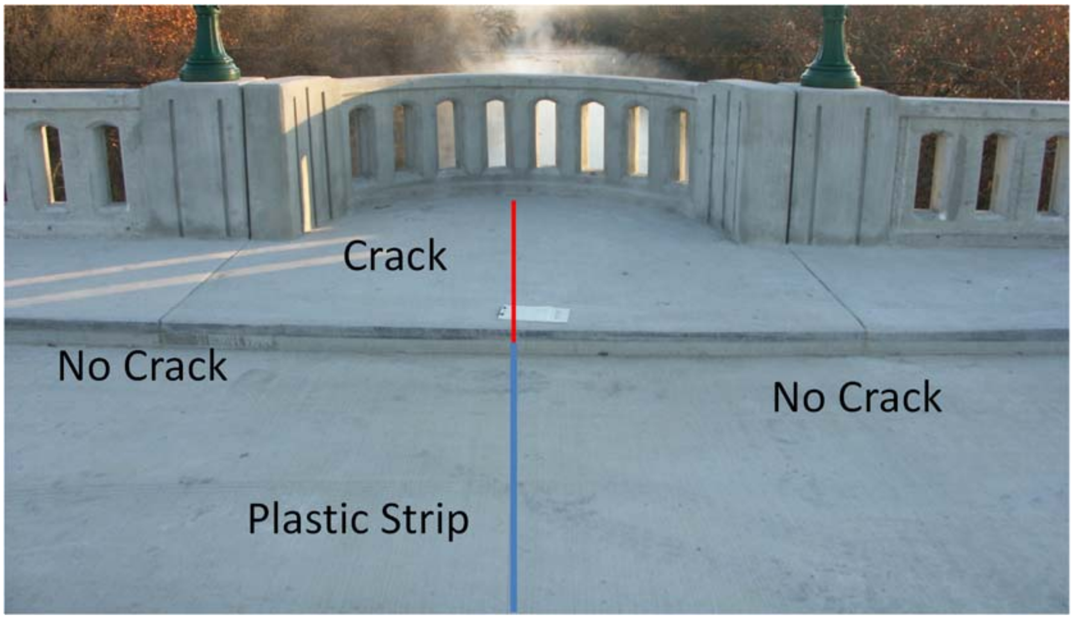

Figure 7.27: Transverse cracking in sidewalk concrete.

7.3.4 Georgetown Bridge Deck Results: Winter Pour

Georgetown Bridge Deck Recorded Temperatures

Figure 7.28 and Figure 7.29 display the temperature data for the middle of the bridge deck cast in the Georgetown winter pour. As with the Georgetown summer pour, the research team was able to instrument the middle and underside of the bridge deck panels, in addition to the measurements taken inside the bridge deck. For this pour, the research team was able to capture much more data than had been available in previous instrumentations. Due to the extended data, the graphs presented in this section span seven and 28 days. Full plots of the bridge deck temperatures are presented in Appendix B. The research team was informed by the contractor that curing blankets for the Georgetown bridge deck winter pour were removed ten days after casting, on November 29, 2009 at approximately 12:00 p.m.

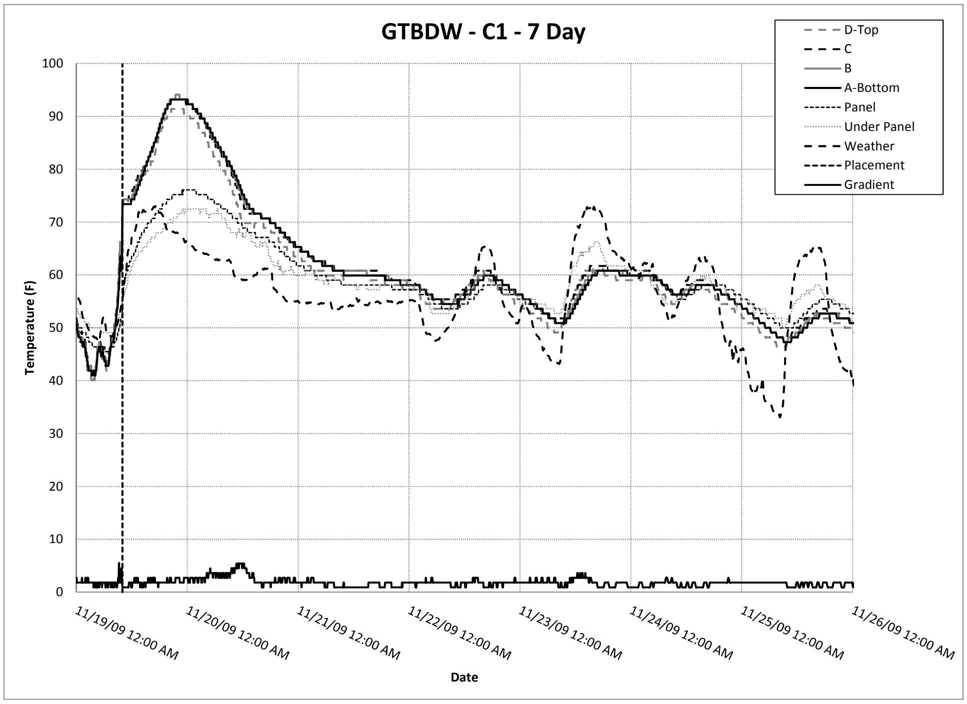

Figure 7.28: Seven-day temperature data: GTBDW—C1.

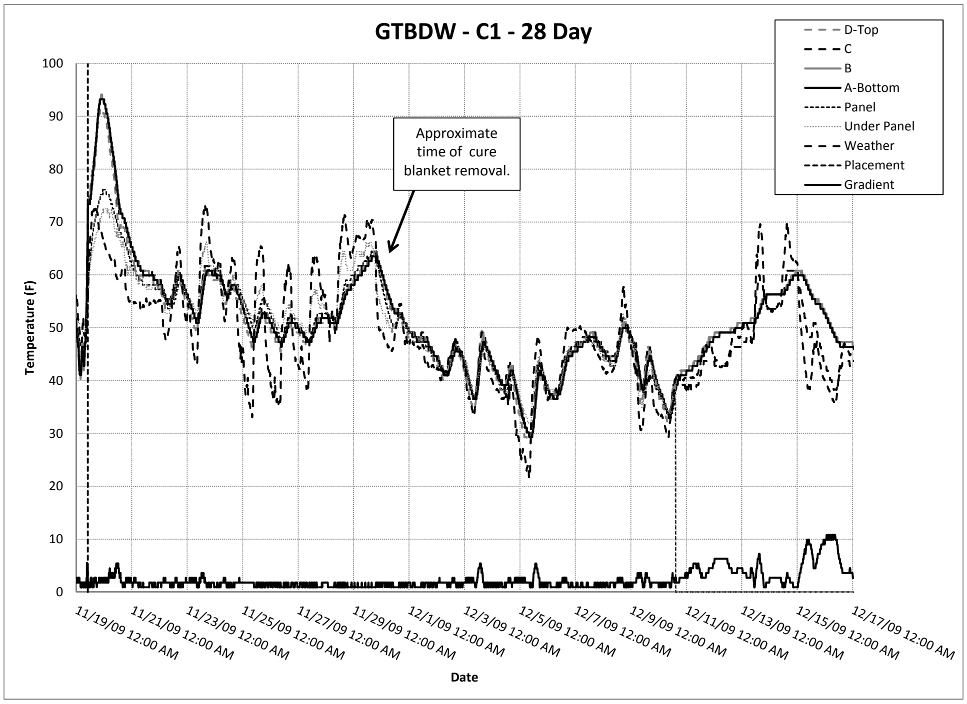

Figure 7.29: Twenty-eight day temperature data: GTBDW—C1.

Fresh Concrete Properties

Table 7.11 provides the fresh concrete properties that were measured by the research team during casting at the field instrumentations. All values were confirmed by tests conducted concurrently by a certified TxDOT inspector.

Table 7.11: Fresh concrete properties—Georgetown winter pour.

Strand	Time	Slump in.	Air %	Temperature °F
A	7:54 AM	5.5	5.4	65
B	8:14 AM	5.4	--	66
C	9:40 AM	5.5	5.0	71
D	10:05 AM	3.5	5.1	73

Chemical Analyses of Field Testing Materials

Cement, fly ash, and admixtures were acquired from the ready mix producers for the Georgetown and Lubbock bridge decks. Table 7.6 presented the results of XRF and Bogue calculated cement phases.

Admixtures

The properties of the admixtures used at the Georgetown bridge deck pour were provided in Table 7.7. AE and WR3 refer to the air-entraining and water reducing admixtures used at both the Georgetown summer and winter pours.

Mechanical Strength Development

Table 7.12 provides the mechanical strength development for the bridge deck mixtures. The choice as to where and when to take cylinders from the field site varied for each site due to decisions made from previous pours, limitations from the contractor, and limitations on what could be transported back to the laboratory.

Table 7.12: Mechanical testing for Georgetown winter pour.

Test		String A	String B	String C	String D
12Hr.	f'c	397	585	319	636
	f'st	58	83	68	87
	E	--	2,171,721	1,671,058	--
24Hr.	f'c	1,475	1,395	1,418	1,713
	f'st	211	211	185	219
	E	--	2,457,722	2,213,622	--
2 Day	f'c	2,546	2,404	2,291	2,693
	f'st	351	351	331	399
	E	--	2,986,560	2,928,232	--
8 Day	f'c	--	3,956	3,762	--
	f'st	--	488	497	--
	E	--	3,660,785	3,705,279	--
14 Day	f'c	--	4,478	4,133	--
	f'st	--	544	516	--
	E	--	4,117,225	3,801,262	--
28 Day	f'c	4,848	5,125	4,869	5,219
	f'st	581	563	523	570
	E	--	3,940,209	3,873,570	--

All values in psi.

7.4 Lubbock Bridge Deck

The next bridge deck that the research team instrumented was in Lubbock, at Loop 289 and Slide Road. The bridge deck had two separate pours for the northbound and southbound lanes. The research team only instrumented the southbound lane pour. The bridge deck consisted of 4 in. of cast-in-place concrete over 4in. precast, prestressed concrete panels, supported by precast, prestressed concrete girders. The pour began on July 15, 2010 at 11:00 p.m. and concluded on July 16, 2010 at 5:30 a.m. Information gained from this field instrumentation included temperature data from July 15 to August 5, semi-adiabatic calorimetry data, and mechanical testing results.

7.4.1 Structural Plans for Lubbock Bridge Deck

The Lubbock bridge deck consisted of 4 in. of cast-in-place concrete, 4 in. precast, prestressed concrete panels, and was supported by precast, prestressed concrete girders. This bridge deck also utilized epoxy coated reinforcement, where none of the previously instrumented bridge decks had done so. Elevation and cross sections of the bridge are provided in Figure 7.30, Figure 7.31, and Figure 7.32.

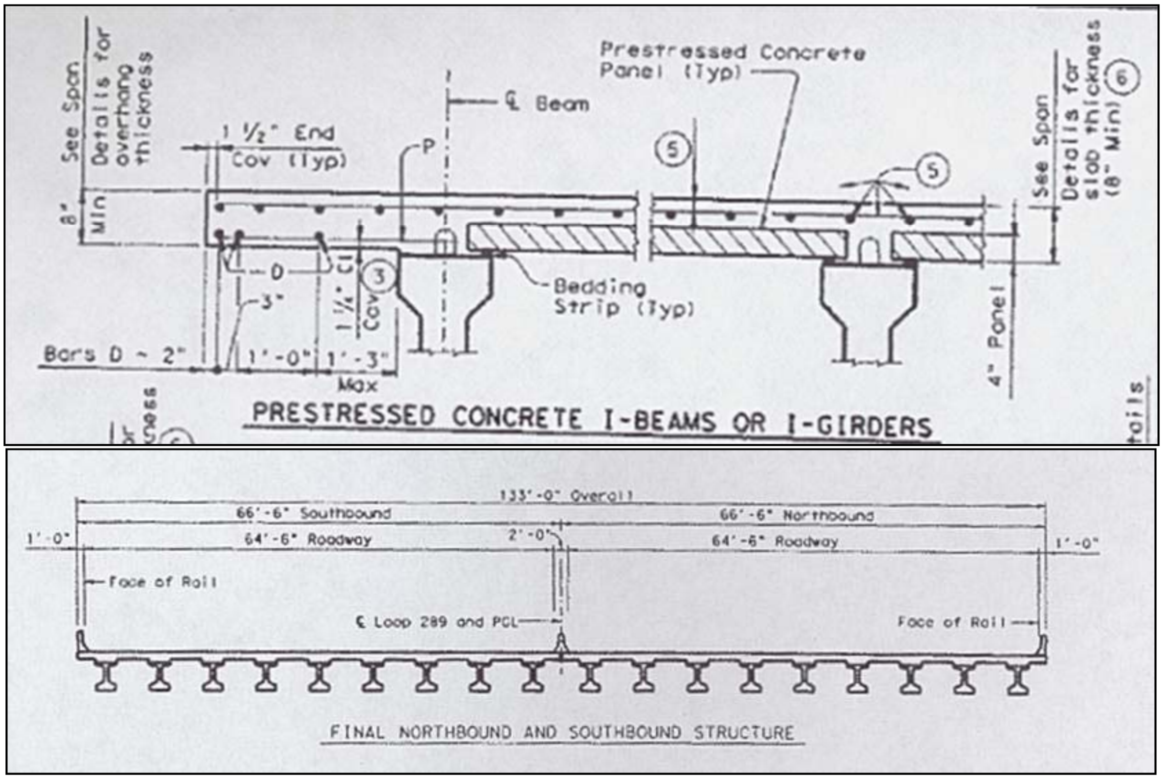

Figure 7.30: Cross section for Lubbock bridge deck.

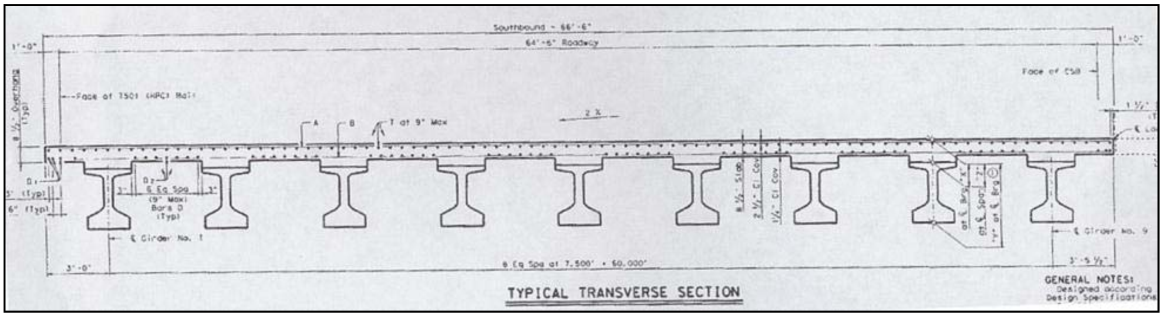

Figure 7.31: Cross section of Lubbock bridge deck southbound lane.

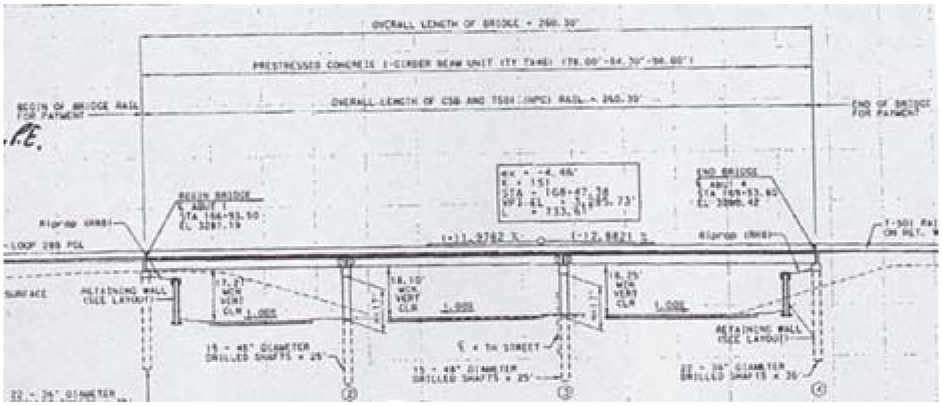

Figure 7.32: Elevation of Lubbock bridge deck.

7.4.2 Mixture Design of Lubbock Bridge Deck

The mixture design for the Lubbock bridge deck is provided in Table 7.13. The cement used was a low-alkali cement, with an ASTM C 618 Class C fly ash used as a 35% replacement for cement. The primary gradation of coarse aggregate was an approximately 1in. MSA siliceous river gravel, while the secondary gradation of coarse aggregate was a TxDOT Gr. 5 siliceous coarse aggregate. River sand was used for the fine aggregate. Only one batch ticket, from the middle of the pour, was collected for this pour. However, discussions with TxDOT during the pour informed the research team that the mixture design was not changing throughout the pour. The Lubbock bridge deck was also the only bridge deck that the research team instrumented that utilized fibrillated polypropylene fibers in the mixture. These fibers provide an easier pathway for bleed water to reach the concrete surface, and help prevent plastic shrinkage cracking. The Lubbock area, with high winds and typically low relative humidity, is well-known for being a high-risk area for plastic shrinkage cracking if precautions are not taken.

Table 7.13: Mixture design for Lubbock bridge deck.

Cement lb/yd^3	Fly Ash lb/yd^3	Water lb/yd^3	Coarse1 lb/yd^3	Coarse2 lb/yd^3	Fine lb/yd^3	AE2 oz/yd^3	WR4 oz/yd^3	Fibers lb/yd^3
380	204	263	1506	475	996	7.5	58.4	1.5

7.4.3 Instrumentation and Testing of Lubbock Bridge Deck

The iButton layout for the Lubbock bridge deck is provided in Figure 7.33 and Figure 7.34. Strands A and D were used to capture the changes between the beginning and end of the bridge deck pour. Strands B and C captured the middle of the pour, with strand B consisting of four-button strings located on the panels, and strand C of six-button strings located above the girders. Further information on the iButton locations and depths can be found in Appendix B.

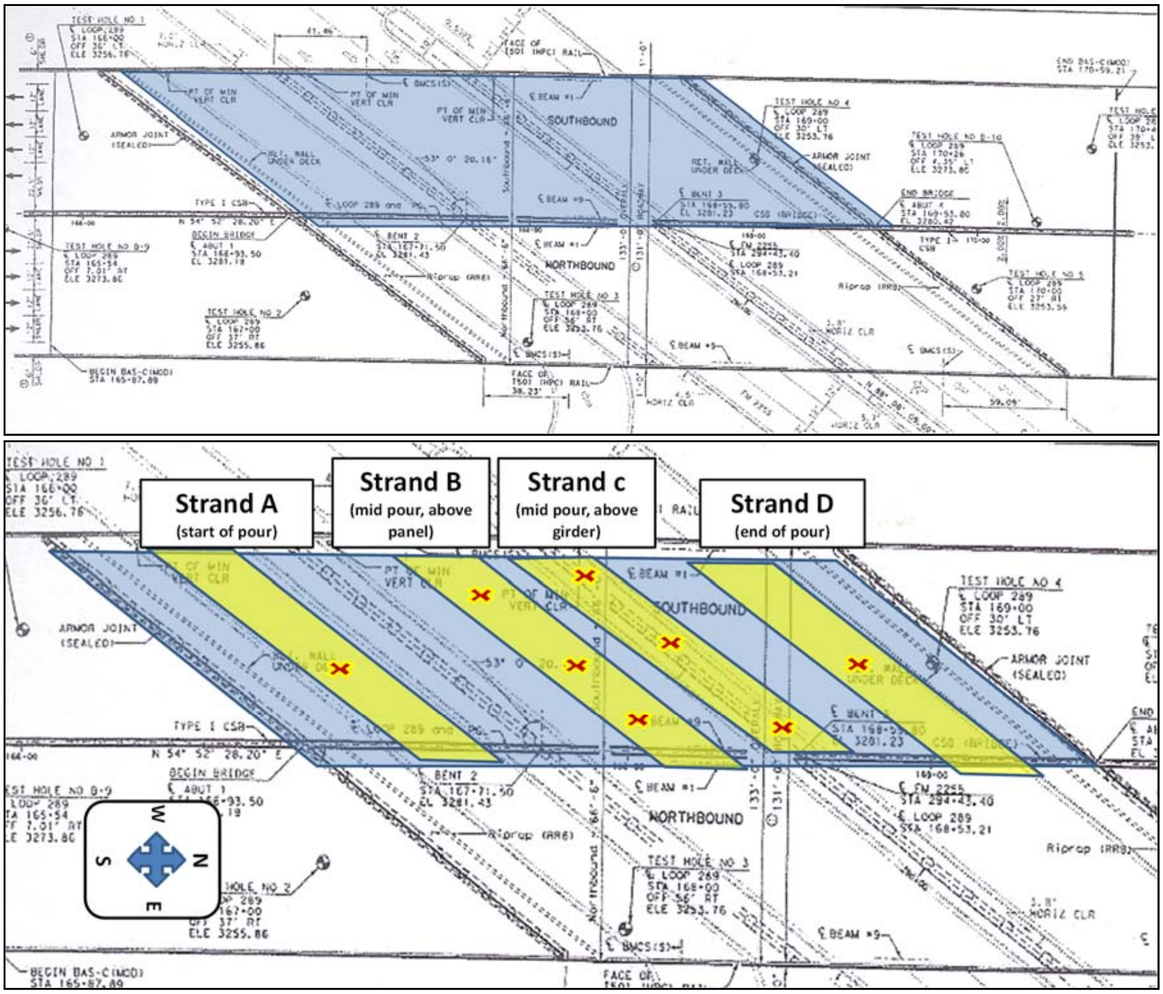

Figure 7.33: iButton string layout for Lubbock bridge deck.

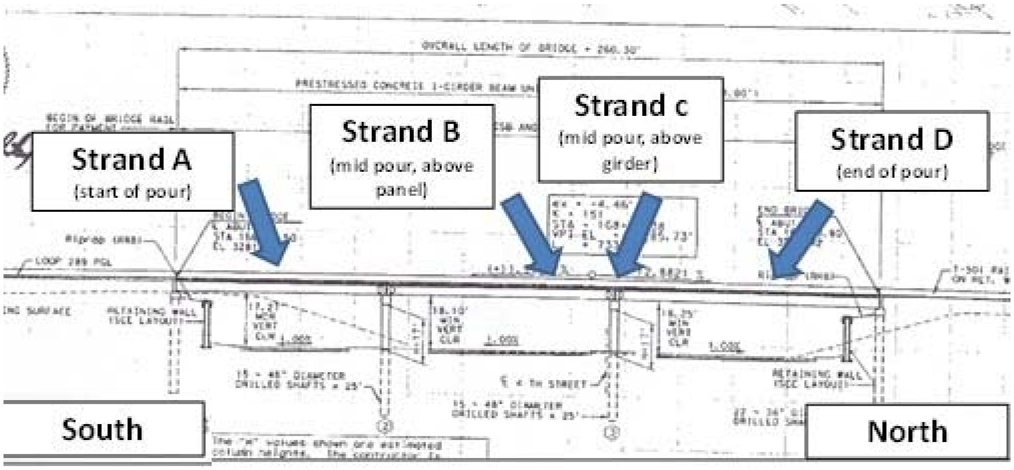

Figure 7.34: iButton strand layout for Lubbock bridge deck.

Because the iButton preparation process used in the Georgetown bridge deck winter pour was successful, the team implemented the same methods for the iButtons used in the Lubbock bridge deck. The only modification was to have the wires connect to the string at the bottom of the plastic rod, between the bottom and second iButton, rather than the top—giving the team greater flexibility in placing the iButton strings. If a plastic rod was too long at the bottom or too tall at the top, with the new preparation method, modifications could be made at the job site. At the Lubbock site, the research team was asked by the contractor to remove the top iButton from their taller, six-button strings, for fear that they would interfere with the finishing crew on the bridge deck. Due to the use of parallel wiring, and the bottom-fed collection wire, the research team was able to meet this request in the field. Figure 7.35 shows the bottom-fed iButton strings that were used in the Lubbock bridge deck pour.

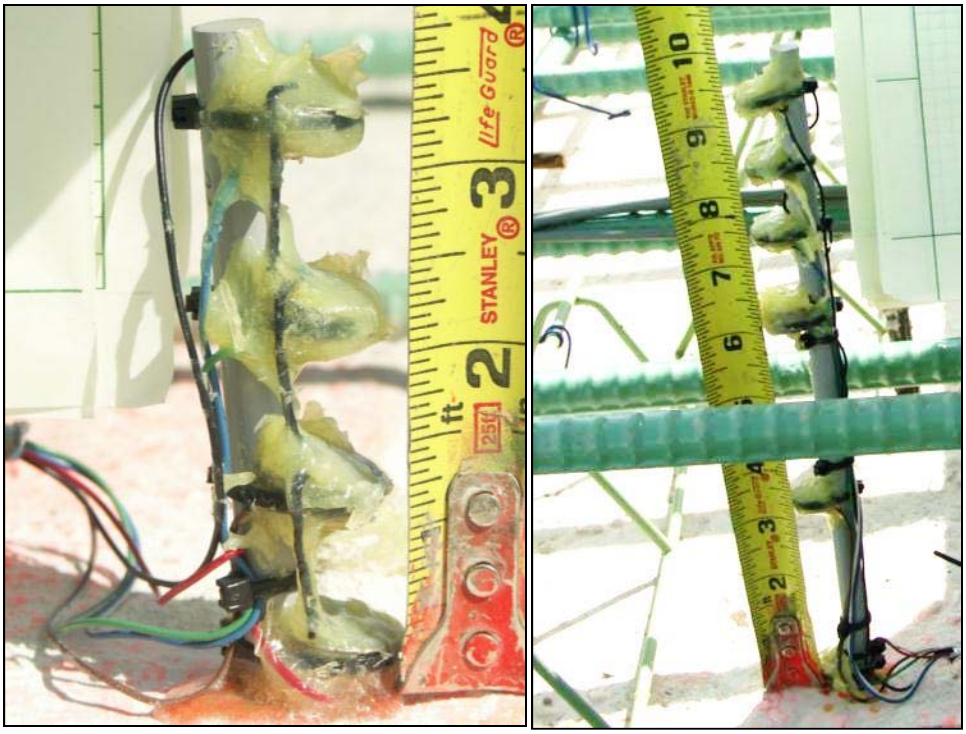

Figure 7.35: iButton strings for Lubbock bridge deck.

Two days after the pour, the research team returned to the bridge deck to collect data and reset the iButton recording interval. In addition to the curing compound that had been applied immediately after the pour, the contractors used wet cotton blankets, with opaque white plastic covering the blankets to cure the concrete, as shown in Figure 7.36.

Figure 7.36: Curing method for Lubbock bridge deck.

No early-age cracking was found when the research team returned to the bridge deck in August 2010.

7.4.4 Lubbock Bridge Deck Results

Lubbock Bridge Deck Recorded Temperatures

Figure 7.37 and Figure 7.38 display the temperature data from the middle of the bridge deck cast in the Lubbock bridge deck pour. As opposed to previous instrumentations, the research team was required to instrument the Lubbock bridge deck with a smaller team and with a smaller time window. As such, the research team was unable to place iButtons under and inside the precast prestressed concrete panels. Through examination of the temperature data, the research team determined that the curing blankets and plastic were removed on July 29, 2010.

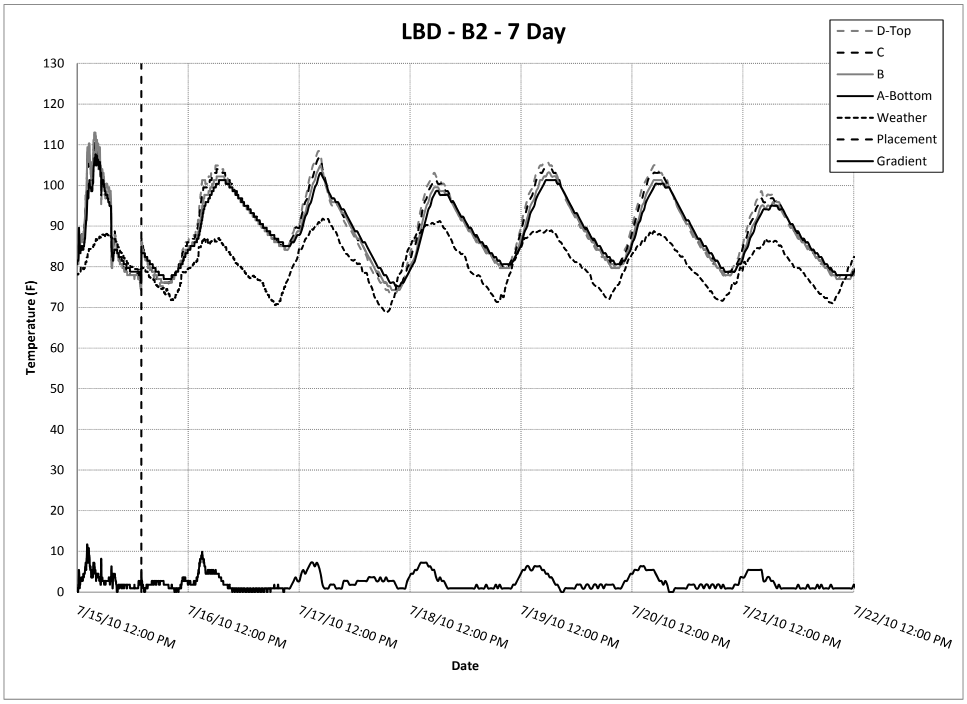

Figure 7.37: Seven-day temperature data: LBD—B2.

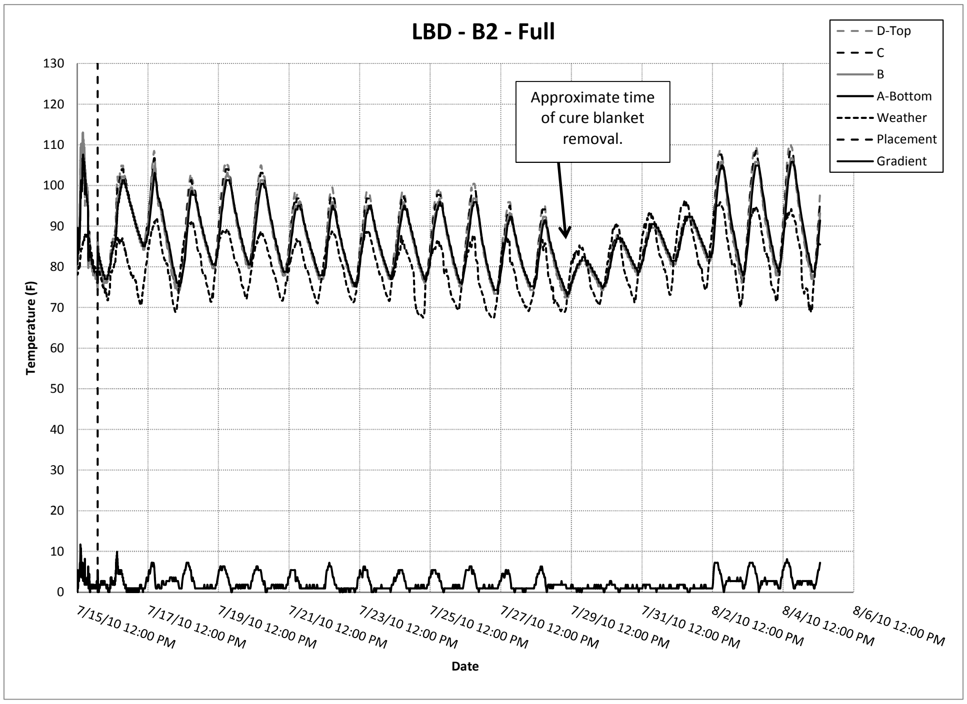

Figure 7.38: Full temperature data: LBD—B2.

Fresh Concrete Properties

Table 7.14 provides the fresh concrete properties that were measured by the research team during casting at the field instrumentations. All values were confirmed by tests conducted concurrently by a certified TxDOT inspector.

Table 7.14: Fresh concrete properties—Lubbock bridge deck.

Strand	Time	Slump in.	Air %	Temperature ° F
B/C	1:50 AM	5.5	5.0	83

Chemical Analyses of Field Testing Materials

Cement, fly ash, and admixtures were acquired from the ready mix producers for the Lubbock bridge decks. Table 7.6 presented the results of XRF and Bogue calculated cement phases.

Admixtures

The properties of the admixtures used at the Lubbock bridge deck pours were provided in Table 7.7. AE2, WR4, and Fibers refer to the admixtures and fibrillated polypropylene fibers used in the Lubbock pour.

Mechanical Strength Development

Table 7.15 provides the mechanical strength development for the bridge deck mixtures. The choice as to where and when to take cylinders from the field site varied for each site due to decisions made from previous pours, limitations from the contractor, and limitations on what could be transported back to the laboratory.

Table 7.15: Mechanical properties for Lubbock bridge deck.

Test		Strand B
12 Hr.	f'c	310
	f'st	--
	E	--
24 Hr.	f'c	1,411
	f'st	209
	E	3,040,221
2 Day	f'c	1,872
	f'st	257
	E	3,389,402
7 Day	f'c	2,837
	f'st	364
	E	3,544,319
28 day	f'c	4,286
	f'st	500
	E	4,490,021

All values in psi.

Semi-Adiabatic Calorimetry

Table 7.9 presented the semi-adiabatic calorimetry results from the field pours. As described in Chapter 3, activation energy, *Ea*, and ultimate heat of hydration, *Hu*, are calculated using empirical equations from previous work done by members of the research team. The hydration parameters α, β, and τ are found using curve fitting to match the heat generated within the Q-drum with that predicted by Equation 2.7.

7.5 Austin Bridge Deck (NBWB Ramp)

The Interstate Highway 35/State Highway 71 (IH35/SH71) interchange, located in southeast Austin, has served many times as the “field” throughout the development of ConcreteWorks. The site has a long history of field instrumentation successes and failures dating back to 2003. The current construction project is in the final stages of completing the remaining connector ramps, making it ideal for the instrumentation of bridge decks.

7.5.1 Instrumentation

For this project, the northbound IH35 ramp to the westbound SH71 was instrumented. As Figure 7.39 illustrates, the bridge deck is built using 4-in.-thick precast panels spanning 54-in. pre-stressed U-beams. A rebar mat is built 2 in. above the precast panels and then a 4-in. layer of concrete is placed for an 8-in.-thick composite section. Heat transfer in a bridge deck occurs vertically, so the aim was to place sensors vertically to get the temperature distribution from top to bottom.

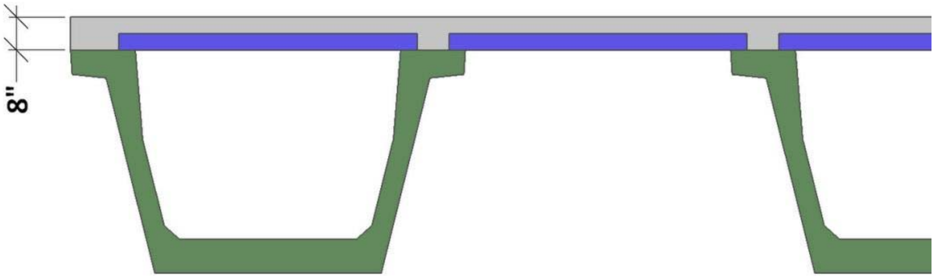

Figure 7.39: Bridge deck cross section.

As with the other bridge decks, iButtons were used to collect temperature data, placed below the precast panel, in the middle of the precast panel, and at 1-in. intervals in the cast-in-place layer of concrete above the precast panel. Figure 7.40 illustrates the instrumentation plan.

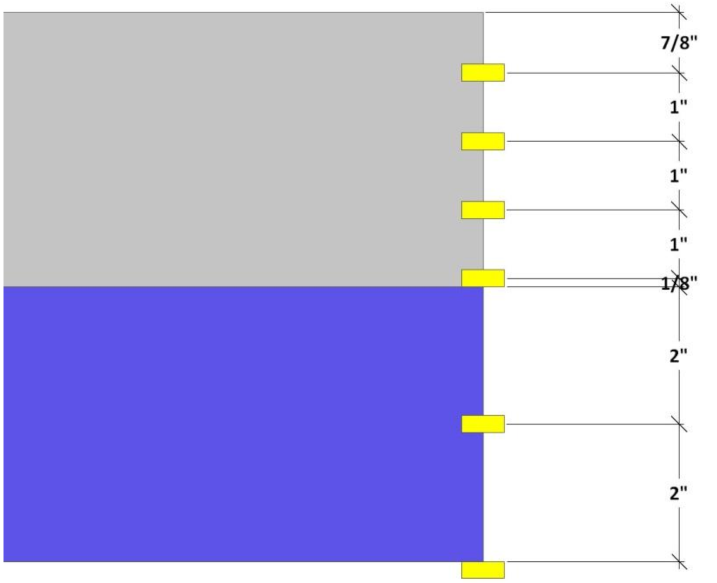

Figure 7.40: Bridge deck instrumentation plan.

To ensure proper 1-in. spacing of the sensors in the cast-in-place section, temperature sticks were fabricated in the lab using 0.25-in. plastic dowel rod for quick installation on site. The sensors were then coated in epoxy to prevent water intrusion. Once on site, the lower end of the dowel rod was inserted into a 0.25-in. hole drilled into the precast panel and epoxied into place. This held the sensors upright while the concrete was placed. The two lower sensors were installed by drilling through the precast panel and backfilling with fast curing epoxy. Figure 7.41 and Figure 7.42 show the temperature sticks before and after installation.

Figure 7.41: Sensor stick prior to epoxy coating.

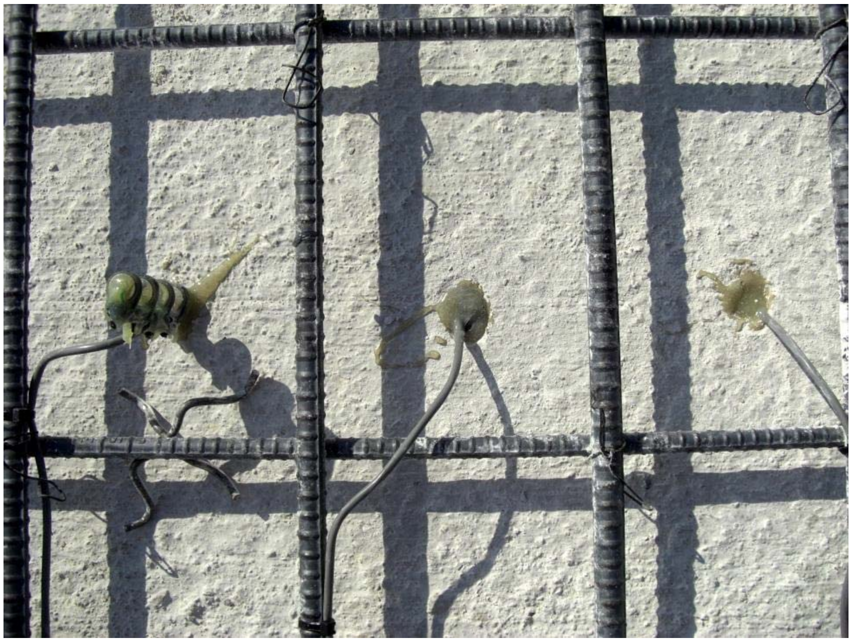

Figure 7.42: Completed bridge deck instrumentation.

Since the curing plastic was 20 feet wide, part of the ramp was sectioned off into three 15-ft wide strips running the width of the deck, which allowed for some overlap of the plastic between sections. For the sake of redundancy, two instrumentations were installed per area. The temperature sticks are particularly vulnerable to getting kicked over during concrete placement; sensor failure due to water intrusion is by no means uncommon. The original intent was to place the sensors between U-beams. However, the multi-conductor wires used to read the sensors were mistakenly cut short, forcing the sensors to be placed near the edges of the deck as illustrated by

Figure 7.43. This meant that the temperature readings would be somewhat skewed by the temperature of the air encased by the U-beams.

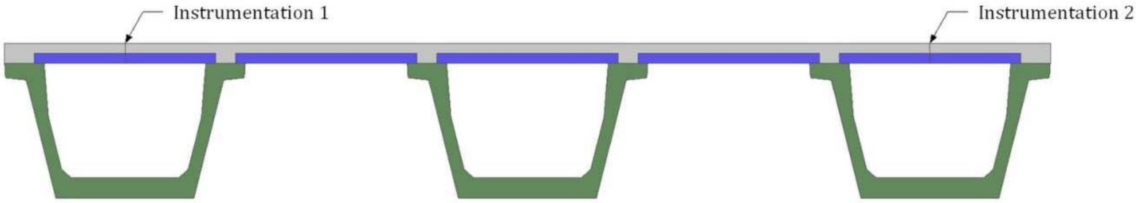

Figure 7.43: Instrumentation locations.

7.5.2 Field Observations

A commercial weather station was set up on site prior to the pour and programed to record temperature, relative humidity, solar radiation, and wind speed on a 15-minute interval.

Concrete placement began early on August 17, 2011, and reached the opaque sensors at approximately 1:15 a.m. soon followed by the black sensors at 1:25 a.m. Shortly after, the pump truck was forced to relocate to the other side of a light post, causing a 1-hour delay in concrete placement; as a result, the white sensors weren't reached until 2:35 a.m. Midway through the pour, 4x8-in. cylinders were taken for mechanical testing, at which point the most important step remained: curing. A curing compound was sprayed on the deck; however, hours went by as the construction team waited for curing blankets. Finally, around noon, a single construction worker arrived to place curing blankets and plastic.

Several days later, the team returned to pull temperature data from the sensors to find that concrete formwork and other miscellaneous construction materials had been piled over the temperature sensors, thus mitigating any effects of weather conditions on the concrete temperature. Considering the circumstances and looking at the data, it's difficult to arrive at any conclusions. The concrete cured with opaque and white plastic exhibited nearly identical behavior, whereas the white plastic experienced significantly lower temperatures. Figure 7.44, Figure 7.45, and Figure 7.46 provide the time temperature history for the bridge decks with the different curing plastics.

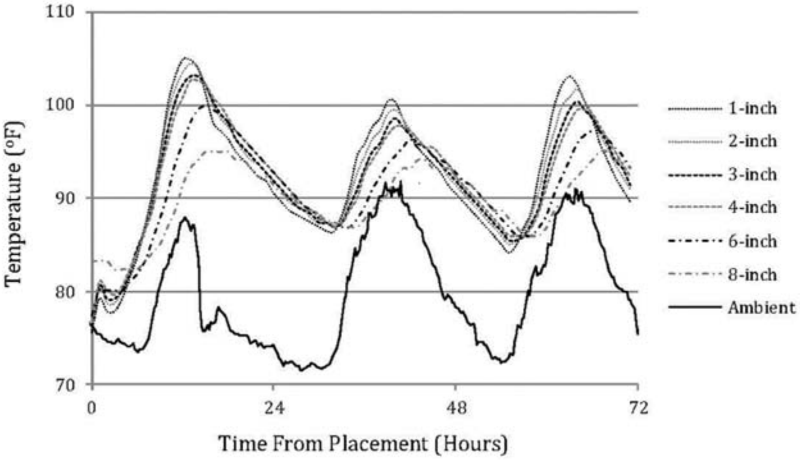

Figure 7.44: Temperature vs. time (opaque curing plastic).

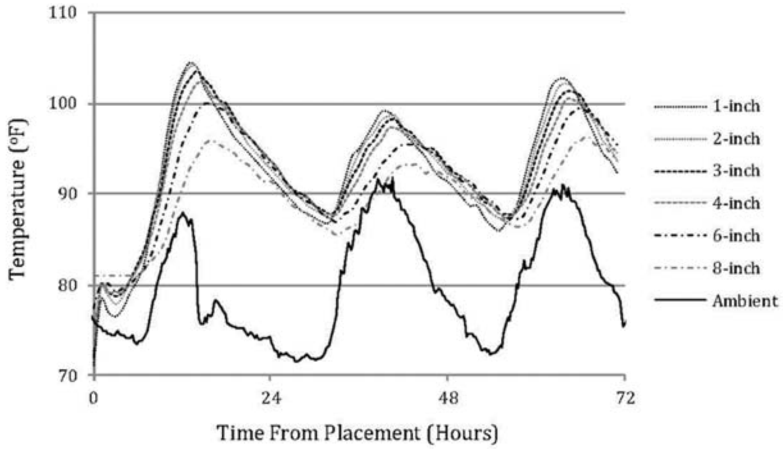

Figure 7.45: Temperature vs. time (black curing plastic).

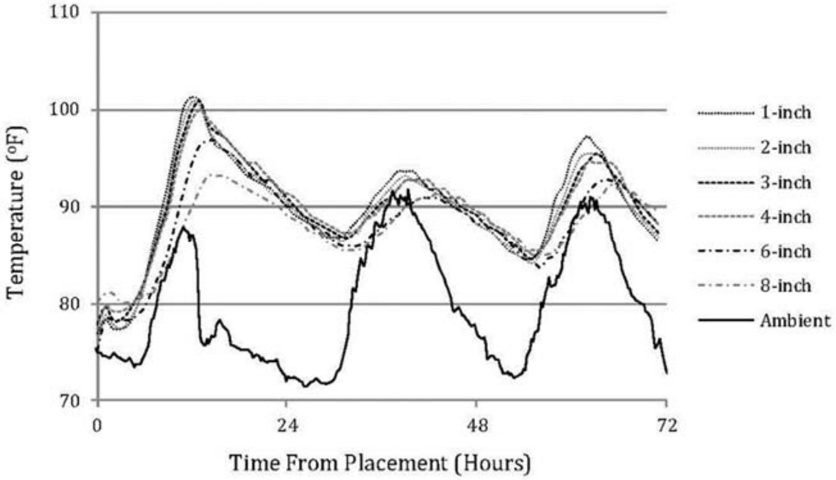

Figure 7.46: Temperature vs. time (white curing plastic).

7.6 Austin Bridge Deck (SBWB Ramp)

With the multitude of difficulties faced on the first bridge deck instrumentation, the research team wanted to make another attempt. On November 22, 2011, the westbound SH71 to southbound IH35 ramp was instrumented. This time, only one set of sensors was installed per panel and the temperature sticks were carefully monitored during the pour to ensure they weren't stepped on. Wires were also made long enough that the sensors could be placed between U-beams.

7.6.1 Instrumentation

As Figure 7.47 depicts, the WBSB ramp is supported by two U-beams; therefore, sensors were placed at the very center of the deck between the beams. Cables were zip-tied to the rebar and exited the concrete through the formwork on one side for later access, as Figure 7.48 shows.

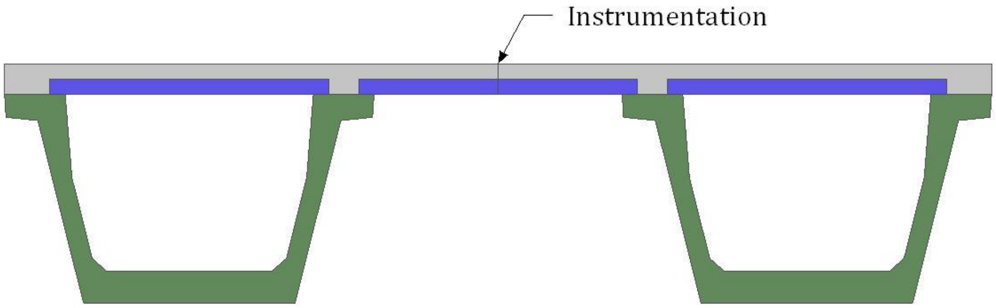

Figure 7.47: Bridge deck instrumentation location.

Figure 7.48: Installed temperature sensors.

7.6.2 Field Observations

A commercial weather station was set up on site prior to the pour and programmed to record temperature, relative humidity, solar radiation, and wind speed on a 15-minute interval.

Concrete reached the black sensors at approximately 8:25 p.m., the white at 8:35 p.m., and the opaque at 9:10 p.m. In the middle of the pour, 4x8-in. cylinders were taken for mechanical testing. Again, a curing compound was sprayed on the deck and after completing the 800-cubic yard pour with no problems, the contractor placed curing blankets and plastic. In the days following, considerable time was spent at the site to ensure the research area was kept free of materials and after 7 days, data was pulled from the sensors. Figure 7.49 shows the different plastic sheathing placed on the different sections of the bridge deck.

Figure 7.49: Bridge deck during removal of curing

Figure 7.50, Figure 7.51, and Figure 7.52 show the results of the black, white, and opaque curing plastics respectively. The graphs are rather busy; however, it is apparent that the opaque plastic caused the greatest concrete temperatures by a significant margin. Even more interesting, the opaque plastic had a profound effect on the temperature distribution through the deck. Whereas the sections cured with white and black curing plastic exhibited relatively uniform temperatures, the concrete cured with opaque plastic higher temperatures with decreasing depth.

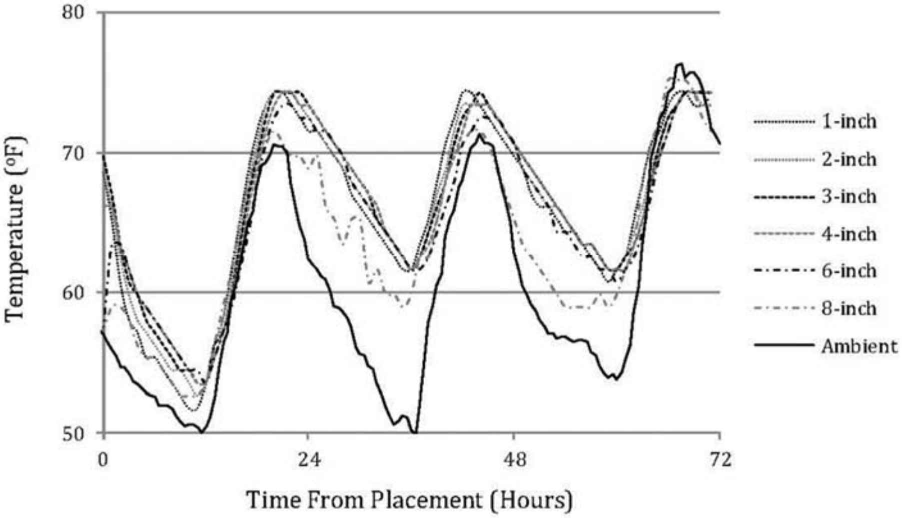

Figure 7.50: Temperature vs. time (black curing plastic).

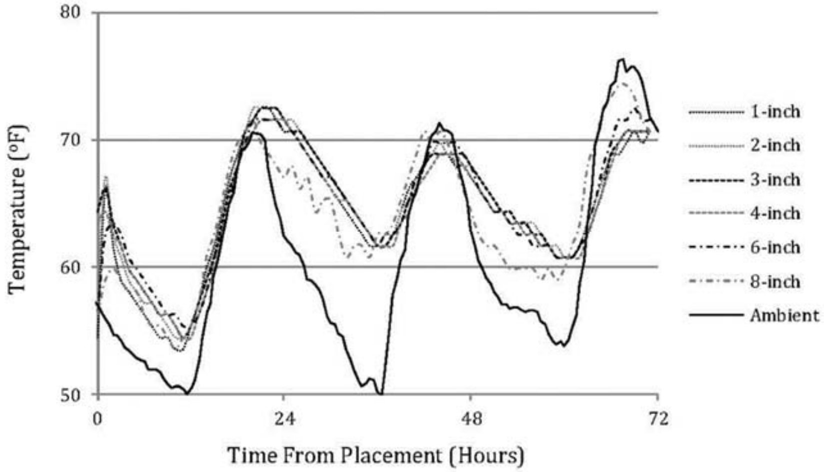

Figure 7.51: Temperature vs. time (white curing plastic).

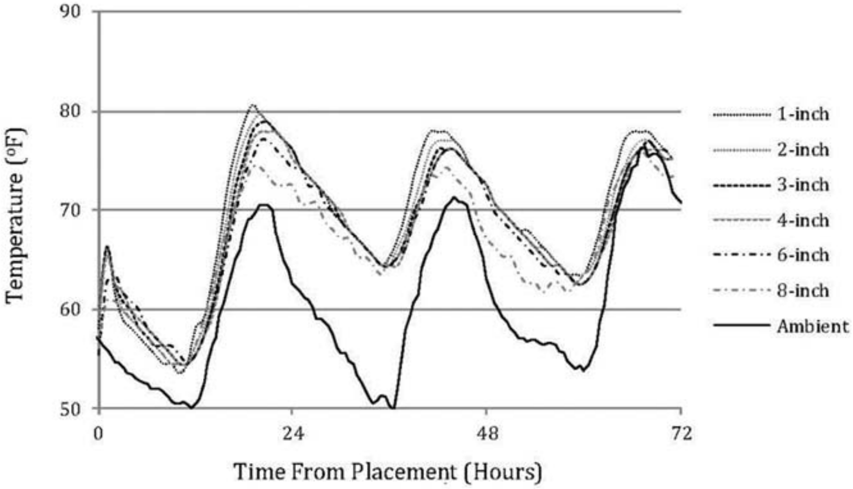

Figure 7.52: Temperature vs. time (opaque curing plastic).

Perhaps the greatest impact the curing plastics have on the cracking susceptibility of the concrete is on maturity. Figure 7.53 plots the maturity at the midpoint of the cast-in-place section, approximately 2 in. below the surface, for each plastic. It's obvious the opaque plastic increased maturity, so Figure 7.54 attempts to quantify the result by comparing the increase in maturity of the black and opaque plastics compared to the white. After three days, the opaque plastic increased maturity by approximately 270 °F-hours beyond the white plastic. The black plastic, on the other hand, increased maturity over the white plastic by only 90 °F-hours. This general trend appears to make sense as we would expect the black plastic to absorb the most solar radiation while the white should be reflective.

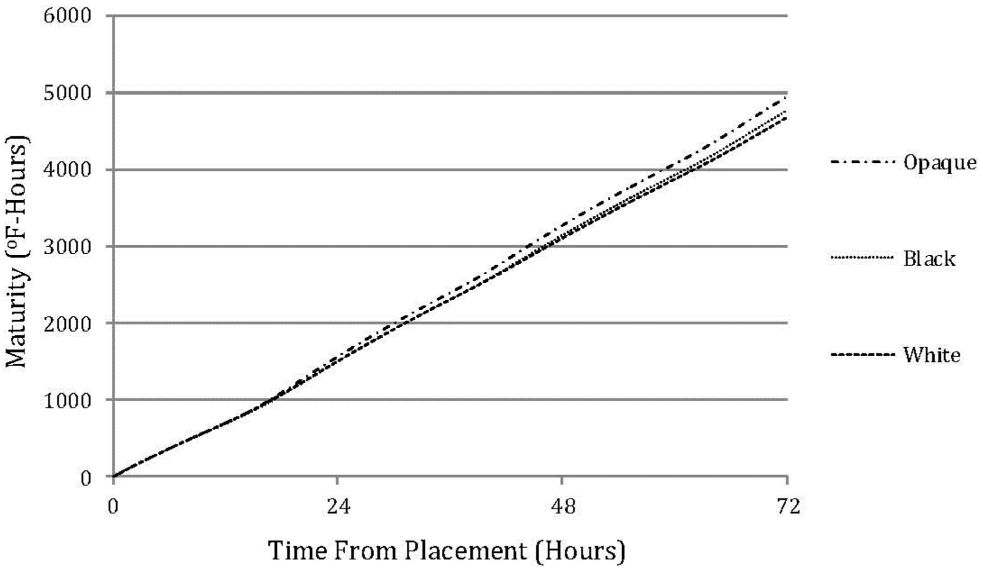

Figure 7.53: Time temperature history at 2-in. below surface.

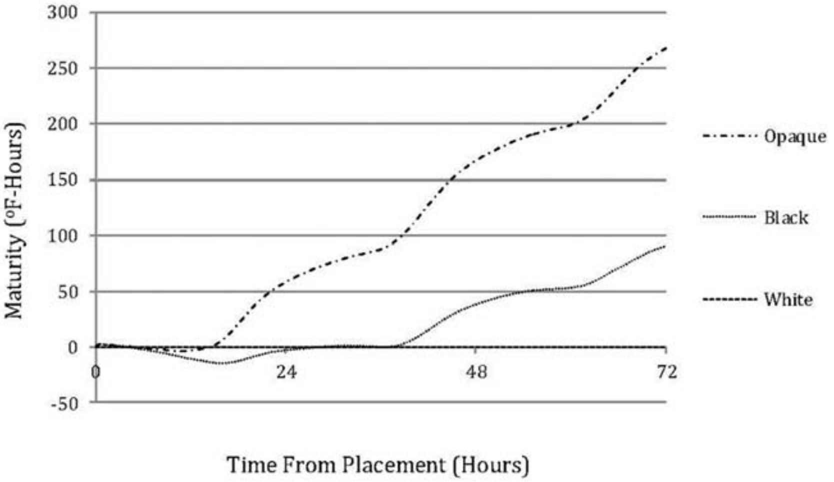

Figure 7.54: Time temp delta at 2-in. below surface (white plastic as baseline).

7.6.3 Discussion

The results fall directly in line with what was expected as the curing plastics all affect incoming solar radiation. The white plastic would be expected to reflect the most solar radiation compared to the black and opaque; therefore, it makes sense that it also exhibited the lowest temperatures and the most uniform temperature distribution. The black plastic, not nearly as reflective as the white, absorbs more solar radiation. Its dark color, however, does not allow for efficient transfer to the concrete below and exhibited only minor increases in temperature. Finally, the opaque plastic allows efficient transfer of solar radiation and, as a result, higher temperatures and maturity—particularly near the surface.

7.6.4 Conclusion and Recommendations

The first bridge deck instrumentation endured many difficulties that would likely preclude it from consideration in the calibration and validation of ConcreteWorks predictive model. The general advice is to use white plastic to maximize uniformity of temperatures as well as mechanical properties. The second instrumentation appears to provide solid information; however, many questions remain to truly understand the effect it has on bridge deck cracking. Some recommendations for future research are as follows:

- A closer look at maturity as it relates to mechanical properties
- CTE testing and/or estimation
- Theoretical analysis of the energy absorption and transfer through the various plastics

Chapter 8. Conclusions and Implementation of Findings into ConcreteWorks Bridge Deck Cracking Module

8.1 Conclusions

Some of the more relevant and important conclusions from this study are as follows:

- Straight cement mixtures generate more heat during hydration than mixtures that contain SCMs, and therefore have higher peak temperatures. High-alkali cements generate more heat and have higher peak temperatures than do low-alkali cements.
- Mixtures incorporating ground granulated blast furnace slag have the lowest peak temperatures. Higher replacements of GGBFS result in lower temperatures than do lower replacements.
- After 96 hours of hot weather simulation, GGBFS and Class F fly ash mixtures had generated the lowest maximum stress. However, when inducing cracking, the stress at cracking and the stress/strength ratio at cracking for the Class F fly ash mixtures were also the lowest. The reserve stress/strength ratio was also the lowest for the Class F fly ash mixtures. Class F fly ash mixtures appeared to be more susceptible to early age cracking.
- After 96 hours of hot weather simulation, Class C fly ash and Control mixtures had the highest maximum stresses. However, the Class C fly ash and Control mixtures also had the highest cracking stresses and therefore high reserve stress/strength ratios.
- Under hot weather simulation, slag-containing mixtures had the lowest maximum stress over the course of 96 hours, and the highest stresses at cracking. This resulted in the largest reserve stress/strength ratio of the mixtures evaluated. Slag-containing mixtures were determined to be the least susceptible to early-age cracking.
- Under cold weather simulations, cracking could not be induced in any of the mixtures evaluated, due to the inability to generate a great enough differential between the concrete temperature and the temperature at initial set. However, after 96 hours of simulation, the Control mixtures had generated the highest maximum stress, and Class F fly ash mixtures had generated the lowest maximum stresses.
- The research team was unable to induce cracking in any of the mixtures containing limestone coarse aggregate. Maximum 96-hour stresses under hot and cold weather simulations were lower for the limestone mixtures than for any other mixtures. Limestone mixtures, during artificial cooling, were able to withstand temperature differentials between the concrete temperature and the temperature at initial set in excess of 35°F. In the river gravel mixtures that cracked, cracking usually occurred at a temperature differential less than 20°F. The reduced coefficient of thermal expansion of limestone results in a considerable decrease in early-age cracking risk.
- Reducing pore water surface tension via shrinkage-reducing admixtures is effective at minimizing the effects of chemical and autogenous shrinkage.

- A novel technique for measuring the early-age tensile strength of concrete was developed. When tests were performed at common ages, the tensile strength measured using this new, direct tension apparatus generally agreed with the data generated from splitting tensile tests, justifying the use of splitting tensile strength as predicted by ConcreteWorks.
- The choice of curing method can have a large impact on the peak concrete temperature. Black plastic exposed to direct sunlight should be avoided during the summer months. In winter months, black plastic may be effective in increasing the rate of mechanical strength development by transferring heat to the concrete through solar radiation.

8.2 Implementation of Findings into ConcreteWorks

Significant progress was made under this project in understanding and quantifying the parameters that impact the potential for bridge deck cracking. A new version of Concrete Works, Version 3.0, was developed under this project and has been submitted to TxDOT, along with a revised user's manual describing the modifications and improvements made to the project with regard to bridge deck cracking. The following are the main components for the newly developed bridge deck cracking module:

- A new **creep** model was developed under this project, as described in Chapter 5. This innovative model bridges the historical gap between early-age and later-age creep and serves as the basis for creep modeling and stress prediction in ConcreteWorks 3.0.
- The data generated using a new **early-age tensile strength** apparatus provided valuable information on very early tensile development and allowed for comparisons with splitting tensile strength data for selected common ages. The results confirm that the use of a computed splitting tensile strength (based on measured compressive strength) is suitable for predicting bridge deck cracking.
- A significant database of **drying shrinkage** data was generated and analyzed under this project. A wide range of materials, mixture proportions, and curing regimes were evaluated, and the results were compared to several predictive models. Based on these efforts, the B3 Model was selected for predicting the drying shrinkage of concrete bridge decks.
- With regard to **plastic shrinkage**, currently no known models are available for assessing the bleeding rate of different concrete mixtures at differing temperatures to know how much protective bleed is available at a given time. Significant emphasis was placed under this project on measuring the bleeding of various concrete mixtures, but it was not possible to develop a robust predictive model that can properly address the various factors affecting bleeding, including materials used, mixture proportions, admixtures, slump, etc. A predictive model was, however, integrated into ConcreteWorks 3.0 that predicts an evaporation rate of water from a bridge deck, based on Schindler (2002). The model is based on the work of Menzel that applied water evaporation rate equations developed by Koehler to concrete.

- **Autogenous** and **thermal** (heat of hydration) strains are calculated as in ConcreteWorks 2.0. Significant data have been generated under this project and TxDOT Project 4563, and this database serves as the basis for predicting heat of hydration and thermal distributions in hydrating bridge decks.

Bridge deck stresses are calculated in ConcreteWorks 3.0 for the first year of service life. The analysis is performed in two stages. First, the concrete stresses are calculated for the time period before the curing methods are removed. During this initial period, the stresses are calculated every half hour. The free concrete strain used to calculate the elastic stress and ultimately creep adjusted stress include thermal and autogenous shrinkage effects as described in Section 4.2.4. The modeled bridge deck temperature is used in the thermal strain calculations. The degree of restraint and elastic modulus is then used to calculate the elastic stress from the free strain. A degree of restraint of 1.0 is used for the concrete bridge decks made with concrete panels as a conservative measure of the larger restraint provided by the panels. A degree of restraint of 0.6 is used for the remaining bridge deck types to simulate the resistance to curvature and movement provided by composite action between the deck and girders (Krauss and Rogalla, 1996). The modified B3 creep model used to relax the elastic stresses calculated is described in detail in Chapter 5.

The free concrete strain after curing methods are removed is calculated using 24 hour time steps. The average daily environmental temperatures are used to calculate the thermal strains. The autogenous strains used in the free strain analysis are those described in Section 4.2.4. Drying shrinkage free strains are calculated using the B3 Model (ACI 209.2, 2008). The relative humidity measurements used in the drying shrinkage strain calculations are assumed to decrease linearly during the first 60 days from 100% relative humidity to the average daily environment relative humidity. Additionally, to be conservative, the relative humidity is also assumed not to increase after decreasing below 100%. The free strains are then multiplied by the elastic modulus and degree of restraint to calculate the elastic stress. Stress relaxation is then applied to the elastic stress using the Modified B3 Model. The stress calculated at the end of the curing period is added after relaxation to the relaxed long term stress to give the total stress from the two periods. The results are plotted against the modeled concrete tensile strength development for the user to see the potential for deck cracking.

8.3 Recommendations for Future Research

The following research is recommended to further understand early-age concrete behavior:

- Further testing within the rigid cracking frame to capture the stresses generated during the temperature drop that is typical when curing blankets and/or plastic are removed.
- Further testing within the rigid cracking frame to evaluate the stresses developed under temperature profiles generated from field instrumentation.
- Further testing within the rigid cracking frame to evaluate the performance of mixtures with no admixtures, and with higher range water reducers and retarders.
- Further evaluation of setting time under simulated temperature profiles with varying concrete placement temperatures.

- Further instrumentation of field and possibly laboratory specimens to better understand the effects of different curing methods on the temperature development of concrete during summer and winter months.
- Further instrumentation of field and possibly laboratory specimens to better understand the interplay between localized environmental conditions underneath concrete bridge decks, and their effects on early-age concrete temperature development.
- Implementation of the newly developed bridge deck cracking module within ConcreteWorks, with the goal of further calibrating and validating the model.

Appendix A: Rigid Cracking Frame Mixture Information

A.1 Sample Report from ConcreteWorks for Mixture CL-RG

Parameter	Value	Units
Results		
TxDOT 2004 Specifications Used		
Max Temperature	115	°F
This mix is not ASR susceptable as defined by:	TxDOT	
Original Concrete Materials CO2 emissions	10	lb/yd³
Steel Corrosion Results		
Time to Top steel Corrosion	19	Years
Time to Concrete Damage From Top Mat Steel Corrosion	25	Years
Time to Bottom Steel Corrosion	> 20	Years
Time to Concrete Damage From Bottom Mat Steel Corrosion	> 26	Years
General Inputs		
Project Location	Lubbock	
Unit System	English	
Chloride Units	Percent of Concrete	
Life Cycle Analysis Duration	20	Years
Analysis Duration	7	days
Concrete placement time	10	am
Concrete placement date	8/15/2008	
Member Inputs		
Shape Choice	Permanent Metal Decking Deck	

Parameter	**Value**	**Units**
Deck Thickness	8	inches
Top Mat Cover	2	inches
Bottom Mat Cover	5.75	inches
Mixture Proportions		
Cement Content	564	lb/yd³
Water Content	254	lb/yd³
Coarse Aggregate Content	1941	lb/yd³
Fine Aggregate Content	1232	lb/yd³
Air Content	2	%
Chemical Admixture ASTM C494	Type A, NRWR	
Chemical Admixture ASTM C494	Type B, Retarder	
Material Properties		
Cement Type	I/II	
C3S content	62.398	%
C2S content	10.525	%
C3A content	5.448	%
C4AF content	11.077	%
Free CaO content	0.9	%
SO3 content	3.07	%
MgO content	0.7	%
Alkali content	0.47	%

Parameter	**Value**	**Units**
Concrete Fresh Temperature	73	°F
Blanket R-Value	2.91	°F
Cure Method Application Age	1	hrs
Cure Method Application Age	1	hrs
White Cure Plastic Used		
Corrosion Inputs		
Top Steel Type	Black Steel	
Bottom Steel Type	Black Steel	
Cast-In-Place Dref	108.9	x 10^-13 (m^2/s)
Cast-In-Place m	0.26	
No Barrier Method Selected		
Exposure Class	Urban Road	

A.2 Sample Report from ConcreteWorks for Mixture F3L-35RGC

Parameter	**Value**	**Units**
Results		
TxDOT 2004 Specifications Used		
Max Temperature	64	°F
This mix is ASR susceptable as defined by:	TxDOT	
Original Concrete Materials CO2 emissions	10	lb/yd³
Steel Corrosion Results		
Time to Top steel Corrosion	> 20	Years
Time to Concrete Damage From Top Mat Steel Corrosion	> 26	Years
Time to Bottom Steel Corrosion	> 20	Years
Time to Concrete Damage From Bottom Mat Steel Corrosion	> 26	Years
General Inputs		
Project Location	Lubbock	
Unit System	English	
Chloride Units	Percent of Concrete	
Life Cycle Analysis Duration	20	Years
Analysis Duration	7	days
Concrete placement time	10	am
Concrete placement date	2/17/2008	
Member Inputs		
Shape Choice	Permanent Metal Decking Deck	

Parameter	**Value**	**Units**
Deck Thickness	8	inches
Top Mat Cover	2	inches
Bottom Mat Cover	5.75	inches
Mixture Proportions		
Cement Content	366.6	lb/yd³
C Fly Ash Content	197.4	lb/yd³
Water Content	254	lb/yd³
Coarse Aggregate Content	1923	lb/yd³
Fine Aggregate Content	1220	lb/yd³
Air Content	2	%
Chemical Admixture ASTM C494	Type A, NRWR	
Chemical Admixture ASTM C494	Type B, Retarder	
Material Properties		
Cement Type	I/II	
C3S content	62.398	%
C2S content	10.525	%
C3A content	5.448	%
C4AF content	11.077	%
Free CaO content	0.9	%
SO3 content	3.07	%
MgO content	0.7	%

Parameter	**Value**	**Units**
Alkali content	0.47	%
Blaine Fineness	371.5	m^2/kg
Activation Energy	25593.502	J/mol
Alpha	1	
Tau	34.748	hrs
Beta	0.718	
Hu	448133.272	
Coarse Agg. type	Siliceous River Gravel	
Fine Agg. type	Siliceous River Sand	
Coarse Agg. type	Siliceous River Gravel	
Fine Agg. type	Siliceous River Sand	
Mechanical Properties		
Maturity Method	Nurse-Saul	
Environment Inputs Summary		
Ave. Daily Max Temp.	55.4	°F
Ave. Daily Min Temp.	33.1	°F
Ave. Max Daily Solar Radiation	630.1	W/m^2
Ave. Max Daily Wind Speed	17.9	m/s
Ave. Max Relative Humidity	71.5	%
Ave. Min Relative Humidity	39	%

Parameter	Value	Units
Construction Inputs		
Concrete Fresh Temperature	65	°F
Blanket R-Value	5.67	°F
Cure Method Application Age	1	hrs
Cure Method Application Age	1	hrs
White Cure Plastic Used		
Corrosion Inputs		
Top Steel Type	Black Steel	
Bottom Steel Type	Black Steel	
Cast-In-Place Dref	108.9	x 10^-13 (m^2/s)
Cast-In-Place m	0.54	
No Barrier Method Selected		
Exposure Class	Urban Road	

A.3 Rigid Cracking Frame Results

A.3.1 Control Mixtures

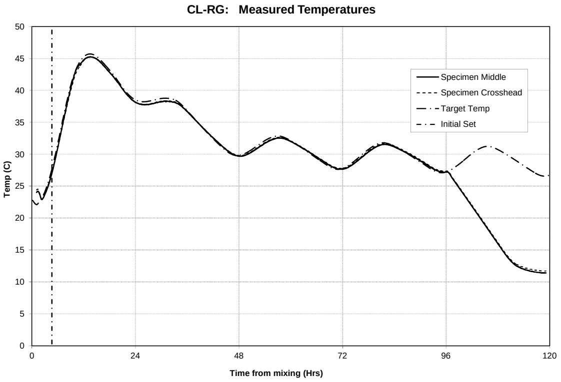

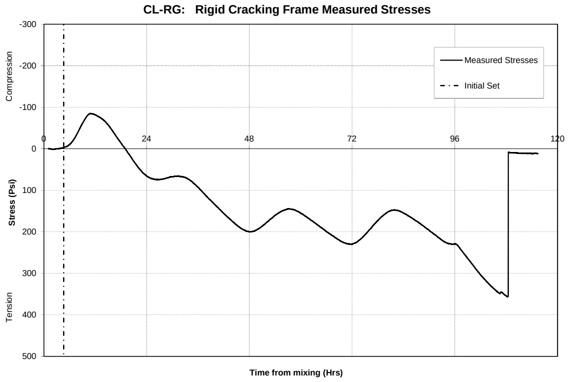

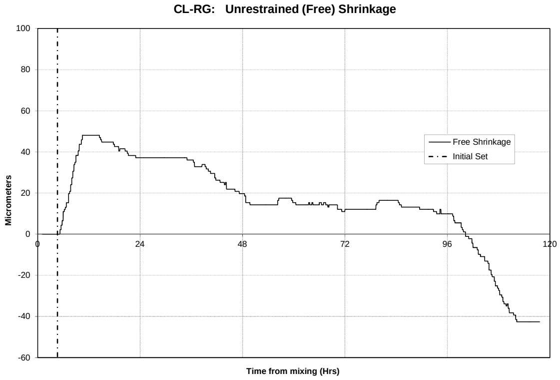

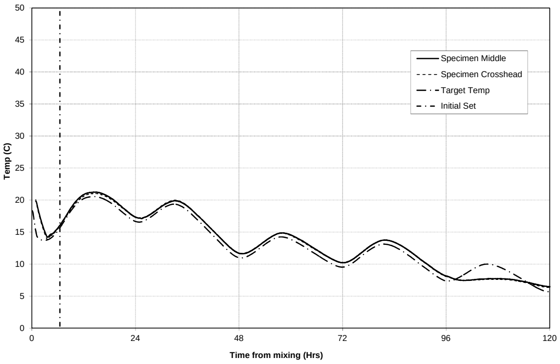
CL-RGC: Measured Temperatures

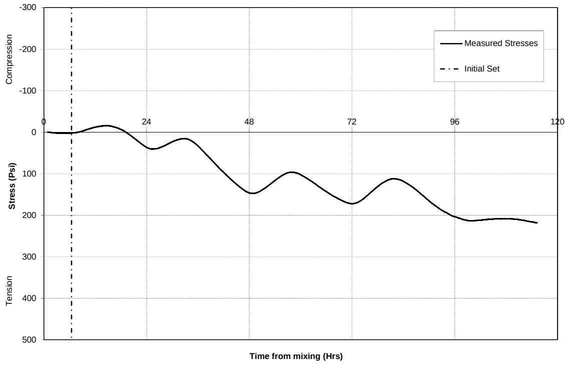
CL-RGC: Rigid Cracking Frame Measured Stresses

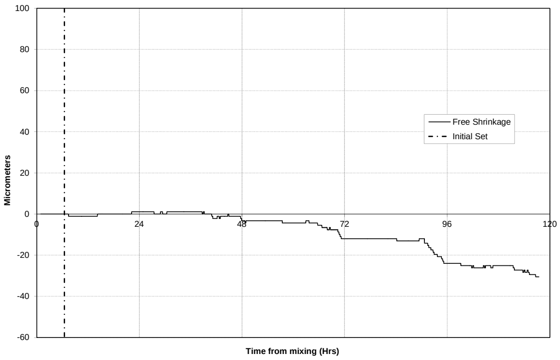
CL-RGC: Unrestrained (Free) Shrinkage

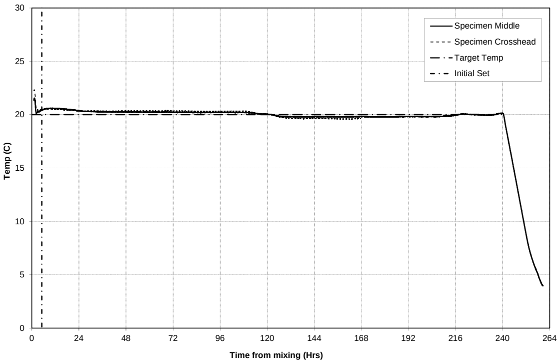
CL-RGI: Measured Temperatures

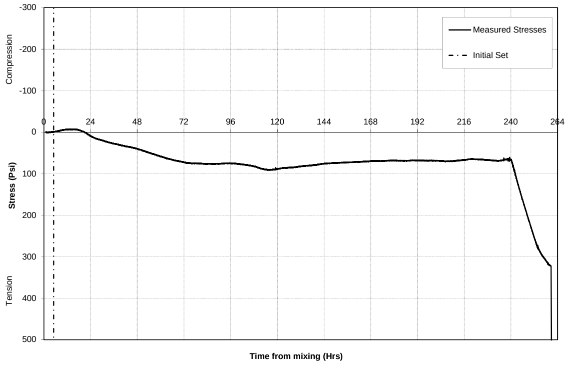
CL-RGI: Rigid Cracking Frame Measured Stresses

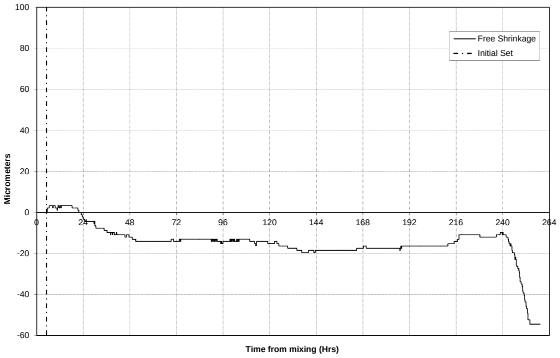
CL-RGI: Unrestrained (Free) Shrinkage

CH-RG: Measured Temperatures

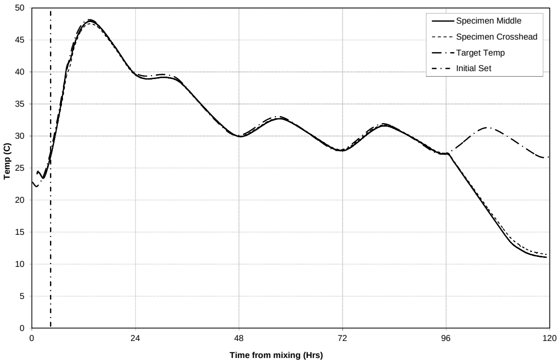

CH-RG: Rigid Cracking Frame Measured Stresses

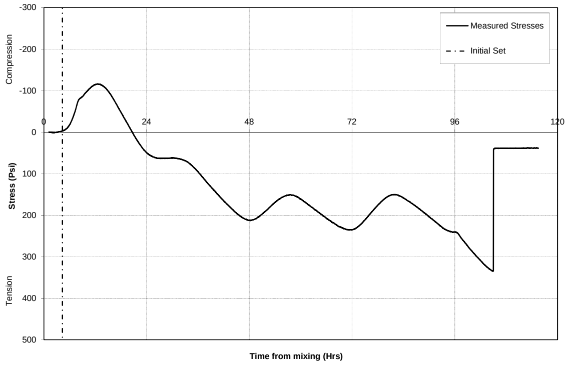

CH-RG: Unrestrained (Free) Shrinkage

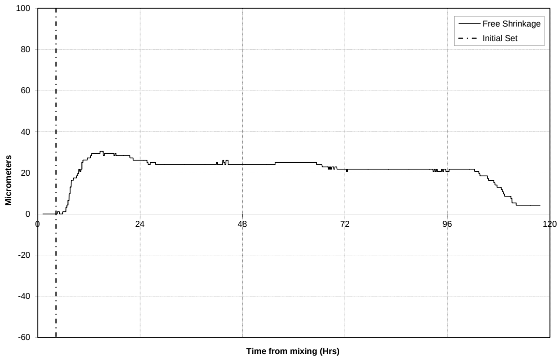

CH-RGC: Measured Temperatures

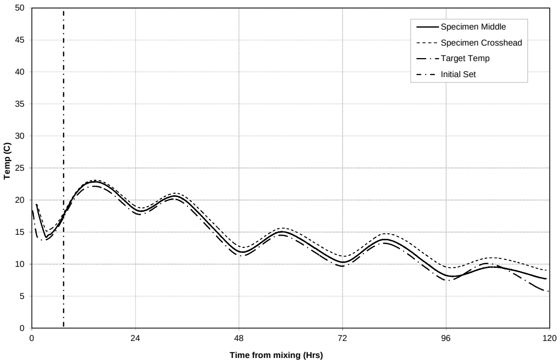

CH-RGC: Rigid Cracking Frame Measured Stresses

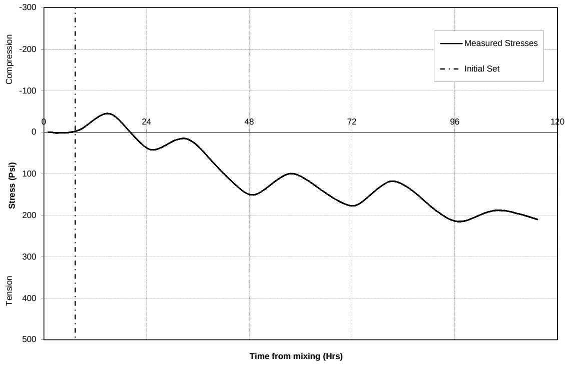

CH-RGC: Unrestrained (Free) Shrinkage

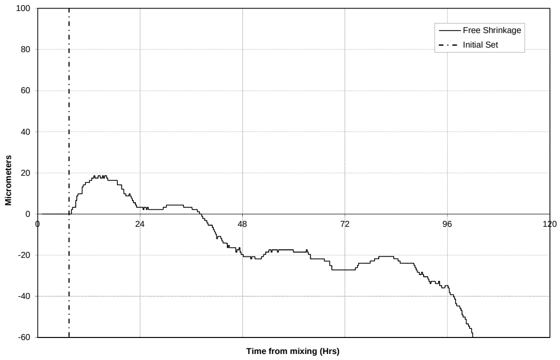

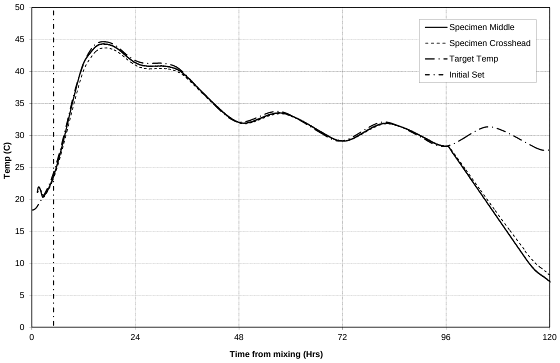

CL-LS: Measured Temperatures

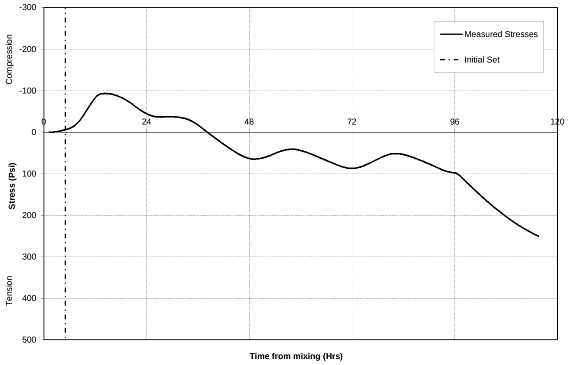

CL-LS: Rigid Cracking Frame Measured Stresses

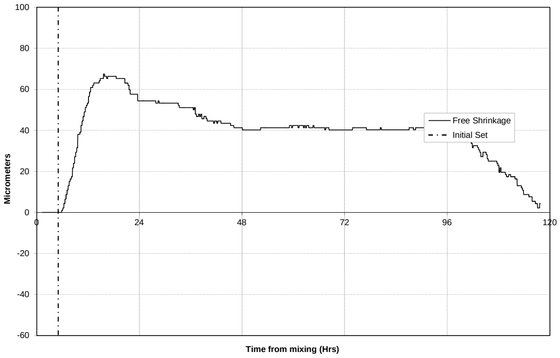

CL-LS: Unrestrained (Free) Shrinkage

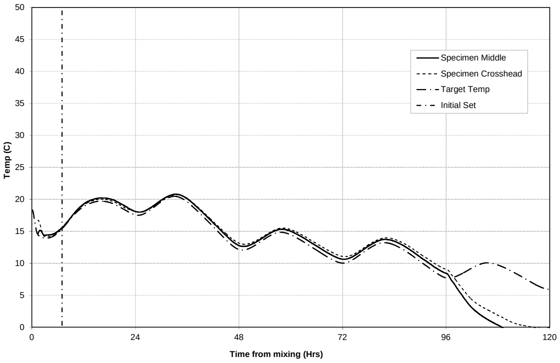

CL-LSC: Measured Temperatures

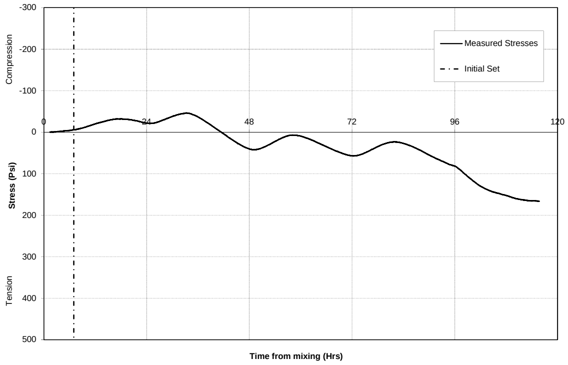

CL-LSC: Rigid Cracking Frame Measured Stresses

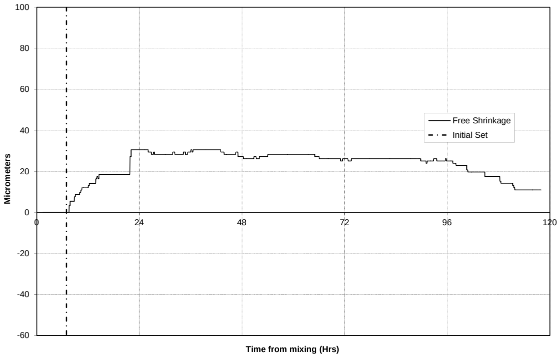

CL-LSC: Unrestrained (Free) Shrinkage

A.3.2 Class C Fly Ash Mixtures

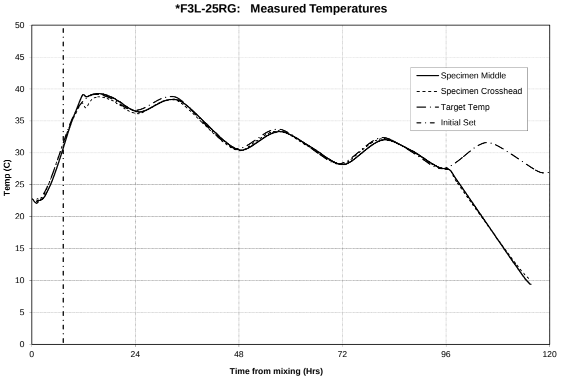
***F3L-25RG: Measured Temperatures**

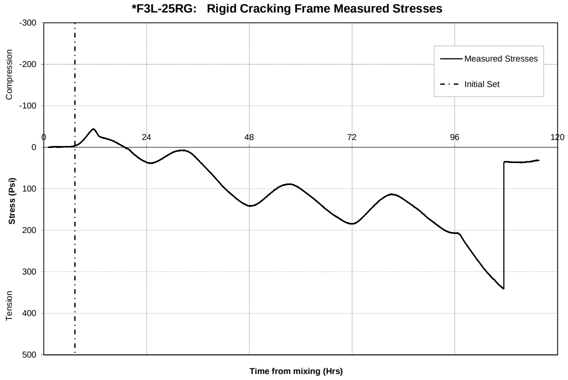
***F3L-25RG: Rigid Cracking Frame Measured Stresses**

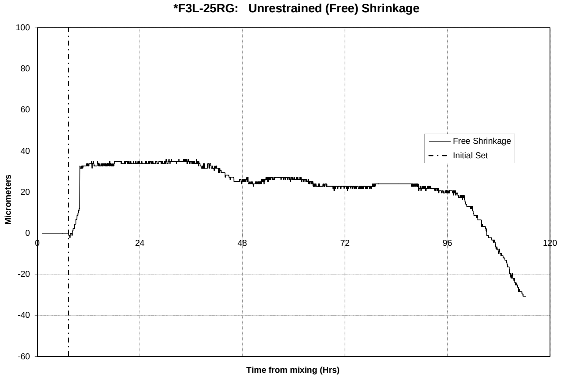
***F3L-25RG: Unrestrained (Free) Shrinkage**

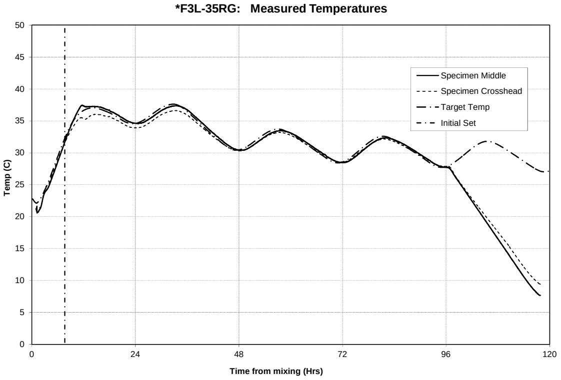
***F3L-35RG: Measured Temperatures**

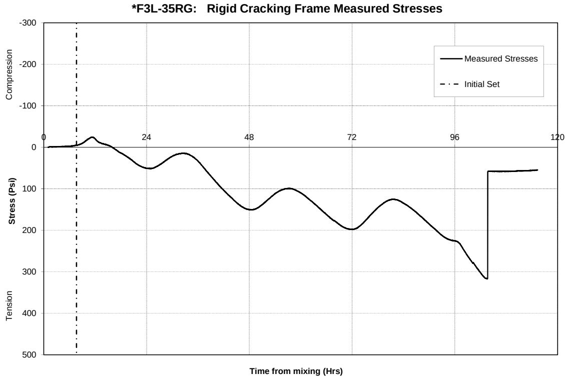
***F3L-35RG: Rigid Cracking Frame Measured Stresses**

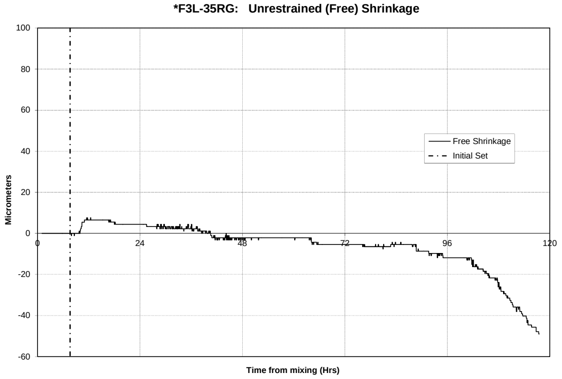
***F3L-35RG: Unrestrained (Free) Shrinkage**

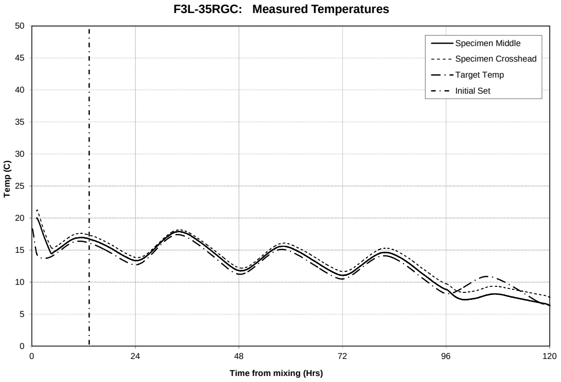
F3L-35RGC: Measured Temperatures
Temp (C)
0
5
10
15
20
25
30
35
40
45
50
Time from mixing (Hrs)
0
24
48
72
96
120
Specimen Middle
Specimen Crosshead
Target Temp
Initial Set

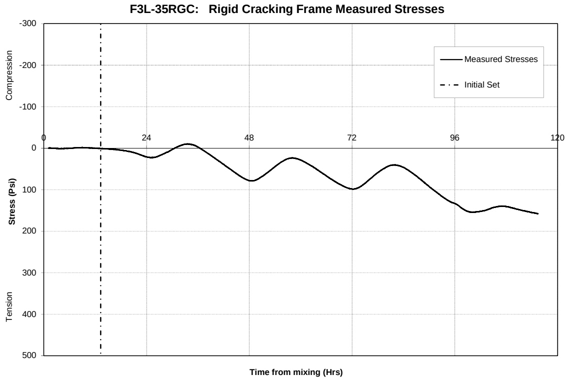
F3L-35RGC: Rigid Cracking Frame Measured Stresses
Compression
Tension
Stress (Psi)
-300
-200
-100
0
100
200
300
400
500
0
24
48
72
96
120
Time from mixing (Hrs)
Measured Stresses
Initial Set

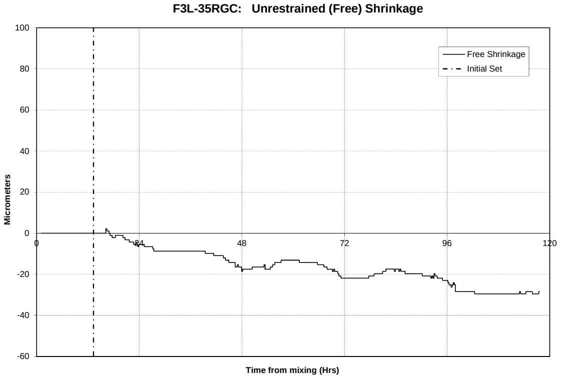
F3L-35RGC: Unrestrained (Free) Shrinkage
Micrometers
100
80
60
40
20
0
-20
-40
-60
0
24
48
72
96
120
Time from mixing (Hrs)
Free Shrinkage
Initial Set

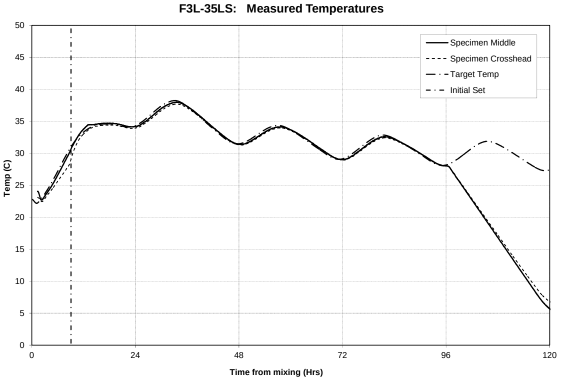
F3L-35LS: Measured Temperatures
Temp (C)
0
5
10
15
20
25
30
35
40
45
50
Time from mixing (Hrs)
0
24
48
72
96
120
Specimen Middle
Specimen Crosshead
Target Temp
Initial Set

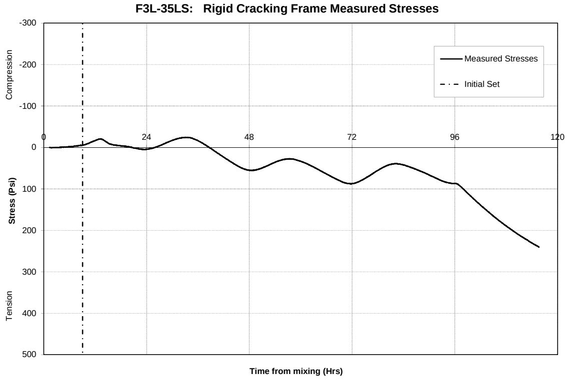
F3L-35LS: Rigid Cracking Frame Measured Stresses
Compression
Tension
Stress (Psi)
-300
-200
-100
0
100
200
300
400
500
0
24
48
72
96
120
Time from mixing (Hrs)
Measured Stresses
Initial Set

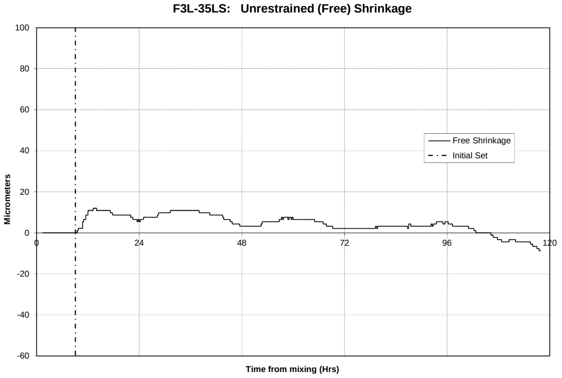
F3L-35LS: Unrestrained (Free) Shrinkage
Micrometers
100
80
60
40
20
0
-20
-40
-60
0
24
48
72
96
120
Time from mixing (Hrs)
Free Shrinkage
Initial Set

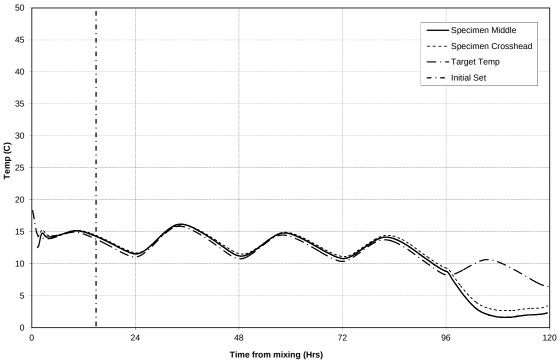
F3L-35LSC: Measured Temperatures

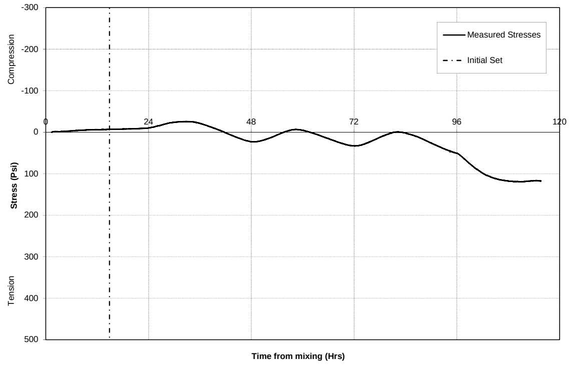
F3L-35LSC: Rigid Cracking Frame Measured Stresses

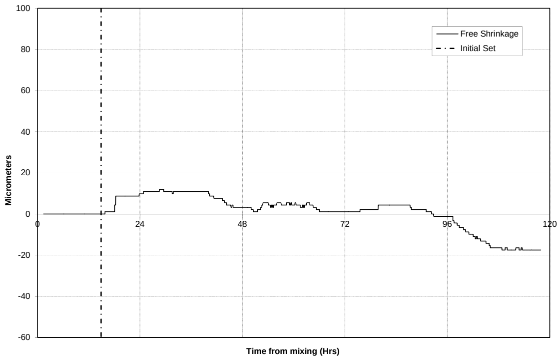
F3L-35LSC: Unrestrained (Free) Shrinkage

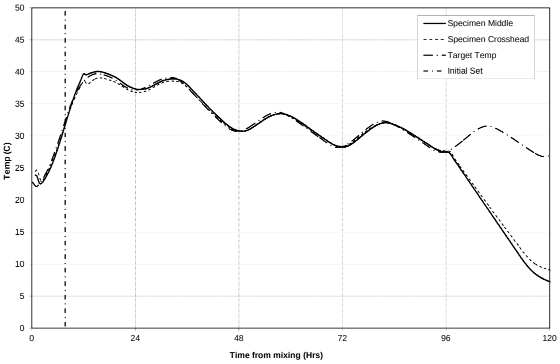
*F4L-25RG: Measured Temperatures

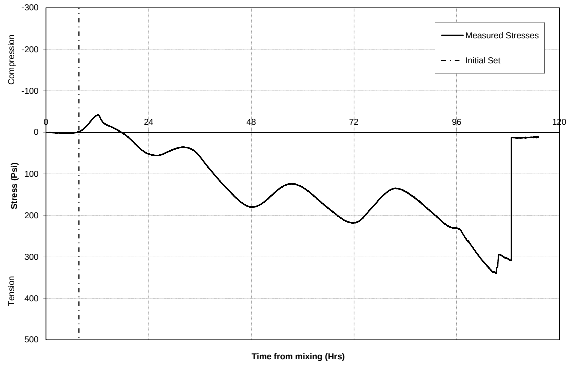
*F4L-25RG: Rigid Cracking Frame Measured Stresses

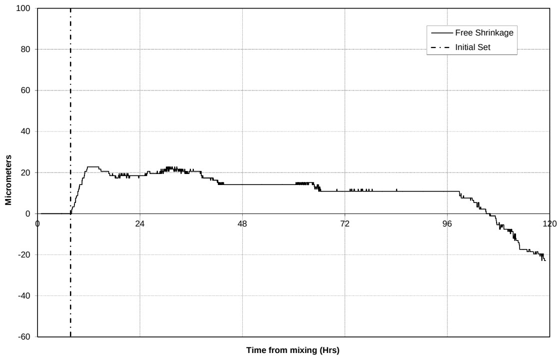
*F4L-25RG: Unrestrained (Free) Shrinkage

F4L-35RGC: Measured Temperatures

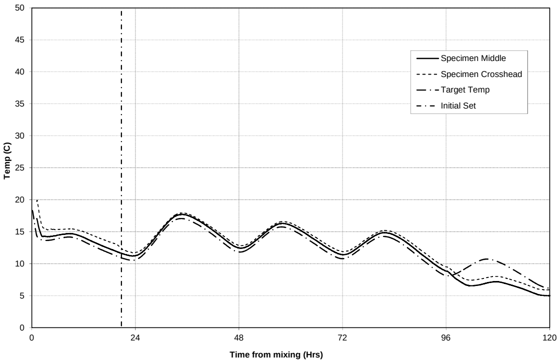

F4L-35RGC: Rigid Cracking Frame Measured Stresses

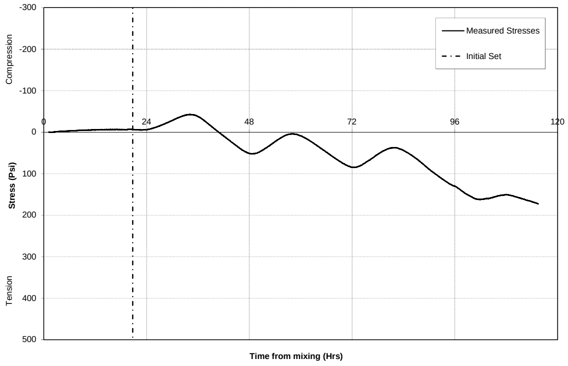

F4L-35RGC: Unrestrained (Free) Shrinkage

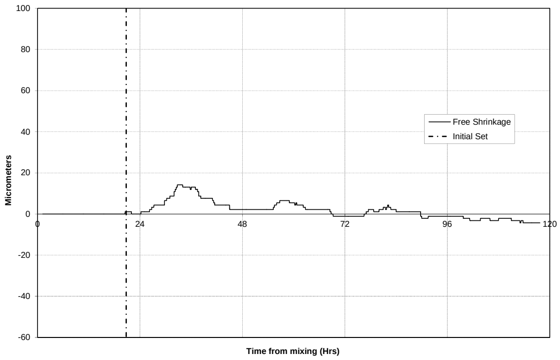

*F4H-25RG: Measured Temperatures

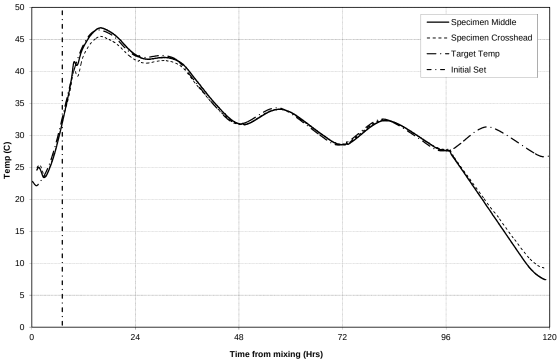

*F4H-25RG: Rigid Cracking Frame Measured Stresses

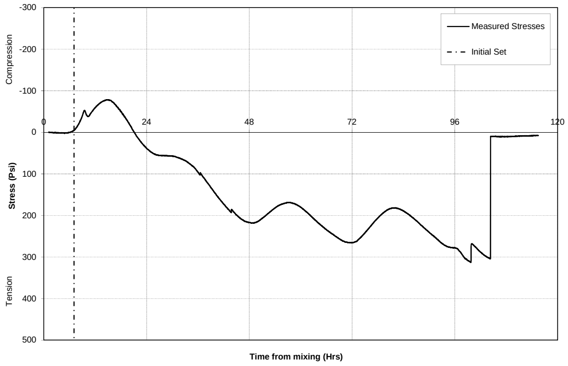

*F4H-25RG: Unrestrained (Free) Shrinkage

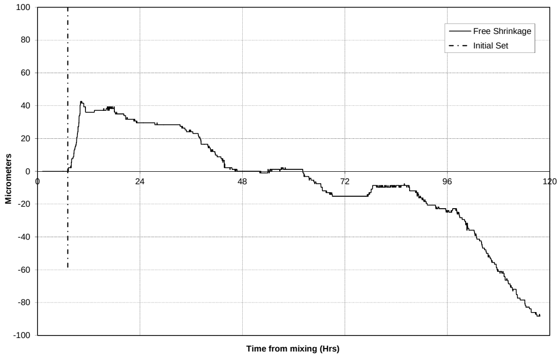

F4H-35RG: Measured Temperatures

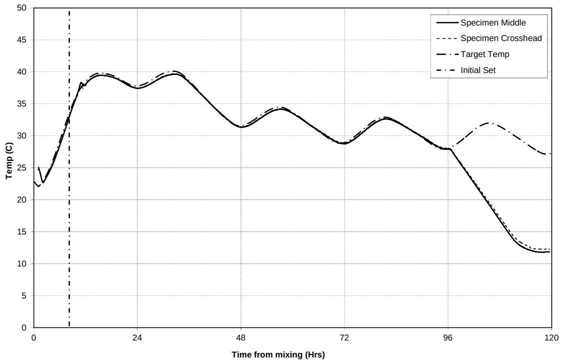

F4H-35RG: Rigid Cracking Frame Measured Stresses

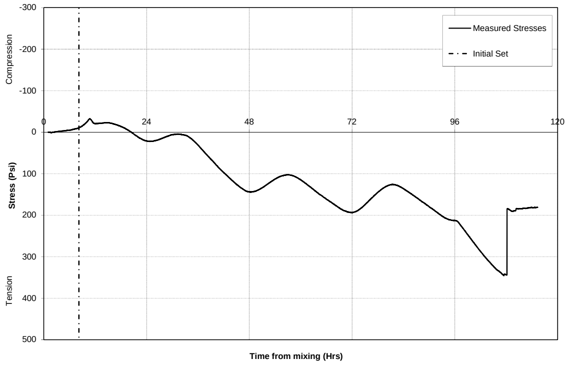

F4H-35RG: Unrestrained (Free) Shrinkage

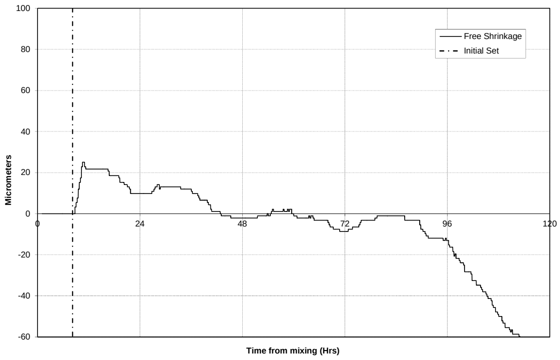

F4H-35RGC: Measured Temperatures

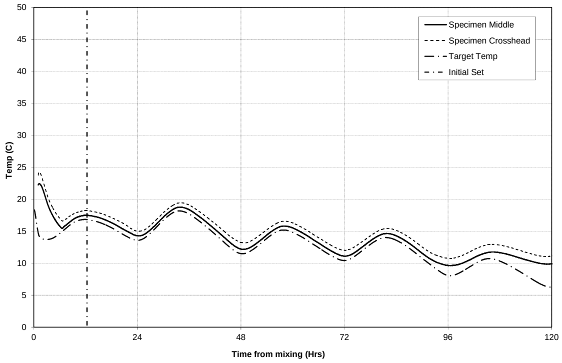

F4H-35RGC: Rigid Cracking Frame Measured Stresses

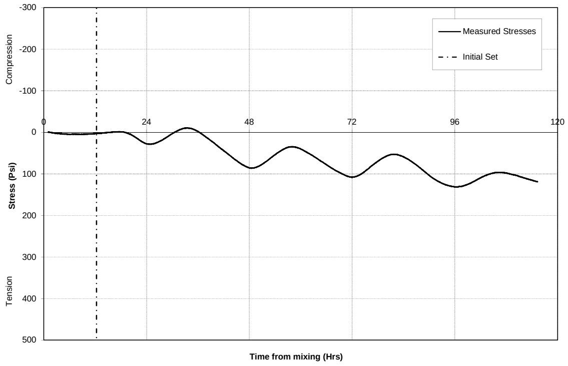

F4H-35RGC: Unrestrained (Free) Shrinkage

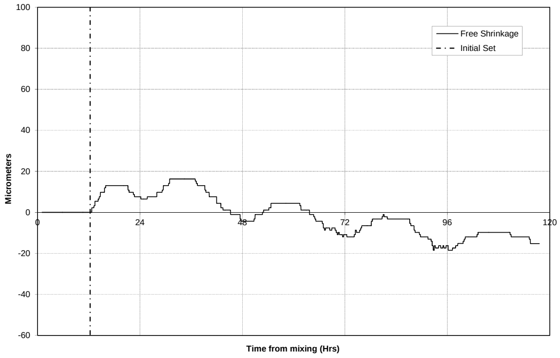

A.3.3 Class F Fly Ash Mixtures

***F1L-25RG: Measured Temperatures**

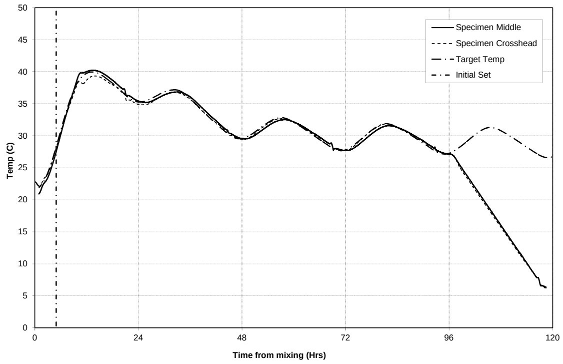

***F1L-25RG: Rigid Cracking Frame Measured Stresses**

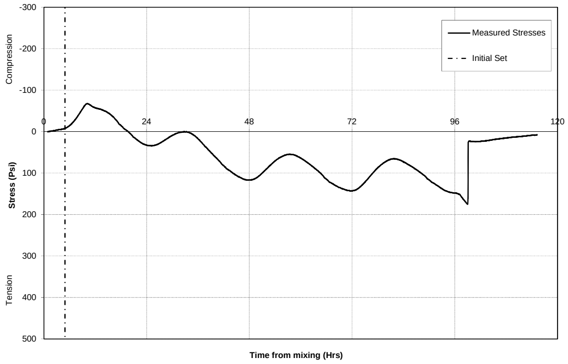

***F1L-25RG: Unrestrained (Free) Shrinkage**

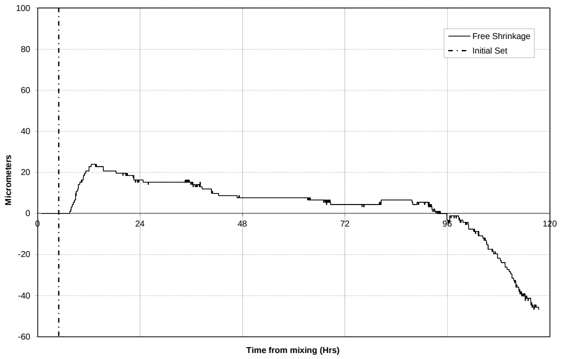

F1L-25RGC: Measured Temperatures

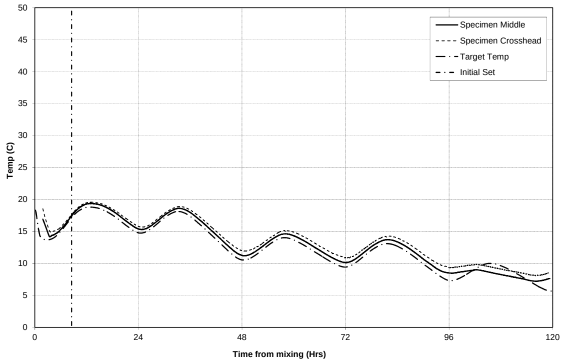

F1L-25RGC: Rigid Cracking Frame Measured Stresses

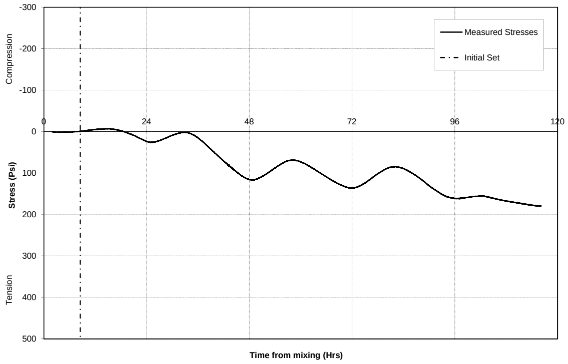

F1L-25RGC: Unrestrained (Free) Shrinkage

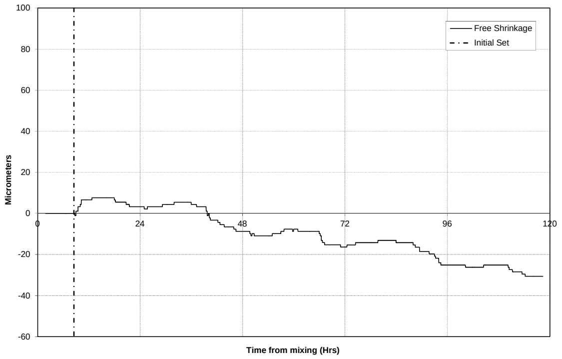

*F1H-25RG: Measured Temperatures

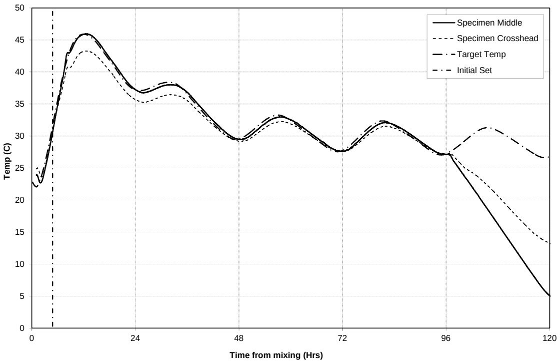

*F1H-25RG: Rigid Cracking Frame Measured Stresses

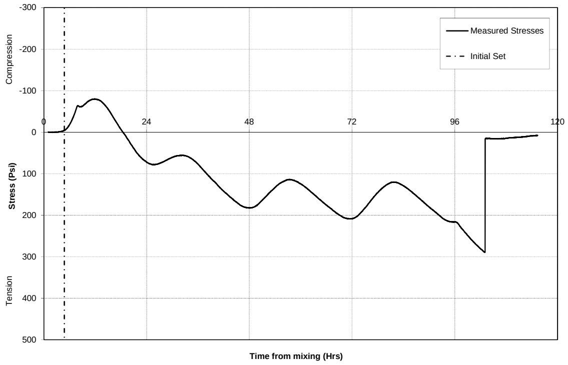

*F1H-25RG: Unrestrained (Free) Shrinkage

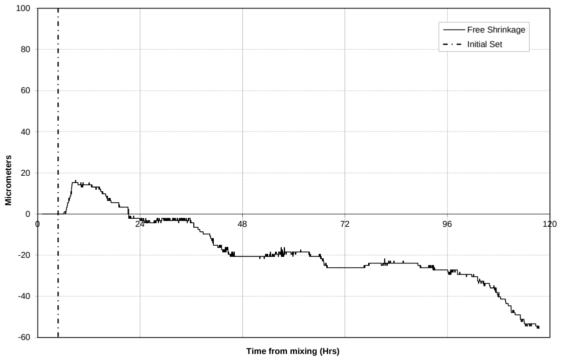

F1H-25RGC: Measured Temperatures

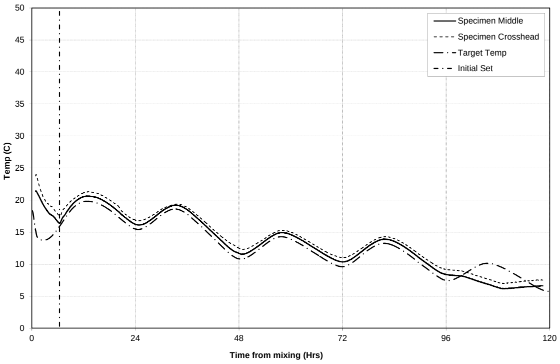

F1H-25RGC: Rigid Cracking Frame Measured Stresses

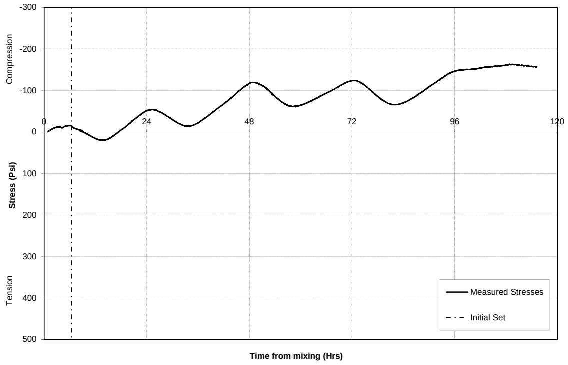

F1H-25RGC: Unrestrained (Free) Shrinkage

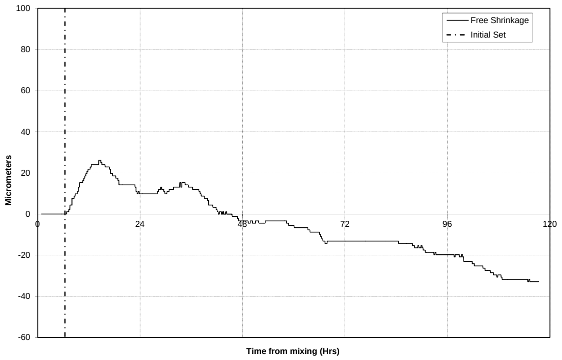

*F2L-25RG: Measured Temperatures

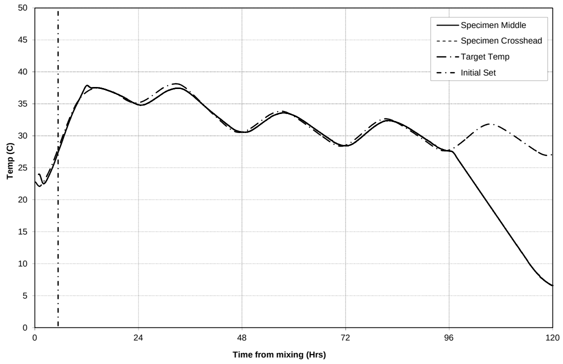

*F2L-25RG: Rigid Cracking Frame Measured Stresses

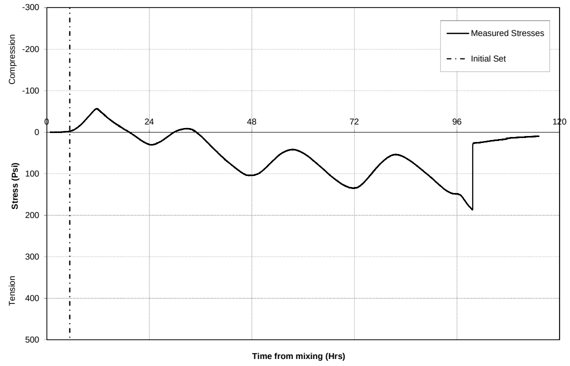

*F2L-25RG: Unrestrained (Free) Shrinkage

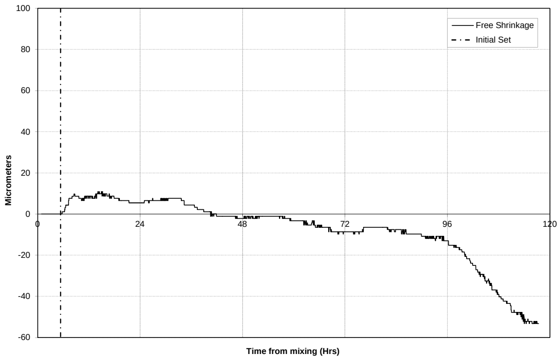

F2L-25RGC: Measured Temperatures

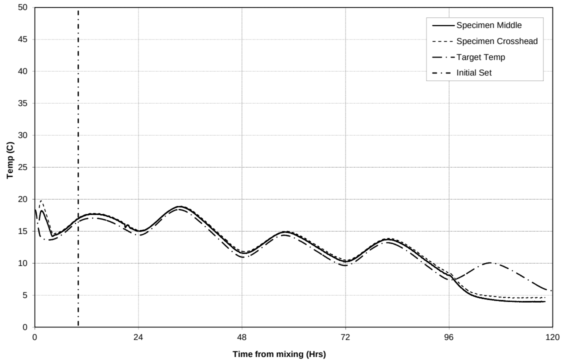

F2L-25RGC: Rigid Cracking Frame Measured Stresses

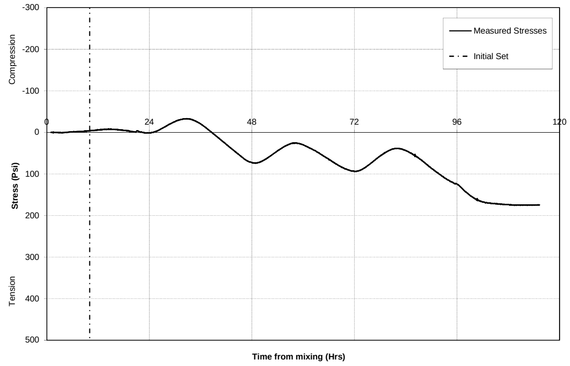

F2L-25RGC: Unrestrained (Free) Shrinkage

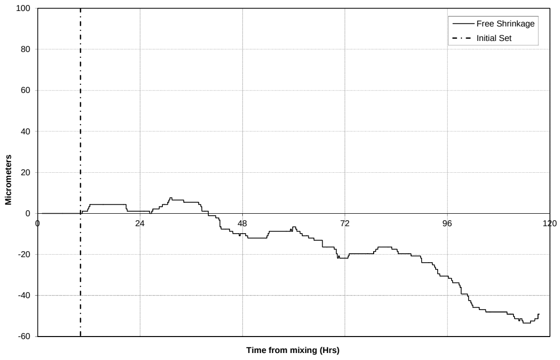

***F2L-35RG: Measured Temperatures**

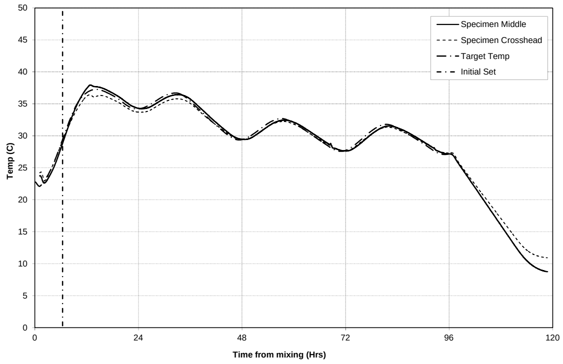

***F2L-35RG: Rigid Cracking Frame Measured Stresses**

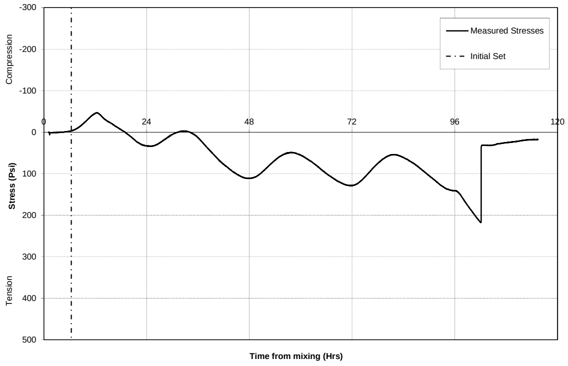

***F2L-35RG: Unrestrained (Free) Shrinkage**

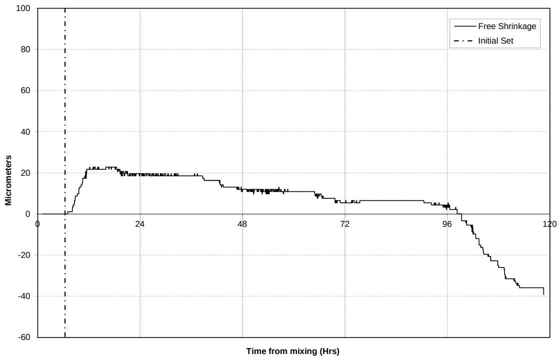

F2L-35RGC: Measured Temperatures

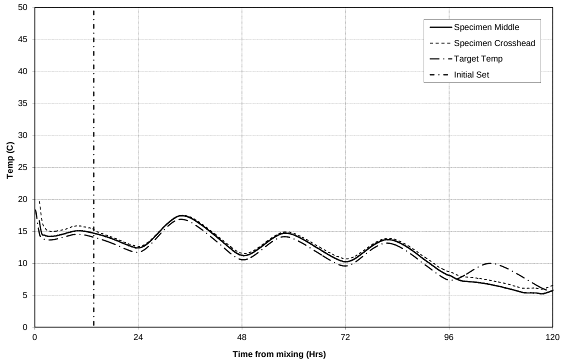

F2L-35RGC: Rigid Cracking Frame Measured Stresses

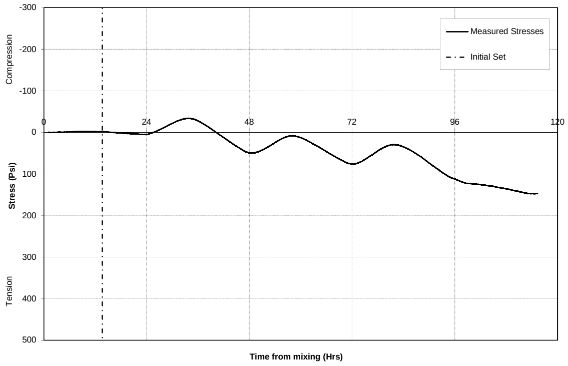

F2L-35RGC: Unrestrained (Free) Shrinkage

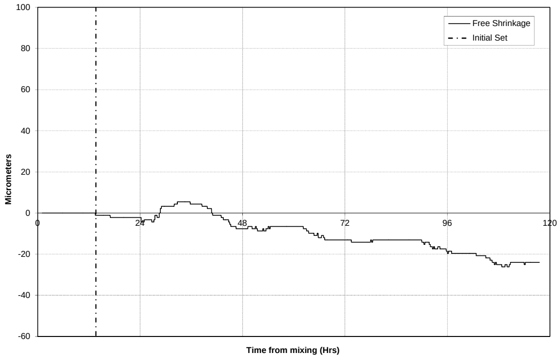

F2H-25RG: Measured Temperatures

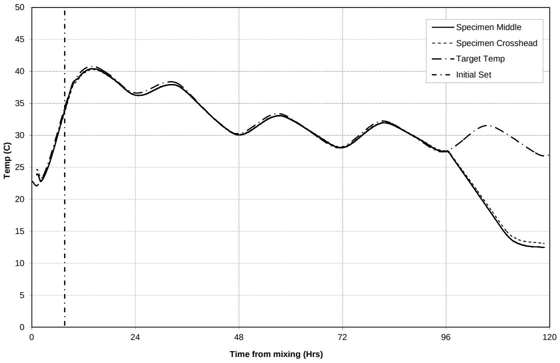

F2H-25RG: Rigid Cracking Frame Measured Stresses

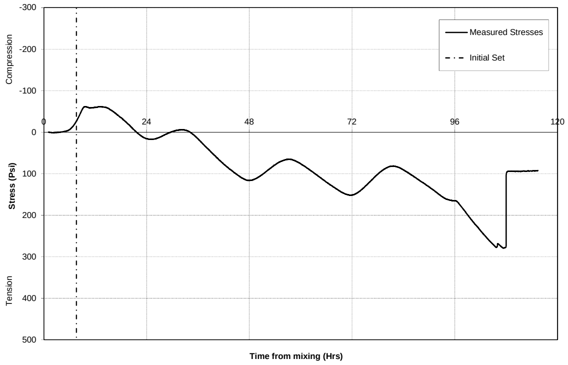

F2H-25RG: Unrestrained (Free) Shrinkage

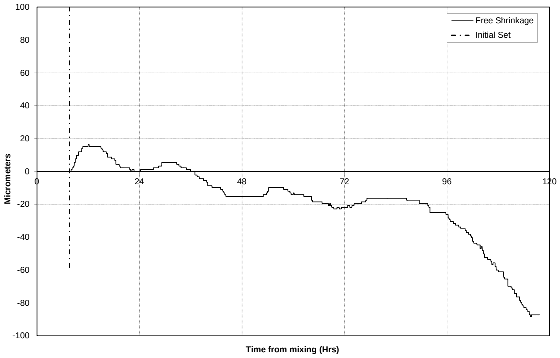

F2H-25RGC: Measured Temperatures

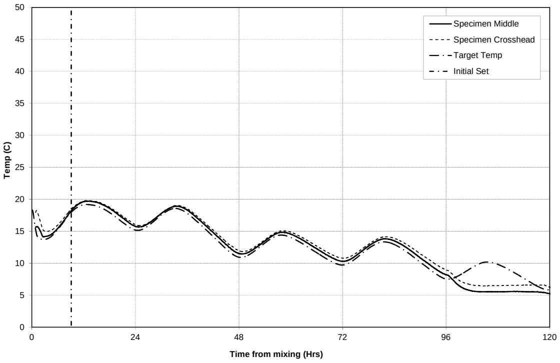

F2H-25RGC: Rigid Cracking Frame Measured Stresses

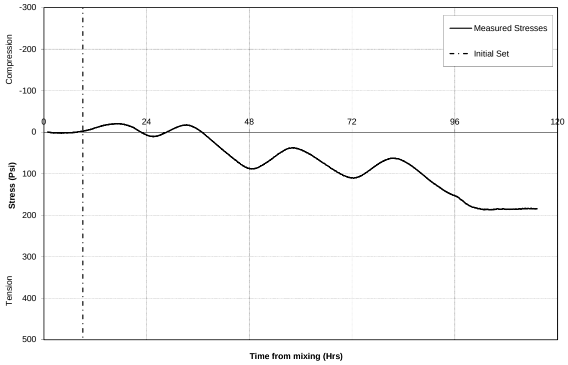

F2H-25RGC: Unrestrained (Free) Shrinkage

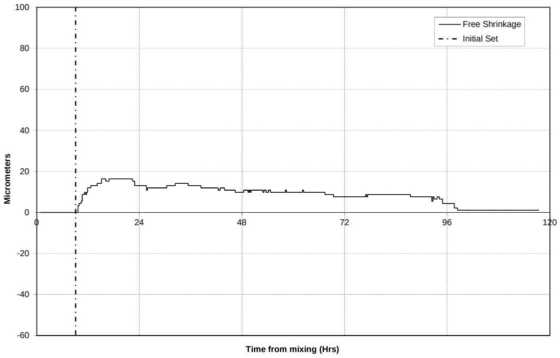

A.3.4 GGBFS Mixtures

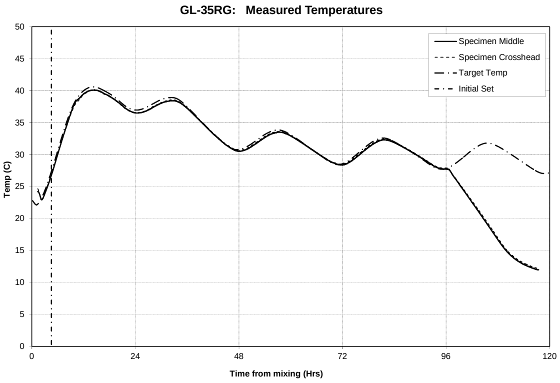
GL-35RG: Measured Temperatures

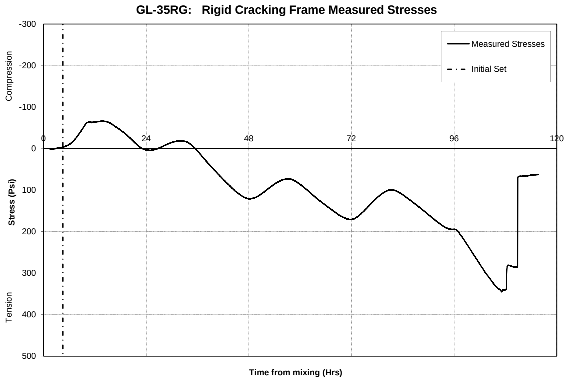
GL-35RG: Rigid Cracking Frame Measured Stresses

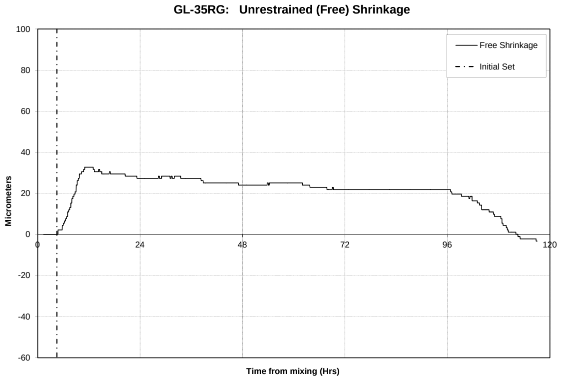
GL-35RG: Unrestrained (Free) Shrinkage

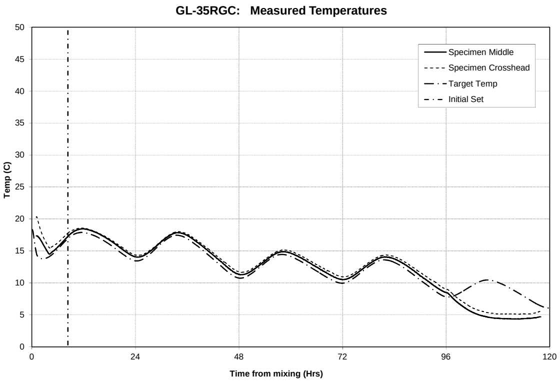
GL-35RGC: Measured Temperatures

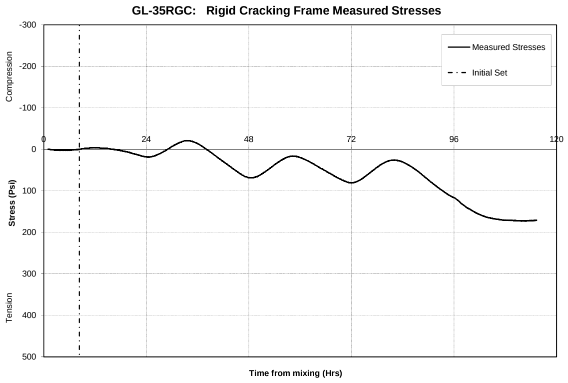
GL-35RGC: Rigid Cracking Frame Measured Stresses

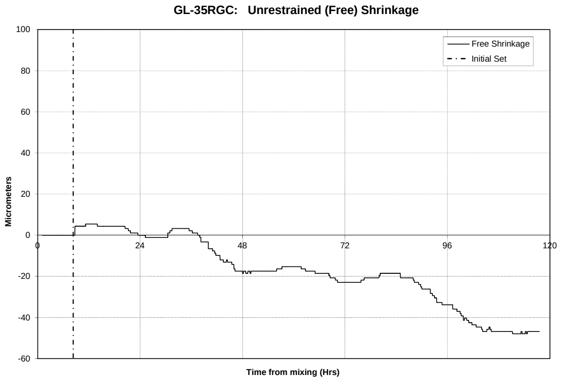
GL-35RGC: Unrestrained (Free) Shrinkage

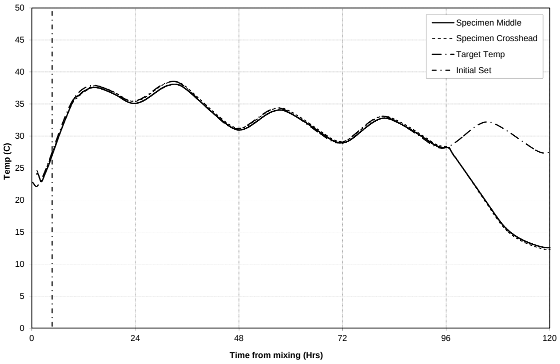
GL-50RG: Measured Temperatures

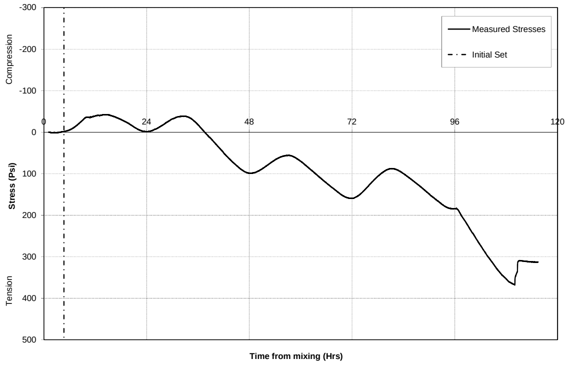
GL-50RG: Rigid Cracking Frame Measured Stresses

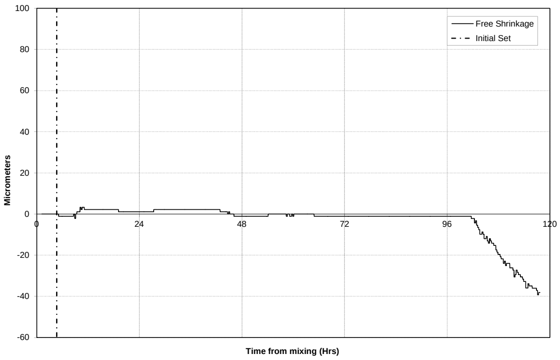
GL-50RG: Unrestrained (Free) Shrinkage

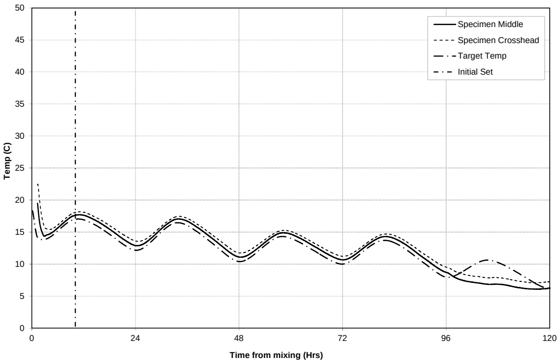
GL-50RGC: Measured Temperatures

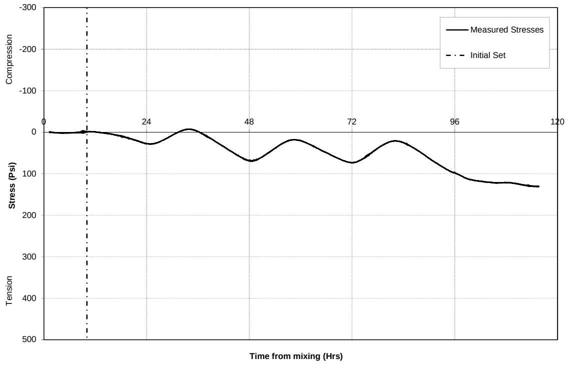
GL-50RGC: Rigid Cracking Frame Measured Stresses

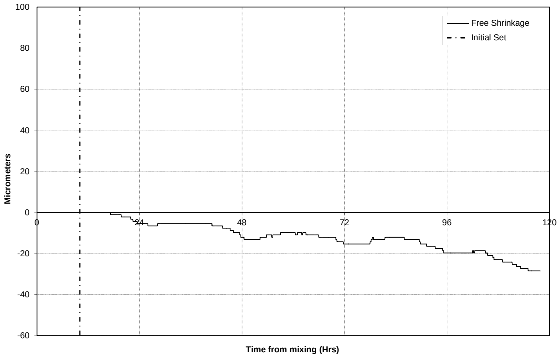
GL-50RGC: Unrestrained (Free) Shrinkage

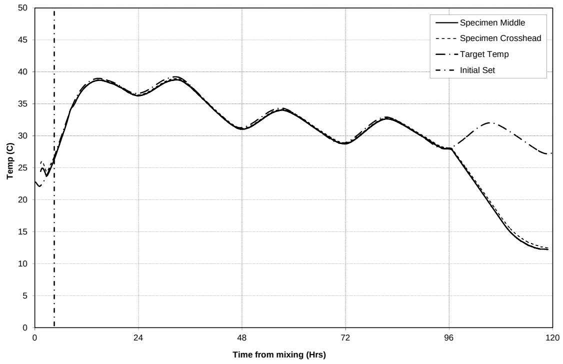

GH-50RG: Measured Temperatures

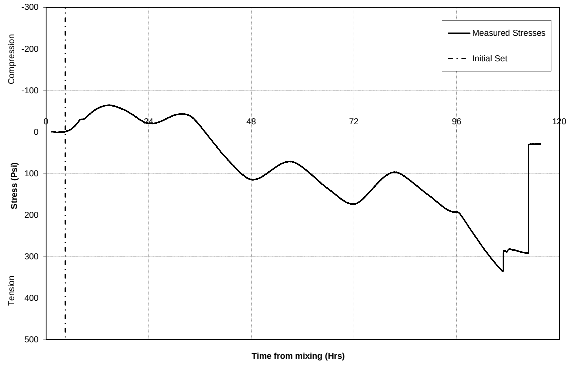

GH-50RG: Rigid Cracking Frame Measured Stresses

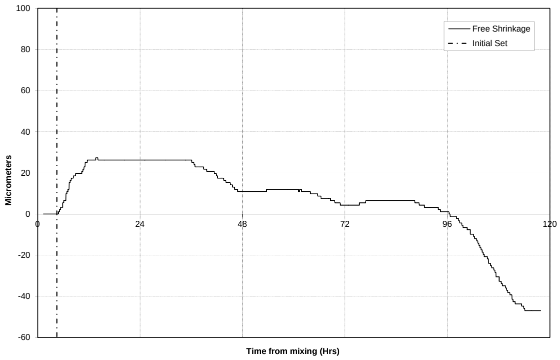

GH-50RG: Unrestrained (Free) Shrinkage

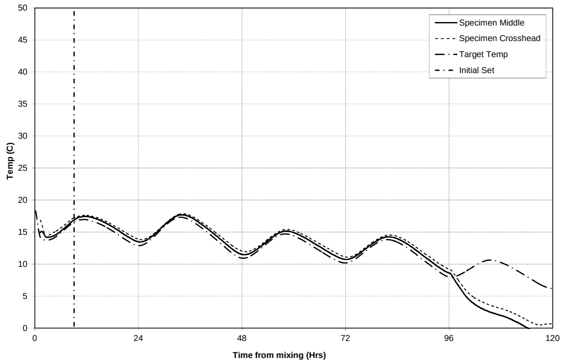

GH-50RGC: Measured Temperatures

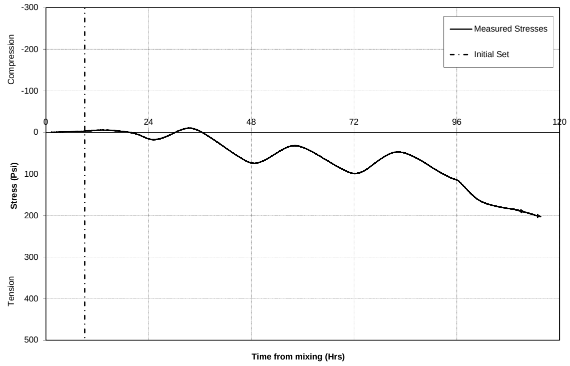

GH-50RGC: Rigid Cracking Frame Measured Stresses

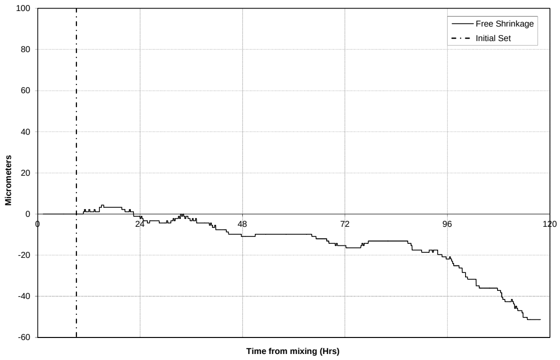

GH-50RGC: Unrestrained (Free) Shrinkage

GL-50LS: Measured Temperatures

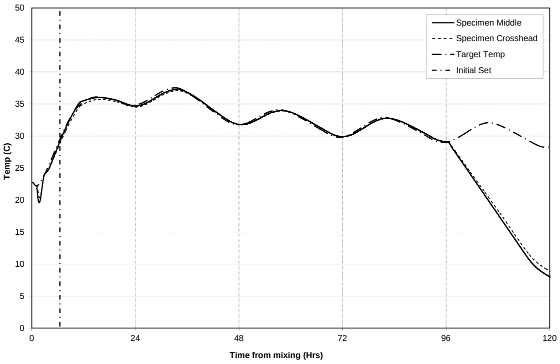

GL-50LS: Rigid Cracking Frame Measured Stresses

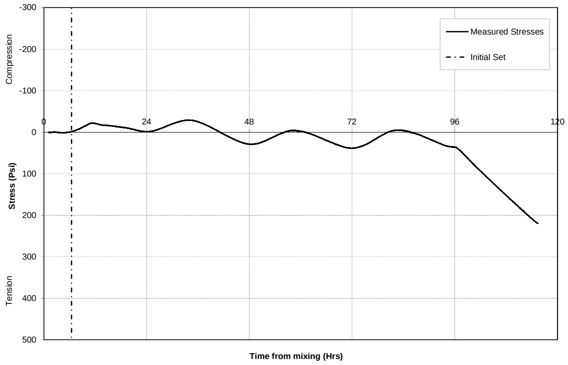

GL-50LS: Unrestrained (Free) Shrinkage

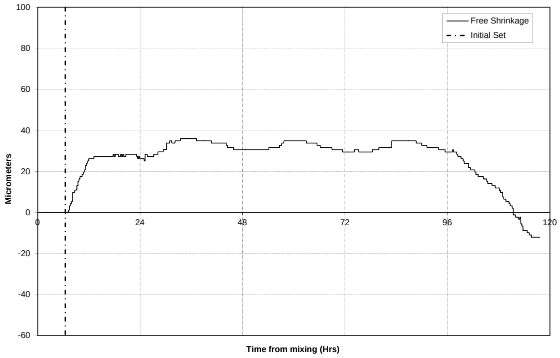

GL-50LSC: Measured Temperatures

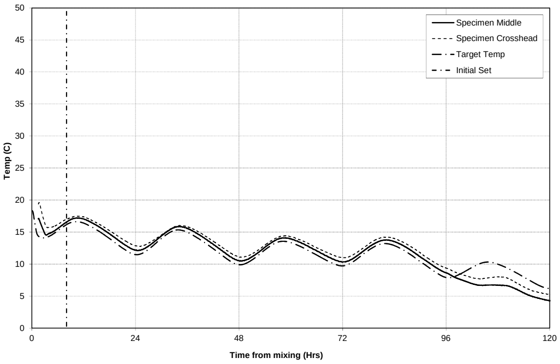

GL-50LSC: Rigid Cracking Frame Measured Stresses

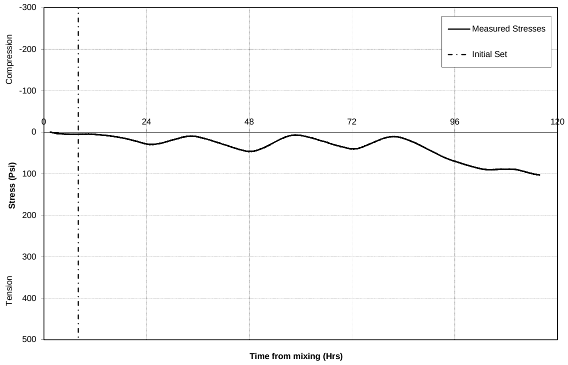

GL-50LSC: Unrestrained (Free) Shrinkage

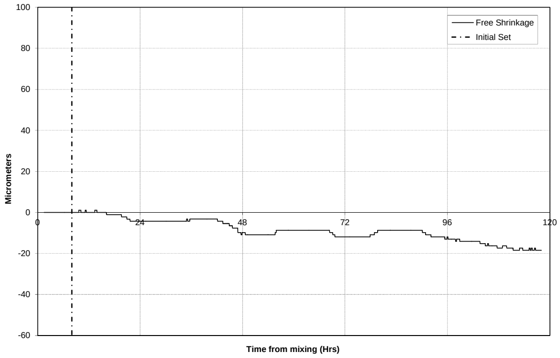

A.3.5 Other Mixtures

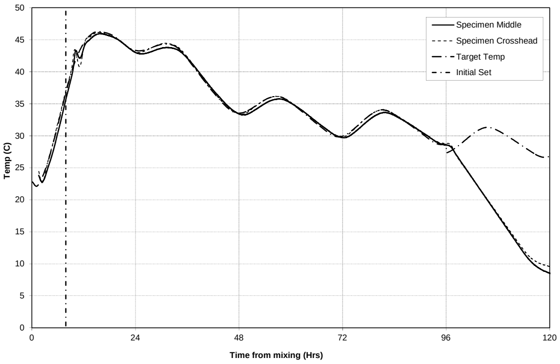
*U4L-35RG: Measured Temperatures

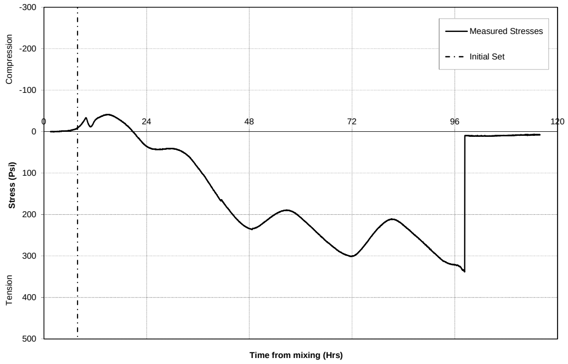
*U4L-35RG: Rigid Cracking Frame Measured Stresses

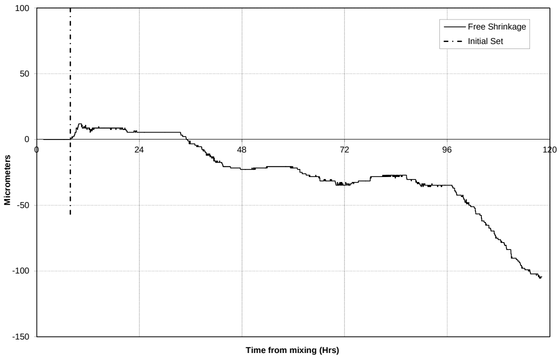
*U4L-35RG: Unrestrained (Free) Shrinkage

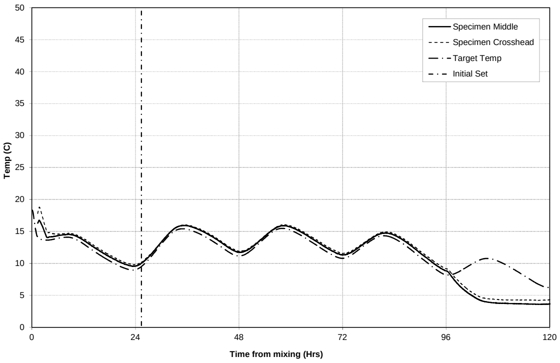
U4L-35RGC: Measured Temperatures

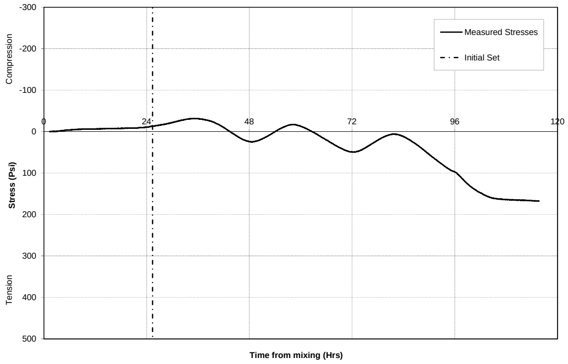
U4L-35RGC: Rigid Cracking Frame Measured Stresses

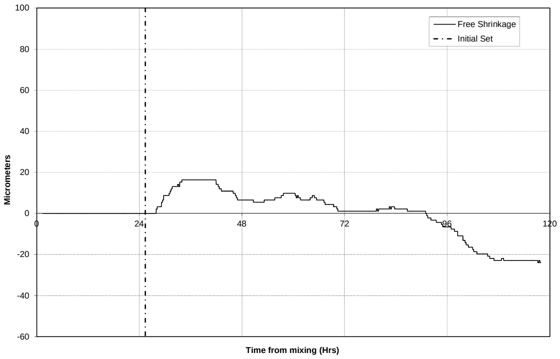
U4L-35RGC: Unrestrained (Free) Shrinkage

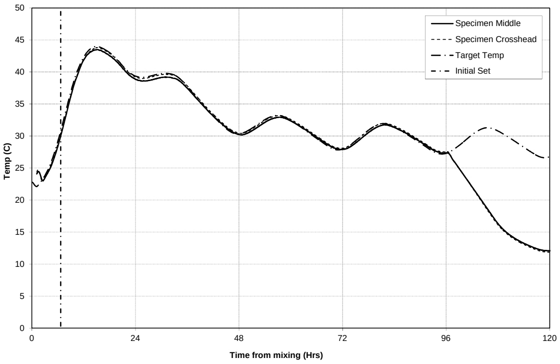
SL-RG: Measured Temperatures

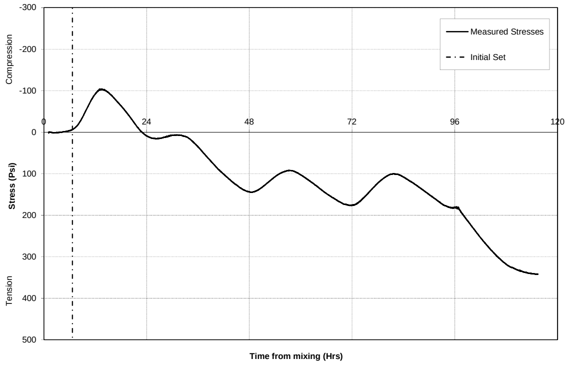
SL-RG: Rigid Cracking Frame Measured Stresses

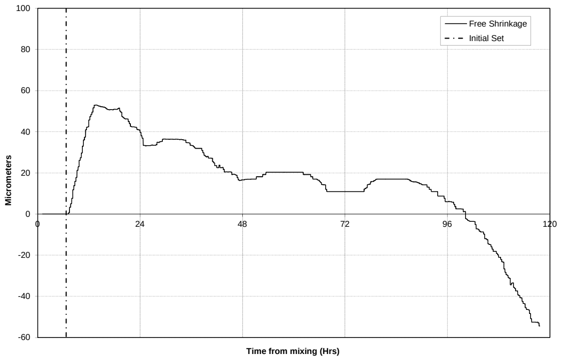
SL-RG: Unrestrained (Free) Shrinkage

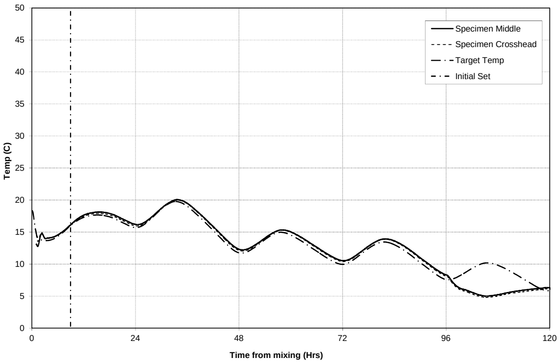
SL-RGC: Measured Temperatures

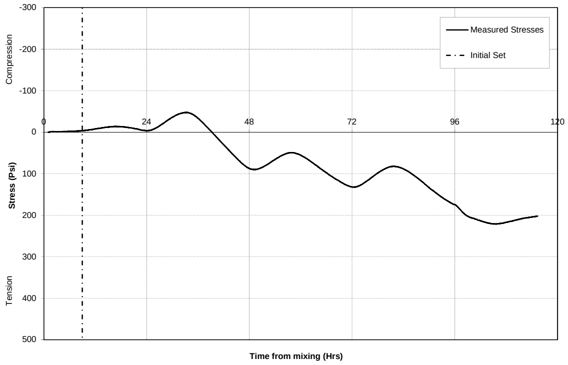
SL-RGC: Rigid Cracking Frame Measured Stresses

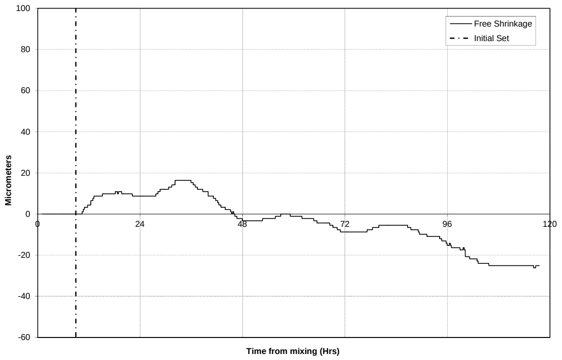
SL-RGC: Unrestrained (Free) Shrinkage

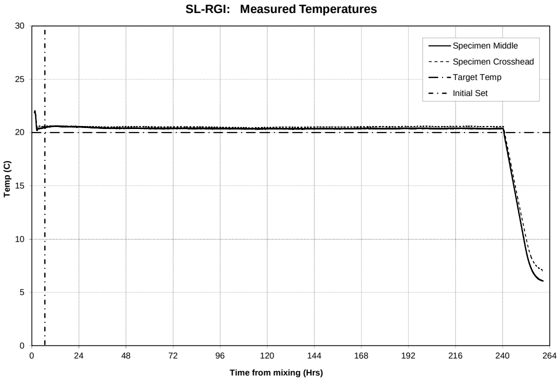
SL-RGI: Measured Temperatures
Specimen Middle
Specimen Crosshead
Target Temp
Initial Set
Temp (C)
30
25
20
15
10
5
0
0
24
48
72
96
120
144
168
192
216
240
264
Time from mixing (Hrs)

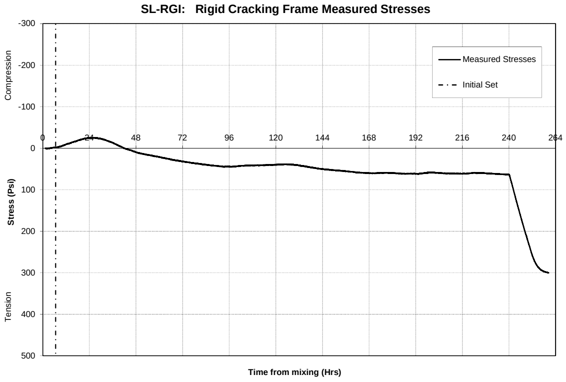
SL-RGI: Rigid Cracking Frame Measured Stresses
Measured Stresses
Initial Set
Compression
Stress (Psi)
Tension
-300
-200
-100
0
100
200
300
400
500
0
24
48
72
96
120
144
168
192
216
240
264
Time from mixing (Hrs)

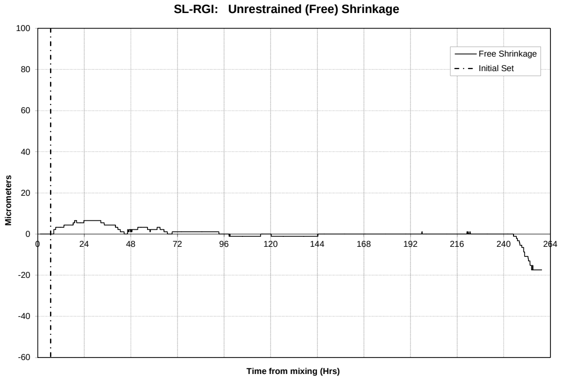
SL-RGI: Unrestrained (Free) Shrinkage
Free Shrinkage
Initial Set
Micrometers
100
80
60
40
20
0
-20
-40
-60
0
24
48
72
96
120
144
168
192
216
240
264
Time from mixing (Hrs)

Appendix B: Bridge Deck Instrumentation

B.1 San Antonio Bridge Deck

B.1.1 iButton String Locations and Placement Times

Locations for this instrumentation, provided in Table B.1, were taken from the west face of the bridge deck. The placement times, as determined from examination of the iButton temperatures, are presented in Table B.2.

Table B.1: iButton string locations—SABD

String	Distance from West face of bridge deck
A1	13.9
B2	16.5
B3	12.9
C1	24.4
C2	13.1
C3	9.6
D1	13.1

All values in feet

Table B.2: Concrete placement times—SABD

Strand	Placement Time
A	7/19/09 9:43 PM
B	7/19/09 10:07 PM
C	7/19/09 11:38 PM
D	7/20/09 1:40 AM

B.1.2 iButton Depths

Table B.3 provides the heights of the iButtons measured from either the steel pan formwork, or the top of the steel girder. While the exact depth of the bridge deck is not known, it is assumed that concrete sections are 8 in. thick over the steel pan formwork, and 11.5 in. thick over the steel girders. Descriptions of the iButton strings are also provided.

Table B.3: iButton depths—SABD

Location	String	Buttons	Height from bottom
Beginning of pour, between girders	A1	C	6.000
		B	4.250
		A	1.500
Over the bent and over the girder	B2	D	7.875
		C	5.875
		B	3.625
		A	2.125
Over the bent and between girders	B3	D	6.625
		C	5.125
		B	1.750
		A	0.500
Middle of long span, middle of deck overhang	C1	C	5.750
		B	3.750
		A	1.500
Mid of long span, Between Girders	C2	D	6.250
		C	4.500
		B	2.500
		A	0.750
Mid of long span, over the girder	C3	E	8.750
		D	6.875
		C	5.375
		B	3.375
		A	1.000
End of pour, between girders	D1	C	6.250
		B	3.875
		A	1.500

All values in inches.

B.1.3 Recorded Temperatures

The following figures present the complete set of temperature data for the San Antonio bridge deck. Figure B.1 presents a comparison of the temperatures recorded for a selected top iButton for each of the strands. The selected iButtons were located in the middle of the bridge deck width, when possible. Figure B.2 presents a comparison of the gradient recorded across the different strands. As before, each strand is represented by the iButton string located in the middle of the bridge deck width, when possible. In the gradient graph, the iButton gradient, in °F, is presented in on the primary vertical axis, while the ambient air temperature, in °F, is presented on the secondary vertical axis. The graphs following Figure B.2 are labeled with the bridge deck pour name, SABD, the iButton string name, and the duration of time presented on that graph. For each string, the first graph presents the 4-day temperature data, such that the first temperature peaks may be examined. The following graph presents the full data set for the iButton string. Due to various factors, some iButton strings may record longer durations than others.

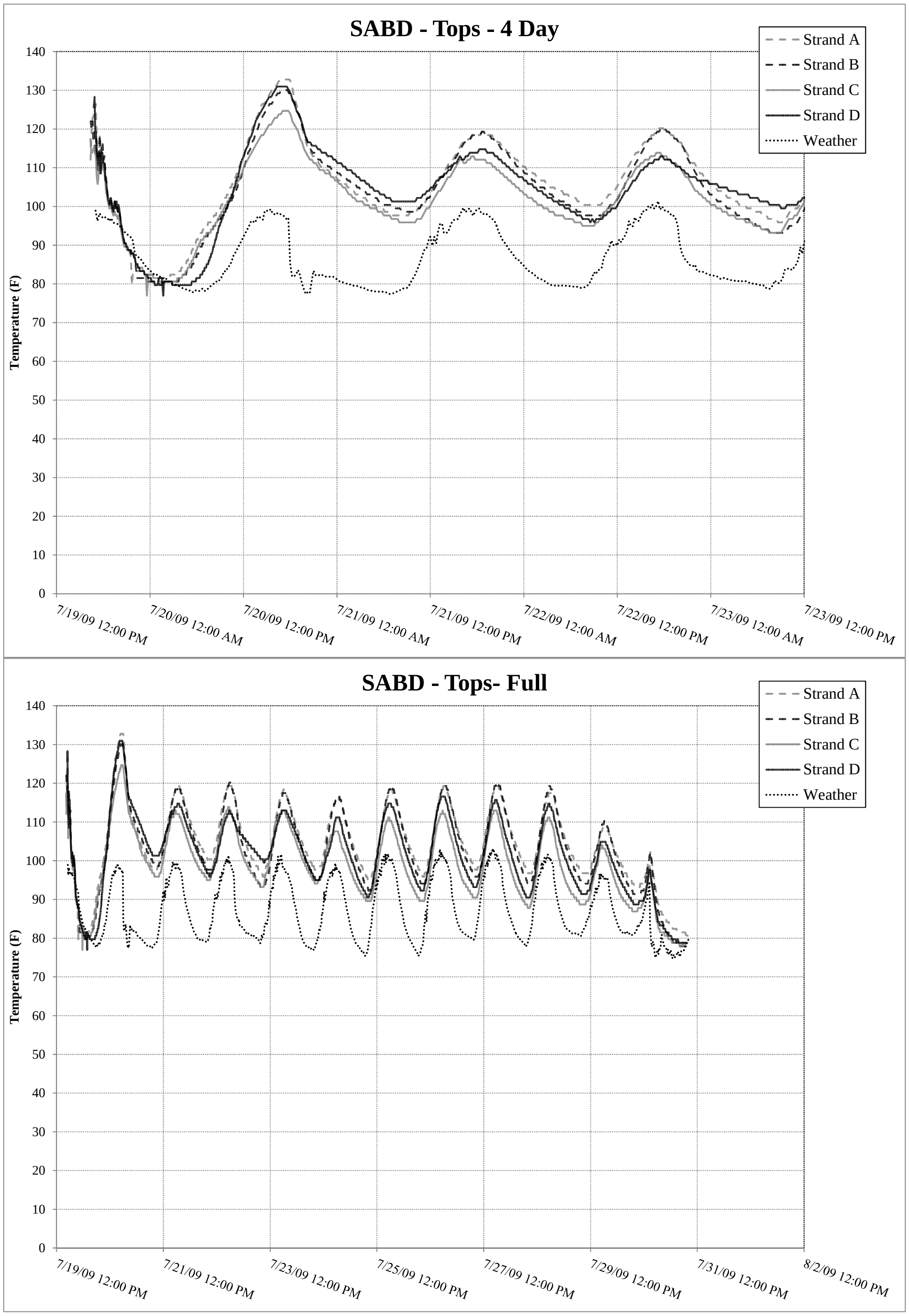

Figure B.1: Comparison of top iButton temperatures—SABD

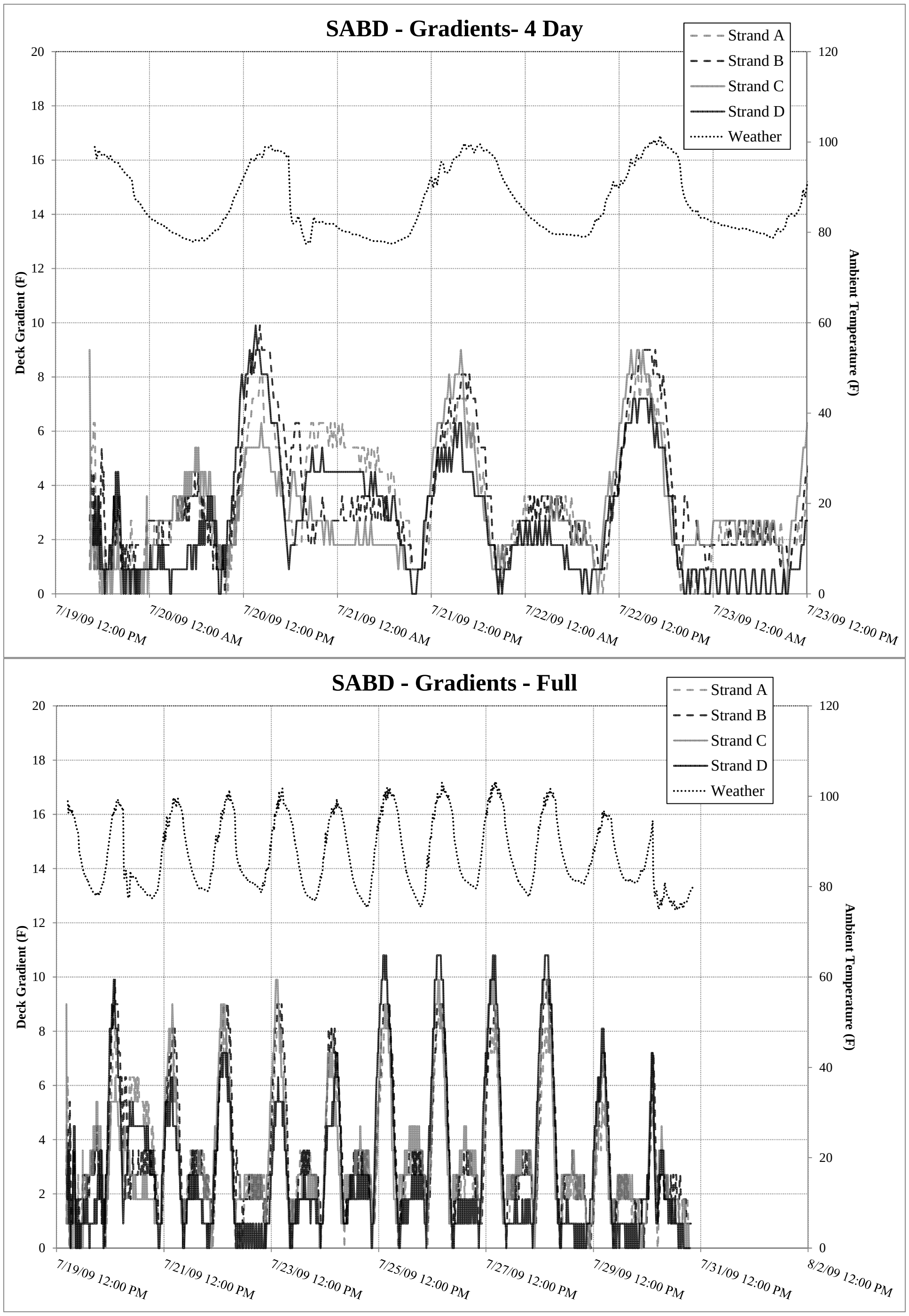

Figure B.2: Comparison of iButton strand gradients—SABD

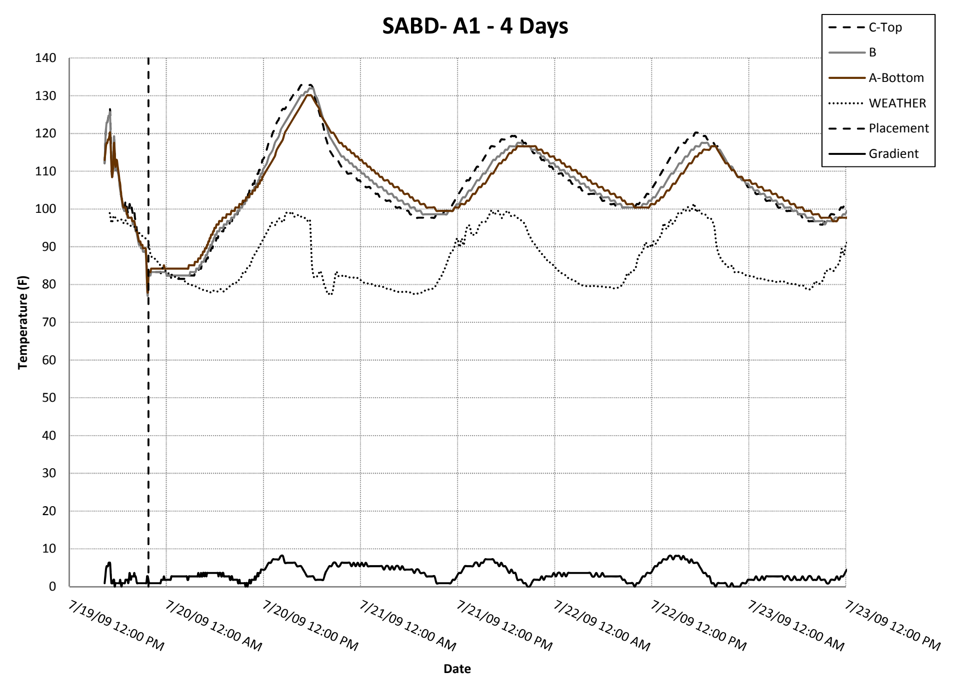
SABD- A1 - 4 Days
C-Top
B
A-Bottom
WEATHER
Placement
Gradient
Temperature (F)
0
10
20
30
40
50
60
70
80
90
100
110
120
130
140
7/19/09 12:00 PM
7/20/09 12:00 AM
7/20/09 12:00 PM
7/21/09 12:00 AM
7/21/09 12:00 PM
7/22/09 12:00 AM
7/22/09 12:00 PM
7/23/09 12:00 AM
7/23/09 12:00 PM
Date

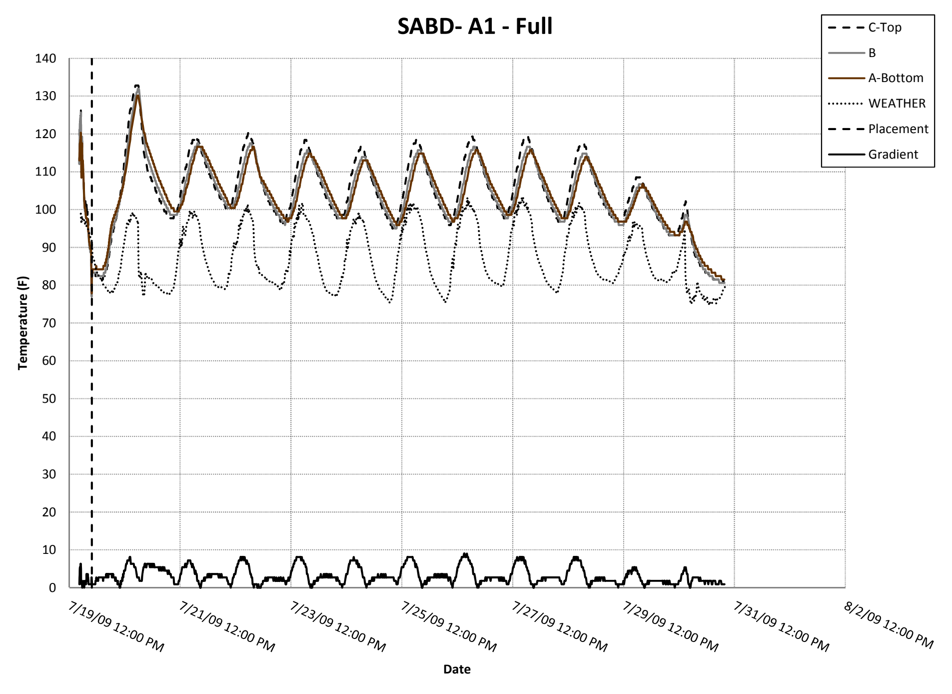
SABD- A1 - Full
C-Top
B
A-Bottom
WEATHER
Placement
Gradient
Temperature (F)
0
10
20
30
40
50
60
70
80
90
100
110
120
130
140
7/19/09 12:00 PM
7/21/09 12:00 PM
7/23/09 12:00 PM
7/25/09 12:00 PM
7/27/09 12:00 PM
7/29/09 12:00 PM
7/31/09 12:00 PM
8/2/09 12:00 PM
Date

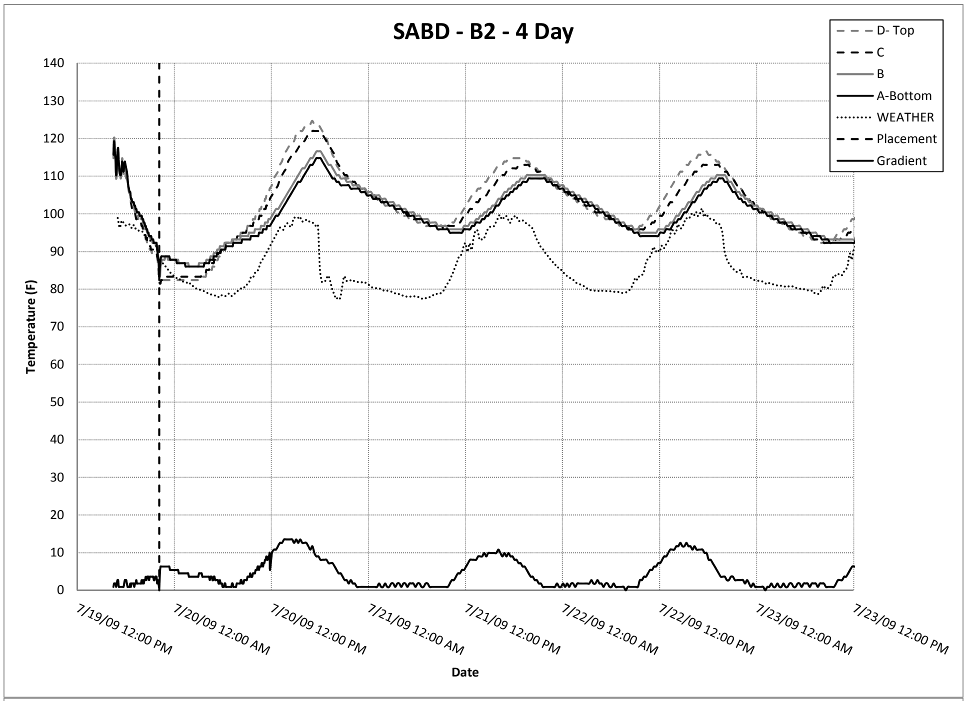
SABD - B2 - 4 Day
D- Top
C
B
A-Bottom
WEATHER
Placement
Gradient
Temperature (F)
140
130
120
110
100
90
80
70
60
50
40
30
20
10
0
7/19/09 12:00 PM
7/20/09 12:00 AM
7/20/09 12:00 PM
7/21/09 12:00 AM
7/21/09 12:00 PM
7/22/09 12:00 AM
7/22/09 12:00 PM
7/23/09 12:00 AM
7/23/09 12:00 PM
Date

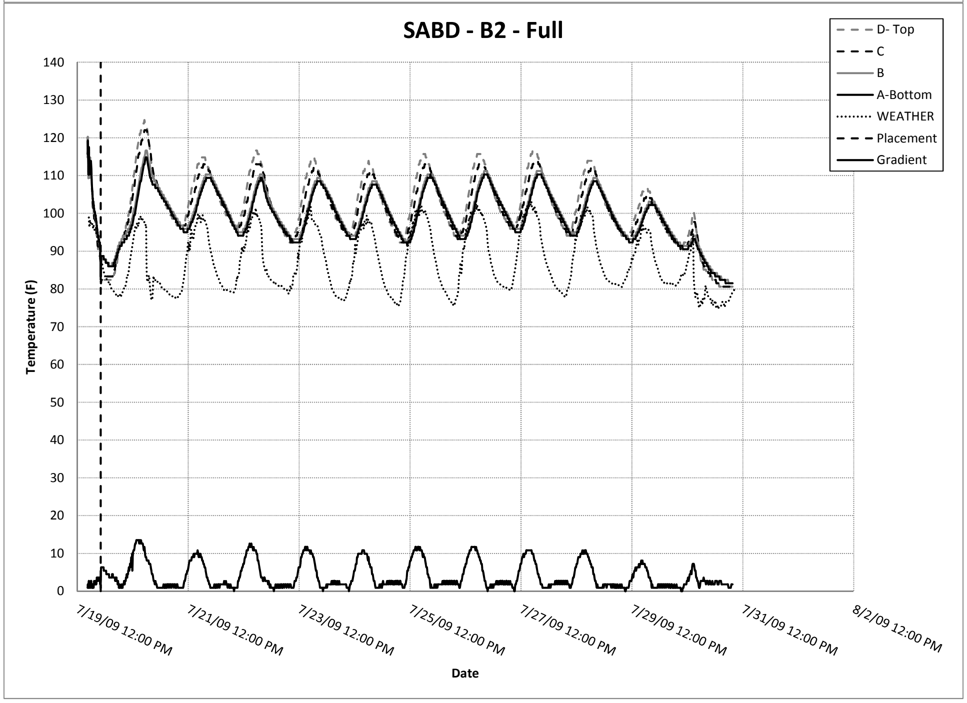
SABD - B2 - Full
D- Top
C
B
A-Bottom
WEATHER
Placement
Gradient
Temperature (F)
140
130
120
110
100
90
80
70
60
50
40
30
20
10
0
7/19/09 12:00 PM
7/21/09 12:00 PM
7/23/09 12:00 PM
7/25/09 12:00 PM
7/27/09 12:00 PM
7/29/09 12:00 PM
7/31/09 12:00 PM
8/2/09 12:00 PM
Date

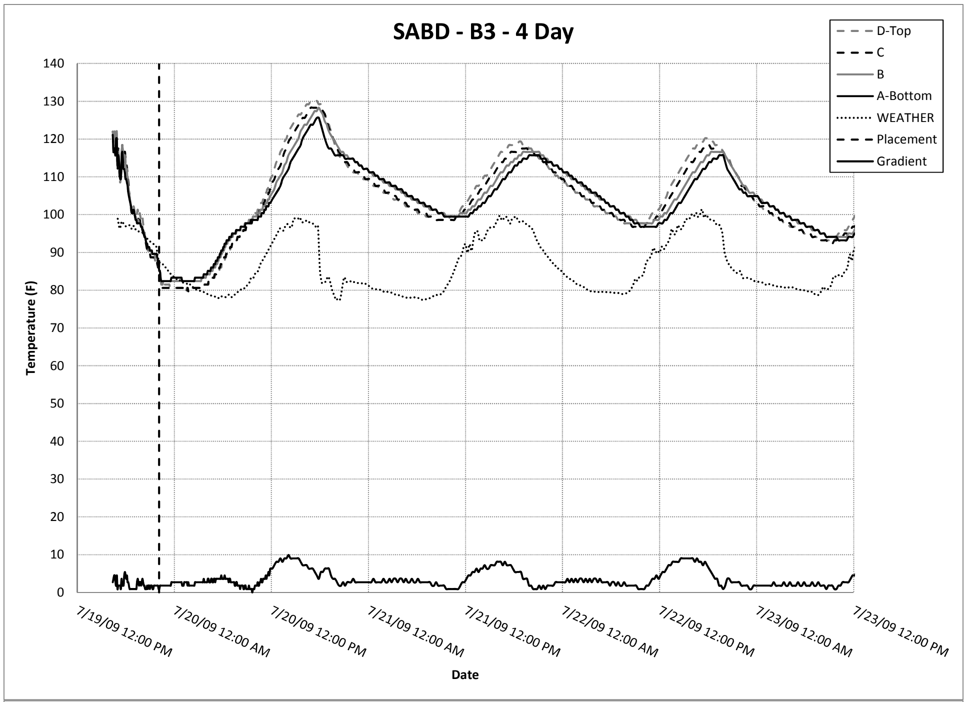
SABD - B3 - 4 Day
D-Top
C
B
A-Bottom
WEATHER
Placement
Gradient
Temperature (F)
140
130
120
110
100
90
80
70
60
50
40
30
20
10
0
7/19/09 12:00 PM
7/20/09 12:00 AM
7/20/09 12:00 PM
7/21/09 12:00 AM
7/21/09 12:00 PM
7/22/09 12:00 AM
7/22/09 12:00 PM
7/23/09 12:00 AM
7/23/09 12:00 PM
Date

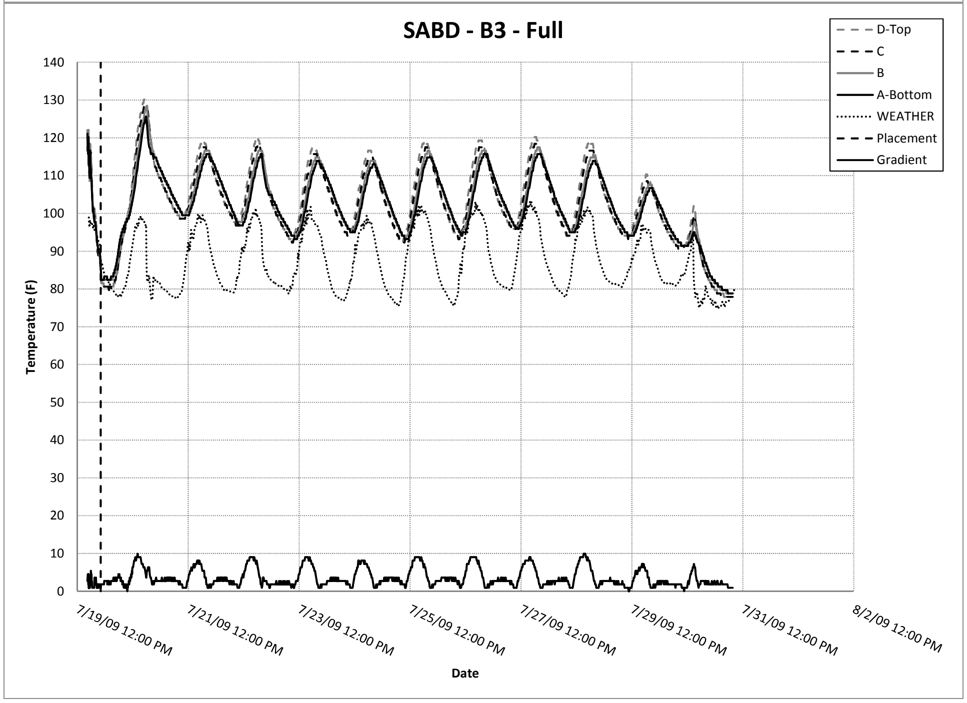
SABD - B3 - Full
D-Top
C
B
A-Bottom
WEATHER
Placement
Gradient
Temperature (F)
140
130
120
110
100
90
80
70
60
50
40
30
20
10
0
7/19/09 12:00 PM
7/21/09 12:00 PM
7/23/09 12:00 PM
7/25/09 12:00 PM
7/27/09 12:00 PM
7/29/09 12:00 PM
7/31/09 12:00 PM
8/2/09 12:00 PM
Date

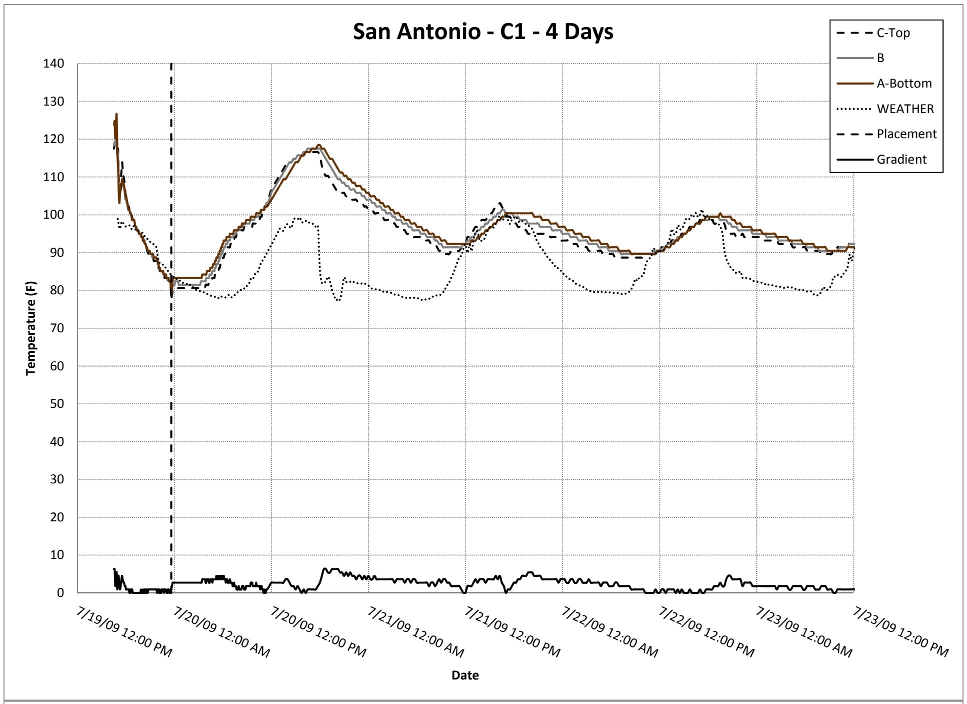
San Antonio - C1 - 4 Days
C-Top
B
A-Bottom
WEATHER
Placement
Gradient
Temperature (F)
140
130
120
110
100
90
80
70
60
50
40
30
20
10
0
7/19/09 12:00 PM
7/20/09 12:00 AM
7/20/09 12:00 PM
7/21/09 12:00 AM
7/21/09 12:00 PM
7/22/09 12:00 AM
7/22/09 12:00 PM
7/23/09 12:00 AM
7/23/09 12:00 PM
Date

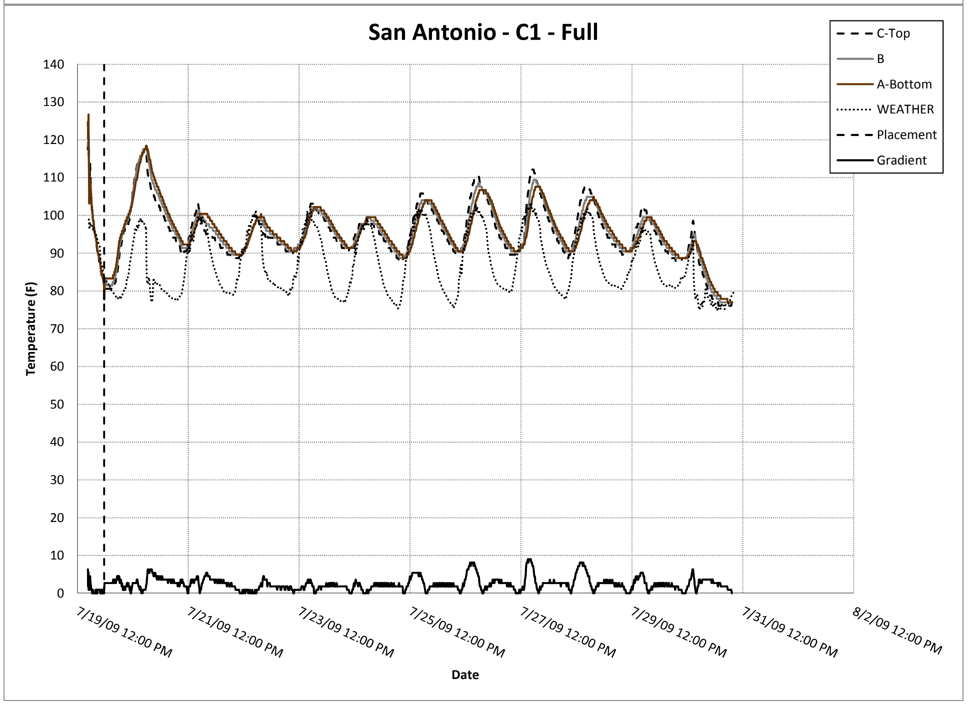
San Antonio - C1 - Full
C-Top
B
A-Bottom
WEATHER
Placement
Gradient
Temperature (F)
140
130
120
110
100
90
80
70
60
50
40
30
20
10
0
7/19/09 12:00 PM
7/21/09 12:00 PM
7/23/09 12:00 PM
7/25/09 12:00 PM
7/27/09 12:00 PM
7/29/09 12:00 PM
7/31/09 12:00 PM
8/2/09 12:00 PM
Date

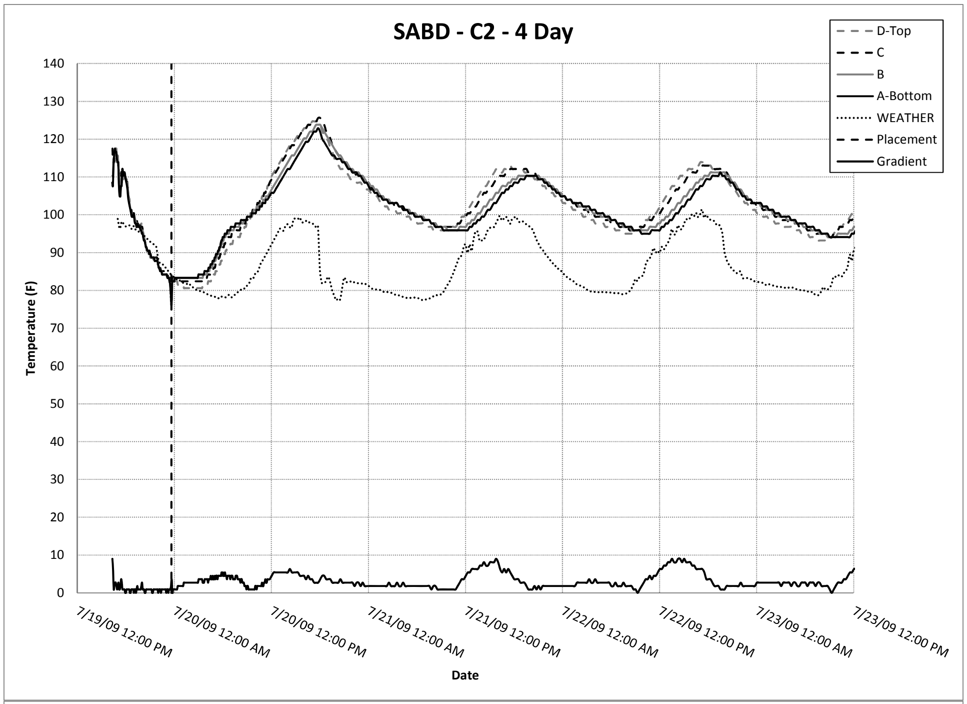
SABD - C2 - 4 Day
Temperature (F)
140
130
120
110
100
90
80
70
60
50
40
30
20
10
0
7/19/09 12:00 PM
7/20/09 12:00 AM
7/20/09 12:00 PM
7/21/09 12:00 AM
7/21/09 12:00 PM
7/22/09 12:00 AM
7/22/09 12:00 PM
7/23/09 12:00 AM
7/23/09 12:00 PM
Date
D-Top
C
B
A-Bottom
WEATHER
Placement
Gradient

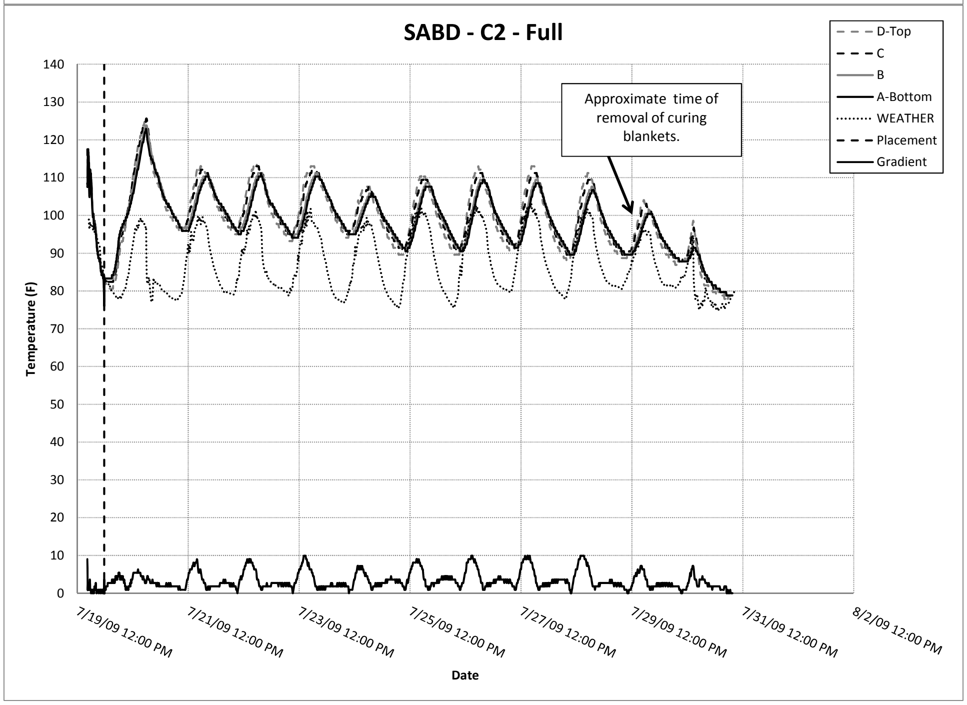
SABD - C2 - Full
Temperature (F)
140
130
120
110
100
90
80
70
60
50
40
30
20
10
0
7/19/09 12:00 PM
7/21/09 12:00 PM
7/23/09 12:00 PM
7/25/09 12:00 PM
7/27/09 12:00 PM
7/29/09 12:00 PM
7/31/09 12:00 PM
8/2/09 12:00 PM
Date
D-Top
C
B
A-Bottom
WEATHER
Placement
Gradient
Approximate time of removal of curing blankets.

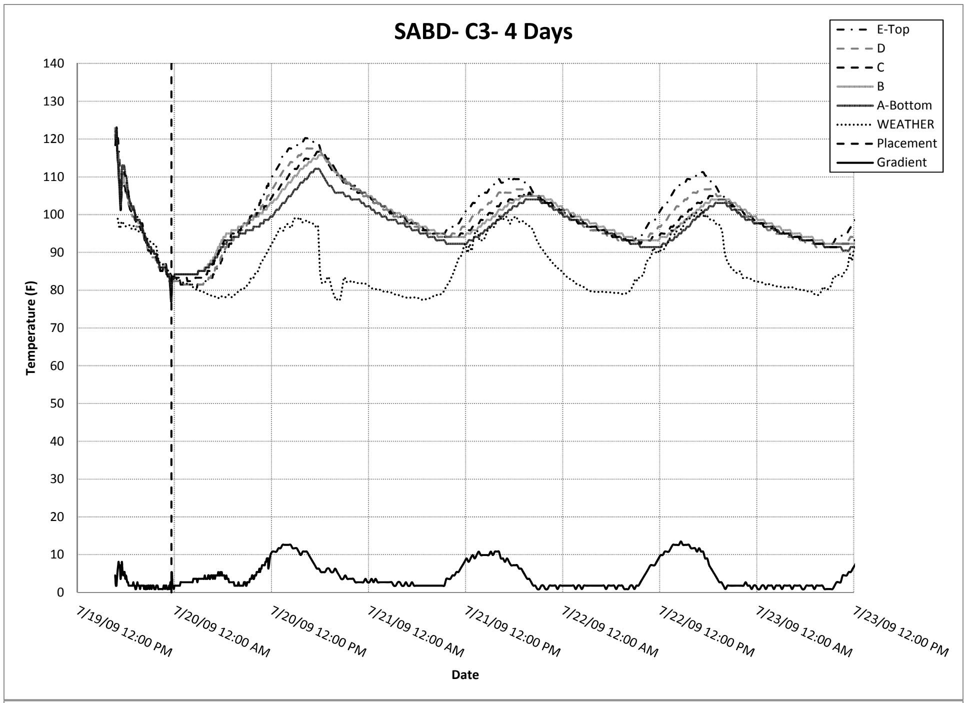
SABD- C3- 4 Days
E-Top
D
C
B
A-Bottom
WEATHER
Placement
Gradient
Temperature (F)
140
130
120
110
100
90
80
70
60
50
40
30
20
10
0
7/19/09 12:00 PM
7/20/09 12:00 AM
7/20/09 12:00 PM
7/21/09 12:00 AM
7/21/09 12:00 PM
7/22/09 12:00 AM
7/22/09 12:00 PM
7/23/09 12:00 AM
7/23/09 12:00 PM
Date

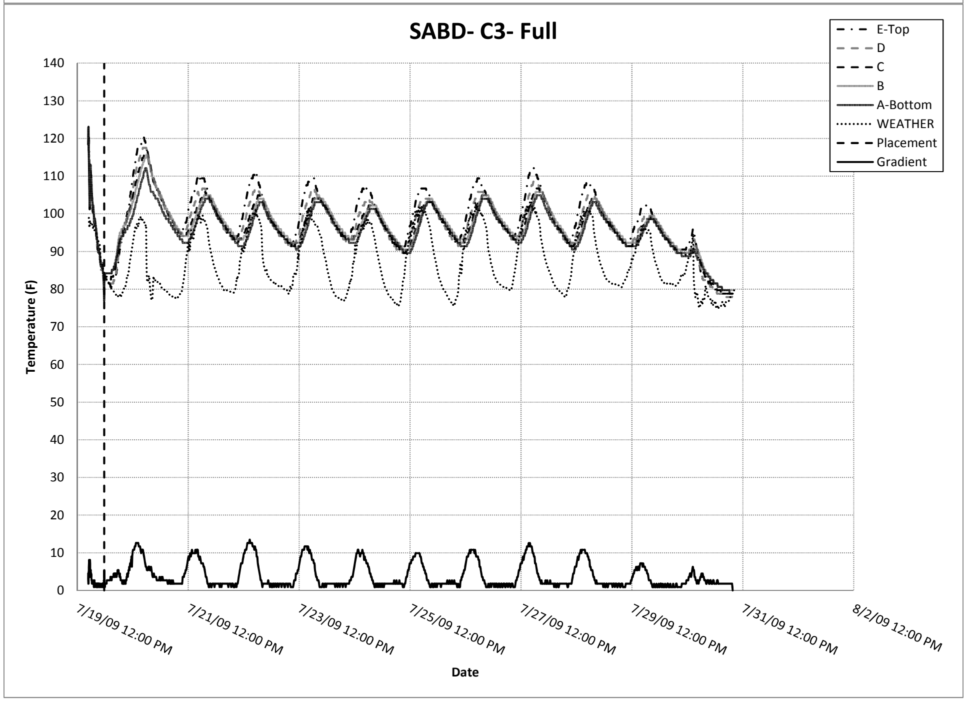
SABD- C3- Full
E-Top
D
C
B
A-Bottom
WEATHER
Placement
Gradient
Temperature (F)
140
130
120
110
100
90
80
70
60
50
40
30
20
10
0
7/19/09 12:00 PM
7/21/09 12:00 PM
7/23/09 12:00 PM
7/25/09 12:00 PM
7/27/09 12:00 PM
7/29/09 12:00 PM
7/31/09 12:00 PM
8/2/09 12:00 PM
Date

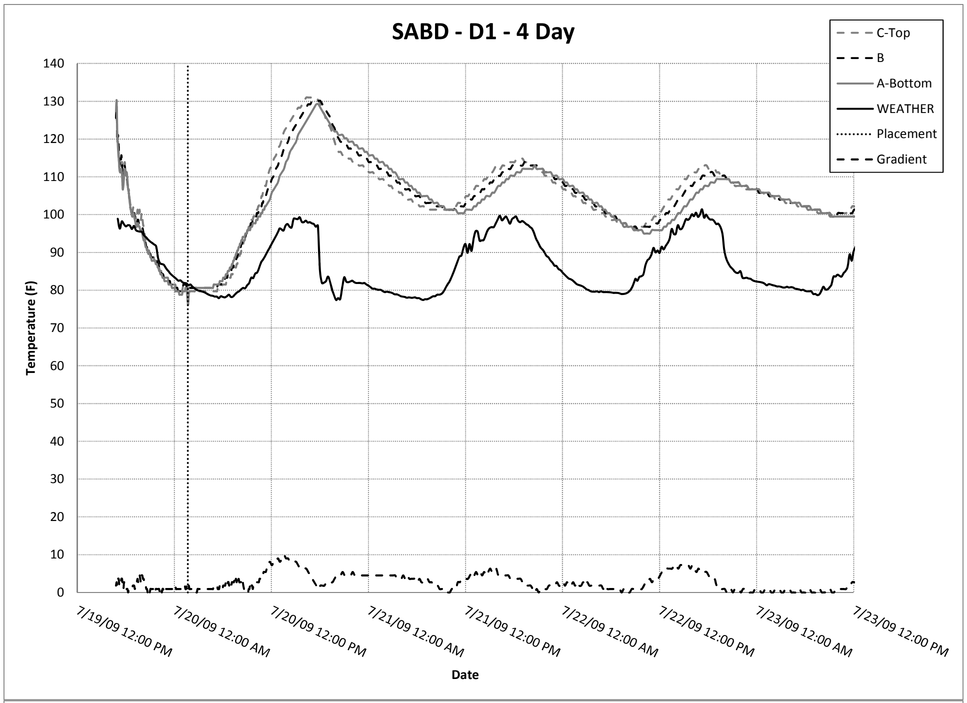
SABD - D1 - 4 Day
C-Top
B
A-Bottom
WEATHER
Placement
Gradient
Temperature (F)
140
130
120
110
100
90
80
70
60
50
40
30
20
10
0
7/19/09 12:00 PM
7/20/09 12:00 AM
7/20/09 12:00 PM
7/21/09 12:00 AM
7/21/09 12:00 PM
7/22/09 12:00 AM
7/22/09 12:00 PM
7/23/09 12:00 AM
7/23/09 12:00 PM
Date

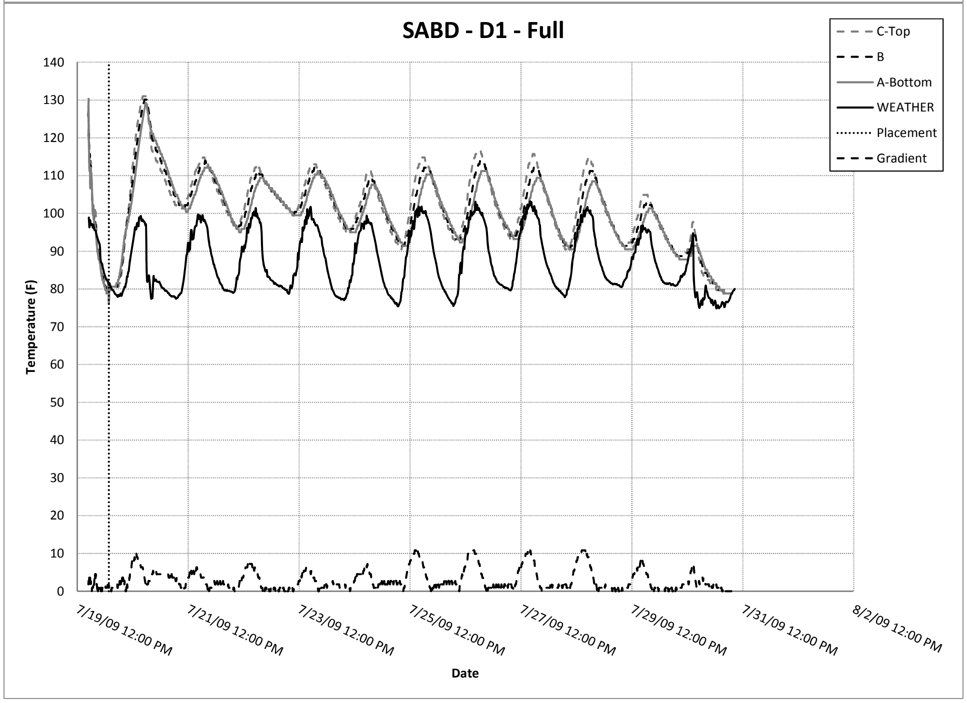
SABD - D1 - Full
C-Top
B
A-Bottom
WEATHER
Placement
Gradient
Temperature (F)
140
130
120
110
100
90
80
70
60
50
40
30
20
10
0
7/19/09 12:00 PM
7/21/09 12:00 PM
7/23/09 12:00 PM
7/25/09 12:00 PM
7/27/09 12:00 PM
7/29/09 12:00 PM
7/31/09 12:00 PM
8/2/09 12:00 PM
Date

B.2 Georgetown Bridge Deck: Summer Pour

B2.1 iButton String Locations and Placement Times

Locations of iButton strings for this instrumentation, provided in Table B.4, were measured from the south end (beginning of pour) and the west face. iButton placement times, provided in Table B.5, were determined from examination of the iButton temperature data.

Table B.4: iButton string locations—GTBDS.

String	Distance from South end	Distance from West face
A1	13	24
B1	49	30.4
C1	99	22
C2	99	6.67
D1	121	21.9

All values in feet.

Table B.5: Concrete placement times—GTBDS

Strand	Placement Time
A	8/19/09 4:30 AM
B	8/19/09 5:47 AM
C	8/19/09 6:47 AM
D	8/19/09 6:57 AM

B2.2 iButton Depths

Table B.6 provides the heights of the iButtons measured from either the precast, prestressed concrete panel, or the top of the precast, prestressed concrete girder. While the exact depth of the bridge deck is not known, it is assumed that concrete sections are 4 in. thick over the concrete panels and 11 in. thick over the concrete girders. Descriptions of the iButton strings are also provided.

Table B.6: iButton depths—GTBDS

Location	String	Buttons	Height from bottom
Start of pour	A1	D	3.250
		C	2.125
		B	1.250
		A	0.375
First line, on panel, middle of deck	B1	D	3.250
		C	2.125
		B	1.125
		A	0.375
Second line, on panel, middle of deck	C1	D	3.500
		C	2.250
		B	1.375
		A	0.250
Second line, on panel, deck overhang	C2	D	3.125
		C	2.125
		B	1.125
		A	0.250
End of pour	D1	D	3.125
		C	2.125
		B	1.125
		A	0.250

All values in inches.

B2.3 Recorded Temperatures

The following figures present the complete set of temperature data for the Georgetown bridge deck summer pour. Figure B.3 presents a comparison of the temperatures recorded for a selected top iButton for each of the strands. The selected iButtons were located in the middle of the bridge deck width, when possible. Figure B.4 presents a comparison of the gradient recorded across the different strands. As before, each strand is represented by the iButton string located in the middle of the bridge deck width, when possible. In the gradient graph, the iButton gradient, in °F, is presented in on the primary vertical axis, while the ambient air temperature, in °F, is presented on the secondary vertical axis. The graphs following Figure B.4 are labeled with the bridge deck pour name, GTBDS, the iButton string name, and the duration of time presented on that graph. For each string, the first graph presents the 4-day temperature data, such that the first temperature peaks may be examined. The following graph presents the full data set for the iButton string. Due to various factors, some iButton strings may record longer durations than others.

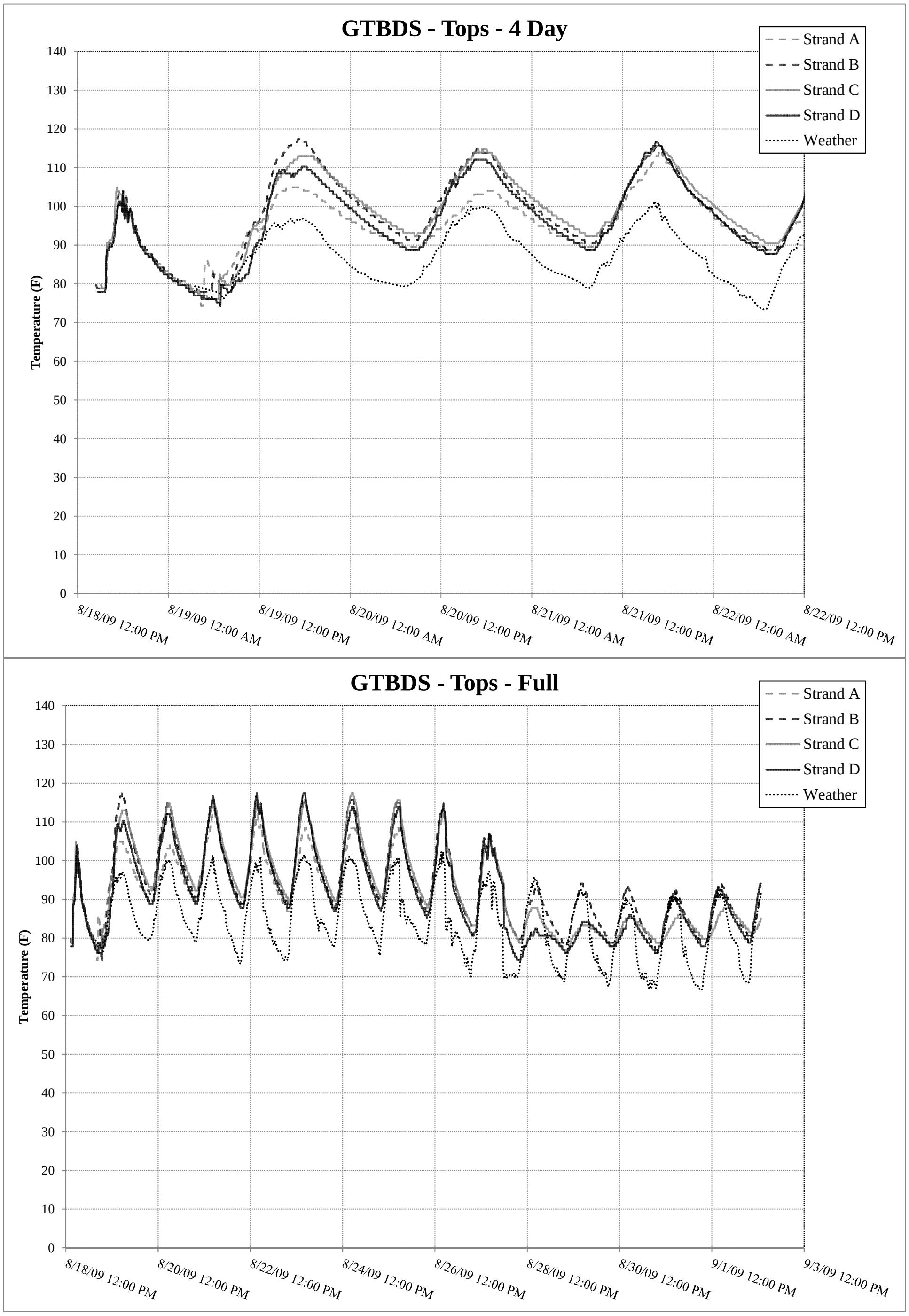

Figure B.3: Comparison of top iButton temperatures—GTBDS

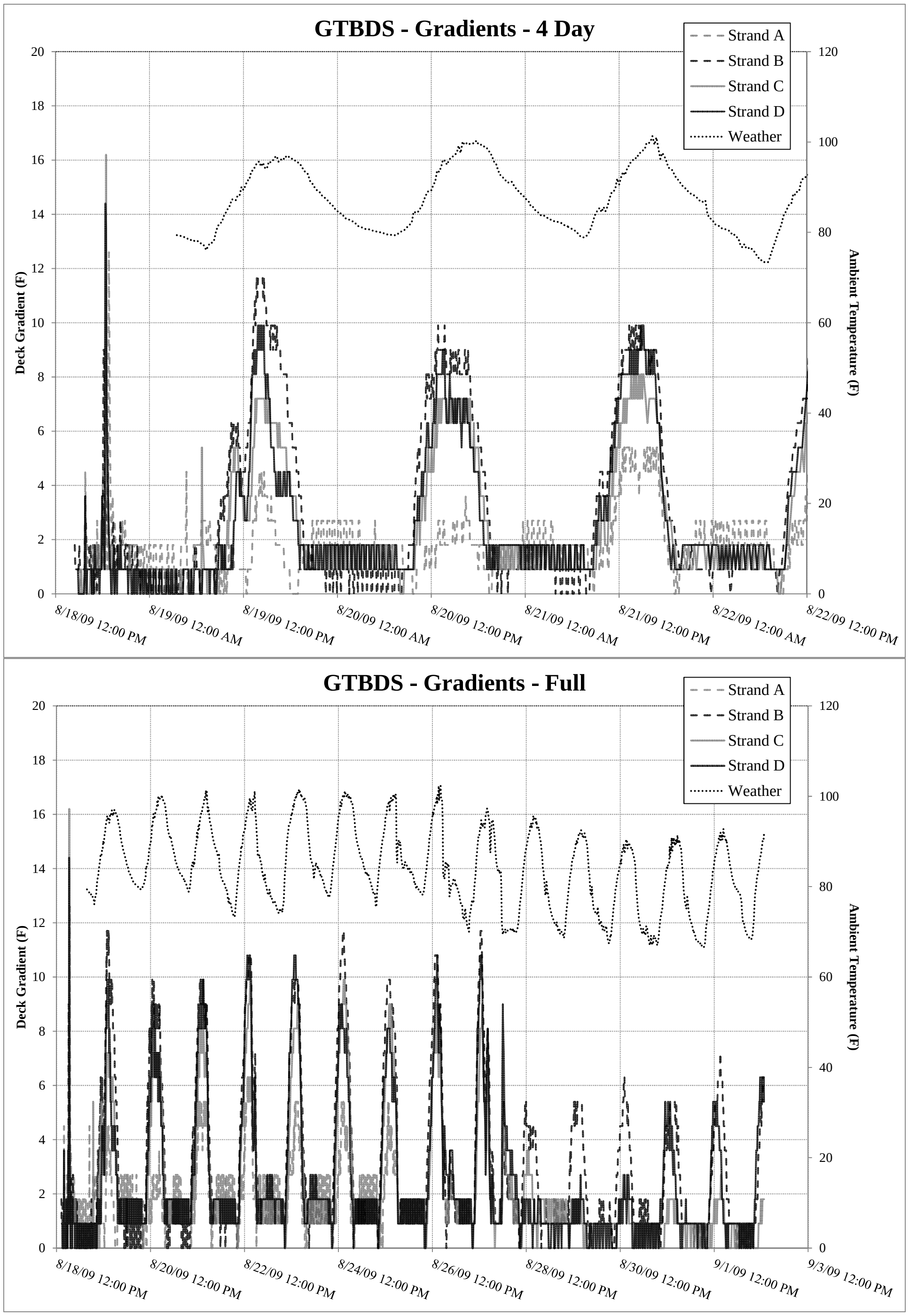

Figure B.4: Comparison of iButton strand gradients—GTBDS

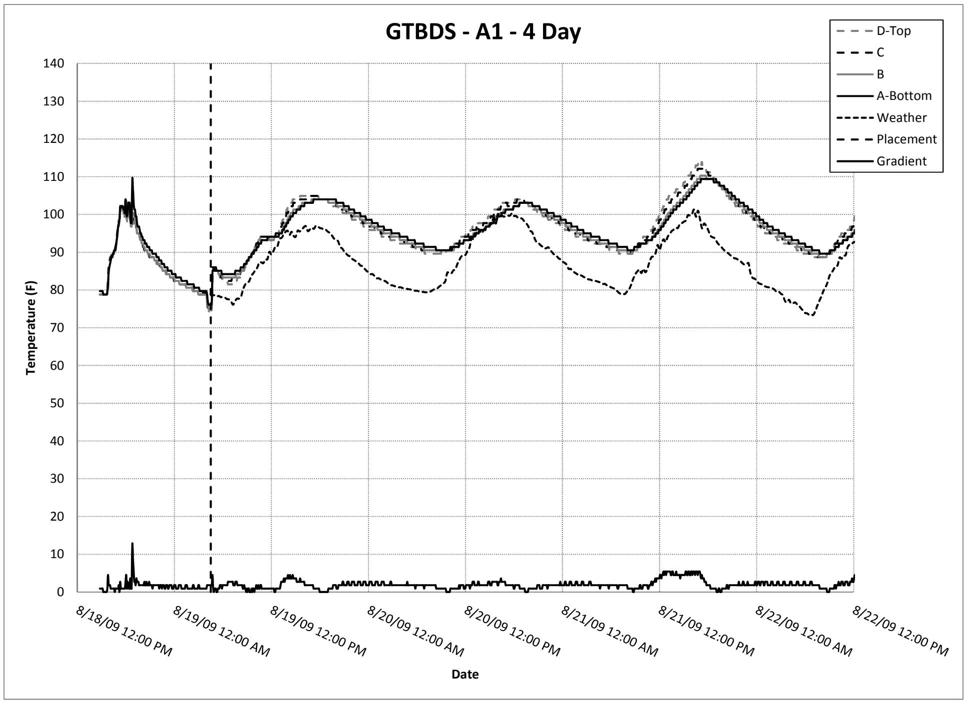
GTBDS - A1 - 4 Day
D-Top
C
B
A-Bottom
Weather
Placement
Gradient
Temperature (F)
140
130
120
110
100
90
80
70
60
50
40
30
20
10
0
8/18/09 12:00 PM
8/19/09 12:00 AM
8/19/09 12:00 PM
8/20/09 12:00 AM
8/20/09 12:00 PM
8/21/09 12:00 AM
8/21/09 12:00 PM
8/22/09 12:00 AM
8/22/09 12:00 PM
Date

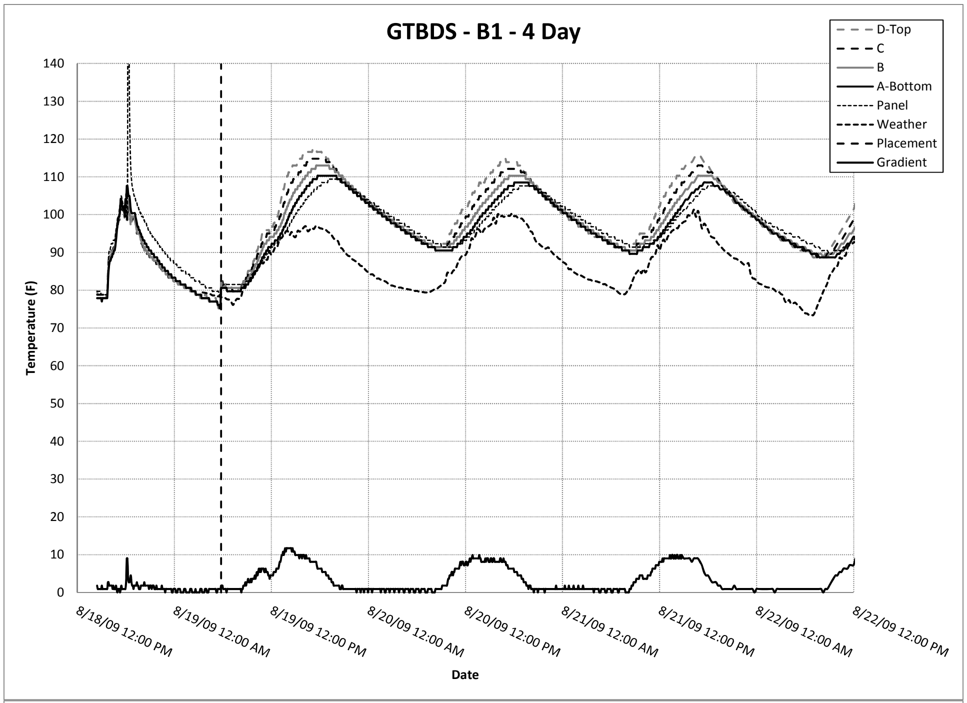
GTBDS - B1 - 4 Day
D-Top
C
B
A-Bottom
Panel
Weather
Placement
Gradient
Temperature (F)
140
130
120
110
100
90
80
70
60
50
40
30
20
10
0
8/18/09 12:00 PM
8/19/09 12:00 AM
8/19/09 12:00 PM
8/20/09 12:00 AM
8/20/09 12:00 PM
8/21/09 12:00 AM
8/21/09 12:00 PM
8/22/09 12:00 AM
8/22/09 12:00 PM
Date

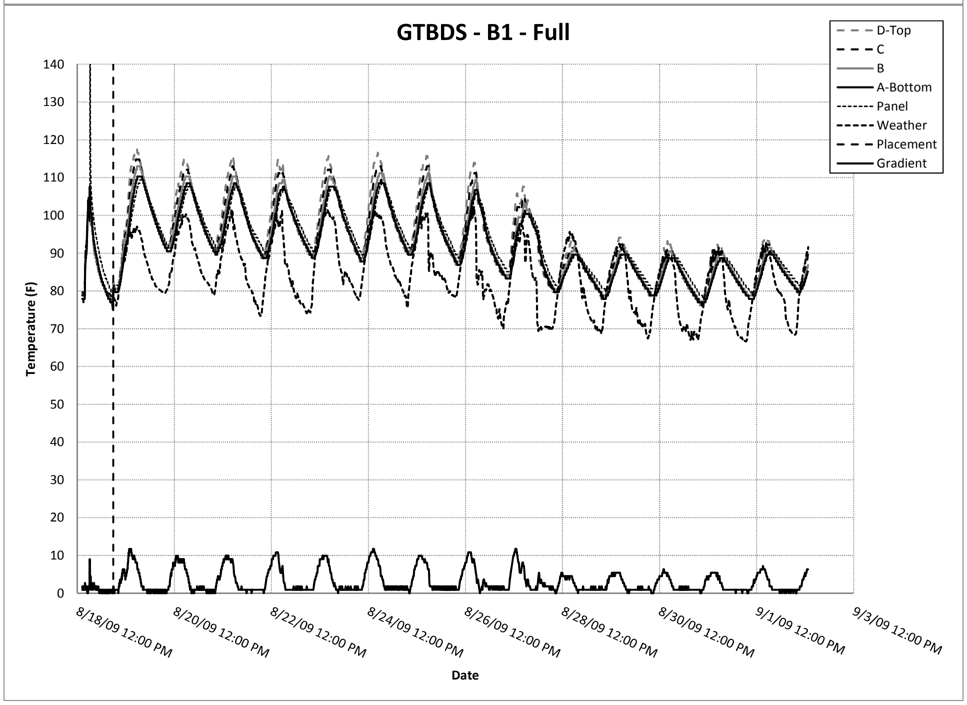
GTBDS - B1 - Full
D-Top
C
B
A-Bottom
Panel
Weather
Placement
Gradient
Temperature (F)
140
130
120
110
100
90
80
70
60
50
40
30
20
10
0
8/18/09 12:00 PM
8/20/09 12:00 PM
8/22/09 12:00 PM
8/24/09 12:00 PM
8/26/09 12:00 PM
8/28/09 12:00 PM
8/30/09 12:00 PM
9/1/09 12:00 PM
9/3/09 12:00 PM
Date

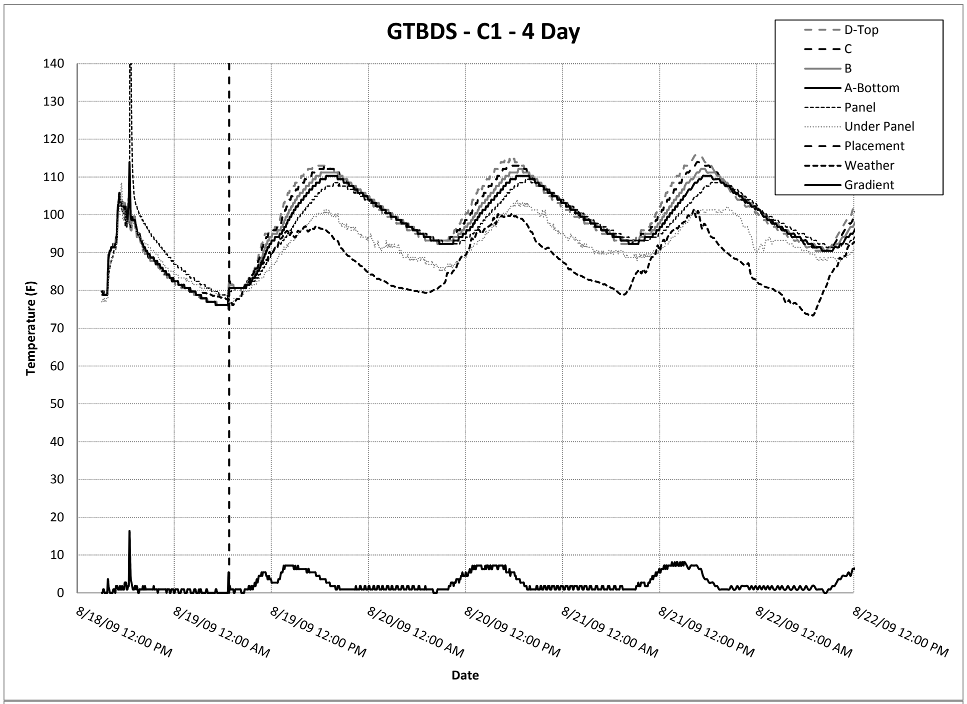
GTBDS - C1 - 4 Day
D-Top
C
B
A-Bottom
Panel
Under Panel
Placement
Weather
Gradient
Temperature (F)
140
130
120
110
100
90
80
70
60
50
40
30
20
10
0
8/18/09 12:00 PM
8/19/09 12:00 AM
8/19/09 12:00 PM
8/20/09 12:00 AM
8/20/09 12:00 PM
8/21/09 12:00 AM
8/21/09 12:00 PM
8/22/09 12:00 AM
8/22/09 12:00 PM
Date

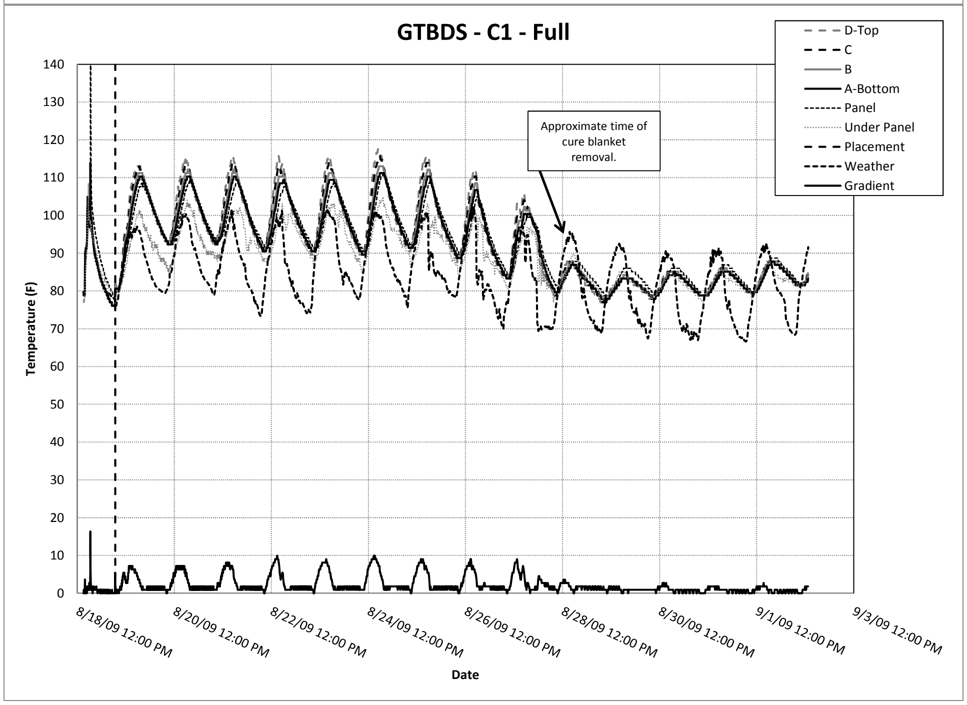
GTBDS - C1 - Full
D-Top
C
B
A-Bottom
Panel
Under Panel
Placement
Weather
Gradient
Approximate time of cure blanket removal.
Temperature (F)
140
130
120
110
100
90
80
70
60
50
40
30
20
10
0
8/18/09 12:00 PM
8/20/09 12:00 PM
8/22/09 12:00 PM
8/24/09 12:00 PM
8/26/09 12:00 PM
8/28/09 12:00 PM
8/30/09 12:00 PM
9/1/09 12:00 PM
9/3/09 12:00 PM
Date

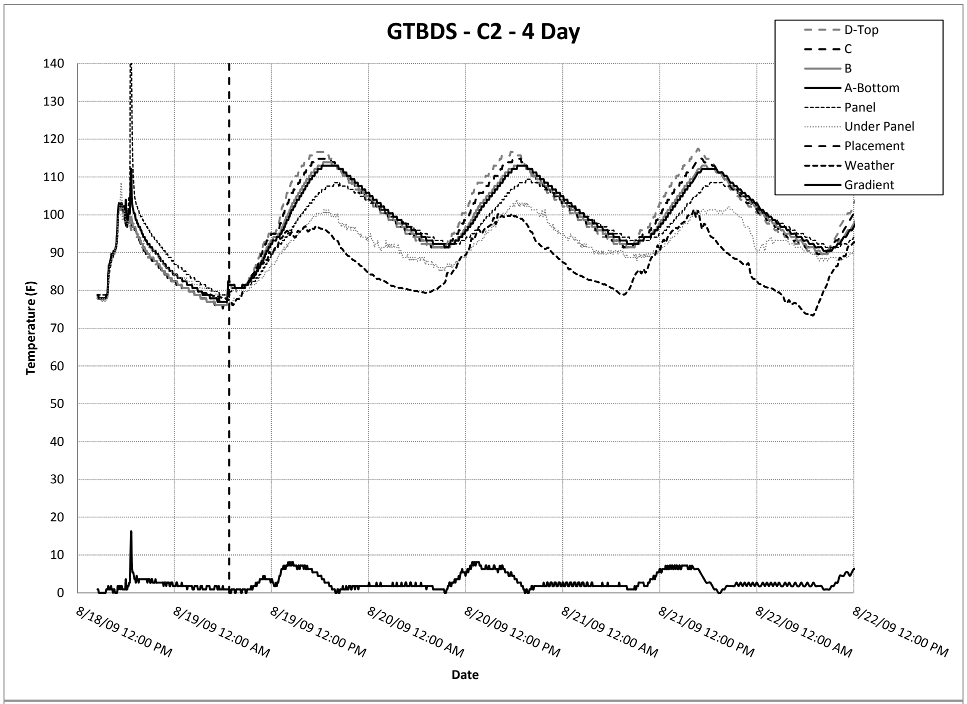
GTBDS - C2 - 4 Day
D-Top
C
B
A-Bottom
Panel
Under Panel
Placement
Weather
Gradient
Temperature (F)
0
10
20
30
40
50
60
70
80
90
100
110
120
130
140
8/18/09 12:00 PM
8/19/09 12:00 AM
8/19/09 12:00 PM
8/20/09 12:00 AM
8/20/09 12:00 PM
8/21/09 12:00 AM
8/21/09 12:00 PM
8/22/09 12:00 AM
8/22/09 12:00 PM
Date

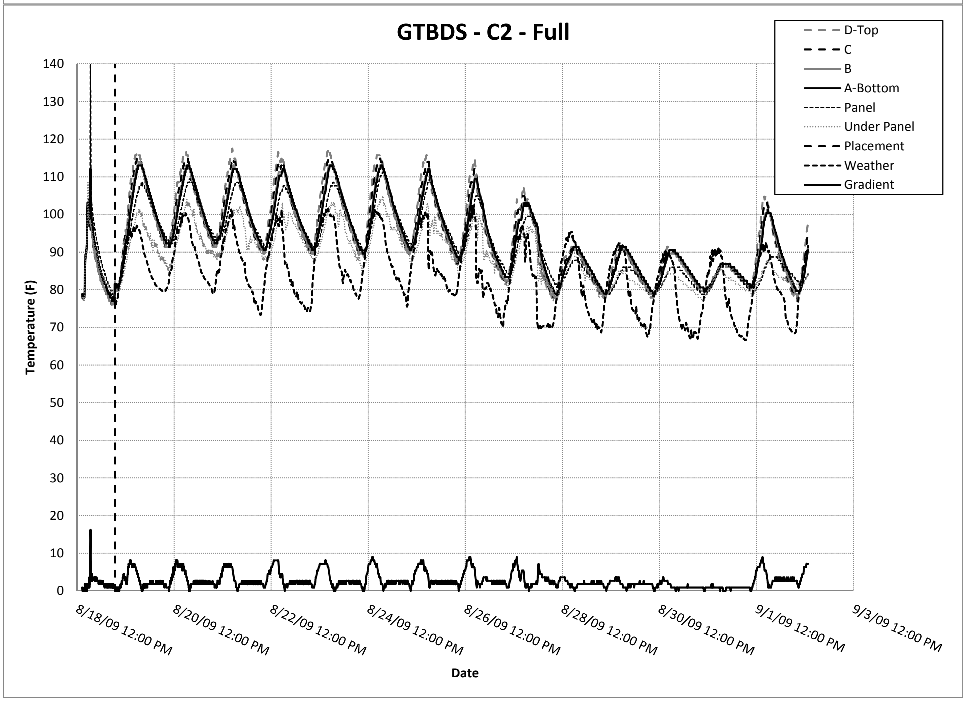
GTBDS - C2 - Full
D-Top
C
B
A-Bottom
Panel
Under Panel
Placement
Weather
Gradient
Temperature (F)
0
10
20
30
40
50
60
70
80
90
100
110
120
130
140
8/18/09 12:00 PM
8/20/09 12:00 PM
8/22/09 12:00 PM
8/24/09 12:00 PM
8/26/09 12:00 PM
8/28/09 12:00 PM
8/30/09 12:00 PM
9/1/09 12:00 PM
9/3/09 12:00 PM
Date

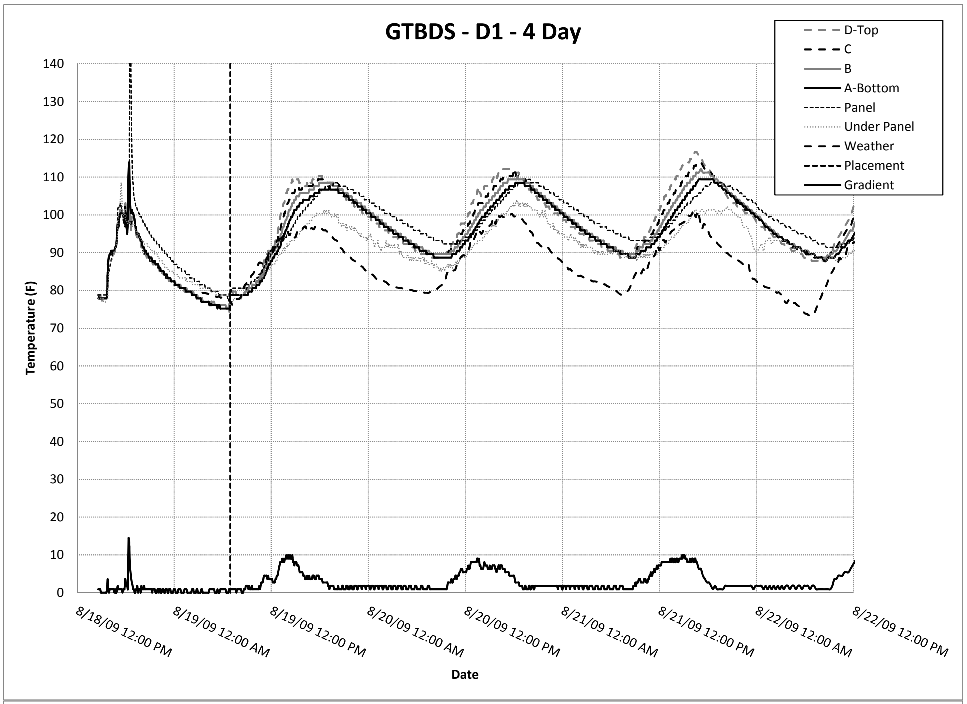
GTBDS - D1 - 4 Day
D-Top
C
B
A-Bottom
Panel
Under Panel
Weather
Placement
Gradient
Temperature (F)
140
130
120
110
100
90
80
70
60
50
40
30
20
10
0
8/18/09 12:00 PM
8/19/09 12:00 AM
8/19/09 12:00 PM
8/20/09 12:00 AM
8/20/09 12:00 PM
8/21/09 12:00 AM
8/21/09 12:00 PM
8/22/09 12:00 AM
8/22/09 12:00 PM
Date

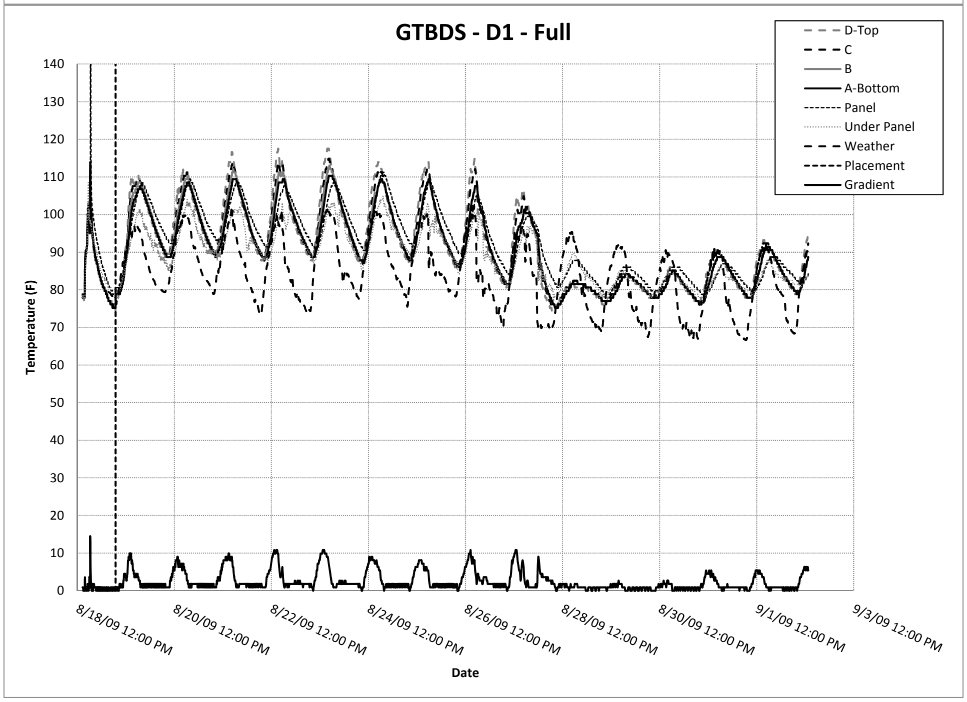
GTBDS - D1 - Full
D-Top
C
B
A-Bottom
Panel
Under Panel
Weather
Placement
Gradient
Temperature (F)
140
130
120
110
100
90
80
70
60
50
40
30
20
10
0
8/18/09 12:00 PM
8/20/09 12:00 PM
8/22/09 12:00 PM
8/24/09 12:00 PM
8/26/09 12:00 PM
8/28/09 12:00 PM
8/30/09 12:00 PM
9/1/09 12:00 PM
9/3/09 12:00 PM
Date

B.3 Georgetown Bridge Deck: Winter Pour

B.3.1 iButton String Locations and Placement Times

Locations of iButton strings for this instrumentation, provided in Table B.7, were measured from the north end (beginning of pour) and the east face. iButton placement times, provided in Table B.8, were determined from examination of the iButton temperature data.

Table B.7: iButton string locations—GTBDW.

String	Distance from North end	Distance from East face
A1	16	22.5
B1	84	24
B2	84	28.5
B3	84	31
C1	170	1
C2	170	19.5
C3	170	23
D1	255	22.5

All values in feet.

Table B.8: Concrete placement times—GTBDW

Strand	Placement Time
A	11/19/09 8:02 AM
B	11/19/09 8:51 AM
C	11/19/09 10:07 AM
D	11/19/09 11:38 AM

B.3.2 iButton Depths

Table B.9 provides the heights of the iButtons measured from either the precast, prestressed concrete panel, or the top of the precast, prestressed concrete girder. While the exact depth of the bridge deck is not known, it is assumed that concrete sections are 4 in. thick over the concrete panels and 11 in. thick over the concrete girders. Descriptions of the iButton strings are also provided.

Table B.9: iButton depths—GTBDW

Location	String	Button	Height from bottom
Start of pour, on panel	A1	D	3.375
		C	2.500
		B	1.250
		A	0.500
First line, mid-width, on panel	B1	D	3.750
		C	2.750
		B	1.750
		A	0.500
First line, West side of deck, on panel	B2	D	3.375
		C	2.375
		B	1.250
		A	0.500
First line, on the girder	B3	F	9.625
		E	8.563
		D	7.625
		C	6.625
		B	3.750
		A	0.500
Second Line, on East overhang, no precast panel	C1	D	6.125
		C	5.000
		B	4.125
		A	3.250
Second line, on girder	C2	F	9.500
		E	8.625
		D	7.500
		C	6.500
		B	3.500
		A	0.500
Second line, mid-width, on panel	C3	D	3.500
		C	2.625
		B	1.625
		A	0.500
End of pour, on panel	D1	D	3.500
		C	2.250
		B	1.250
		A	0.375

All values in inches.

B3.3 Recorded Temperatures

The following figures present the complete set of temperature data for the Georgetown bridge deck winter pour. Figure B.5 presents a comparison of the temperatures recorded for a selected top iButton for each of the strands. The selected iButtons were located in the middle of the bridge deck width, when possible. Figure B.6 presents a comparison of the gradient recorded across the different strands. As before, each strand is represented by the iButton string located in the middle of the bridge deck width, when possible. In the gradient graph, the iButton gradient, in °F, is presented in on the primary vertical axis, while the ambient air temperature, in °F, is presented on the secondary vertical axis. The graphs following Figure B.6 are labeled with the bridge deck pour name, GTBDW, the iButton string name, and the duration of time presented on that graph. For each string, the first graph presents the 7-day temperature data, such that the first temperature peaks may be examined. Seven days was chosen rather than four due to the reduced early-age peaks, and the increased duration of total iButton measurements. The following graph presents the 28-day data set for the iButton string, followed by the full data set. Due to various factors, some iButton strings may record longer durations than others.

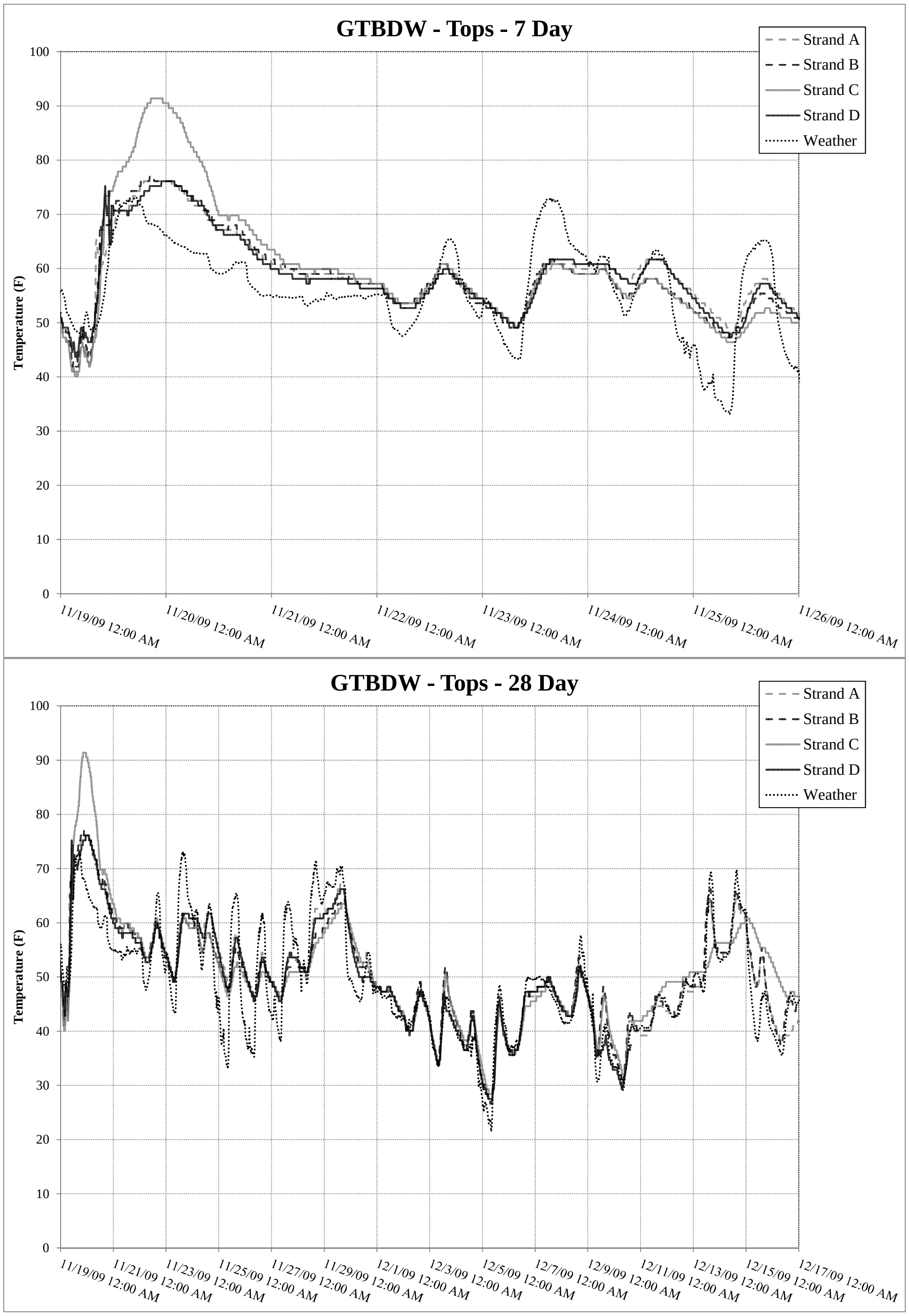

Figure B.5: Comparison of top iButton temperatures—GTBDW

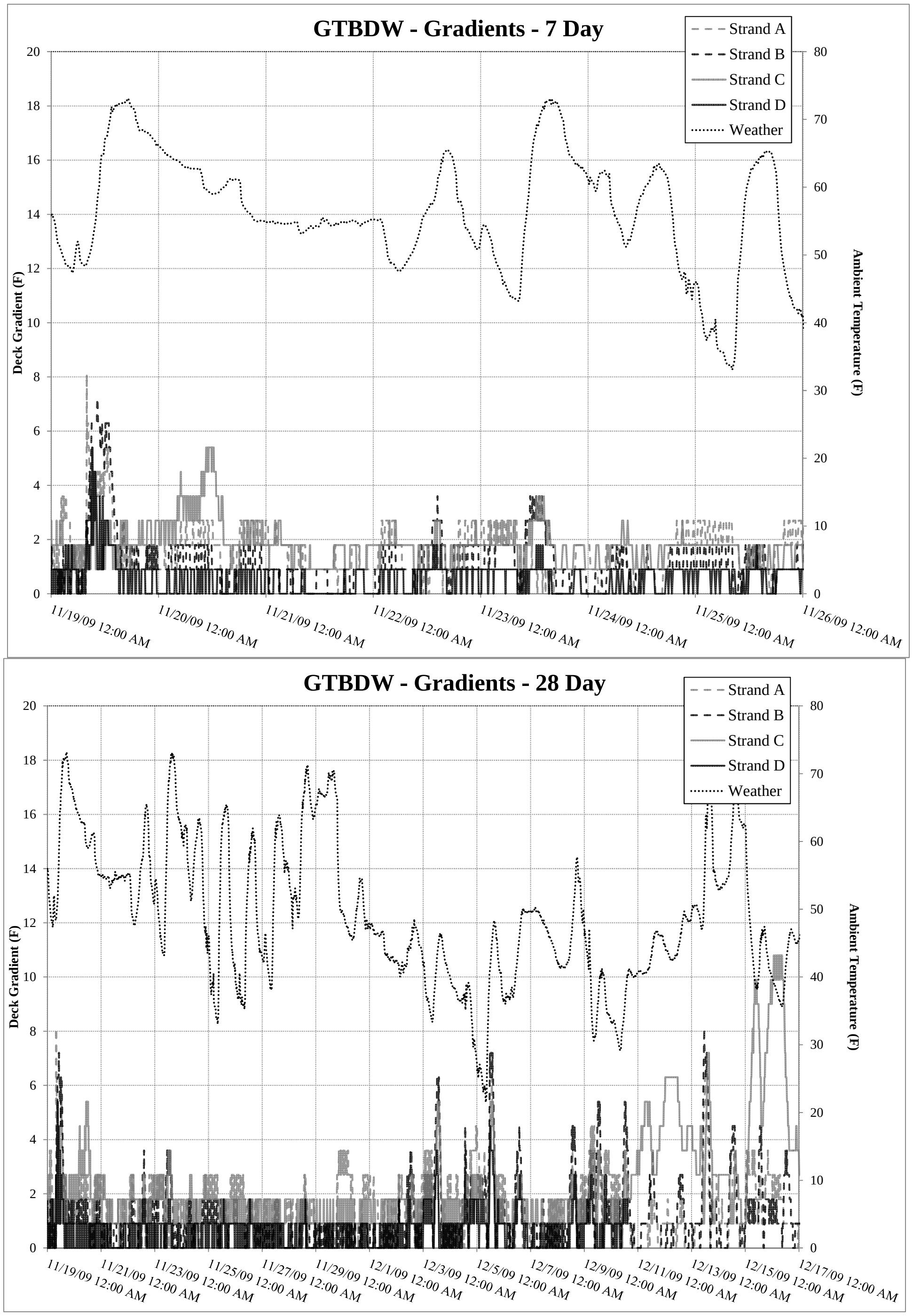

Figure B.6: Comparison of iButton strand gradients—GTBDW

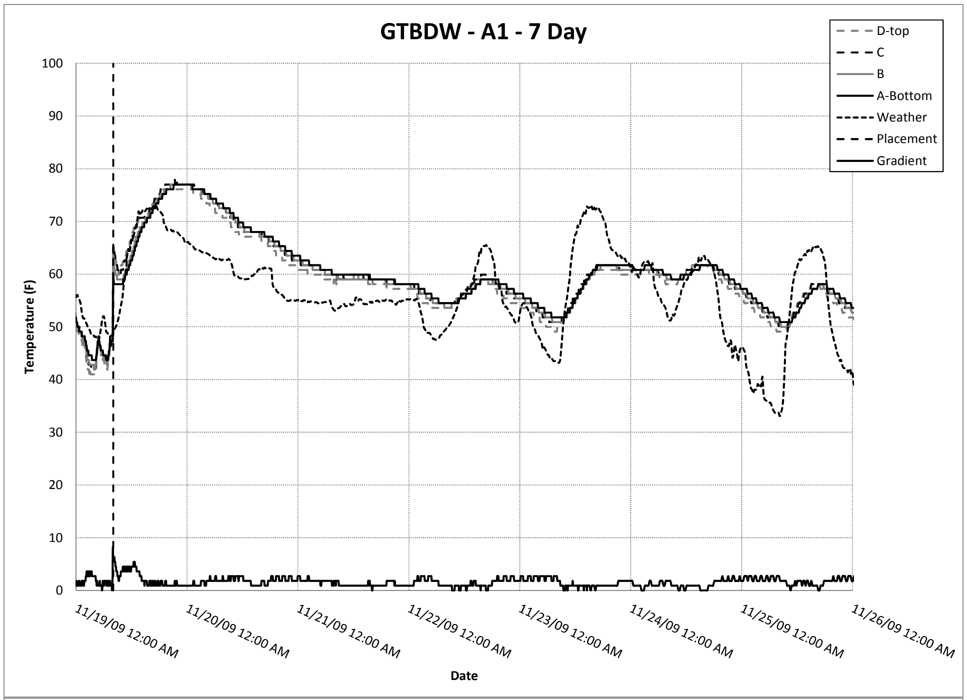
GTBDW - A1 - 7 Day
D-top
C
B
A-Bottom
Weather
Placement
Gradient
Temperature (F)
100
90
80
70
60
50
40
30
20
10
0
11/19/09 12:00 AM
11/20/09 12:00 AM
11/21/09 12:00 AM
11/22/09 12:00 AM
11/23/09 12:00 AM
11/24/09 12:00 AM
11/25/09 12:00 AM
11/26/09 12:00 AM
Date

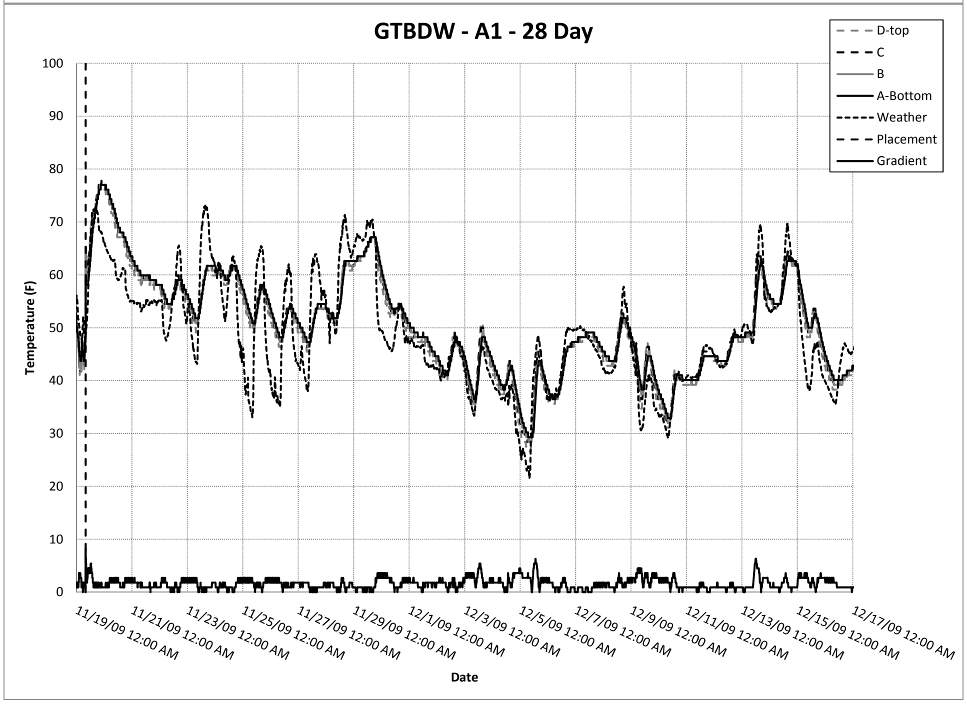
GTBDW - A1 - 28 Day
D-top
C
B
A-Bottom
Weather
Placement
Gradient
Temperature (F)
100
90
80
70
60
50
40
30
20
10
0
11/19/09 12:00 AM
11/21/09 12:00 AM
11/23/09 12:00 AM
11/25/09 12:00 AM
11/27/09 12:00 AM
11/29/09 12:00 AM
12/1/09 12:00 AM
12/3/09 12:00 AM
12/5/09 12:00 AM
12/7/09 12:00 AM
12/9/09 12:00 AM
12/11/09 12:00 AM
12/13/09 12:00 AM
12/15/09 12:00 AM
12/17/09 12:00 AM
Date

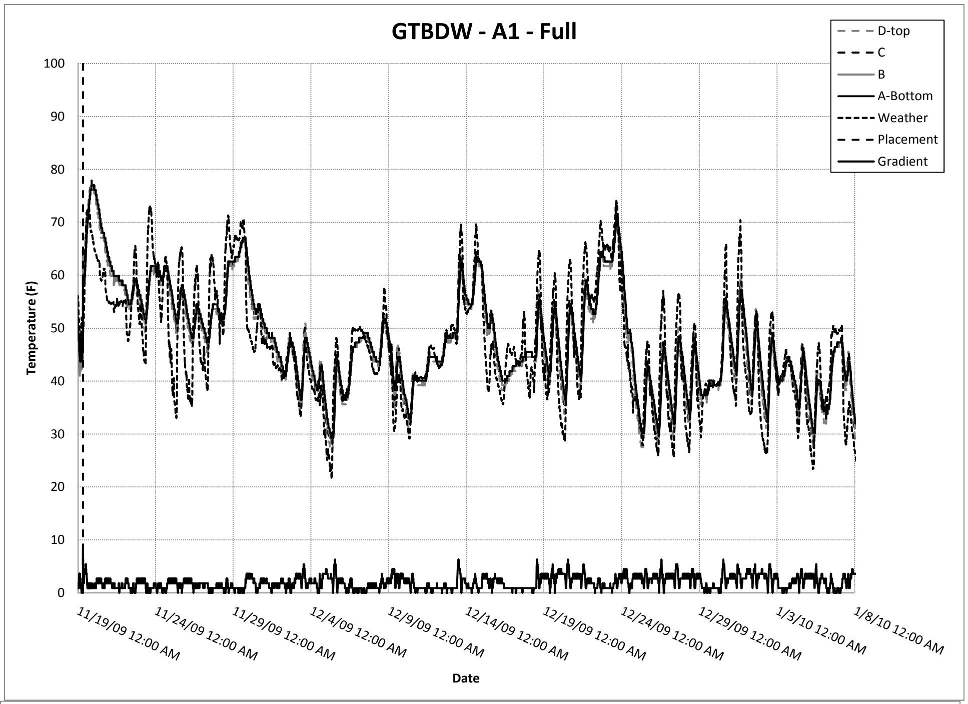
GTBDW - A1 - Full
D-top
C
B
A-Bottom
Weather
Placement
Gradient
Temperature (F)
100
90
80
70
60
50
40
30
20
10
0
11/19/09 12:00 AM
11/24/09 12:00 AM
11/29/09 12:00 AM
12/4/09 12:00 AM
12/9/09 12:00 AM
12/14/09 12:00 AM
12/19/09 12:00 AM
12/24/09 12:00 AM
12/29/09 12:00 AM
1/3/10 12:00 AM
1/8/10 12:00 AM
Date

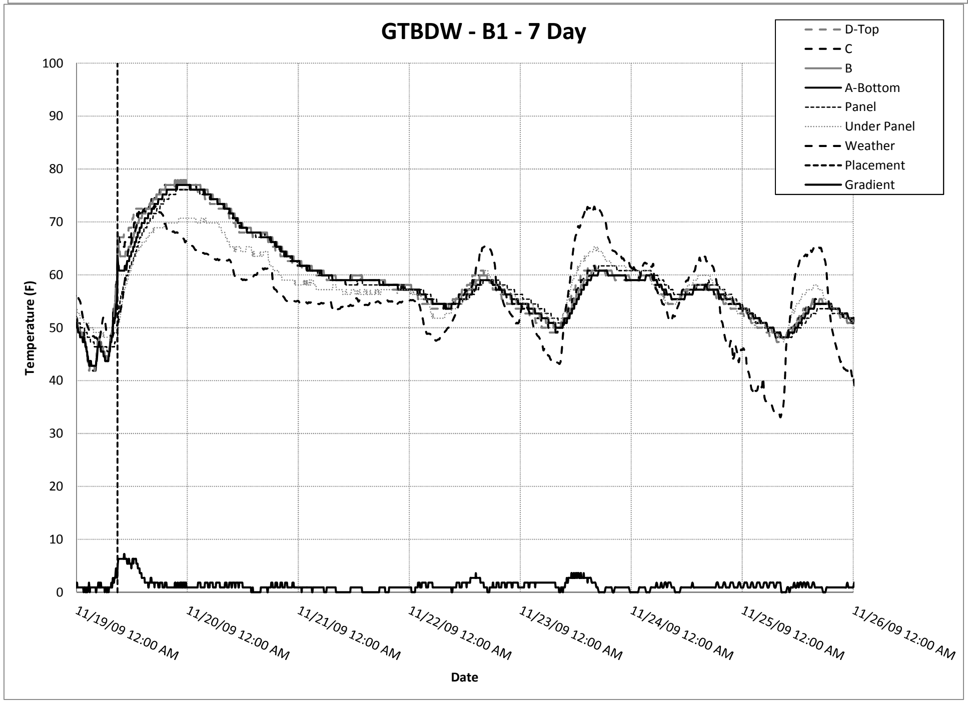
GTBDW - B1 - 7 Day
D-Top
C
B
A-Bottom
Panel
Under Panel
Weather
Placement
Gradient
Temperature (F)
100
90
80
70
60
50
40
30
20
10
0
11/19/09 12:00 AM
11/20/09 12:00 AM
11/21/09 12:00 AM
11/22/09 12:00 AM
11/23/09 12:00 AM
11/24/09 12:00 AM
11/25/09 12:00 AM
11/26/09 12:00 AM
Date

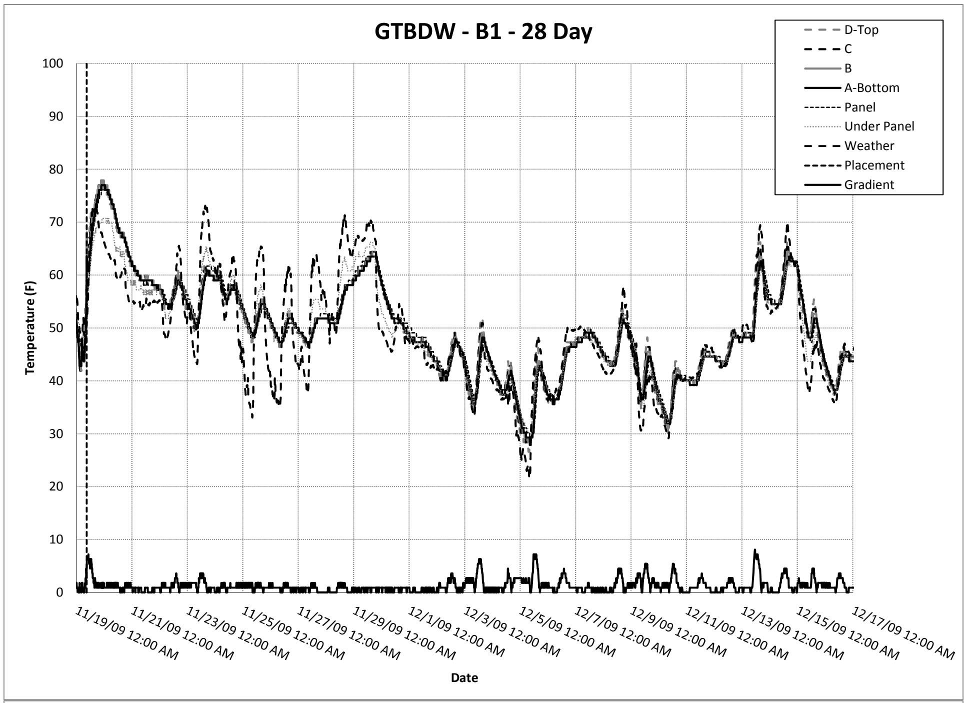
GTBDW - B1 - 28 Day
D-Top
C
B
A-Bottom
Panel
Under Panel
Weather
Placement
Gradient
Temperature (F)
100
90
80
70
60
50
40
30
20
10
0
11/19/09 12:00 AM
11/21/09 12:00 AM
11/23/09 12:00 AM
11/25/09 12:00 AM
11/27/09 12:00 AM
11/29/09 12:00 AM
12/1/09 12:00 AM
12/3/09 12:00 AM
12/5/09 12:00 AM
12/7/09 12:00 AM
12/9/09 12:00 AM
12/11/09 12:00 AM
12/13/09 12:00 AM
12/15/09 12:00 AM
12/17/09 12:00 AM
Date

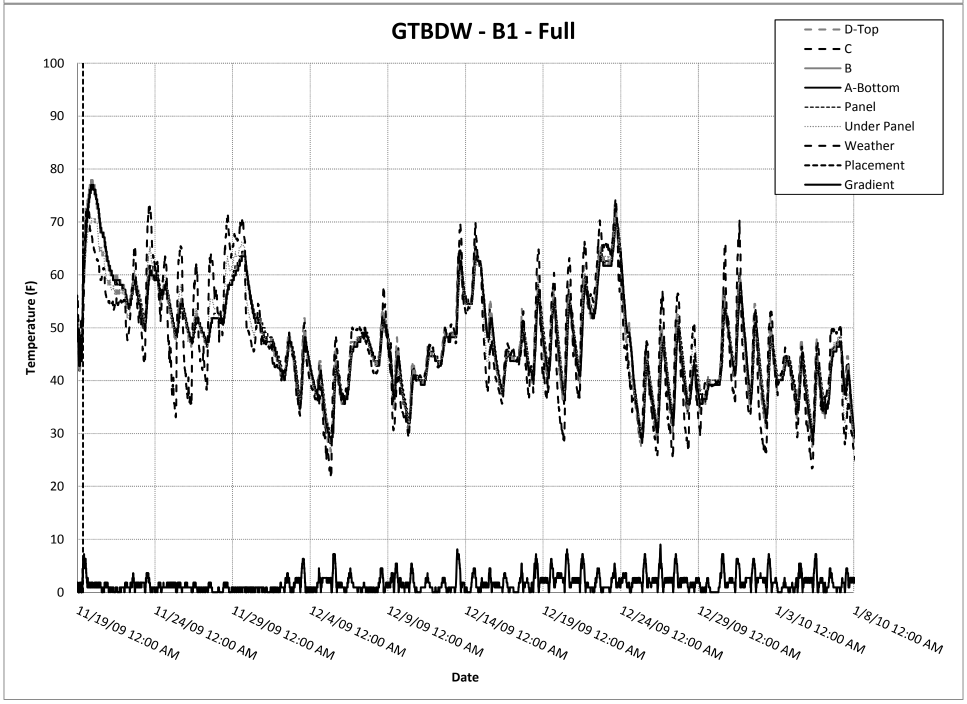
GTBDW - B1 - Full
D-Top
C
B
A-Bottom
Panel
Under Panel
Weather
Placement
Gradient
Temperature (F)
100
90
80
70
60
50
40
30
20
10
0
11/19/09 12:00 AM
11/24/09 12:00 AM
11/29/09 12:00 AM
12/4/09 12:00 AM
12/9/09 12:00 AM
12/14/09 12:00 AM
12/19/09 12:00 AM
12/24/09 12:00 AM
12/29/09 12:00 AM
1/3/10 12:00 AM
1/8/10 12:00 AM
Date

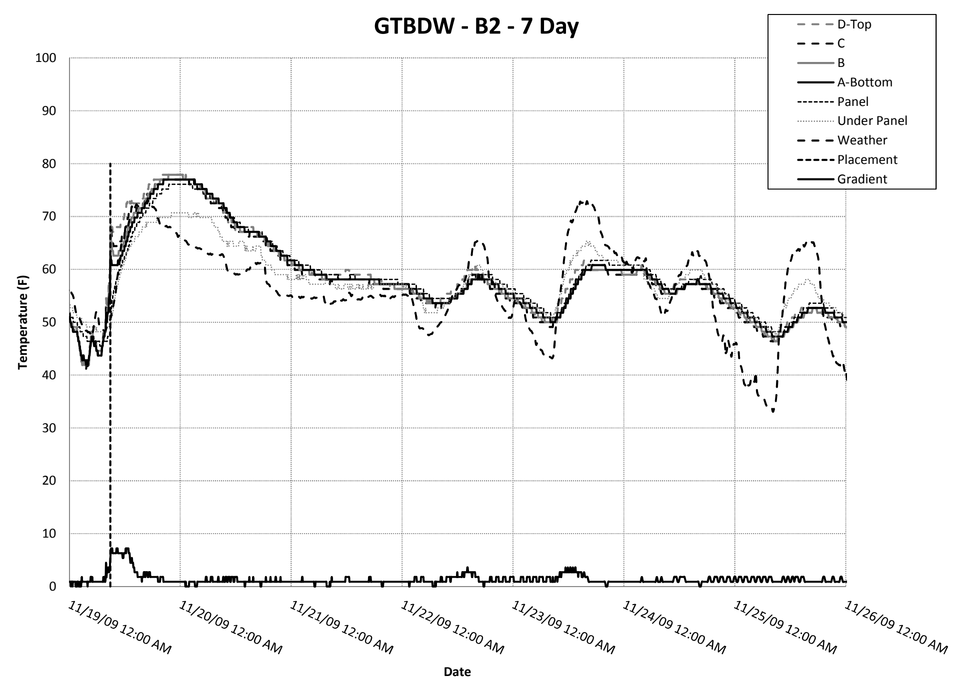
GTBDW - B2 - 7 Day
D-Top
C
B
A-Bottom
Panel
Under Panel
Weather
Placement
Gradient
Temperature (F)
100
90
80
70
60
50
40
30
20
10
0
11/19/09 12:00 AM
11/20/09 12:00 AM
11/21/09 12:00 AM
11/22/09 12:00 AM
11/23/09 12:00 AM
11/24/09 12:00 AM
11/25/09 12:00 AM
11/26/09 12:00 AM
Date

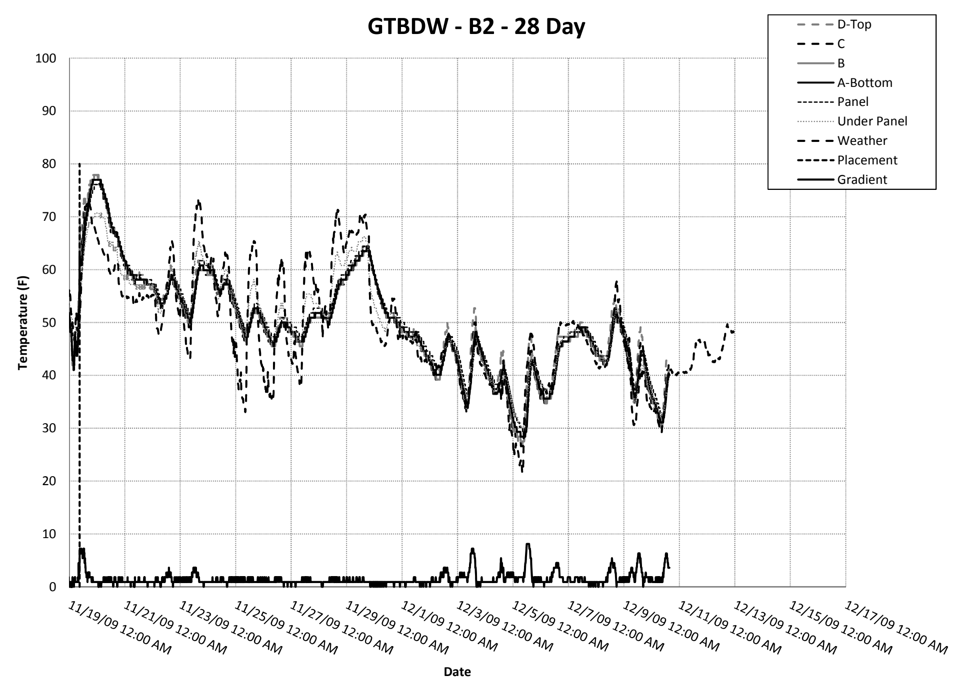
GTBDW - B2 - 28 Day
D-Top
C
B
A-Bottom
Panel
Under Panel
Weather
Placement
Gradient
Temperature (F)
100
90
80
70
60
50
40
30
20
10
0
11/19/09 12:00 AM
11/21/09 12:00 AM
11/23/09 12:00 AM
11/25/09 12:00 AM
11/27/09 12:00 AM
11/29/09 12:00 AM
12/1/09 12:00 AM
12/3/09 12:00 AM
12/5/09 12:00 AM
12/7/09 12:00 AM
12/9/09 12:00 AM
12/11/09 12:00 AM
12/13/09 12:00 AM
12/15/09 12:00 AM
12/17/09 12:00 AM
Date

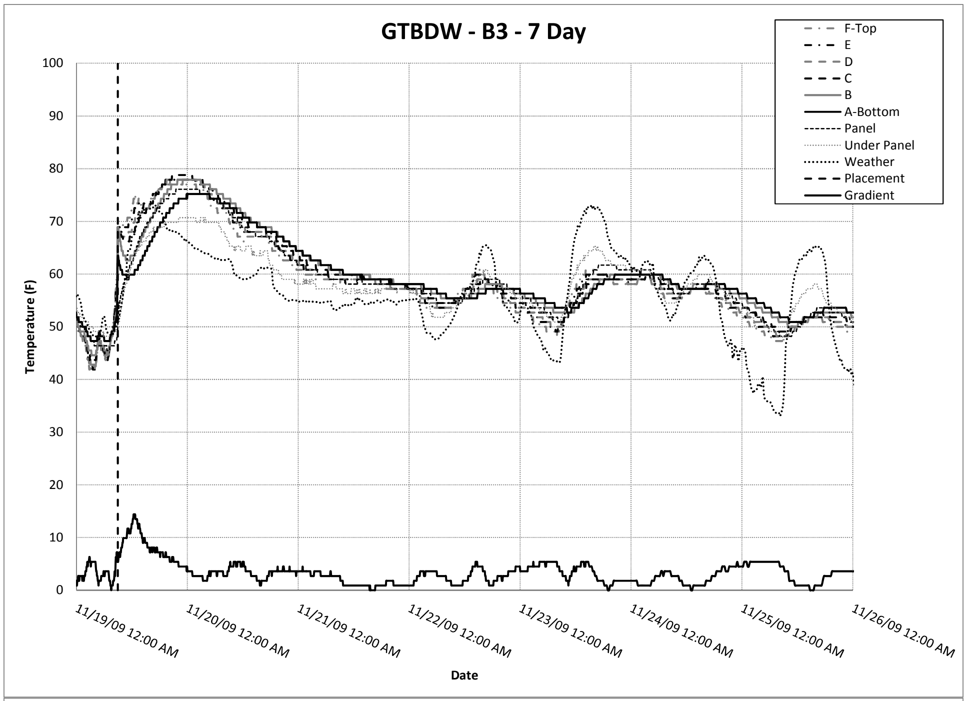
GTBDW - B3 - 7 Day
F-Top
E
D
C
B
A-Bottom
Panel
Under Panel
Weather
Placement
Gradient
Temperature (F)
100
90
80
70
60
50
40
30
20
10
0
11/19/09 12:00 AM
11/20/09 12:00 AM
11/21/09 12:00 AM
11/22/09 12:00 AM
11/23/09 12:00 AM
11/24/09 12:00 AM
11/25/09 12:00 AM
11/26/09 12:00 AM
Date

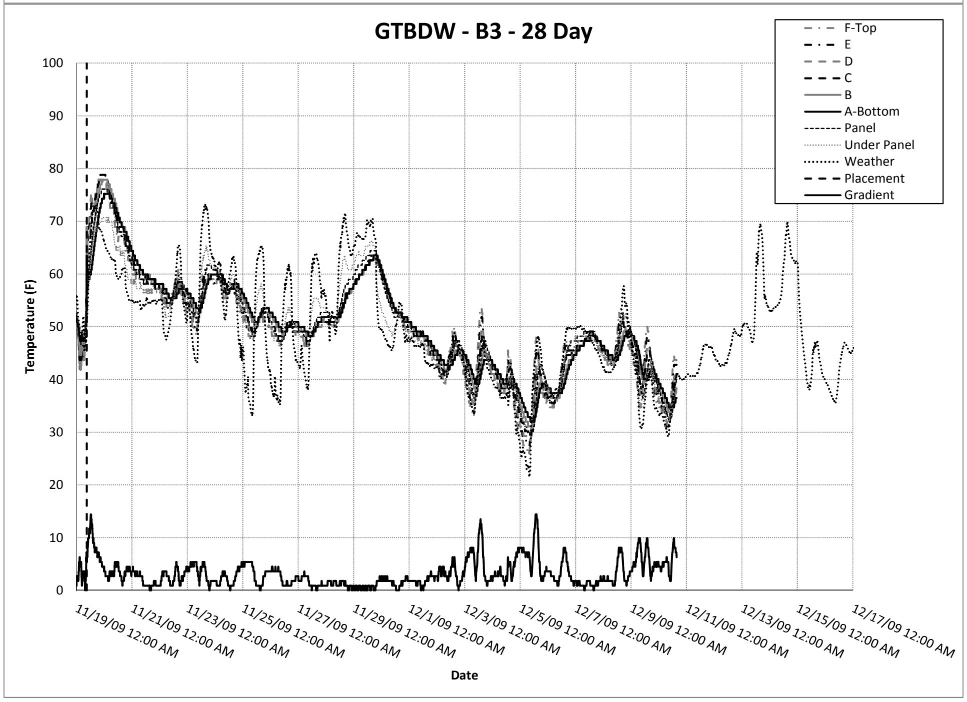
GTBDW - B3 - 28 Day
F-Top
E
D
C
B
A-Bottom
Panel
Under Panel
Weather
Placement
Gradient
Temperature (F)
100
90
80
70
60
50
40
30
20
10
0
11/19/09 12:00 AM
11/21/09 12:00 AM
11/23/09 12:00 AM
11/25/09 12:00 AM
11/27/09 12:00 AM
11/29/09 12:00 AM
12/1/09 12:00 AM
12/3/09 12:00 AM
12/5/09 12:00 AM
12/7/09 12:00 AM
12/9/09 12:00 AM
12/11/09 12:00 AM
12/13/09 12:00 AM
12/15/09 12:00 AM
12/17/09 12:00 AM
Date

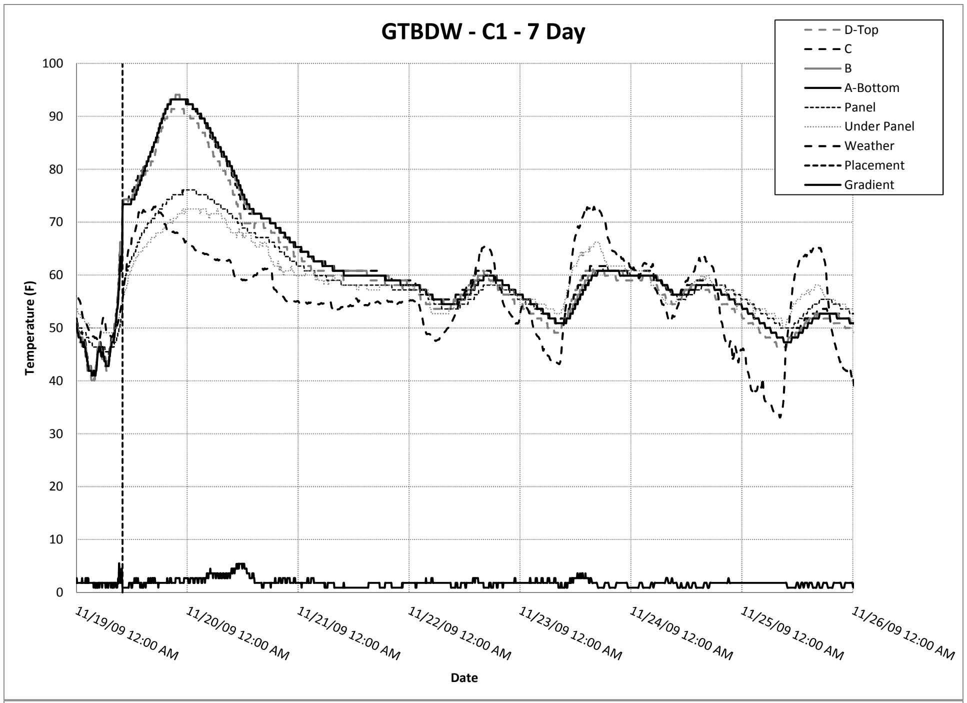
GTBDW - C1 - 7 Day
D-Top
C
B
A-Bottom
Panel
Under Panel
Weather
Placement
Gradient
Temperature (F)
100
90
80
70
60
50
40
30
20
10
0
11/19/09 12:00 AM
11/20/09 12:00 AM
11/21/09 12:00 AM
11/22/09 12:00 AM
11/23/09 12:00 AM
11/24/09 12:00 AM
11/25/09 12:00 AM
11/26/09 12:00 AM
Date

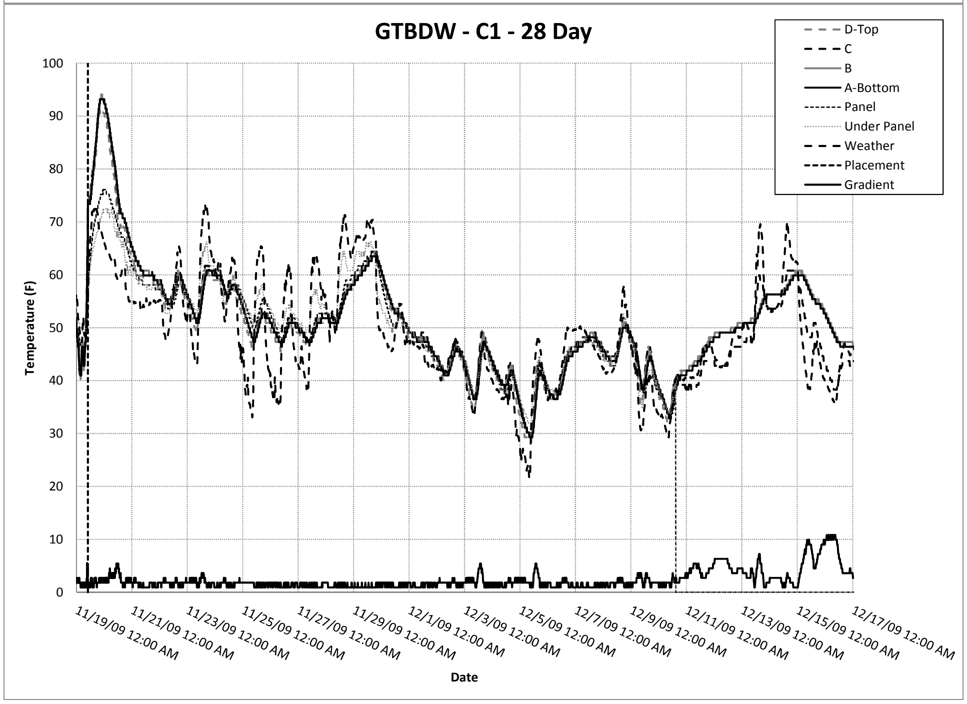
GTBDW - C1 - 28 Day
D-Top
C
B
A-Bottom
Panel
Under Panel
Weather
Placement
Gradient
Temperature (F)
100
90
80
70
60
50
40
30
20
10
0
11/19/09 12:00 AM
11/21/09 12:00 AM
11/23/09 12:00 AM
11/25/09 12:00 AM
11/27/09 12:00 AM
11/29/09 12:00 AM
12/1/09 12:00 AM
12/3/09 12:00 AM
12/5/09 12:00 AM
12/7/09 12:00 AM
12/9/09 12:00 AM
12/11/09 12:00 AM
12/13/09 12:00 AM
12/15/09 12:00 AM
12/17/09 12:00 AM
Date

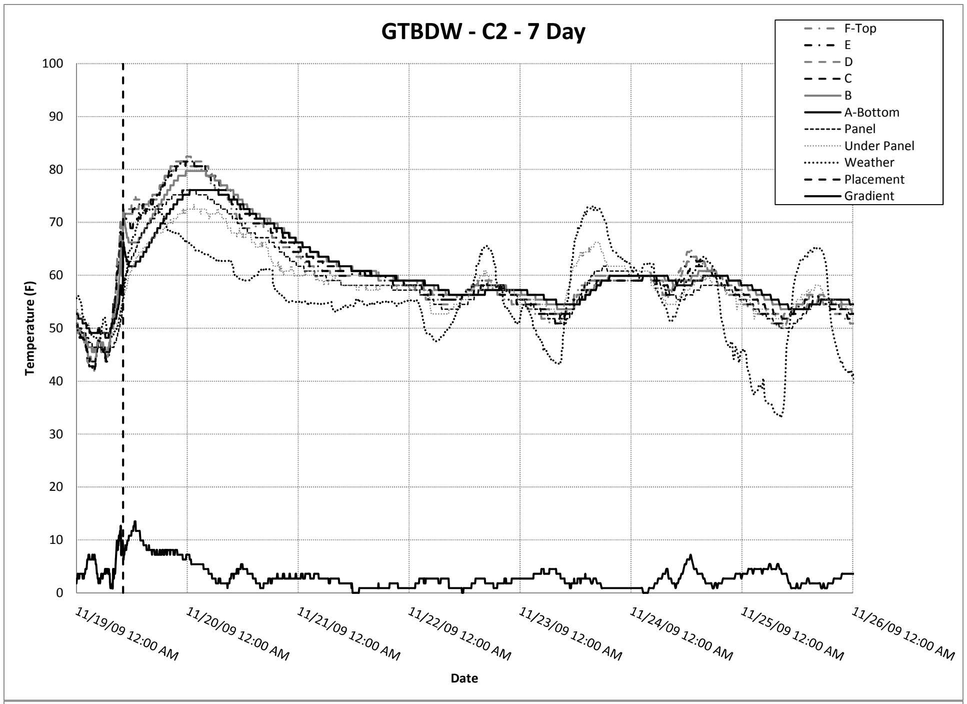
GTBDW - C2 - 7 Day
F-Top
E
D
C
B
A-Bottom
Panel
Under Panel
Weather
Placement
Gradient
Temperature (F)
0
10
20
30
40
50
60
70
80
90
100
11/19/09 12:00 AM
11/20/09 12:00 AM
11/21/09 12:00 AM
11/22/09 12:00 AM
11/23/09 12:00 AM
11/24/09 12:00 AM
11/25/09 12:00 AM
11/26/09 12:00 AM
Date

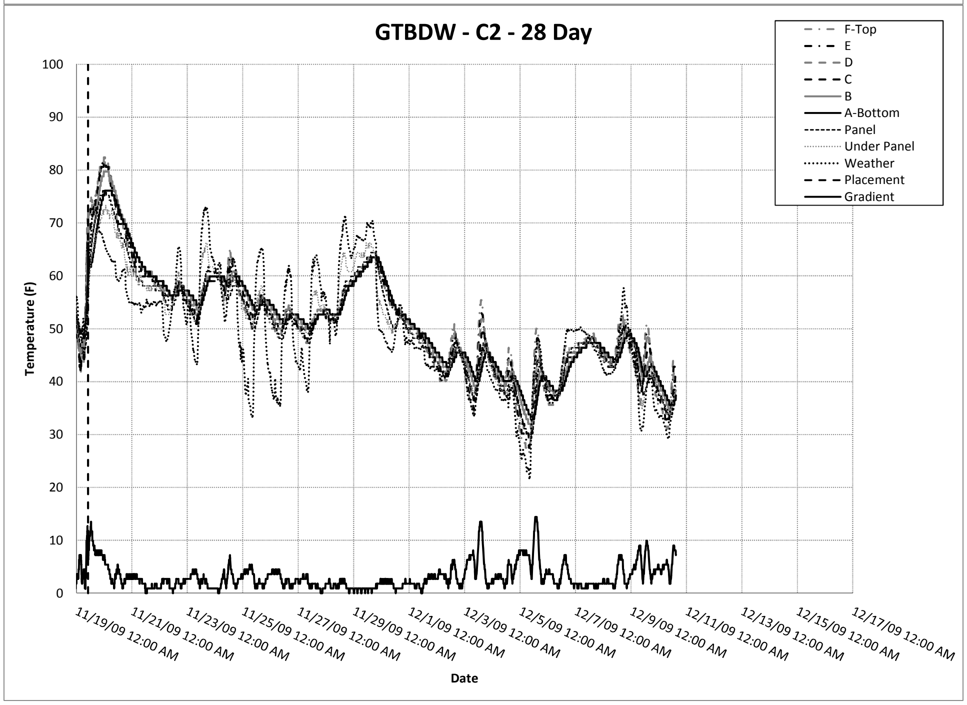
GTBDW - C2 - 28 Day
F-Top
E
D
C
B
A-Bottom
Panel
Under Panel
Weather
Placement
Gradient
Temperature (F)
0
10
20
30
40
50
60
70
80
90
100
11/19/09 12:00 AM
11/21/09 12:00 AM
11/23/09 12:00 AM
11/25/09 12:00 AM
11/27/09 12:00 AM
11/29/09 12:00 AM
12/1/09 12:00 AM
12/3/09 12:00 AM
12/5/09 12:00 AM
12/7/09 12:00 AM
12/9/09 12:00 AM
12/11/09 12:00 AM
12/13/09 12:00 AM
12/15/09 12:00 AM
12/17/09 12:00 AM
Date

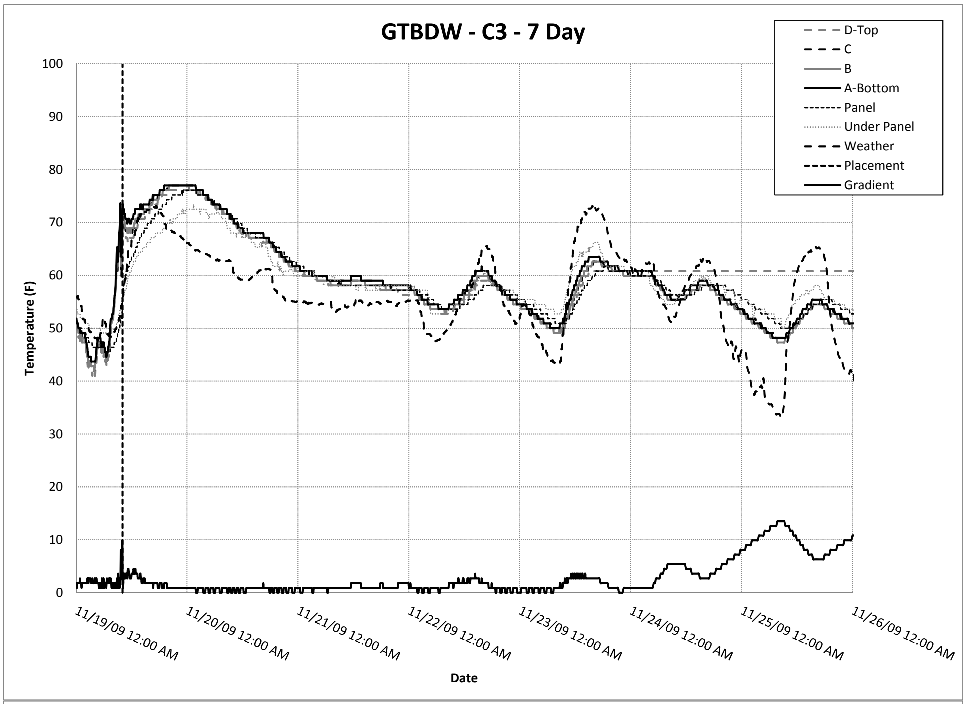
GTBDW - C3 - 7 Day
D-Top
C
B
A-Bottom
Panel
Under Panel
Weather
Placement
Gradient
Temperature (F)
100
90
80
70
60
50
40
30
20
10
0
11/19/09 12:00 AM
11/20/09 12:00 AM
11/21/09 12:00 AM
11/22/09 12:00 AM
11/23/09 12:00 AM
11/24/09 12:00 AM
11/25/09 12:00 AM
11/26/09 12:00 AM
Date

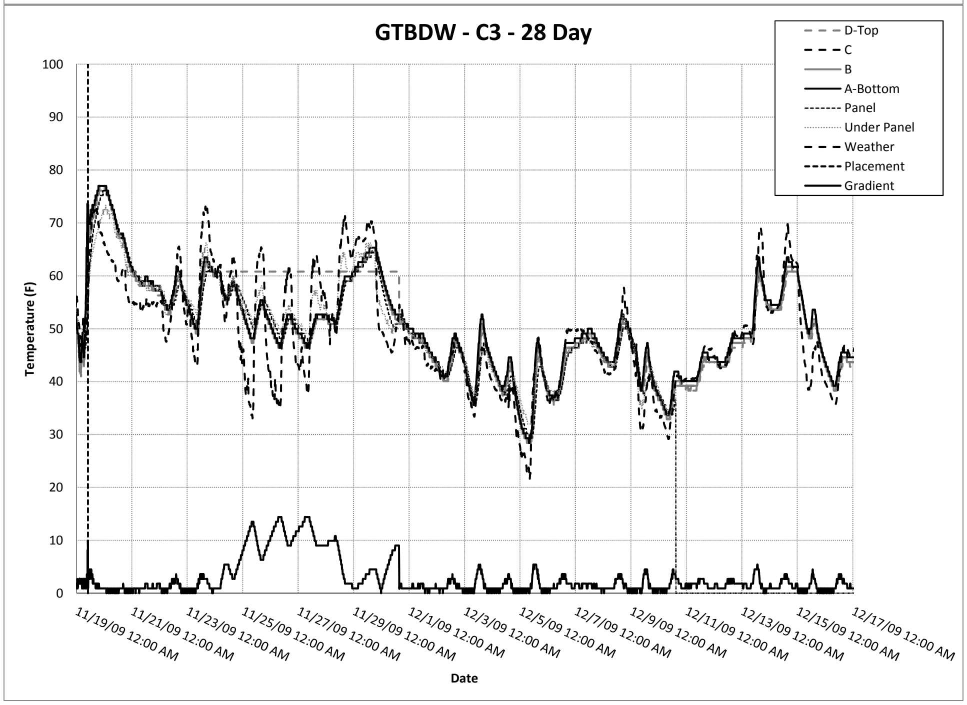
GTBDW - C3 - 28 Day
D-Top
C
B
A-Bottom
Panel
Under Panel
Weather
Placement
Gradient
Temperature (F)
100
90
80
70
60
50
40
30
20
10
0
11/19/09 12:00 AM
11/21/09 12:00 AM
11/23/09 12:00 AM
11/25/09 12:00 AM
11/27/09 12:00 AM
11/29/09 12:00 AM
12/1/09 12:00 AM
12/3/09 12:00 AM
12/5/09 12:00 AM
12/7/09 12:00 AM
12/9/09 12:00 AM
12/11/09 12:00 AM
12/13/09 12:00 AM
12/15/09 12:00 AM
12/17/09 12:00 AM
Date

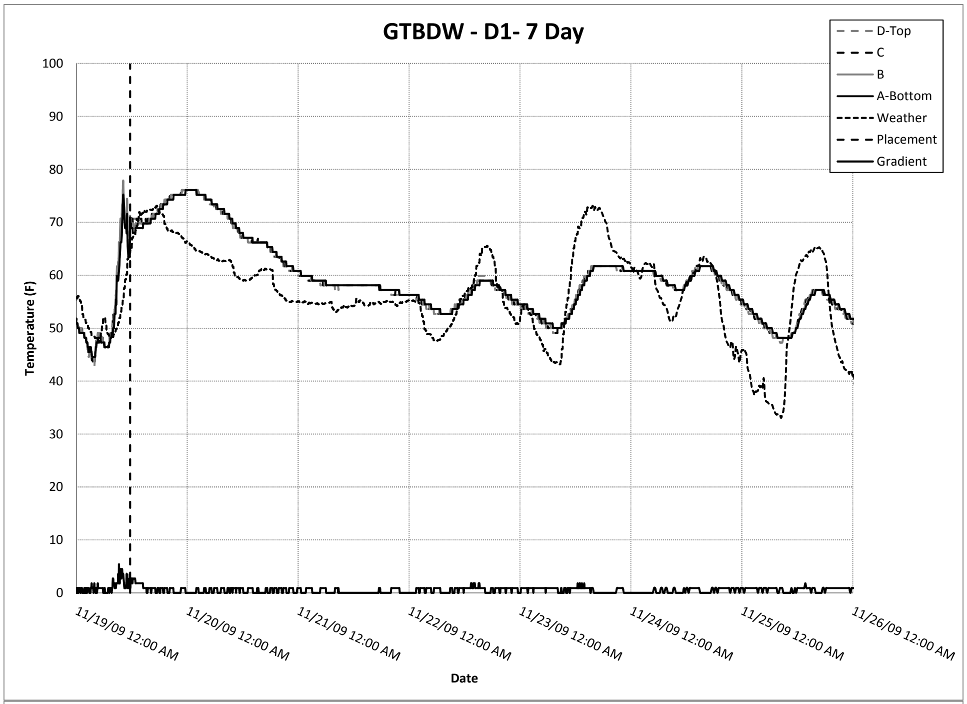
GTBDW - D1- 7 Day
D-Top
C
B
A-Bottom
Weather
Placement
Gradient
Temperature (F)
100
90
80
70
60
50
40
30
20
10
0
11/19/09 12:00 AM
11/20/09 12:00 AM
11/21/09 12:00 AM
11/22/09 12:00 AM
11/23/09 12:00 AM
11/24/09 12:00 AM
11/25/09 12:00 AM
11/26/09 12:00 AM
Date

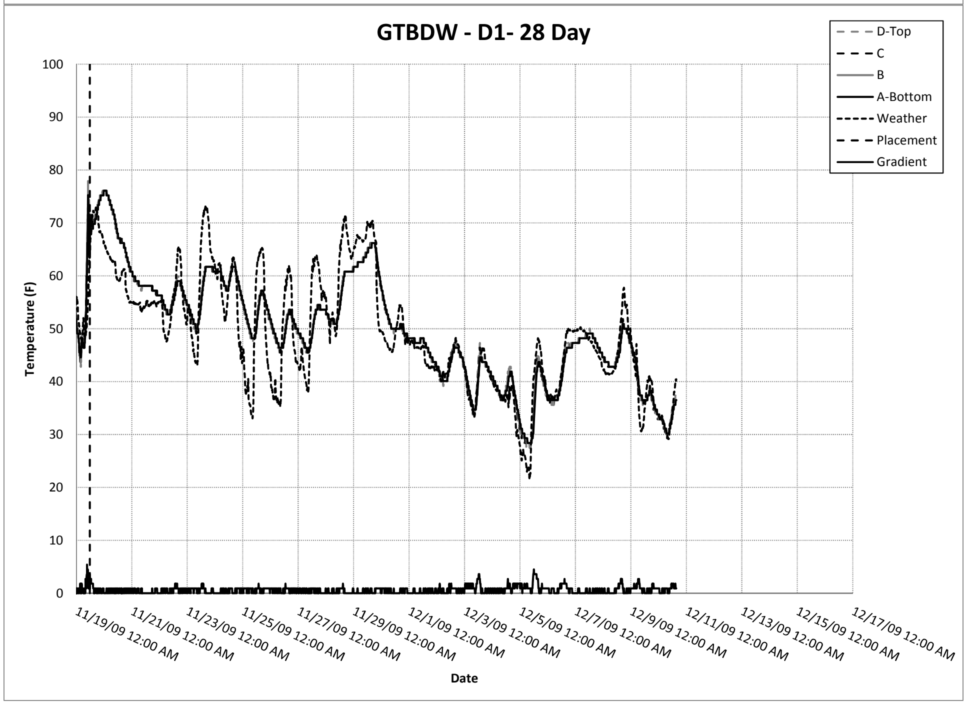
GTBDW - D1- 28 Day
D-Top
C
B
A-Bottom
Weather
Placement
Gradient
Temperature (F)
100
90
80
70
60
50
40
30
20
10
0
11/19/09 12:00 AM
11/21/09 12:00 AM
11/23/09 12:00 AM
11/25/09 12:00 AM
11/27/09 12:00 AM
11/29/09 12:00 AM
12/1/09 12:00 AM
12/3/09 12:00 AM
12/5/09 12:00 AM
12/7/09 12:00 AM
12/9/09 12:00 AM
12/11/09 12:00 AM
12/13/09 12:00 AM
12/15/09 12:00 AM
12/17/09 12:00 AM
Date

B.4 Lubbock Bridge Deck

B.4.1 iButton String Locations and Placement Times

Locations of iButton strings for this instrumentation, provided in Table B.10, were measured from the north end (end of pour) and the east face. iButton placement times, provided in Table B.11, were determined from examination of the iButton temperature data.

Table B.10: iButton string locations—LBD

String	Distance from North end	Distance from East face
A1	246	28.9
B1	138	51.58
B2	137.33	30
B3	137.5	6.58
C1	137.58	55.5
C2	137.5	25.83
C3	136.5	2.58
D1	13.83	29.75

All values in feet.

Table B.11: Concrete placement times—LBD

Strand	Placement Time
A	7/15/10 11:15 PM
B	7/16/10 1:55 AM
C	7/16/10 1:55 AM
D	7/16/10 5:11 AM

B.4.2 iButton Depths

Table B.12 provides the heights of the iButtons measured from either the precast, prestressed concrete panel, or the top of the precast, prestressed concrete girder. While the exact depth of the bridge deck is not known, it is assumed that concrete sections are 4 in. thick over the concrete panels and 11 in. thick over the concrete girders. Descriptions of the iButton strings are also provided. While their original heights are listed in Table B.12, all ‘F’ iButtons from the six-button strings were removed at the request of the contractor.

Table B.12: iButton depths—LBD

Location	String	Button	Height from bottom.
Start of pour, above panel	A1	D	3.125
		C	2.250
		B	1.250
		A	0.250
Mid-pour, above panel, West side	B1	D	3.375
		C	2.500
		B	1.375
		A	0.250
Mid-pour, above panel, mid-width	B2	D	3.250
		C	2.250
		B	1.250
		A	0.250
Mid-pour, above panel, East side	B3	D	3.250
		C	2.250
		B	1.250
		A	0.250
End of pour, above panel	D1	D	3.250
		C	2.125
		B	1.125
		A	0.250

Location	String	Button	Height from bottom.
Mid-pour, above girder, West side	C1	F	9.500
		E	8.500
		D	7.500
		C	6.250
		B	3.250
		A	0.250
Mid-pour, above girder, mid-width	C2	F	9.375
		E	8.375
		D	7.375
		C	6.375
		B	3.500
		A	0.250
Mid-pour, above girder, East side	C3	F	9.250
		E	8.250
		D	7.500
		C	6.375
		B	3.375
		A	0.250

All values in inches.

B.4.3 Recorded Temperatures

The following figures present the complete set of temperature data for the Lubbock bridge deck. Figure B.7 presents a comparison of the temperatures recorded for a selected top iButton for each of the strands. The selected iButtons were located in the middle of the bridge deck width, when possible. Figure B.8 presents a comparison of the gradient recorded across the different strands. As before, each strand is represented by the iButton string located in the middle of the bridge deck width, when possible. In the gradient graph, the iButton gradient, in °F, is presented in on the primary vertical axis, while the ambient air temperature, in °F, is presented on the secondary vertical axis. The graphs following Figure B.8 are labeled with the bridge deck pour name, LBD, the iButton string name, and the duration of time presented on that graph. For each string, the first graph presents the 7-day temperature data, such that the first temperature peaks may be examined. Seven days was chosen rather than four due to the reduced early-age peaks, and the increased duration of total iButton measurements. The following graph presents either the 28-day data set for the iButton string or the full data set, depending on how long the iButton was able to record temperatures. Due to various factors, some iButton strings may record longer durations than others.

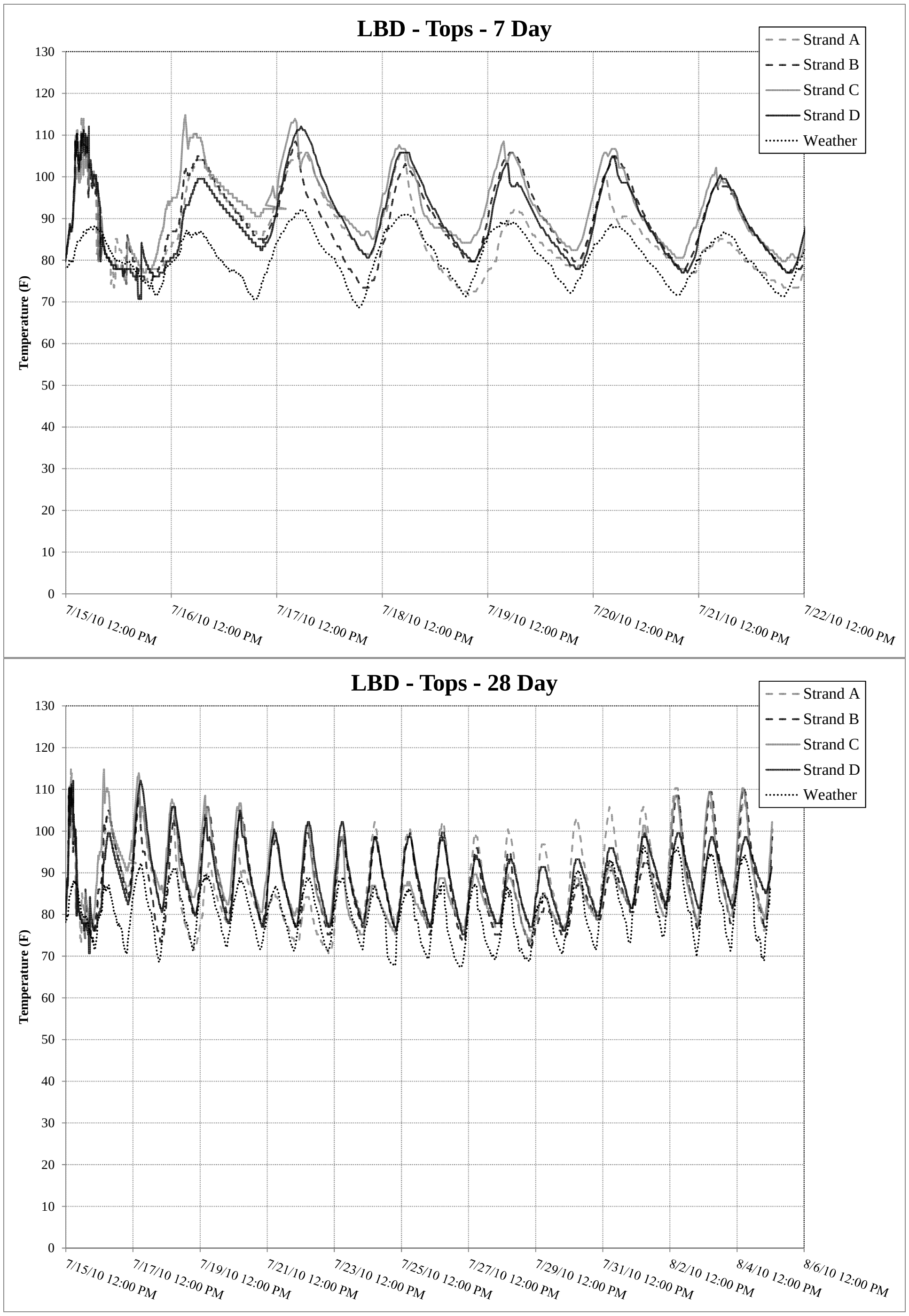

Figure B.7: Comparison of top iButton temperatures—LBD

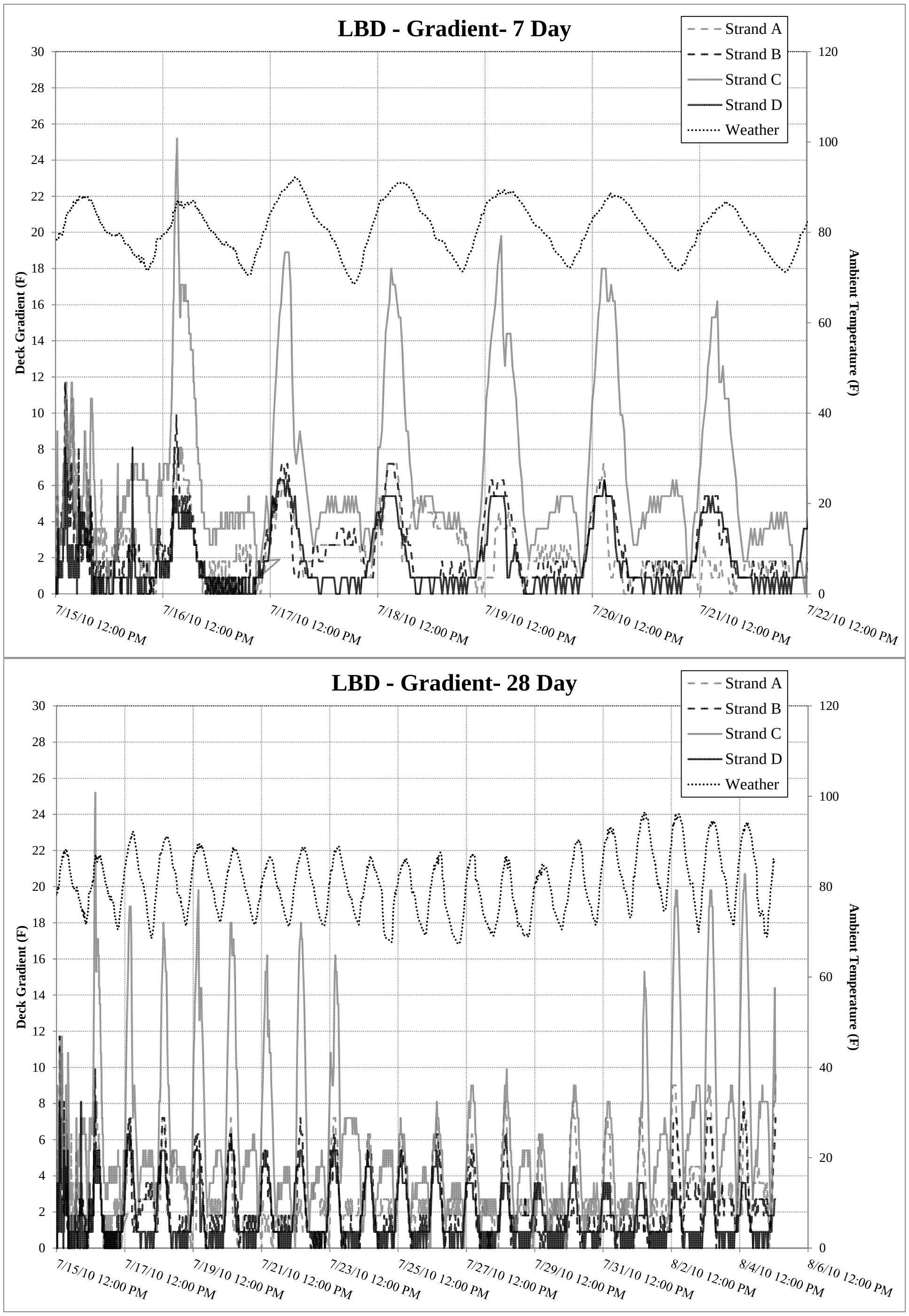

Figure B.8: Comparison of iButton strand gradients—LBD

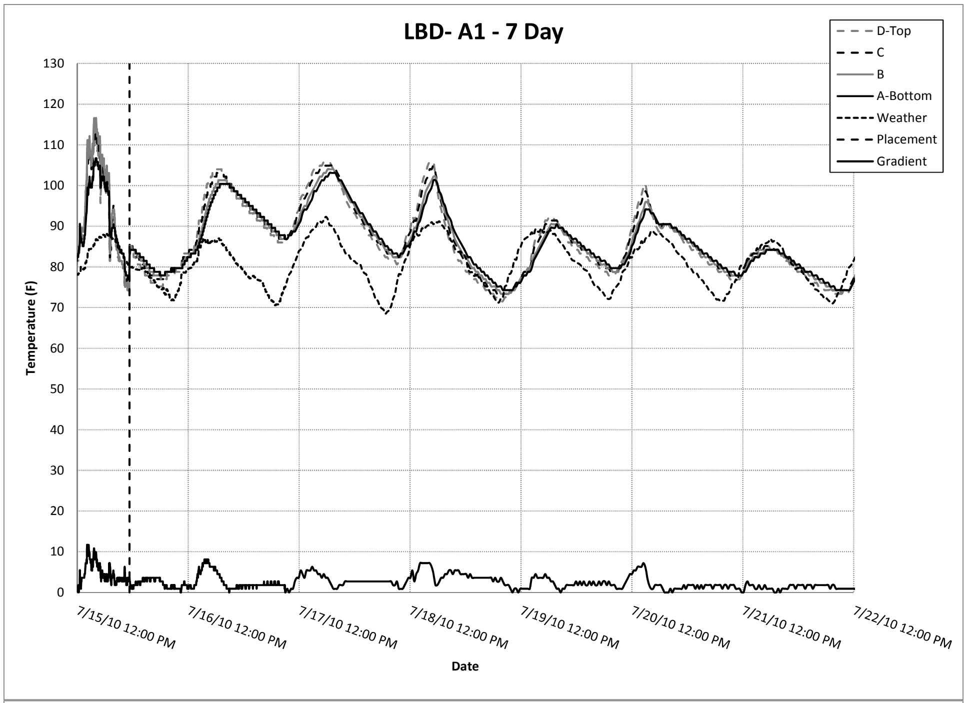
LBD- A1 - 7 Day
D-Top
C
B
A-Bottom
Weather
Placement
Gradient
Temperature (F)
130
120
110
100
90
80
70
60
50
40
30
20
10
0
7/15/10 12:00 PM
7/16/10 12:00 PM
7/17/10 12:00 PM
7/18/10 12:00 PM
7/19/10 12:00 PM
7/20/10 12:00 PM
7/21/10 12:00 PM
7/22/10 12:00 PM
Date

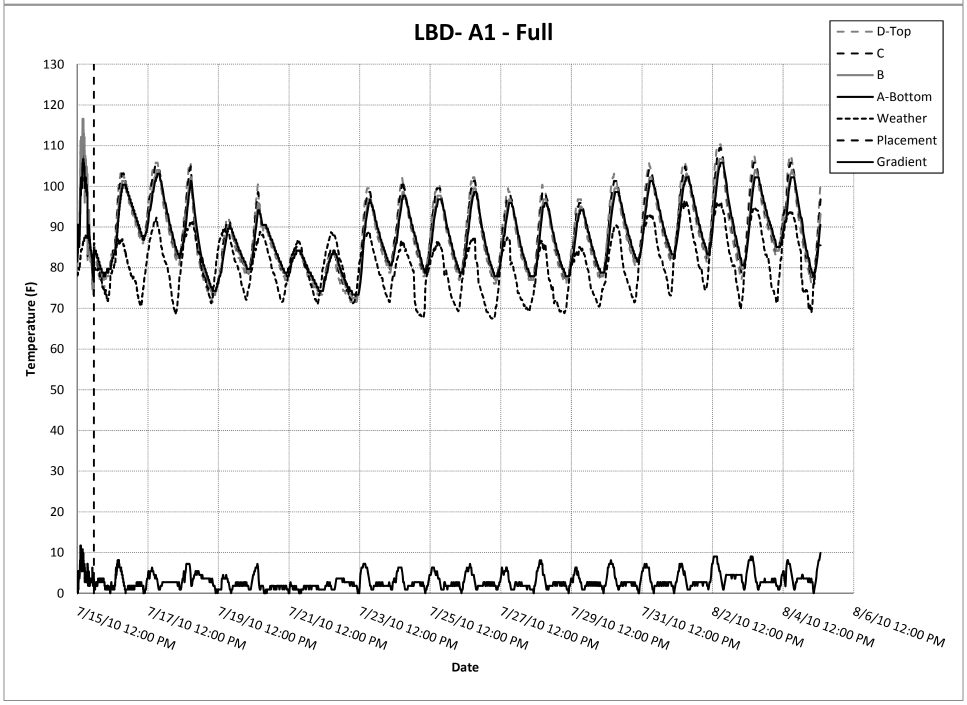
LBD- A1 - Full
D-Top
C
B
A-Bottom
Weather
Placement
Gradient
Temperature (F)
130
120
110
100
90
80
70
60
50
40
30
20
10
0
7/15/10 12:00 PM
7/17/10 12:00 PM
7/19/10 12:00 PM
7/21/10 12:00 PM
7/23/10 12:00 PM
7/25/10 12:00 PM
7/27/10 12:00 PM
7/29/10 12:00 PM
7/31/10 12:00 PM
8/2/10 12:00 PM
8/4/10 12:00 PM
8/6/10 12:00 PM
Date

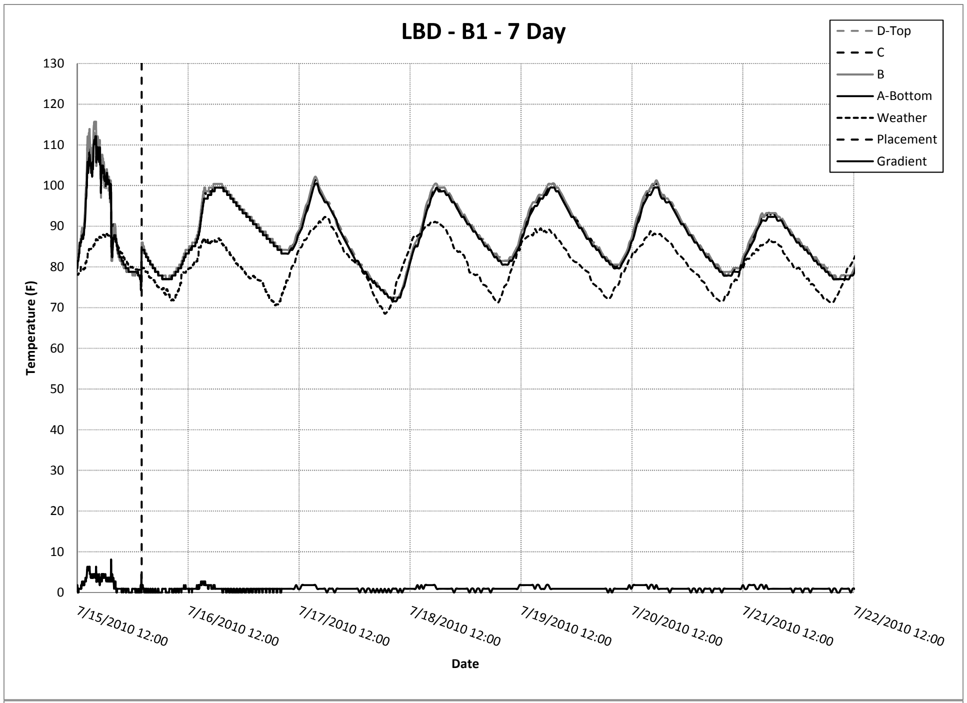
LBD - B1 - 7 Day
D-Top
C
B
A-Bottom
Weather
Placement
Gradient
Temperature (F)
130
120
110
100
90
80
70
60
50
40
30
20
10
0
7/15/2010 12:00
7/16/2010 12:00
7/17/2010 12:00
7/18/2010 12:00
7/19/2010 12:00
7/20/2010 12:00
7/21/2010 12:00
7/22/2010 12:00
Date

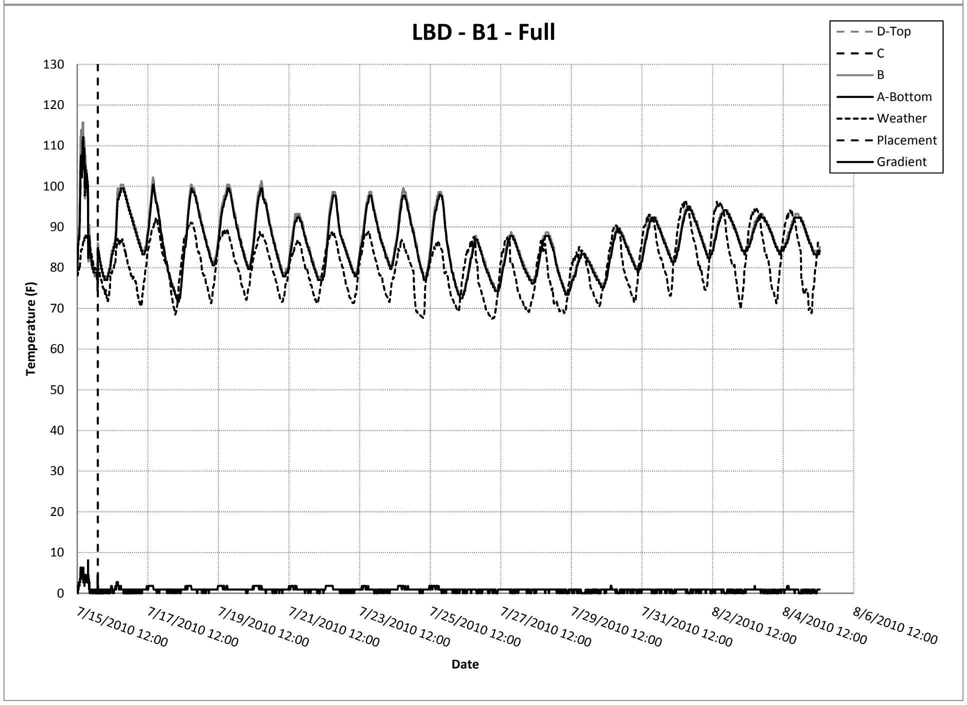
LBD - B1 - Full
D-Top
C
B
A-Bottom
Weather
Placement
Gradient
Temperature (F)
130
120
110
100
90
80
70
60
50
40
30
20
10
0
7/15/2010 12:00
7/17/2010 12:00
7/19/2010 12:00
7/21/2010 12:00
7/23/2010 12:00
7/25/2010 12:00
7/27/2010 12:00
7/29/2010 12:00
7/31/2010 12:00
8/2/2010 12:00
8/4/2010 12:00
8/6/2010 12:00
Date

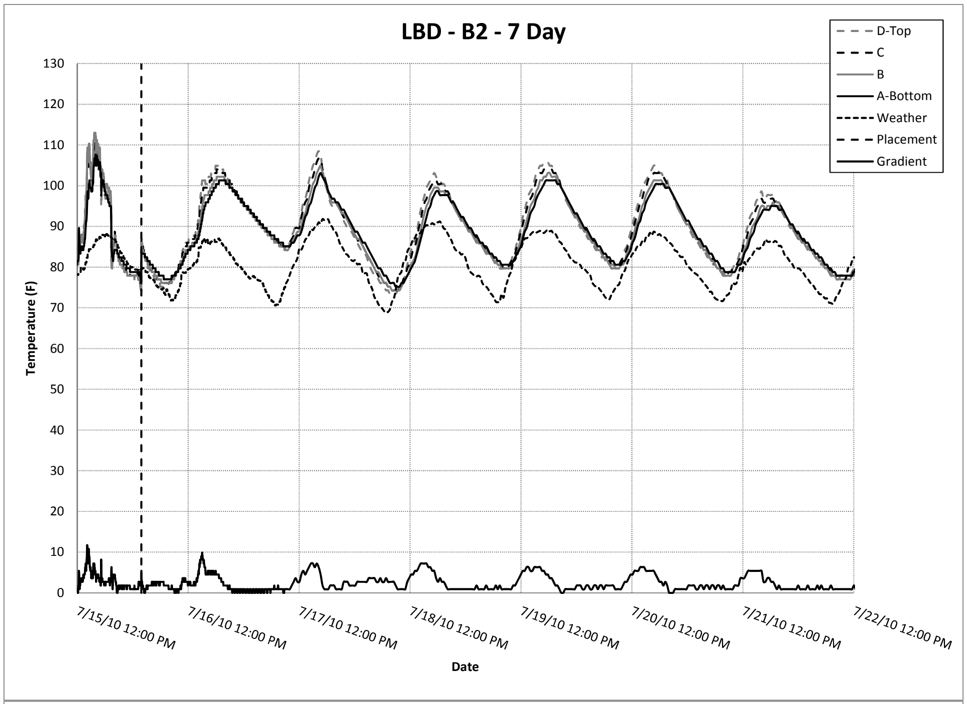

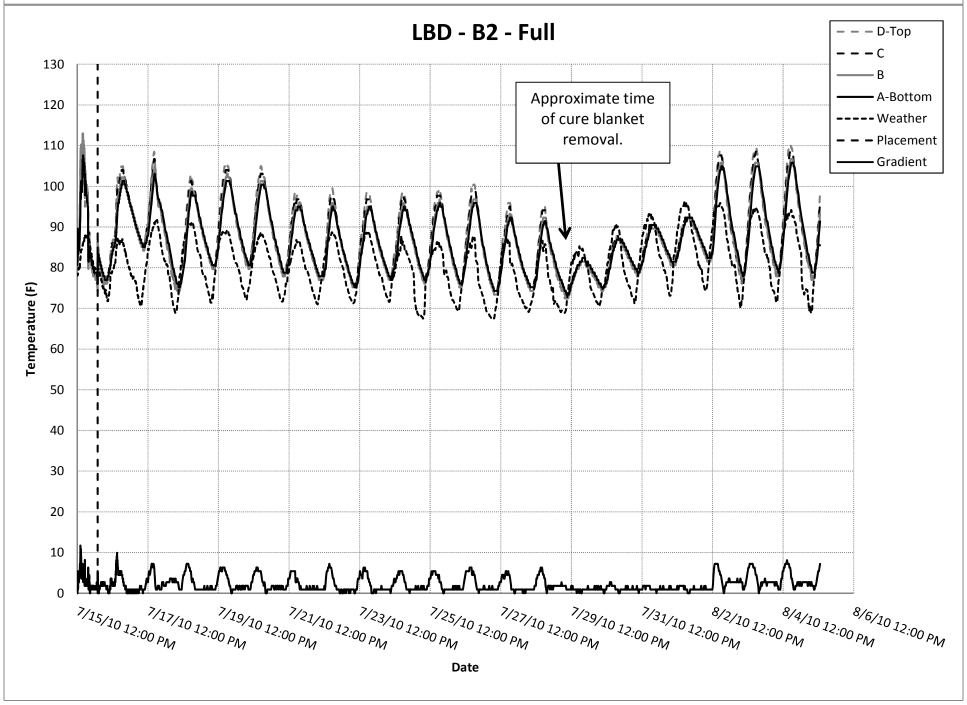

Approximate time of cure blanket removal.

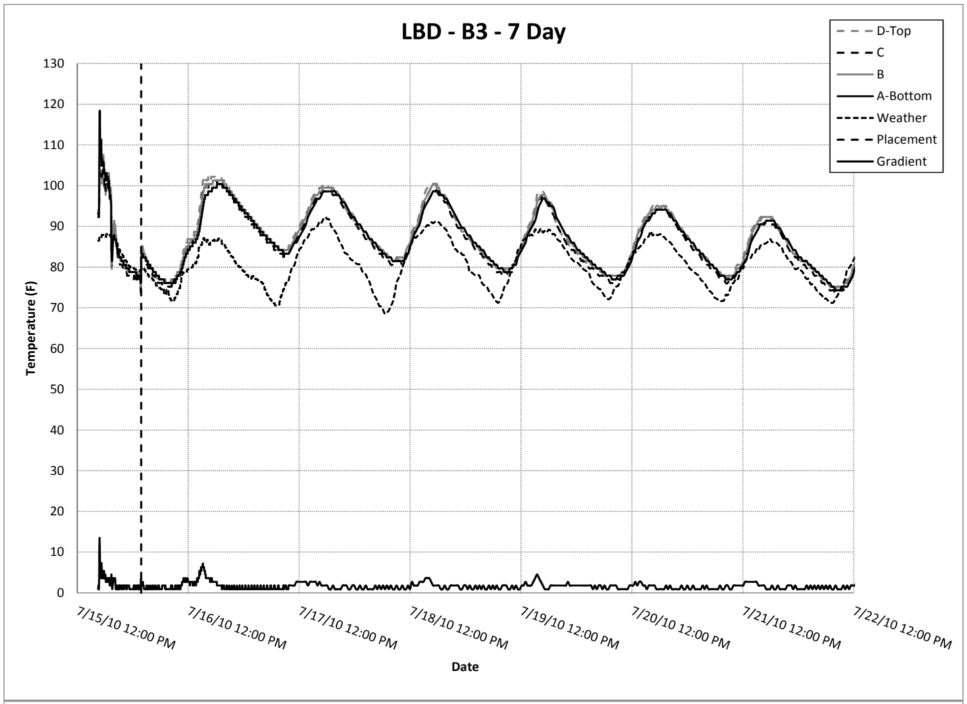
LBD - B3 - 7 Day
D-Top
C
B
A-Bottom
Weather
Placement
Gradient
Temperature (F)
130
120
110
100
90
80
70
60
50
40
30
20
10
0
7/15/10 12:00 PM
7/16/10 12:00 PM
7/17/10 12:00 PM
7/18/10 12:00 PM
7/19/10 12:00 PM
7/20/10 12:00 PM
7/21/10 12:00 PM
7/22/10 12:00 PM
Date

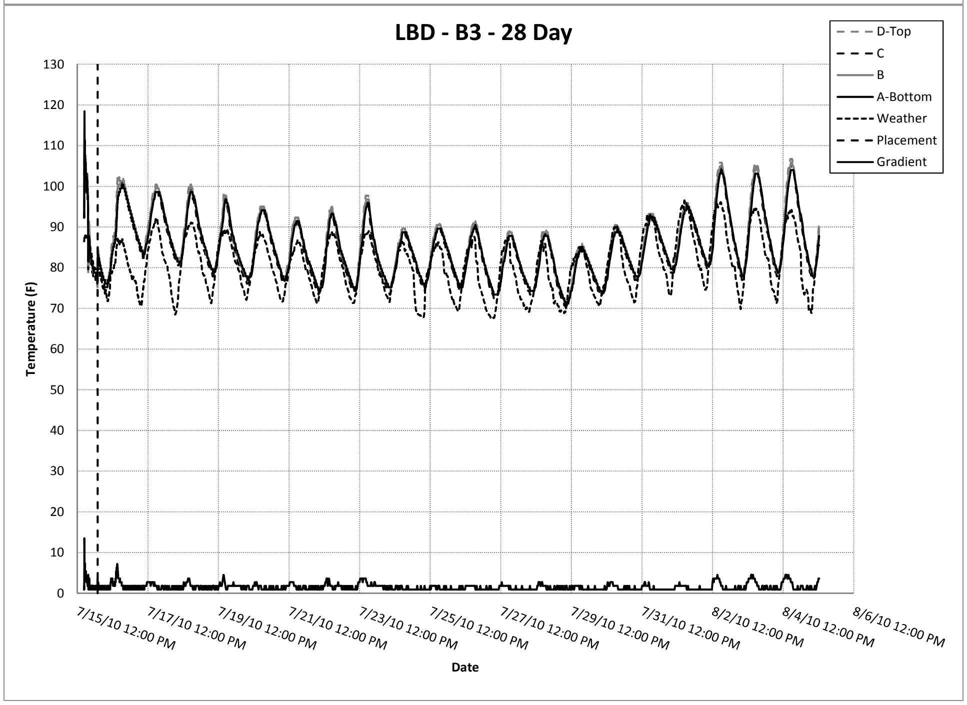
LBD - B3 - 28 Day
D-Top
C
B
A-Bottom
Weather
Placement
Gradient
Temperature (F)
130
120
110
100
90
80
70
60
50
40
30
20
10
0
7/15/10 12:00 PM
7/17/10 12:00 PM
7/19/10 12:00 PM
7/21/10 12:00 PM
7/23/10 12:00 PM
7/25/10 12:00 PM
7/27/10 12:00 PM
7/29/10 12:00 PM
7/31/10 12:00 PM
8/2/10 12:00 PM
8/4/10 12:00 PM
8/6/10 12:00 PM
Date

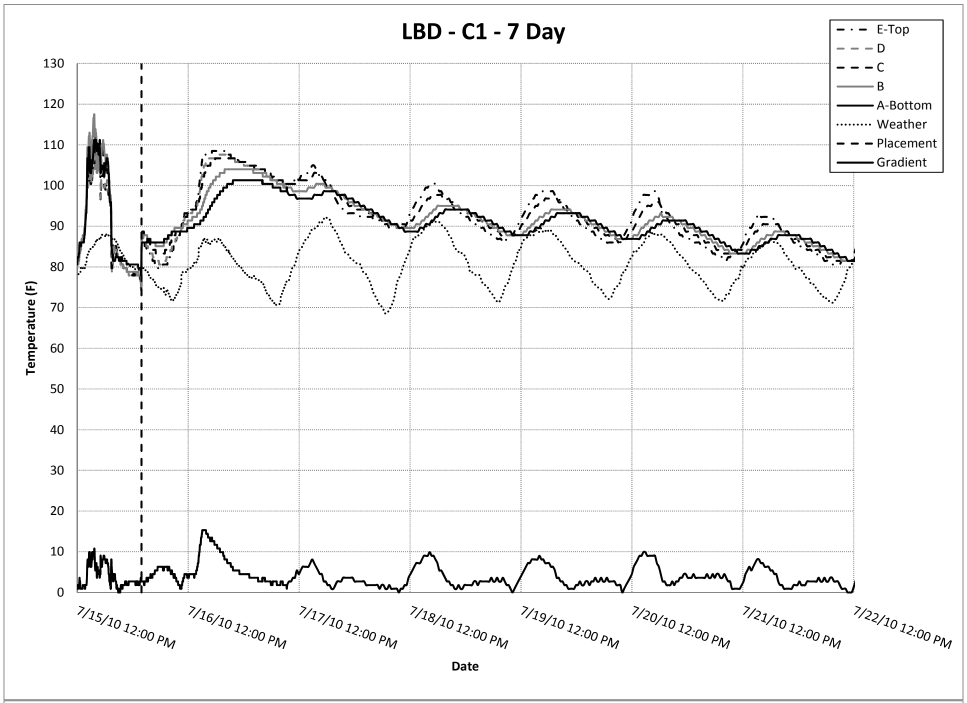
LBD - C1 - 7 Day
E-Top
D
C
B
A-Bottom
Weather
Placement
Gradient
Temperature (F)
130
120
110
100
90
80
70
60
50
40
30
20
10
0
7/15/10 12:00 PM
7/16/10 12:00 PM
7/17/10 12:00 PM
7/18/10 12:00 PM
7/19/10 12:00 PM
7/20/10 12:00 PM
7/21/10 12:00 PM
7/22/10 12:00 PM
Date

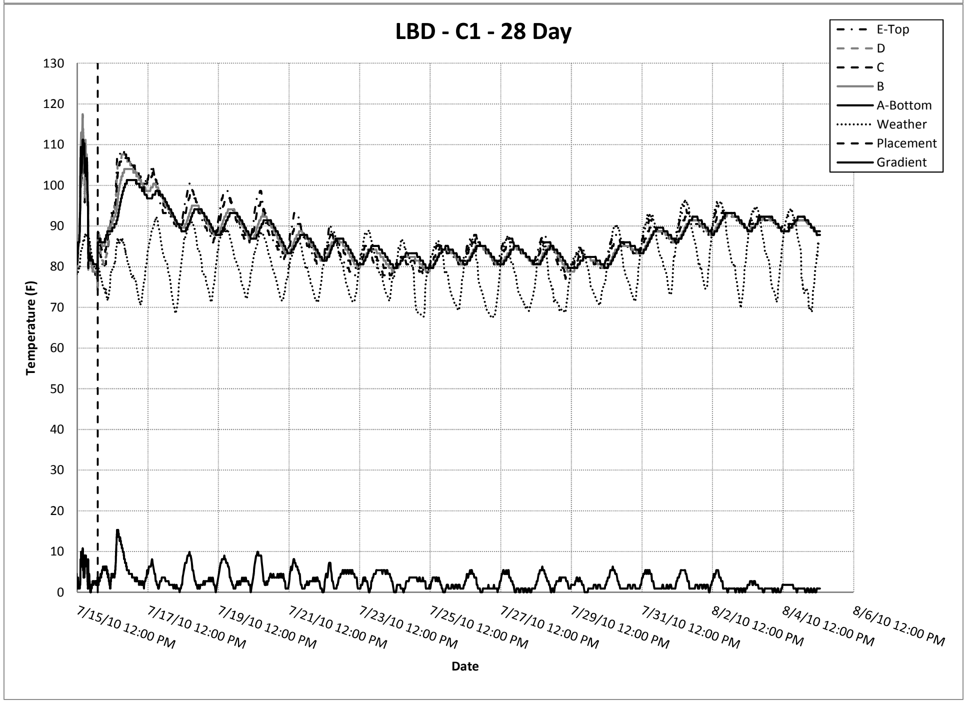
LBD - C1 - 28 Day
E-Top
D
C
B
A-Bottom
Weather
Placement
Gradient
Temperature (F)
130
120
110
100
90
80
70
60
50
40
30
20
10
0
7/15/10 12:00 PM
7/17/10 12:00 PM
7/19/10 12:00 PM
7/21/10 12:00 PM
7/23/10 12:00 PM
7/25/10 12:00 PM
7/27/10 12:00 PM
7/29/10 12:00 PM
7/31/10 12:00 PM
8/2/10 12:00 PM
8/4/10 12:00 PM
8/6/10 12:00 PM
Date

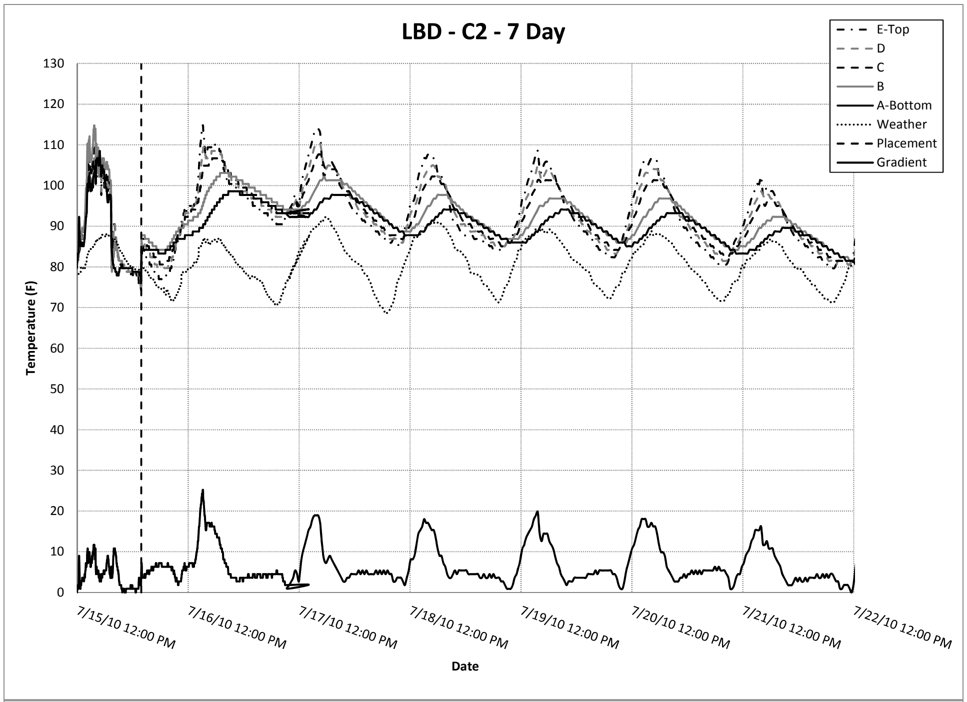
LBD - C2 - 7 Day
E-Top
D
C
B
A-Bottom
Weather
Placement
Gradient
Temperature (F)
130
120
110
100
90
80
70
60
50
40
30
20
10
0
7/15/10 12:00 PM
7/16/10 12:00 PM
7/17/10 12:00 PM
7/18/10 12:00 PM
7/19/10 12:00 PM
7/20/10 12:00 PM
7/21/10 12:00 PM
7/22/10 12:00 PM
Date

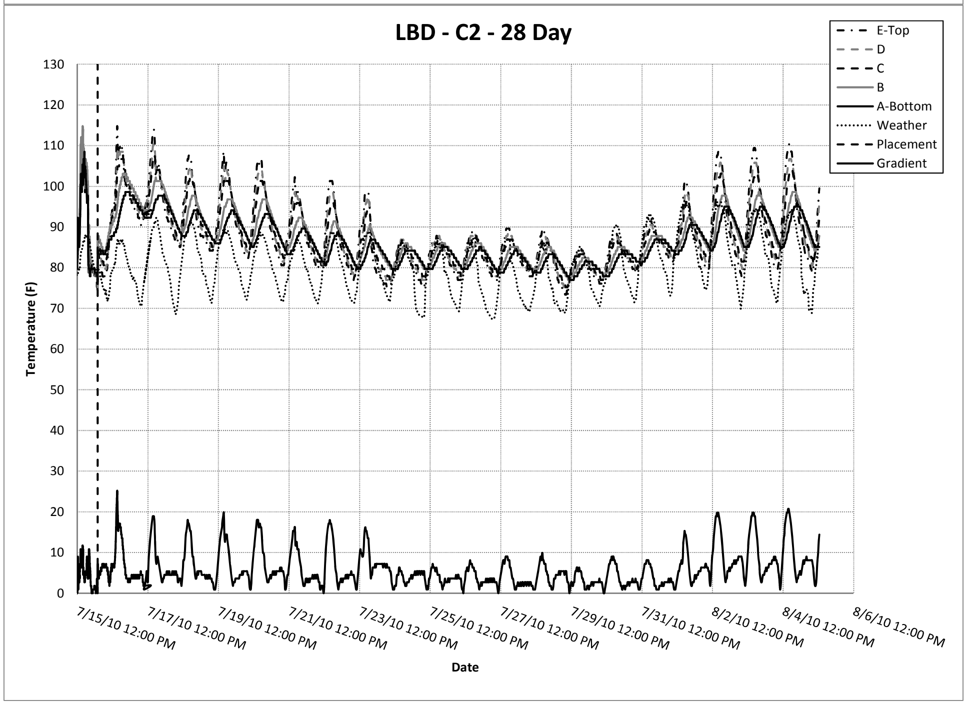
LBD - C2 - 28 Day
E-Top
D
C
B
A-Bottom
Weather
Placement
Gradient
Temperature (F)
130
120
110
100
90
80
70
60
50
40
30
20
10
0
7/15/10 12:00 PM
7/17/10 12:00 PM
7/19/10 12:00 PM
7/21/10 12:00 PM
7/23/10 12:00 PM
7/25/10 12:00 PM
7/27/10 12:00 PM
7/29/10 12:00 PM
7/31/10 12:00 PM
8/2/10 12:00 PM
8/4/10 12:00 PM
8/6/10 12:00 PM
Date

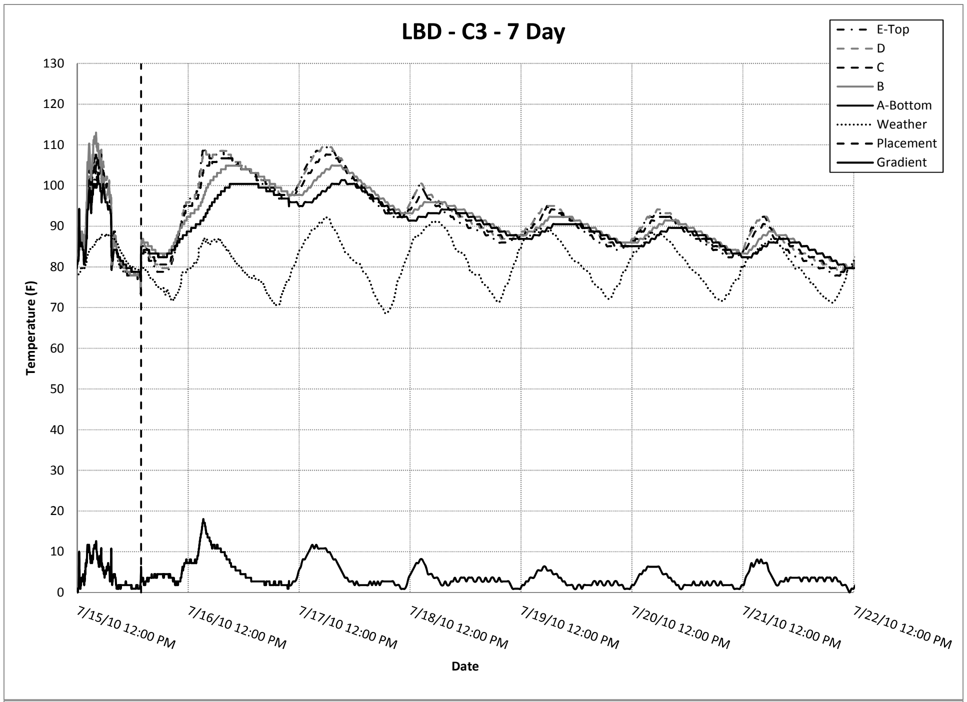
LBD - C3 - 7 Day
E-Top
D
C
B
A-Bottom
Weather
Placement
Gradient
Temperature (F)
130
120
110
100
90
80
70
60
50
40
30
20
10
0
7/15/10 12:00 PM
7/16/10 12:00 PM
7/17/10 12:00 PM
7/18/10 12:00 PM
7/19/10 12:00 PM
7/20/10 12:00 PM
7/21/10 12:00 PM
7/22/10 12:00 PM
Date

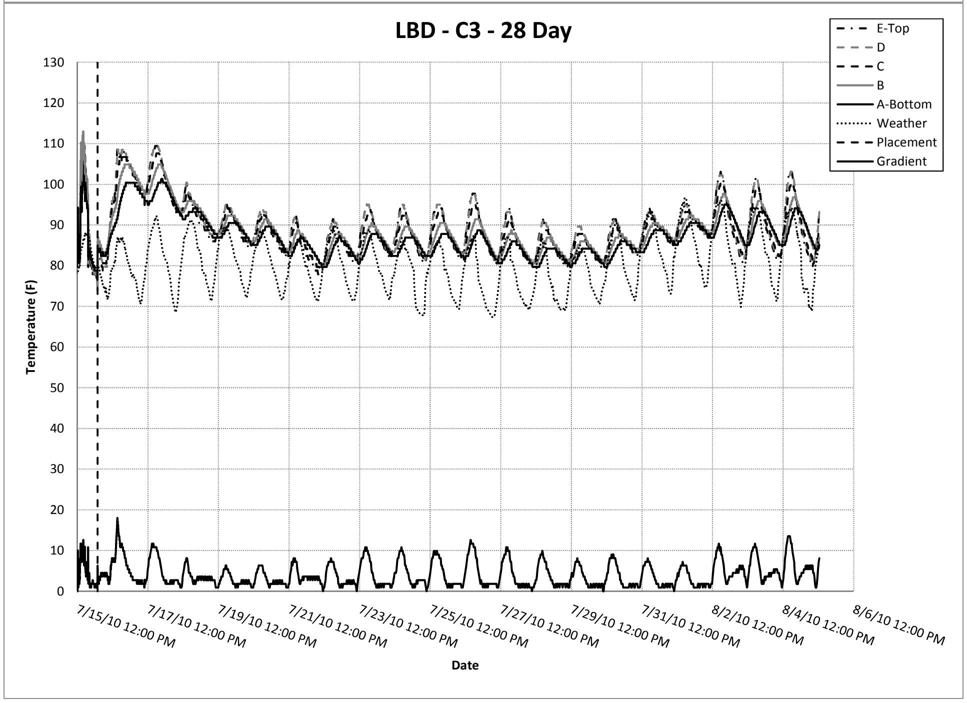
LBD - C3 - 28 Day
E-Top
D
C
B
A-Bottom
Weather
Placement
Gradient
Temperature (F)
130
120
110
100
90
80
70
60
50
40
30
20
10
0
7/15/10 12:00 PM
7/17/10 12:00 PM
7/19/10 12:00 PM
7/21/10 12:00 PM
7/23/10 12:00 PM
7/25/10 12:00 PM
7/27/10 12:00 PM
7/29/10 12:00 PM
7/31/10 12:00 PM
8/2/10 12:00 PM
8/4/10 12:00 PM
8/6/10 12:00 PM
Date

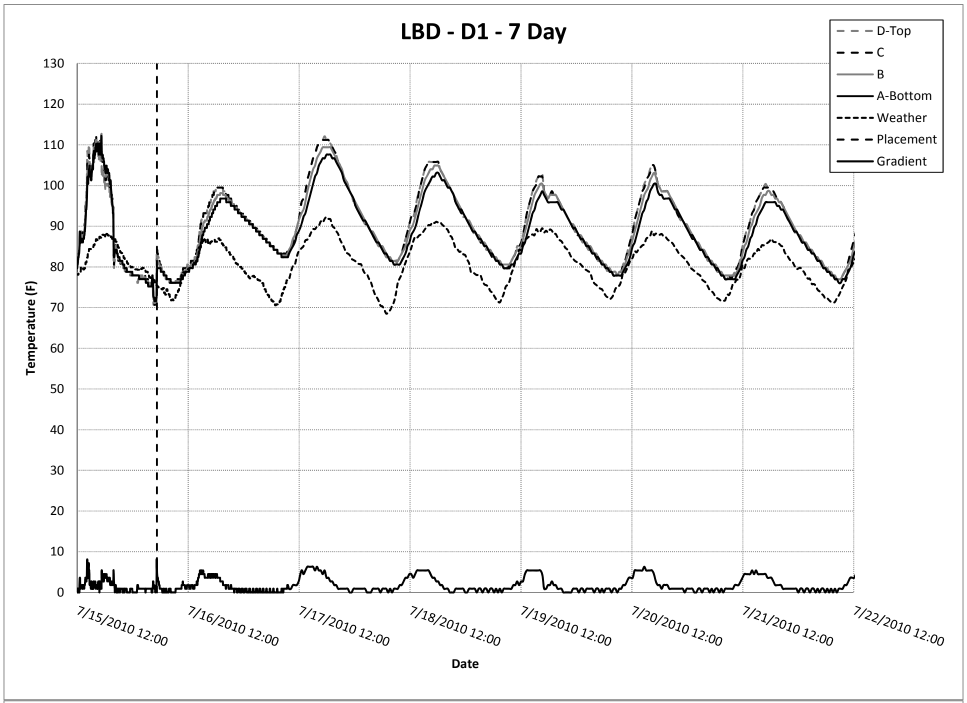
LBD - D1 - 7 Day
D-Top
C
B
A-Bottom
Weather
Placement
Gradient
Temperature (F)
130
120
110
100
90
80
70
60
50
40
30
20
10
0
7/15/2010 12:00
7/16/2010 12:00
7/17/2010 12:00
7/18/2010 12:00
7/19/2010 12:00
7/20/2010 12:00
7/21/2010 12:00
7/22/2010 12:00
Date

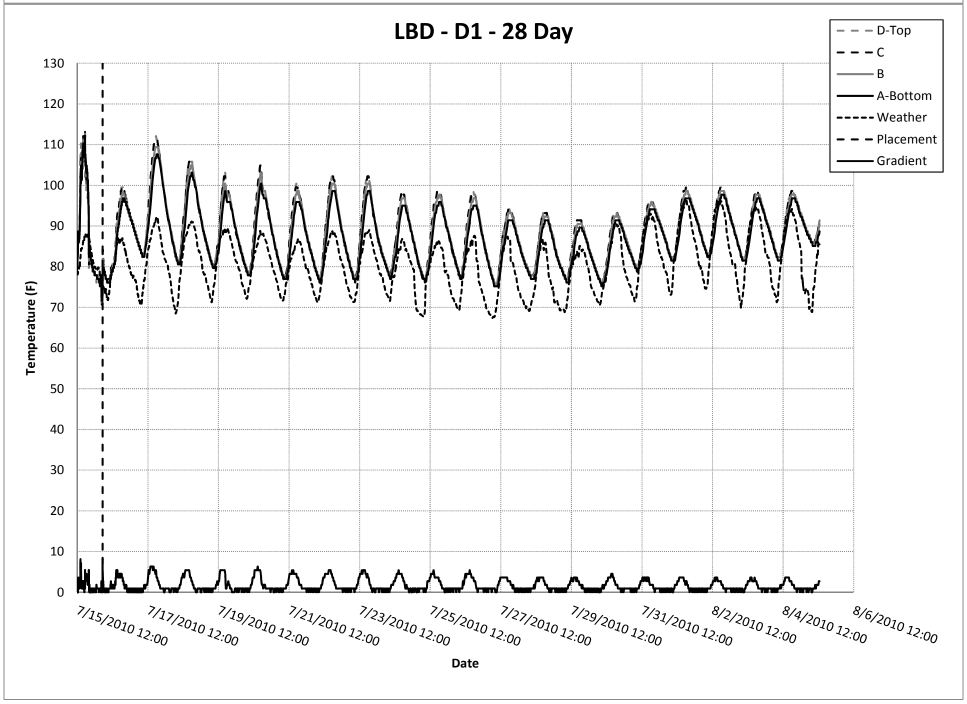
LBD - D1 - 28 Day
D-Top
C
B
A-Bottom
Weather
Placement
Gradient
Temperature (F)
130
120
110
100
90
80
70
60
50
40
30
20
10
0
7/15/2010 12:00
7/17/2010 12:00
7/19/2010 12:00
7/21/2010 12:00
7/23/2010 12:00
7/25/2010 12:00
7/27/2010 12:00
7/29/2010 12:00
7/31/2010 12:00
8/2/2010 12:00
8/4/2010 12:00
8/6/2010 12:00
Date

Appendix C: New Rigid Cracking Frame Formwork

Before testing began on TxDOT Project 6332, the formwork that had been previously used for rigid cracking frame testing was replaced with formwork built by the author. After many mixtures and years of testing, the previous wooden formwork exhibited considerable distress, including rotting wood, separation of copper flashing, and fatiguing of the walls. Fatigue of the sides of the formwork led to the sides shifting during concrete placement in the formwork, which later caused stress concentrations at the formwork-crosshead interface. The new formwork was built with a steel frame, and consists of three separate pieces. The new design was constructed to provide a greater ease of use, and to create formwork that would withstand the rigors of the set-up and removal procedure for many years. The copper flashing used was also approximately twice as thick as that previously used. Pictures of the previously used formwork and pictures taken during the construction of the new formwork are presented in Figures C.1–C.12. Further information regarding the dimensions of the steel formwork can be acquired through contacting the laboratory manager at CMRG, or though contacting the author.

Figure C.1: Stress concentrations from formwork fatigue.

Figure C.2: Separation of copper flashing.

Figure C.3: Deterioration of existing formwork.

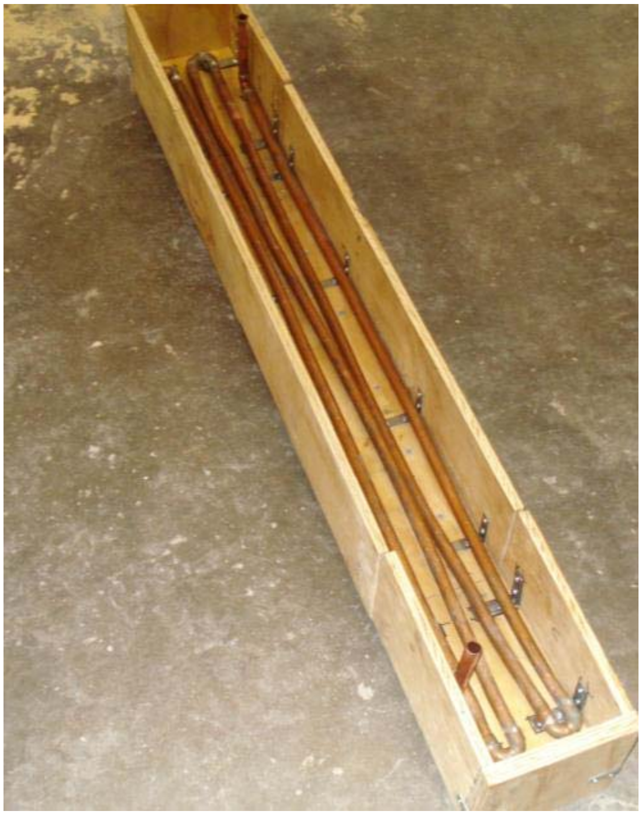

Figure C.4: Formwork for side insulation pouring.

Figure C.5: Fitting of steel formwork.

Figure C.6: Measurements for cutting new flashing with fold-over flaps.

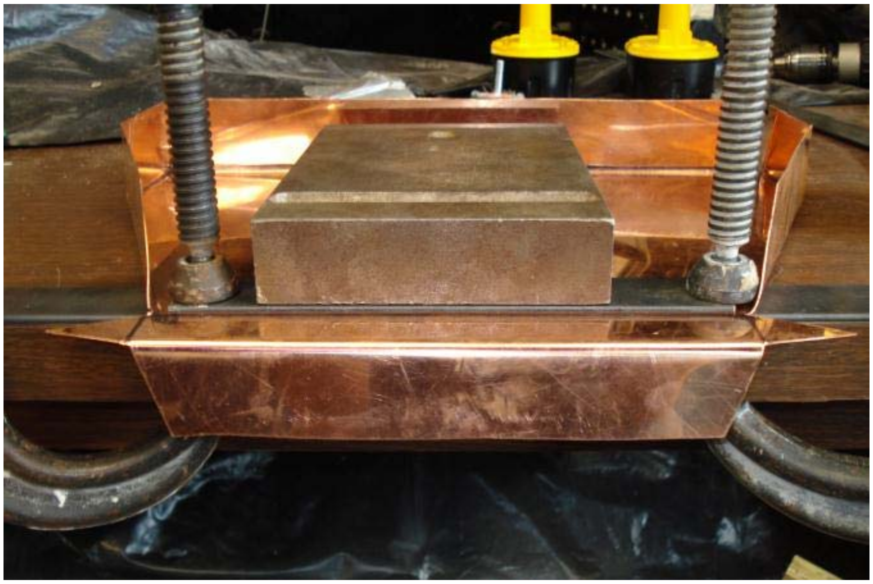

Figure C.7: Bending of copper flashing.

Figure C.8: Painting of steel formwork.

Figure C.9: Side walls prior to application of flashing.

Figure C.10: Bottom formwork before application of flashing.

Figure C.11: Seating of flashing prior to drilling for screw holes.

Figure C.12: Installation process to reduce free edges of flashing.

References

Abel, J., & Hover, K. (1998). Effect of Water/Cement Ratio on the Early Age Tensile Strength of Concrete. *Transportation Reserch Record, 1610*.

Abel, J., & Hover, K. (1998). Effect of Water/Cement Ratio on the Early-Age Tensile Strength of Concrete. *Transportation Research Board, 1610*, 33–38.

ACI Committee 209. (2008). *Prediction of Creep, Shrinkage and Temperature Effects in Concrete Structures (ACI209R-92).* Farmington Hills, Mich.: American Concrete Institute.

ACI Committee 209. (2008). Guide for Modeling and Calculating Shrinkage and Creep in Hardened Concrete *(ACI209.2R-08).* Farmington Hills, Mich.: American Concrete Institute.

ACI Committee 224. (2001). *Control of Cracking in Concrete.* Farmington Hills, Mich.: American Concrete Institute.

ACI Committee 318. (2008). *Buidling Code Requirements for Structural Concrete.* Farmington Hills, Mich.: American Concrete Institute.

Akita, H., Fujuwara, T., & Ozaka, Y. (1997). Practical Procedure for the Analysis of Moisture Transfer Within concrete Due to Drying. *Magazine of Concrete Research, 49*(179), 1–7.

Al-Fadhala, M., & Hover, K. (2001). Rapid Evaporation from Freshly Cast Concrete and the Gulf Environment. *Construction and Building Materials, 15*, 1–7.

Al-Manseer, & Lam, J. (2005). Statistical Evaluation of Shrinkage and Creep Models. *ACI Materials Journal, 102*(3).

ASTM C 39 (2005). Standard Test Method for Compressive Strength of Cylindrical Concrete Specimen, American Society of Testing Materials, West Conshohocken, PA.

ASTM C 192 (2007). Standard Practice for making and Curing Concrete Test Specimen in the Lab, American Society of Testing Materials, West Conshohocken, PA.

ASTM C 403 (2008). Standard Test Method for Time of Setting of Concrete Mixtures by Penetration Resistance, American Society of Testing Materials, West Conshohocken, PA.

ASTM C 469 (2002). Standard Test Method for Modulus of Elasticity and Poisons ratio of Concrete in Compression, American Society of Testing Materials, West Conshohocken, PA.

ASTM C 496 (2004). Standard Test Method for Splitting Tensile Strength of Cylindrical Concrete Specimen, American Society of Testing Materials. West Conshohocken, PA.

ASTM C 618. (2008). *Standard Specification for Coal Fly Ash and Raw or Caclined Natural Pozzolan for Use in Concrete.* Pennsylvania: American Society of Testing and Materials.

ASTM C 989. (2010). *Standard Specification for Slag Cement for Use in Concrete and Mortars.* Pennsylvania: American Society of Testing and Materials.

ASTM C138. (2010). *Standard Test Method for Density (Unit Weight), Yield, and Air Content (Gravimetric). of Concrete.* Pennsylvania: American Society of Testing and Materials.

ASTM C143. (2010). *Standard Test Method for Slump of Hydraulic-Cement Concrete.* Pennsylvania: American Society of Testing and Materials.

ASTM C150. (2011). *Standard Specification for Portland Cement.* Pennsylvania: American Society of Testing and Materials.

ASTM C157. (2008). *Standard Test Method for Length Change of Hardened Hydraulic-Cement Mortar and Concrete.* Pennsylvania: American Society of Testing and Materials.

ASTM C231. (2010). *Standard Test Method for Air Content of Freshly Mixed Concrete by the Pressure Method.* Pennsylvania: American Society of Testing and Materials.

ASTM C33. (2011). *Standard Specification for Concrete Aggregates.* Pennsylvania: American Society of Testing and Materials.

ASTM C39. (2010). *Standard Test Method for Compressive Strength of Cylindrical Concrete Specimens.* Pennsylvania: American Society of Testing and Materials.

ASTM C403. (2008). *Standard Test Method for Time of Setting of Concrete Mixtures by Penetration Resistance.* Pennsylvania: American Society of Testing and Materials.

ASTM C469. (2010). *Standard Test Method for Static Modulus of Elasticity and Poisson's Ratio of Concrete in Compression.* Pennsylvania: American Society of Testing and Materials.

ASTM C494. (2010). *Standard Specification for Chemical Admixtures for Concrete.* Pennsylvania: American Society of Testing and Materials.

ASTM C496. (2004). *Standard Test Method for Splitting Tensile Strength of Cylindrical Concrete Specimens.* Pennsylvania: American Society of Testing and Materials.

Babaei, K., & Fouladgar, A. (1997). Solustions to Concrete Bridge Deck Cracking. *Concrete International, 19*(7), 34–37.

Bažant, Z.P, and Prasannan, S. (1989a). Solidification Theory for Concrete Creep I: Formulation. ASCE Journal of Engineering Mechanics, Vol. 115, No. 8. pp. 1691-1703.

Bažant, Z.P, and Prasannan, S. (1989b). Solidification Theory for Concrete Creep I: Formulation. ASCE Journal of Engineering Mechanics, Vol. 115, No. 8. pp. 1704-1725.

Bazant, Z. (1995). Creep and Shrinkage Prediction Model for Analysis and Design of Concrete Structures- Model B3. *Materials and Structures, 28*, 357–365.

Bažant, Z.P., and Baweja, S. (2000). Creep and Shrinkage Prediction Model for Analysis and Design of Concrete Structures (B3), The Adam Neville Symposium: Creep and Shrinkage-Structural Design Effects, ACI SP-194. A. Al-Manaseer (Ed), ACI, Farmington Hills, MI, pp. 1-83.

Bentz, D., Garboczi, E., & Quenard, D. (1997). Modeling Drying Shrinkage in Reconstructed Porous Materials: Application to Vycor Glass. *Modeling and Simulation in Material Science and Engineering, 6*, 211–236.

Byard, B. (2011). (Personal Communication).

Byard, B. (2011). Early-Age Behavior of Lightweight Aggregate Concrete, Doctoral Dissertation, Auburn University, Auburn, AL.

Carino, N.J. (2004). The Maturity Method. In Handbook on Nondestructive Testing of Concrete, 2nd ed., V.M. Malhotra and N.J. Carino, (Eds). 5.1-5.47, West Conshocken, Pennsylvania: ASTM International.

CEB-FIP (1993). *CEB-FIP Model Code '90.* Tomas Telford, London: Comite Euro-International du Beton.

Darwin, D., and Browning, J. (2008). *Construction of Low Cracking High Performance Concrete Bridge Decks: Field Experience*. Proceedings of the Concrete Bridge Conference, St. Louis, MO. May 4-7, 2008.

Edson, A. (2007). *Effects of Supplementary Cementing Materials on the Setting Time and Early Strength of Concrete.* University of Texas at Austin.

Emborg, M. (1998). Models and Methods for Computation of Thermal Stresses. In R. Springenschmid (Ed.), *Prevention of thermal cracking in concrete at early ages: state of the art report prepared by RILEM Technical Committee 119, Avoidance of Thermal Cracking in Concrete at Early Ages*, (pp. 178–230).

Emborg, M. (1989). Thermal Stresses in Concrete Structures at Early Ages, Doctoral Thesis. Luleå University of Technology, Luleå, Sweden.

Emmanuel, J., & Hulsey, J. (1977, April). Prediction of the Thermal Coefficient of Expansion of Concrete. *Journal of the American Concrete Institute*, *74*(4), 149–155.

Folliard, K., & Berke, N. (1997). Properties of High-Performance Concrete Containing Shrinkage-Reducing Admixture. *Cement and Concrete Research, 27*(9), 1357–1364.

Folliard, K., Smith, C., Sellers, G., Brown, M., & Breen, J. (2003). *Evaluation of Alternative Materials to Contorl Drying-Shrinkage Cracking in Concrete Bridge Decks.* Texas Department of Transportation.

Folliard, K., Smith, C., Sellers, G., Brown, M., & Breen, J. (2003). *Evaluation of Alternative Materials to Control Drying-Shrinkage Cracking in Concrete Bridge Decks.* Texas Department of Transportation. Center for Transportation Reserach.

Freiesleben Hansen, P., and J. Pederson. (1977) *Maturity Computer for Controlled Curing and Hardening of Concrete*. Nordisk Betong, Vol.1, No. 19, (1977). pp.19-34.

Gardner, N., & Lockman, M. (2001, March-April). Design Provisions for Drying Shrinkage and Creep of Normal-Strength Concrete. *ACI Materials Journal*, 159–167.

Grace Construction Products. (2007). *Eclipse Plus.* Retrieved from Concrete Products: http://www.buildsite.com/dbderived/wrgrace/derived_files/derived320838.pdf

Grace Construction Products. (2009). *WRDA 64.* Retrieved from Concrete Admixtures: http://www.na.graceconstruction.com/concrete/download/CMD-366G.pdf

Grasley, Z., & Lange, D. (2004). Modeling Drying Shrinkage Stress Gradients in Concrete. *Cement, Concrete, and Aggregates, 26*(2), 115–122.

Gutch, A. and F. S. Rostásy (1995). Young Concrete Under High Tensile Stresses – Creep, Relaxation, and Cracking, In RILEM Proceedings 25, Thermal Cracking in Concrete at Early Ages, R. Springenschmid (ed), London, E & FN Spon, pp. 111-118.

Hedlund, H. (2000). *Hardening Concrete. Measurements and Evaluation of Non-Elastic Deformation and Associated Restraint Stresses.* PhD Thesis, Lulea University of Technology, Division of Structural Engineering.

Holt, E. (2001). *Early Age Autogenous Shrinkage of Concrete.* Technical Research Centre of Finland , VTT Building and Transport. VTT Publications 446.

Jensen, O., & Hansen, P. (2004). Autogenous deformation and RH-change in perspecitve. *Cement and Concrete Research, 31,* 1859–1865.

Krauss, P., & Rogalla, E. (1996). *Transverse Cracking in Newly Constructed Bridge Decks.* National Cooperative Higway Research Program (NCHRP), Report 380. Transportation Research Board.

Larson, M., & Jonasson, J. (2003). Linear Logarithmic Model for Concrete Creep. II: Prediction Formulas for Description of Creep Behaviour. *Journal of Advanced Concrete Technology, 1*(2), 188–200.

Maxim. (2011). *DS1921G Thermochron iButton*. Retrieved from http://www.maxim-ic.com/datasheet/index.mvp/id/4023

McCuen, R.H. (1985). Statistical Methods for Engineers, Prentice-Hall, Upper Saddle River, NJ.

McHenry, D. (1943). A New Aspect of Creep in Concrete and its Application to Design, Proceedings of the American Society of Testing Materials, Vol. 43. pp. 1069-1084.

Meadows, J. (2007). *Early-Age Cracking of Mass Concrete Structures.* Masters Thesis, Auburn University.

Mehta, P.K., and Monteiro, P.J.M. (2005). *Concrete: Microstructure, Properties, and Materials,* third ed., McGraw-Hill, Inc. New York, NY.

Mehta, P., & Monteiro, P. (2006). *Concrete: Microstructure, Properties, and Materials* (3rd ed.). McGraw-Hill.

Mindess, S., Young, J., & Darwin, D. (2002). *Concrete.* Englewood Cliffs, N.J.: Prentice Hall.

Mokarem, D. (2002). *Development of Concrete Shrinkage Performance Specifications.* PhD Thesis, Virginia Polytechnic Institute and State University, Civil and Enviromental Engineering.

National Instruments. (2006, Sept.). *Measuring Position and Displacement with LVDTs*. Retrieved from NI Developer Zone: http://zone.ni.com/devzone/cda/tut/p/id/3638

Neville, A.M., Dilger, W.H., and Brooks, J.J. (1983). *Creep of Plain and Structural Concrete,* Construction Press, Essex, England.

Østergaard, L., Lange, D.A., Altoubat, S.A., and Stang, H. (2001). *Tensile Basic Creep of Early-Age Concrete Under Constant Load*. Cement and Concrete Research, Vol. 31. pp. 1895-1899.

Pinto, R, and Hover, K.C. (1999). Application of Maturity Approach to Setting Times. ACI Materials Journal. Vol. 96, No.6, pp.686-691.

Poole, J. (2007). *Modeling Temperature Sensitivity and Heat Evolution of Concrete.* PhD Thesis, University of Texas at Austin.

Rao, A. (2008). *Evaluation of Early-Age Cracking Sensitivity in Bridge Deck Concrete.* Masters Thesis, Auburn University.

Raphael, J. (1984, March). Tensile Strength of Concrete. *ACI Journal, 81*(2), 158–165.

Riding, K. (2007). *Early age concrete thermal stress measurement and modeling.* PhD Thesis, University of Texas at Austin, Civil Engineering.

Riding, K., Poole, J.K., Folliard, Juenger, M.C.G., and Schindler, A.K. (2011). New Model for Estimating Apparent Activation Energy of Cementitious Systems. ACI Materials Journal. Vol. 108, No. 5, pp. 550-557.

RILEM Technical Committee 119-TCE. (1998). Testing of the Cracking Tendency of Concrete at Early Ages in the Cracking Frame Test, In RILEM Report 15, Prevention of Thermal Cracking in Concrete at Early Ages, R. Springenschmid (Ed), London, E & FN Spon, pp. 315-339.

Scheaffer, R.L., Mulekar, M.S., and McClave, J.T. (2010). Probability and Statistics for Engineers, fifth ed, Brooks/Cole, Boston, Massachusetts.

Schindler, A. (2004). Prediction of Concrete Setting. In J. Weiss, K. Kovler, J. Marchand, & S. Mindess (Ed.), *International RILEM Symposium on Concrete Science and Engineering.* RILEM Publications SARL.

Schindler, A. (2004), Effect of Temperature on Hydration of Cementitious Materials. ACI Materials Journal. Vol. 101, No. 1, pp. 72-81.

Schindler, A., & Folliard, K. (2005). Heat of Hydration Models for Cementitious Materials. *ACI Materials Journal*, 24–33.

Shilstone, J. (1990, June). Concrete Mixture Optimization. *Concrete International, 12*(6), 33–39.

TxDOT. (2011). *Chemical Admixtures for Concrete.* Retrieved from Material Producer List: http://ftp.dot.state.tx.us/pub/txdot-info/cmd/mpl/admixtur.pdf

TxDOT. (2011, April). *Hydraulic Cement.* Retrieved from Materials Producer List: http://ftp.dot.state.tx.us/pub/txdot-info/cmd/mpl/cement.pdf

Viviani, M. (2005). *Monitoring and Modeling of Construction Materials During Hardening.* PhD Thesis, Swiss Federal Institute of Technology, Lausanne, Switzerland.

Westman, G. (1999). Concrete Creep and Thermal Stresses: New Creep Models and their Effect on Stress Development, Doctoral Thesis, Luleå University of Technology, Luleå, Sweden.

Whigham, J. (2005). *Evaluation of Restraint Stresses and Cracking in Early-Age Concrete with the Rigid Cracking Frame.* Masters Thesis, Auburn University.

Wittman, F., & Roelfstra, P. (1980). Total Deformation of Loaded Drying Concrete. *Cement and Concrete Research, 10,* 601–610.